

UNIVERSITY OF OXFORD

Laser Writing of Coherent Colour Centres in Diamond

by

Yu-Chen Chen

St Anne's College

A thesis submitted the degree of

Doctor of Philosophy

in the

Department of Materials

December 2017

Abstract

Optical active point defects in crystals have gained widespread attention as photonic systems that could be applied in quantum information technologies[1, 2]. However, challenges remain in the placing of individual defects at desired locations, an essential element of device fabrication. Here we report the controlled generation of single negatively charged nitrogen-vacancy (NV^-) centres in diamond using laser writing[3]. Aberration correction in the writing optics allows precise positioning of the vacancies within the diamond crystal and subsequent annealing produces single NV^- centres with a probability of success of up to 45%, located within about 200 nm of the desired position in the transverse plane. A simple model was established to understand the mechanism of vacancies generation and estimate the success probability of NV^- centres generation. Selected NV^- centres display stable, coherent optical transitions at cryogenic temperatures, a prerequisite for the creation of distributed quantum networks of solid-state qubits. Strain measurement results of selected NV^- centres show that the broadening of NV^- optical transitions is due to local strain. The results illustrate the potential of laser writing as a tool for defect engineering in quantum technologies and extend laser processing to the single-defect domain.

Popular Abstract

The microelectronic industry has exponentially improved the process power by miniaturizing the electronics in computer since the development of the silicon transistor. However, this trend is reaching a fundamental limit in the near future since the size of the transistor is approaching the atomic scale. Efforts has been shifted to establish a new type of computer, operated in completely different way from traditional computer, called quantum computer. A quantum computer exploits the quantum phenomena of superposition and entanglement of the unique properties of subatomic particles, resulting in extending beyond the binary on/off capability of the transistor. As a result, the quantum computer provides more powerful capability. This device is expected to be able to calculate the most complicated systems in nature, in turn accelerating the developments in area such as physics and medicine. The challenge now is to realize a system in practice.

There are many candidates to realize a quantum computer, but colour centres in diamond have been demonstrated to be one of the most promising candidates. The isolated colour centres can form a quantum bit, also called qubit, which is the fundamental building block of the quantum system. Unlike the current processors controlled by electric signals, the qubits in diamond will be manipulated and read out with pulses of *light*. To realize a scalable device, a method to engineer isolated colour centres which persist optimal optical and quantum properties at any place on demand with high accuracy.

This thesis studies and develops a new method to place colour centres in diamond using a ultrafast pulsed laser. After illuminating laser pulses on diamond and subsequent annealing, the probability of generating isolated colour centres is up to 45%, located within about 200 nm of the desired position. These colour centres still persist good quantum properties and moreover, possess perfect optical properties, which has never been achieved by all current placement methodologies. These achievements form the highlights of this thesis.

Citations to Previously Published Work

Large portions of Chapter 5, large portions of Chapter 6, Most of Chapter 7 and some portions of Chapter 8 have appeared in the following paper:

”Laser writing of coherent colour centres in diamond”, Yu-Chen Chen, Patrick S. Salter, Sebastian Knauer, Laiyi Weng, Angelo C. Frangeskou, Colin J. Stephen, Shazeaa N. Ishmael, Philip R. Dolan, Sam Johnson, Ben L. Green, Gavin W. Morley, Mark E. Newton, John G. Rarity, Martin J. Booth and Jason M. Smith, *Nat. Photonics* **11**, 77-80 (2017).

Acknowledgements

This thesis cannot have been accomplished without the Photonic Nanomaterials Group. Thanks to all group members, past and present, who have established such fun and inspiring working environment over the past 4 years. I would like to particular thanks Phil and Sam for training, support and advises in research. Without them, I could not have achieved such a successful DPhil research. In addition, thanks goes to Laiyi for the support in PLE measurements. Everyone in the group is acknowledged for the supports and advises in daily lab works. Phil, Sam, Sanmi and Shazeaa are acknowledged for their proofreading help. Matthew Wincott has to be mentioned too, for having written the confocal software which has worked so well. Thanks also must go to Patrick Salter and Prof. Martin Booth in Department of Engineering for laser writing in our samples, advises and helpful discussions. Angelo Frangeskou and Colin Stephen in University of Warwick are thanks for help with annealing the diamond samples. Ben Green and Shazeaa Ishmael in University of Warwick are acknowledged for help with cross polarization and Raman mapping. Sebastian Knauer and Prof. John Rarity in University of Bristol are gratefully acknowledged for their collaboration on the spin coherence work. Outside of the lab, I have to thanks for my friends in St Anne's College who have made my dairy life in Oxford so enjoyable. Special thanks must go to De Beers for the financial support to my DPhil study.

Foremost, I would like to express my sincerest gratitude to my supervisor Prof. Jason Smith. It is very enjoyable and fantastic that I study my DPhil under his supervision. Jason always offers excellent science guidance and inspires me to design new experiments to explore the physics in my project. He is the fantastic mentor and this project is indebted to him.

Last but not least, I would like to thank my family Hui-Shuang and Yu-Hsuan. I cannot have been here without your love, inspiration and support throughout my life.

Contents

Abstract	i
Acknowledgements	iv
List of Figures	viii
List of Tables	xvi
Abbreviations	xvii
Physical Constants	xviii
Symbols	xix
1 Introduction	1
1.1 Quantum applications of colour centres in crystal	1
1.2 The NV centre in diamond	2
1.3 Generating NV centres with high position accuracy	4
1.4 Thesis outline	5
2 Literature Review	9
2.1 Colour centres in diamond	10
2.1.1 The NV ⁻ centre	11
2.2 Ion implantation	16
2.2.1 Annealing	17
2.2.2 Coherence properties of the ion-implanted NV ⁻ centre	18
2.2.3 Light-weight ion implantation	19
2.3 Electron irradiation and δ -doped diamond	20
2.4 Ultra-fast laser writing	20
2.5 Summary	22
3 Theoretical background	24
3.1 Mechanism of laser-induced damage	25

3.1.1	Tunneling ionization and multiphoton ionization	26
3.1.2	Avalanche ionization	29
3.2	Vacancy diffusion	30
3.3	The NV centre in diamond	31
3.3.1	The energy level structure	31
3.3.2	Photon emission statistics	33
3.4	Excited state and strain splitting	36
3.4.1	Excited state fine structure	36
3.4.2	Strain splitting	38
3.4.3	The ionization and repump of the NV ⁻ centre	41
3.4.4	Broadening of the zero-phonon line	43
3.4.4.1	Homogeneous broadening mechanism	43
3.4.4.2	Inhomogeneous broadening mechanism	45
3.5	Optically detected magnetic resonance	46
3.6	Theory for estimating the probability of generating NV ⁻ centres	48
3.7	Summary	51
4	Experimental Methods	53
4.1	Laser writing	54
4.1.1	Experimental set-up	54
4.1.2	Aberration correction and size of focal spot	55
4.2	Diamond samples and annealing	58
4.3	Confocal microscope	59
4.4	Hanbury-Brown and Twiss and lifetime	63
4.5	Optically Detected Magnetic Resonance	65
4.5.1	Continuous wave optically detected magnetic resonance	65
4.5.2	Hahn echo measurements	66
4.6	Low temperature	68
4.6.1	Photoluminescence excitation measurements	68
4.6.2	Methods of full zero-phonon line spectra measurements	72
4.7	Summary	75
5	Laser Fabrication and Nitrogen-Vacancy Generation	76
5.1	Introduction	76
5.2	Laser fabrication	78
5.2.1	Damage array and pulsed laser energy	78
5.3	Characterization of laser written array pre-annealing	82
5.3.1	Photoluminescence Image	82
5.3.2	Spectroscopy	83
5.4	Vacancy generation mechanism	85
5.4.1	Models	85
5.4.2	Experimental results and fits	86
5.5	Characterization of post-annealing array	89
5.5.1	Annealing at 800°C	91

5.5.2	Annealing at 900°C	93
5.5.3	Annealing at 1000° C	100
5.5.4	Annealing at 1200° C	109
5.6	Optical properties and statistics analyses of the laser-generated NV ⁻ centres	111
5.7	Estimation of the probability of generating NV ⁻ centres	117
5.8	Summary	121
6	Positioning Accuracy of Laser Written NV Centres	125
6.1	Introduction	125
6.2	Size of laser-induced features and number of vacancies	126
6.3	Displacement of the laser-generated NV ⁻ centre	129
6.3.1	Distortion of the PL image and recovery	129
6.3.2	Displacement of the NV ⁻ centres after annealing	132
6.4	Summary	138
7	Coherent Properties of Laser Written NV Centres	140
7.1	Introduction	140
7.2	Spin properties of the NV ⁻ centres	141
7.2.1	Continuous wave optically detected magnetic resonance measurements	141
7.2.2	T ₂ coherence time	144
7.3	Optical coherent properties	148
7.3.1	Spectroscopy in 4.2 K	148
7.3.2	Photoluminescence excitation measurements	149
7.4	Summary	160
8	Strain Environment of Laser Written NV Centres	162
8.1	Cross polarization	163
8.2	Raman mapping	164
8.3	Photoluminescence excitation	167
8.3.1	PLE strain measurement results	168
8.3.2	Comparison of the strain splitting with theory	172
8.3.3	Linewidth and strain splitting	174
8.4	Summary	177
9	Conclusion & Outlook	180
9.1	Conclusion	180
9.2	Future prospects	184
	Bibliography	186

List of Figures

1.1	The NV ⁻ centre in diamond. a , The schematic picture of its energy level structure. There is a zero-field splitting of about 2.88 GHz (1.42 GHz) between the spin sublevels (m_s) of the ground state (excited state). The zero-phonon line (ZPL) is at 637 nm. Figure adapted from [4]. b , Fluorescence spectrum of single NV ⁻ centre at 4 K. The ZPL at 637 nm and the phonon sideband (PSB) from 650 nm are indicated. The inset picture is the chemical structure of the NV ⁻ centre[4]. The NV centre consists of a Nitrogen atom and an adjacent vacancy along the [111] crystalline direction. Reproduced with permission from [4].	3
2.1	Summary of the spectra of the single photon emitters in diamond up to date. For the centres with wavelengths shorter than 730 nm, the length of the coloured lines indicate the approximately width of emission spectra of them including phonon sideband. The wavelength given for each colour centre represents the ZPL wavelength. Black arrows denote centres which exhibit spin manipulation[5]. Reproduced with permission from [5].	11
2.2	Nanoscale engineering and optical addressing of single NV centres in diamond. The nanoscale implantation is realised through the pierced hollow tip of the atomic microscope. A fluorescence image (confocal scan) shows a hexagonal pattern implanted in diamond with N ions at 5 keV and fluence of $1 \times 10^{13} \text{ cm}^{-2}$. A stimulated emission depletion microscopy image of one particular spot reveals an ensembles of about 12 single NV centres. Two NV centres separated by 16 nm are resolved[6]. Reproduced with permission from [6].	16
2.3	a , PLE spectrum showing the narrowest linewidth (top) obtained by averaging twenty-one successive PLE scans (bottom). b , PLE spectrum taken using 575 nm resonant excitation of the NV ⁰ state to repump back to NV ⁻ [7]. Reproduced with permission from [7]. . .	18
3.1	Schematic graphs of the ionization of an electron in a band structure for different values of the Keldysh parameter[8]. In fact, the electron is excited from the valence band to conduction band, instead of ionized. a , Tunneling ionization. b , Intermediate. c , MPI.	26

3.2	Schematic graphs of Avalanche ionization. a , An initial free electron linearly absorbs several photons via free-carrier absorption. b , The free electron in a impacts on another atom, resulting in ionizing another electron.	29
3.3	a , Typical spectra of single NV^0 (blue curve) and NV^- (red curve) centre. The ZPLs of them are labelled by asterisk (*). The inset shows schematic representation of the nitrogen vacancy centre structure illustrating the lattice vacancy (open circle), the substitutional nitrogen atom (pink) and the carbon atoms forming diamond matrix (olive)[9]. b , The energy position of NV^- ground state relative to the energy band structure of diamond. The electron spins (blue arrow) fill the molecular orbitals following the Hund's rules[4]. Reproduced with permission from [4].	32
3.4	a , Schematically theoretical HBT spectra for coherent light (blue), a two-level quantum system (green) and a three-level quantum system (red). b , Schematic three-level system of the NV centre with transition rate constants, k . Level $ 1\rangle$ is the ground state, level $ 2\rangle$ is the excited state and level $ 3\rangle$ is intermediate state. The red solid lines denote optical transition and the blue dash lines indicate the non-radiative transition. Adapted from [10].	33
3.5	Schematic picture of the excited state fine structure due to spin-orbit and spin-spin interactions. The electron configuration of the NV^- excited state is also shown. The spin-orbit interaction separates the states $\{A_1, A_2\}$, $\{E_x, E_y\}$ and $\{E_1, E_2\}$ by λ_z . The spin-spin interaction further change the energies difference between different spin projections and also splits the A_1 and A_2 states. According to Maze et al's theory, the spin-spin interaction also mixes the $E_{1,2}$ and $E_{x,y}$ states[11]. Figure is adapted from [11].	37
3.6	Energies of the excited states as a function of uniaxial transverse strain, expressed in the units of the splittings between the E_x and E_y states[11]. Figure is reproduced from [11].	40
3.7	Optical transitions of the NV^- centre. a , All possible transitions between the ground and excited states, with direct transitions indicated with solid lines, and Fermi's golden rule forbidden transitions indicated with dash lines. b , PLE spectrum. c , Frequencies of all transitions shown in a as a function of strain[136].	41
3.8	Schematic picture of the charge transfer process for the NV^- and NV^0 centre. a , Ionization process from NV^- to NV^0 includes two-photon absorption and an Auger process that releases enough energy to detach an electron from the defect. b , NV^- restoring process includes two electrons excited by laser and migration of deep hole[12]. Figures are adapted from [12].	42
3.9	Log-log scatter plot of the PLE linewidths as a function of temperature from two single NV^- centres and the PL linewidths from other three NV^- centres. The solid line is the best fit to Equation 3.21[13]. Reproduced with permission from [13].	43

3.10	Spectral jumping of the NV ⁻ centre with two to different types of repump, a , 532 nm repump and b , 575 nm repump[12]. Reproduced with permission from [12].	45
3.11	ODMR spectra of the a , ¹⁴ N and ¹⁵ N hyperfine structure and b , ¹³ C hyperfine structure. The spectra were obtained at ambient temperature without applied external magnetic field[14]. Reproduced with permission from [14].	47
4.1	a , Schematic of laser processing optical set-up. The phase pattern of the laser beam is modified by the liquid crystal phase-only spatial light modulator (SLM) to correct the aberrations in the system and those introduced by focussing into the diamond. b , The effect of the aberration correction on the laser focal intensity distribution when focused through the interface between the immersion oil and diamond to a depth of 50 μm. Left graph shows that the focus is significantly elongated in z axis by spherical aberration without aberration correction. Right graph presents that a good z axis focus is achieved with the SLM. Figure courtesy of Patrick Salter.	55
4.2	Typical PL image of single NV ⁻ centre.	59
4.3	Schematic layout of the optical components for room temperature operation and the custom-built confocal microscope set-up, including all actuators to align the system. All optics are mounted onto a optical table. The output end of the excitation single mode fibre is mounted on a XY-positioner to align the position of the laser beam and the laser beam is collimated by using a ×10 0.25NA objective lens. A 550 nm dichroic mirror is used to separate the excitation and photoluminescence to different direction.	60
4.4	a , Schematic layout of the cw ODMR experimental apparatus. b , Schematic layout of the metal wire and diamond sample.	65
4.5	Pulse sequence for the Hahn echo measurements. Laser gating is indicated in green and microwave gating in blue.	67
4.6	Image of Helmholtz coil in the Hahn echo setup. The optical axis and the microwave input is shown. Inset: example of a sample holder. The image is taken by Sebastian Knauer.	67
4.7	a , Schematic detail layout of the PLE experimental apparatus and the reconfiguration of the scanning head for PLE measurements. b , Schematic diagram of the low temperature apparatus.	69
4.8	A schematic graph of lambda transition.	72
4.9	An example of the PLE spectrum a , with EOM modulation and b , without EOM modulation. The labels with .2 indicate the PLE signals of the second NV ⁻ centre in the same site.	74
5.1	Schematic picture of the damage array.	79
5.2	Transmission microscope image of three graphitization marker rows.	81

5.3	Photoluminescence image of the laser-fabricated array immediately after laser processing (before annealing) of a , sample A and b , sample B. The laser pulse energy increase from the bottom to the top of both images and there are 20 repeats for each energy distribute along the other axis. The red solid lines indicate the lowest laser pulse energy to generate visible fluorescence.	82
5.4	a , Fluorescence spectra from laser-induced features (pre-annealing) of sample A at different laser pulse energies. b , Power saturation measurement of the PL intensity of the GR1 centre.	83
5.5	Logarithmic plot of measured GR1 photoluminescence intensity as a function of laser pulse energy (black squares). The red line is the least-square fit of a power-law relationship corresponding to multi-photon ionization, and provides a much better fit to the five data points below 25 nJ than does the blue line, the best fit to a simple Zener breakdown field model.	86
5.6	a , Room temperature fluorescence spectra of the Array 1 in sample B after annealing at 800°C. b , The scatter plots of the PL intensity of laser-induced damage in Array 1, generated with laser pulse energy of 38.8 nJ as a function of excitation power. The scatter graphs show the photon count rates measured when aligned to the damage feature (squares), off the feature (circles) and the difference between the two (triangles) which present only PL from the feature. The red solid line is the least-squares fit of the saturation Equation 3.15 to the PL intensity.	91
5.7	The optical characterization results of 4P1R, 5P7R and 5P10R in Array 1 sample B after an hour annealing at 900°C. a , Spectra. b , The scatter plots of power dependence measurements of the PL intensity. The red solid lines are the best fits to Equation 3.15. c , HBT measurements of the photon correlation function ($g^{(2)}(\delta t)$). The red lines are the best fits to Equation 3.12 and the depths of the anti-bunching dips are given.	95
5.8	The optical characterization results of 4P1R, 5P7R and 5P10R in Array 1 sample B after three hours annealing at 900°C. a , Spectra of the features. b , The scatter plots of power dependence measurements of the PL intensity. The red solid lines are the best fits to Equation 3.15. c , HBT measurements of the photon correlation function ($g^{(2)}(\delta t)$). The red lines are the best fits to Equation 3.12 and the depths of the anti-bunching dips are given.	98
5.9	The optical characterization results of 4P1R, 5P7R and 5P10R in Array 1 sample B after three hours annealing at 1000°C. a , Spectra of the features. b , The scatter plots of power dependence measurements of the PL intensity. The red solid lines are the best fits to Equation 3.15. c , HBT measurements of the photon correlation function ($g^{(2)}(\delta t)$). The red lines are the best fits to Equation 3.12 and the depths of the anti-bunching dips are given.	101

- 5.10 The summary of the optical properties of 4P1R, 5P7R and 5P10R as a function of annealing conditions. 900-1, 900-3 and 1000-3 indicate the annealing at 900°C for an hour, at 900°C for three hours and at 1000°C for three hours, respectively. **a**, A scatter plot of the P_{sat} values. **b**, A scatter plot of the depth of anti-bunching dips. 103
- 5.11 **a**, The PL image of Array 2 in sample B after annealing 1000°C for 3 hours. The blue square labels four laser-generated NV^- centres without optically detectable residual defects and the red circle labels 'NV pair'. **b**, The PL image of the 'NV pair', circled in **a**. 105
- 5.12 Summary of the optical properties of the NV^- centres generated by various laser pulse energies. **a**, **c**, and **e**, Power dependence measurements of 12P4R, 14P7R and 15P4R, respectively. The solid red lines are the best fits to Equation 3.15. **b**, **d** and **f**, HBT measurements of 12P4R, 14P7R and 15P4R respectively. The red lines are the best fits to Equation 3.12. The P_{sat} values and depths of anti-bunching dips are given in each graph. 106
- 5.13 Typical optical properties of the four NV^- centres labelled by blue square in Figure 5.11a. **a**, Spectrum. **b**, The scatter plots of power dependence measurements of the PL intensity. The red solid line are the best fit to Equation 3.15. **c**, HBT measurements of the photon correlation function ($g^{(2)}(\delta t)$). The red line is the best fit to Equation 3.12. 108
- 5.14 **a**, The PL image of the Array 6 of sample A before annealing. The laser pulse energy increases from the bottom to the top of the the image. The red solid line at laser pulse energy E_{1A} indicates the lowest energy laser pulse that produces visible fluorescence. The decrease in intensity of the features toward the edge of the array is due to off axis aberrations in the confocal microscope. **b**, Typical spectra measured from points in **a** (lower plot) characteristic of GR1 defects, from **c** below energy E_{2A} (middle plot) characteristic of the negatively charged nitrogen-vacancy (NV^-) centre, and **c** above energy E_{2A} (upper plot) characteristic of the radiation B-band. **c**, PL image of the Array 6 of sample A after 1000°C annealing for 3 hours, showing the NV^- centre emission from multiple sites processed with laser pulse energies both above and below E_{1A} . The green line at pulse energy E_{2A} indicates the graphitization threshold. **d** and **e**, The PL image of Array 4 in sample B before annealing and after annealing at 1000°C for 3 hours. The red line at laser pulse energy E_{1B} indicates the lowest energy laser pulse that generates visible fluorescence. The green solid line at laser pulse energy E_{2B} indicates the graphitization threshold. 112
- 5.15 **a**, A typical PL spectrum of the new features below red line in Figure 5.14, indicating they are NV^- centres. **b**, A typical scatter plot of saturation curve for the PL intensity from the laser-generated NV^- centres below the red line. The red solid line is the least square fit of the saturation equation. 113

5.16	Spectra from the sites with laser pulse energy greater than E_{2A} . B-band emission is observed (top plot), and spectra in which B-band and the NV^- centre emission are both present (middle plot). The spectra are offset in the vertical direction for clarity.	114
5.17	a , A typical histogram showing photon autocorrelation function $g^{(2)}(\delta t)$ from a single NV^- centre. Fits to Equation 3.12 is shown as solid red line. b , Histogram of $g^{(2)}(0)$ for the different laser processing sites, allowing identification of sites of single, double, and triple NV^- centres generation. c , Map of the number of NV centres generated at different sites. 'NV pair' refers to a double NV where the two defects are spatially resolved. d , Plot of the number of single (red), double or 'pair' (yellow), and triple (blue) NV^- centres generated in each row of 20 sites as a function of laser pulse energy measured before the objective lens in the writing apparatus. The total number generated per row is shown in black.	115
5.18	A typical semilogarithmic plot of time-resolved PL for the laser-generated NV^- centre. The data are corrected for background and shown as scatter graphs. Fits to single exponential decays are shown as red line.	116
5.19	A scatter plot of the probability of the number of NV centres per laser damage site for a sample A and b sample B. The black squares are calculated from the Poisson distribution with mean value equal to 1 for sample A and with mean value equal to 0.75 for sample B. The red circles are the experimental data set from the first row below the GR1 visibility threshold.	119
6.1	Magnified image of the NV^- centre fluorescence relative to the laser processing grid. Red circles centre on the grid points are 1 μm in diameter.	130
6.2	Scatter plot of the mean value of the nearest neighbor distance (M_d) as a function of the radial distance from the centre of field of view. The red solid line is the least-square fit of Equation 6.5.	131
6.3	Schematic graph of the geometry of the $n-1^{th}$ and n^{th} shell points.	133
6.4	Positional accuracy of the NV^- centres generation in a sample A and b sample B. Labels show the displacement of NV centres from their theoretical grid positions (in μm), after removal of a quadratic field distortion. The labels are colour-coded into four magnitude groups to reveal systematic trends that would indicate further uncompensated field distortion.	135
6.5	Histogram of the displacement in the image plane for the NV^- centres in sample B measured after correction for field distortion in the confocal microscope. The data are fitted with a cylindrical distribution function, Equation 6.9.	136

7.1	a , A typical scatter plot of cw ODMR spectrum of a laser-generated NV ⁻ centre well below the GR1 visibility threshold. The red line is the least square fit of a Lorentzian function. b , A typical scatter plot of the hyperfine structure of the laser-generated NV ⁻ centres. The red line is the least square fit of 3 Lorentzian functions.	141
7.2	Typical ODMR results of the NV ⁻ centers above the GR1 visibility threshold. a , A PL image of an 'NV pair'. b and c , ODMR spectra from the top and bottom NV ⁻ in a , indicated by red arrows. The red circle is a illustrated label of the initial laser writing position.	143
7.3	Pulse sequence for Hahn echo measurements. Laser gating indicated in green and microwave gating in blue.	144
7.4	Hahn echo data for a 21P7R, b 20P5R, c 20P18R and d 15P1R in sample A. The red lines are the best fits to Equation 7.1. The inset in d is the PL image of 15P1R, showing that it is an 'NV pair' and the red circle is a schematic label of the position of original laser damage. The Hahn echo measurement was carried out on the bottom NV ⁻ centre.	145
7.5	Hahn echo data for a NV3 and b NV22 in sample B. The red lines are the best fits to Equation 7.1.	146
7.6	A typical spectrum of the laser-generated NV ⁻ centre at 4.2 K. The sharp line is the ZPL of the NV ⁻ centre.	148
7.7	a , Histogram of the single-scan linewidths from sample A. b , Histogram of linewidths including spectral jumping from sample A.	149
7.8	a , Histogram of the single-scan linewidths from sample B. b , Histogram of linewidths including spectral jumping from sample B.	150
7.9	a , Photoluminescence excitation (single sweep) of three different NV ⁻ centres, with two showing Lorentzian peaks below 14 MHz in width. Full-width-at-half-maximum values from Lorentzian peak fits are given, with errors in parentheses. b , Colourscale map of repeated PLE spectra of NV3, showing a stable line over 70 laser sweeps with an inhomogeneous line width of 16.1 MHz. c , Spectral jumping as a result of a 532 nm repump pulse required to restore the negative charge state upon ionization. Lower plots in b and c are aggregates of the consecutive sweeps in the colourscale images. d , Scatter plot of the single-scan linewidth (solid circles) and repump-broadened linewidth (open circles) for different energies of laser writing pulse. Data from sample A and B are shown as red and black circles respectively. The dashed blue line is a guide showing a trend to larger single-scan linewidths with higher pulse energies.	152
7.10	Time-resolved photoluminescence result of NV3 in sample B at 4.2 K, fitted with a single exponential decay convoluted with the instrument response of the TCSPC apparatus.	153

7.11	A semilogrithic scatter plot of the inhomogeneously broaden linewidths from sample B as a function of their displacements from the initial laser writing position. The dashed blue line is a guide showing a trend to larger inhomogeneously broaden linewidth with larger displacement.	154
7.12	A semilogrithic scatter plot of the single-scan linewidths from sample B as a function of their ZPL wavelength.	156
7.13	Map of the single-scan linewidths of the measured NV ⁻ centres in sample B. The laser pulse energy decreases from the bottom to the top of the image.	157
8.1	Birefringence image of sample B measured using orthogonal linear polarizers. Red arrows indicate the locations of the rows of features created by the three highest writing pulse energies in the main array.	163
8.2	a , Colourscale map of the width of the first order Raman peak. b , Example fits of the pseudo-Voigt function for the three points labelled in plot a . c and d are maps of the Raman peak position and peak amplitude obtained from the fits.	165
8.3	Full PLE spectra of the NV ⁻ centres without detectable strain field. a , NV3. b , NV4. c , NV29. d , NV6. e , NV31. NV31 is a double NV ⁻ site and the PLE lines without labels in the low energy region are from the second NV ⁻ centres. The question marks of the E _{1,2} lines in b , c and d indicate that they are too far away from the theoretical value.	169
8.4	Full PLE spectra of the NV ⁻ centres with detectable strain field and the splitting between E _x and E _y states are given in each graph. The PLE lines from the second NV ⁻ centre are labelled with ₂ . a , NV24. b , NV25. Forbidden means that the transition lines are from Fermi's golden rule forbidden transition. c , NV30. d , NV27. e , NV18. f , NV16.	171
8.5	Excited state energy structure as a function of the transverse strain for 7 measured NV ⁻ centres. The data sets of the 7 NV ⁻ centres were labelled by blue circles. The solid lines are the eigenvalues of excited states from theory. The red line is A ₂ state, the blue line is A ₁ state, the green line is E _x state, the pink line is the E _y state, the yellow line is E ₁ state and the black line is E ₂ state.	173
8.6	Scatter plot of the strain-induced PLE splitting as a function of the laser writing pulse energy.	175
8.7	Scatter plot of the strain-induced PLE splitting as a function of the linewidth of E _x PLE line.	176
8.8	a , Scatter plot of the strain-induced splitting as a function of the ZPL position. b , Scatter plot of the line width of ZPL as a function of the ZPL position.	177

List of Tables

3.1	Photon polarization for the optical transitions between the excited states and ground state. Linear polarizations are denoted by \hat{x} and \hat{y} , while circular polarizations are represented by $\hat{\sigma}_{\pm} = \hat{x} + i\hat{y}$ [11]. Reproduced with permission from [11].	41
5.1	Laser pulse energies used for the generation of vacancies. The energies measured before the objective lens are the values quoted in this work. The first row is the parameters of the graphitization features and there is a 30 μm gap between the graphitization features and the actual array.	80
5.2	The temperature and duration of the three-step annealing recipe following Chu et al's works[7]. Adapted from [7].	90
5.3	The summary of the annealing history of the arrays in sample A and B.	90
5.4	Summary of the laser pulse energy of the three laser-induced NV ⁻ centres in Array 1 sample B.	94
5.5	Summary of the optical properties of 4P1R, 5P7R and 5P10R after an hour and 3 hours annealing at 900°C.	99
5.6	Summary of the laser pulse energy and optical properties of the three selected NV ⁻ centres in Array 2.	107
6.1	Summary of the size of the laser-induced damage and the numbers of vacancy for 9-photons and 15-photons absorption cases. Here, $N_{37.7}$ denotes the number of vacancies created at graphitization threshold, N_{GR1} denotes the number of vacancies created at the first row below the GR1 visibility threshold and N_{single} is the number of vacancies at the lowest pulse energy to produce single NV ⁻ centres.	127
7.1	Summary of the laser pulse energy of the NV ⁻ centres which T_2 times measurements were carried on. 21P7R, 20P5R, 20P18R and 15P1R are in sample A. NV3 and NV18 are in sample B.	144
8.1	The single-scan linewidths of the E_x transitions of NV3, NV4, NV29, NV6 and NV31.	170
8.2	The strain-induced splitting and local stress of NV24, NV25, NV30, NV27, NV18 and NV16. The local stresses are estimated using Equation 3.20.	174

Abbreviations

AFM	A tomic F orce M icroscopy
AOM	A cousto- O ptic M odulator
CVD	C hmical V apor D eposition
CW	C ontinuous W ave
DLW	D irect L aser W riting
EPR	E lectron P aramagnetic R esonance
FWHM	F ull W idth H alf M aximum
HBT	H anbury- B rown and T wiss
MPI	M ulti- P hoton I onization
NA	N umerical A perture
NV	N itrogen- V acancy
ODMR	O ptically D etected M agnetic R esonance
PL	P hoto L uminescence
PLE	P hoto L uminescence E xcitation
PSB	P honon S ide B and
QD	Q uantum D ot
QIP	Q uantum I nformation P rocessing
SLM	S patial L ight M odulator
SNR	S ignal to N oise R atio
SPAD	S ingle P hoton A valanche D etecor
SiV	S ilicon- V acancy
TRPL	T ime- R esolved P hoto L uminescence
ZPL	Z ero P honon L ine

Physical Constants

Speed of Light	c	$=$	$2.997\,924\,58 \times 10^8 \text{ ms}^{-1}$
Planck's Constant	h	$=$	$6.626 \times 10^{-34} \text{ J s}^{-1}$
Reduced Planck's Constant	\hbar	$=$	$1.054 \times 10^{-34} \text{ J s}^{-1}$
Permittivity of Free Space	ε_0	$=$	$8.85 \times 10^{-12} \text{ F m}^{-1}$
Boltzmann Constant	k_B	$=$	$1.38 \times 10^{-23} \text{ J K}^{-1}$
Bohr Magneton	μ_B	$=$	$9.274 \times 10^{-24} \text{ J T}^{-1}$
Charge of the electron	e	$=$	$1.602 \times 10^{-19} \text{ C}$

Symbols

D_{gs}	Zero-field splitting of the NV ⁻ ground state	
$d_{ }$	Axial electric dipole component	
d_{\perp}	Non-axial electric dipole component	
Π_k	K component of the total effective electric field	
\bar{g}	Effective g-factor tensor	
λ_z	Axial strength of the spin-orbital interaction of the NV ⁻ excited state	
Δ	Zero-field splitting of the NV ⁻ excited state	
Δ'	Gap between A ₁ and A ₂ states	
Δ''	Spin mixing term	
δ	Strain parameter	
\tilde{v}	Orbital operator	
ω	Laser frequency	
m	Reduced mass	
n	Refractive index	
E_g	Direct bandgap	eV
D	Diffusion coefficient	cm ² s ⁻¹
E_a	Activation energy	eV
I_{sat}	Saturation intensity	counts/s
P_{sat}	Saturation power	mW
τ	Lifetime	ns

For Hui-Shuang & Yu-Hsuan

Chapter 1

Introduction

1.1 Quantum applications of colour centres in crystal

The quantum information processing (QIP), quantum sensing and quantum key distribution (QKD) have attracted many researchers' attentions, because these technology can outperform their classical counterpart. The significant difference between these quantum applications and their classical counterpart is the usage of the superposition and entanglement of spin states. Colour centres in wide bandgap materials such as diamond and silicon carbide have been believed to be one of the promising quantum systems due to the following reasons. First, they can be optically excited and readout, showing promise as quantum light sources and providing an optical interface[15–19]. Moreover, some of them are photostable single photon emitters[5, 18, 20] which is important in QIP and QKD applications[21–24]. The

realization of entangled networks for sensing or QIP with the colour centres in solid state[25, 26] needs coherent photon emission, namely indistinguishable photons. The coherence of the optical transition have been observed in some defects at cryogenic temperatures[27, 28].

Secondly, the superposition and entanglement of spin states will be broken down via the interaction with environment. The crystal can provide a defect-free and low noise environment, ensuring the colour centres to maintain good spin and optical coherence properties. The colour centres in defect-free crystal are perfect systems for the detection of weak environmental change at nanoscale, such as magnetic field, electric field and temperature sensing[29–31].

Finally, solid state also provides a flexible and robust platform in engineering 2D and 3D pattern of colour centres[32, 33]. The 2D array of colour centres is useful to measure the gradient of spatial distribution of fields and temperature[34] and engineer scalable quantum bit (qubit).

1.2 The NV centre in diamond

Diamond crystals provide a robust platform to generate photostable single photons at room temperature[35, 36]. Diamond is an almost spin-free material, with only 1.1% ^{13}C (spin = 1/2) natural abundance, which would benefit the spin coherence properties of any confined spin system. The wide bandgap of 5.5 eV has allowed over 500 impurities or defects to be optically emissive[37]. Among many colour centres in diamond, the negatively charged Nitrogen-Vacancy (NV^-) centre, as

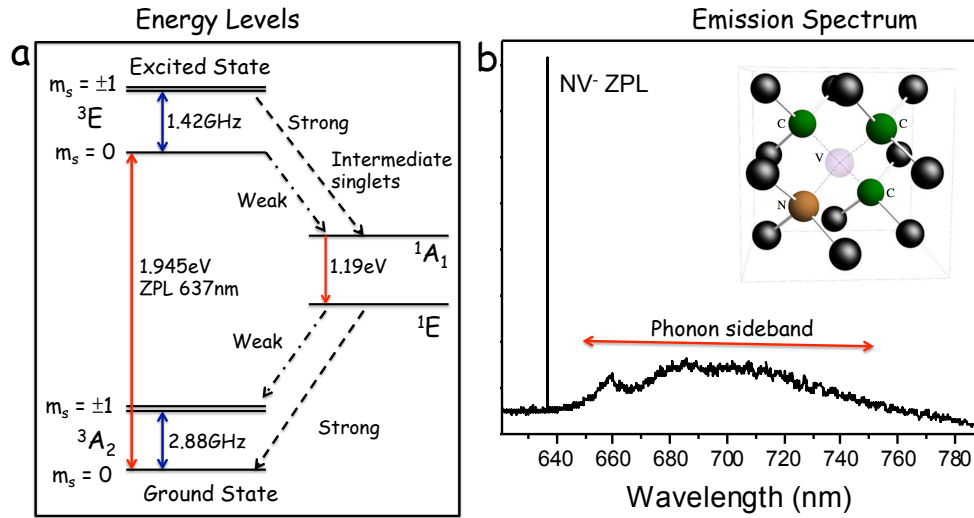


FIGURE 1.1: The NV⁻ centre in diamond. **a**, The schematic picture of its energy level structure. There is a zero-field splitting of about 2.88 GHz (1.42 GHz) between the spin sublevels (m_s) of the ground state (excited state). The zero-phonon line (ZPL) is at 637 nm. Figure adapted from [4]. **b**, Fluorescence spectrum of single NV⁻ centre at 4 K. The ZPL at 637 nm and the phonon sideband (PSB) from 650 nm are indicated. The inset picture is the chemical structure of the NV⁻ centre [4]. The NV centre consists of a Nitrogen atom and an adjacent vacancy along the [111] crystalline direction. Reproduced with permission from [4].

shown in Figure 1.1, is the most well studied and is believed to be one of the best candidates for many quantum applications.

The NV centre consists of a Nitrogen atom and an adjacent vacancy, shown in the inset of Figure 1.1b. The discrete defect levels are deep within the band gap of diamond, so that the continuum of valence and conduction band levels are not involved in the optical transitions, resulting in the sharp ZPL and well defined phonon sideband [4], as shown in Figure 1.1b. The fluorescence of the NV⁻ centre is spin-dependent due to the spin-selective non-radiative relaxation transition to the intermediate state, resulting in the emission which is directly related to the spin state. Thanks to the spin-dependent fluorescence and the zero-field splitting of the ground state triplet, the spin states can be read out by optically

detected magnetic resonance (ODMR). Thus, the spin state can be manipulated by applying various microwave sequences. It has been demonstrated that two spatially separated NV centres can generate indistinguishable photons[38, 39] using Hong-Ou-Mandel (HOM) interference. In order to obtain high generation efficiency of distinguishable photons, the NV centres with stable and coherent optical transition are required.

1.3 Generating NV centres with high position accuracy

The NV centre has been demonstrated as a promising candidate for many applications in the fields of quantum information, quantum optics and metrology[30, 31, 39, 40]. However, it is desirable for any technology based on NV centres to be able to place them at desired locations in a piece of diamond. Engineering them at desired positions with an accuracy of 10 nm~1 μ m enables to place them under solids immersion lenses, in photonic structure or making arrays for magnetometry[41–43]. Most placement methodologies of NV⁻ centres involve irradiation of diamond with electrons or ions, generating a large number of residual defects in the diamond. The residual defects degrade the coherence properties of the colour centre. Although progress has recently been made using advanced annealing recipes and low-energy electron beams[7, 44], new methods for placement of colour centres with minimum residual lattice damage are desired.

This thesis will demonstrate the generation of single NV^- centres with good coherence properties using a femtosecond pulsed laser. Laser writing has a 3D fabrication capability for defects in diamond, so it ought to be able to generate deeper NV^- centres, eliminating the degradations of coherence properties from surface defects. In addition, the non-linearity may allow to develop colour centre writing processes that produce less residual defects. Therefore, it is proposed that laser writing is capable of generating NV^- centres with good coherence properties. This thesis will also demonstrate that laser writing can generate the NV^- centres with optical coherence properties, which have never been achieved by the current methods. The fundamental objective of this project is to find out the laser energy and annealing conditions generating single NV^- centres, along with optical and spin characterizations of the laser-generated NV^- centres. The positioning accuracy of the laser-generated NV^- centres in x-y plane is demonstrated to be sub-micron, which is of interest for some quantum applications.

1.4 Thesis outline

The thesis will be structured as follows:

Chapter 2 : Literature Review

A review of the studies of the NV^- centre will first be discussed. The diversity of applications of the NV will be also mentioned. This chapter will review various current methods used to generate the NV^- centre and discuss their significant achievements and challenges, including the nitrogen ion-implantation, light-weight ion implantation and the electron irradiation

combined with δ -doped diamond method. Since the anneal is an essential and critical process to generate the NV^- centre with good properties, the development of annealing conditions will be discussed. Finally, the attempts of creating NV^- centres using femtosecond pulsed laser will be reviewed.

Chapter 3 : Theoretical Background

The fundamental theories required to describe the laser writing of the NV^- centres and characterizations of the optical and spin properties will be discussed in two parts. The first part will describe three possible models of laser writing of vacancies and the theory of the vacancy diffusion. Secondly, the electronic structures of the NV^- centre and its single photon emission properties will be stated. The spin Hamiltonian of the excited state under transverse strain will be presented. Two ZPL broadening mechanisms will be described along with the mechanism of ionization of the NV^- centre and repump. The ODMR experiments will also described.

Chapter 4 : Experimental Methods

The laser writing apparatus is first described (laser writing process conducted by Patrick Salter). The aberration correction of the laser writing apparatus will then be described, since it helps a lot to reduce the size of laser-induced damage. Other parameters which decreases the damage size will also be briefly discussed. Information of the diamond samples will be presented, along with the methods and equipments used to anneal the samples (performed by Angelo Frangeskou and Colin Stephen at University of Warwick). Finally, many experimental set-up and methods used to characterize the

properties of the laser-induced NV^- centre will be described.

Chapter 5 : Laser fabrication and Nitrogen-Vacancy Generation

This chapter will present the optical characterization of the laser-induced damage and NV^- centres after annealing. These include PL images, spectra, power dependence, HBT and lifetime measurements. The mechanism of vacancy generation has been determined both theoretically and experimentally to be multiphoton ionization. Various annealing conditions have been tried and the results of them will be presented and discussed. The successful probability of generating single NV^- centres will be determined using the result of HBT measurements. A simple model was established to estimate the probability of generating single NV^- centres per site.

Chapter 6 : Positioning Accuracy of Laser Written NV Centres

The number of the laser-generated vacancies have been estimated based on the graphitization threshold and the size of the laser-induced damage with the consideration of multiphoton absorption. The displacement of the laser-generated NV^- centres with aberration correction has been calculated from the PL image. The positioning accuracy of laser writing will be given, based on the fitting of a vacancy diffusion function to the displacement histogram.

Chapter 7 : Coherent Properties of Laser-generated NV Centres

The spin and optical coherence properties of the laser-generated NV^- centres will be discussed in this chapter. Cw ODMR measurements have been used

in the preliminary investigation of the spin properties of the laser-generated NV⁻ centres. Hahn echo measurements have been carried out on them to obtain the T₂ coherence times (conducted by Sebastian Knauer in University of Bristol). The optical coherence properties of the laser-generated NV⁻ centres have been determined by measuring the linewidth of their ZPL at 4.2 K.

Chapter 8 : Strain Measurements

The optical coherence properties of the laser-generated NV⁻ centres are influenced by the local strain. Three methods have been used to measure the local strain. Cross polarization and Raman mapping provide a 2D image of the strain distribution with low sensitivity of the strain. PLE strain measurements of a selection of the laser-generated NV⁻ centres will be presented and discussed. The PLE strain results will be fitted with the theory of the excited state strain splitting.

Chapter 9 : Conclusions

Here the thesis will be summarized and the future outlook will be also discussed.

Chapter 2

Literature Review

Colour centres in diamond are believed to be a good candidate for many quantum applications, so a selective review of the colour centres in diamond is presented the achievements of greatest note that build up to this work.

Secondly, this chapter will focus on three methods to engineer single NV^- centres, the properties of which are optimized for quantum applications. The ion-implantation method is currently the most common way to generate a single NV^- centre with good coherence properties and high positioning accuracy. The most NV^- centre generation methods involve an annealing process, it will be discussed in detail.

Some alternative methods have been proposed to solve the problems in ion-implantation. The ideas of adjusting the species of the ion, He-implantation, method will be compared. The second idea is using electron beam to replace the ion beam and the detail of this method will be given, as well.

Recently, a few groups have tried to use the laser writing method to generate the NV^- centres. Although these attempts have not yet successfully generated a single NV^- centre, it is still worth mentioning to compare with the results of this work.

2.1 Colour centres in diamond

Colour centres in wide bandgap materials such as diamond and silicon carbide are attractive and important for many quantum applications [4, 15–18]. The diamond crystal provides a robust, flexible and spin-free platform to fabricate photostable single photon emitters which can operate at ambient temperature[33, 45]. There are more than 10 colour centres in diamond which have been proven to be single photon emitters[5]. Figure 2.1 shows a summary of the single photon emitters discovered in diamond up to date. However, for many quantum applications, the single photon emission property is not enough and the spin of the colour centre must be controllable. Only three colour centres have demonstrated spin manipulation, indicated by the black arrows in Figure 2.1. After a few decades of study, the NV^- centre has proven to be one of the best candidates for quantum information applications and its properties are most profoundly understood among the colour centres in diamond. The NV^- centre is the best platform to demonstrate the new method of generating colour centres in wide bandgap materials. Thus, this review will focus solely on the NV^- centre.

Although the NV^- centre is a promising candidate in quantum applications, the

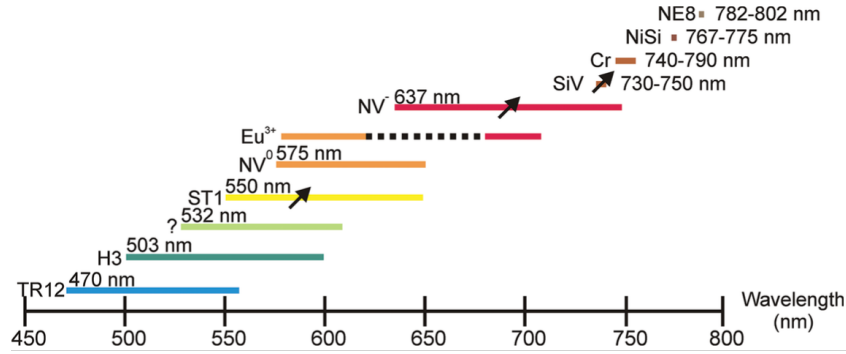


FIGURE 2.1: *Summary of the spectra of the single photon emitters in diamond up to date. For the centres with wavelengths shorter than 730 nm, the length of the coloured lines indicate the approximately width of emission spectra of them including phonon sideband. The wavelength given for each colour centre represents the ZPL wavelength. Black arrows denote centres which exhibit spin manipulation[5]. Reproduced with permission from [5].*

negatively charged Silicon-Vacancy centre (SiV^-) has recently drawn many researchers' attentions due to its outstanding optical properties. Up to 70% emission of the SiV^- centre comes from ZPL[46] and the linewidth of the ZPL is about 0.7 nm at room temperature[47]. Recently, many groups have observed SiV^- centres with near lifetime-limited linewidths, $200 \sim 400$ MHz[48–50]. Moreover, the wavelength of the ZPL is very stable because of the inversion symmetry. Becker et al have demonstrated that the spin of the SiV^- centre can be manipulated via an optical method[16].

2.1.1 The NV^- centre

The NV^- centre is a point defect with C_{3v} symmetry, consisting of a substitutional nitrogen atom and a neighbouring lattice vacancy. Nitrogen is one of the most common impurities in diamond, leading to the two general classifications of diamond materials. Type I diamond contains nitrogen impurities of more than

20 ppm (parts per million) and type II diamond has no measurable nitrogen impurities. Further relevant sub-classifications of them as named as type Ib: the nitrogen atoms are dispersed throughout the crystal in isolated sites and type IIa: it is almost or entirely devoid of all impurities.

Many properties and applications of the NV^- centre have been established in the 50 years research following the first optical studies. An overview of the significant achievements, proving that the NV^- centre is a good candidate for quantum applications, is presented as follows.

- 1965** Du Preez reported the first systematic research into the 637 nm (1.945 eV) optical transition band in diamond, obtained after type Ib diamonds underwent the electron irradiation and subsequent annealing at 600°C[51].
- 1977** Loubser and van Wyk found the electron spin resonance (EPR) signals of the NV^- ensemble under light illumination and determined the total spin to be $S=1$ (spin-triplet state) with energy splitting at 2.88 GHz. They are also the first to propose the electron and chemical structure of the NV^- centre[52, 53].
- 1988** van Oort et al demonstrated that the spin-triplet state of the NV^- ensemble can be measured by optically detected magnetic resonance (ODMR) method at 1.3 K[54]. They also presented the first spin coherence properties experiments of the NV^- centre at low temperature. They assigned the spin-triplet state to be the ground state of the NV^- centre.

- 1990** Mason et al's studies proved the optical spin-polarization phenomenon and has led to a belief of that the $m_s=0$ ground state sublevel is the bright state[55–58]. The optical spin-polarization mechanism enables the spin state of the NV^- centre to be initialized to a pure state easily, which is critical for many quantum applications[59].
- 1997** Gruber et al reported that the generation of the isolated single NV centres can be achieved by reducing the dosage of the electron irradiation[60]. They used a scanning confocal microscope to investigate single NV centres and also demonstrated that the ODMR signals can be observed at room temperature with continuous wave excitation.
- 2000** Kurtsiefer et al proved that the NV^- centre is a single photon emitter by measuring its photon autocorrelation function ($g^{(2)}(\tau)$) with Hanbury-Brown and Twiss (HBT) interferometry[35]. They also demonstrated that the fluorescence of the NV^- centre is very stable against photobleaching. Based on these two optical properties, the NV^- centre is believed to be a potential candidate for many quantum optics applications.
- 2004** Jelezko et al measured the coherent oscillations of a single electron spin which is one of the first such measurements in solid states at room temperature[61]. The coherence times (T_2) of single NV^- centre were measured to be about 2 μs . Single NV^- centre is identified as a good candidate for quantum network integration due to this long coherence time and optical readout mechanism[59].

- 2004** Popa et al showed the hyperfine structure of the NV^- centre coupling to ^{14}N and ^{13}C nuclear spins[62]. The coherence time of the nuclear spins is measured to be tens of microseconds. This long coherence time suggests that this system can be applied to a two-qubit gate.
- 2006** Tamarat et al first reported the lifetime-limited ZPL of 13 MHz spectral linewidth by studying single NV^- centres in a natural type IIa diamond at 1.8 K, indicating that the NV^- centre also has coherent optical properties[63]. They also demonstrated that the energy of the NV^- excited states can be tuned via the Stark effect by applying external electric field. The controlling of the ZPL wavelength is critical for two-photon quantum interference from different centres.
- 2009** Balasubramanian et al reported that the T_2 time of single NV^- centres can be extended to be longer than 1.8 ms by reducing the concentration of ^{13}C isotope in diamond from 1.1% (natural abundance) to 0.3%[64]. The nuclear spin of the ^{13}C is spin-1/2 and this work implies that the ^{13}C isotope is the main source of electron spin dephasing.
- 2009** Batalov et al reported the NV^- centres' excited-state structure with local strain field at 4 K, showing the strain-induced splitting of the excited state[65]. They also established a theoretical model to explain strain-induced splitting of the excited states. This enables spin-photon entanglement to be achieved.

- 2010** Hadden et al demonstrated that the photon collection efficiency from the NV^- centre is enhanced by using integrated solid immersion lenses, reducing refraction losses at the diamond-air interface[66]. The significant advantage of this method is that the NV^- centre does not necessarily have to be close to surface, preserving its coherence properties.
- 2015** Hensen et al demonstrated loophole-free Bell inequality violation by measuring the entangled states of two single NV^- centres separated by 1.3 km[67]. This work is the first Bell test which simultaneously addresses both the detection and locality loophole. This demonstrates that entangled NV^- centres can be used to solve quantum mechanics problems.

This list only includes a fraction of the significant developments and research related to the NV centre. It is worth mentioning that entanglement can also be achieved using an NV pair[68]. Recently, many research groups have demonstrated coupling single NV^- centres to photonic structures to enhance the intensity of ZPL, increasing the efficiency of entanglement event generation[43, 69–71]. In addition to applications in quantum information processing, the NV^- centre can be used for environmental sensing. Nanoscale scanning probe magnetometry can be achieved by attaching a nanodiamond with the NV^- centres on the tip of atomic force microscopy (AFM)[40, 72]. Moreover, the NV^- centre can also be used to detect single charge[73] and proton nuclear magnetic resonance[74, 75] at ambient temperature. The NV^- centre can also be used for electrometry[30] and temperature sensing[31].

2.2 Ion implantation

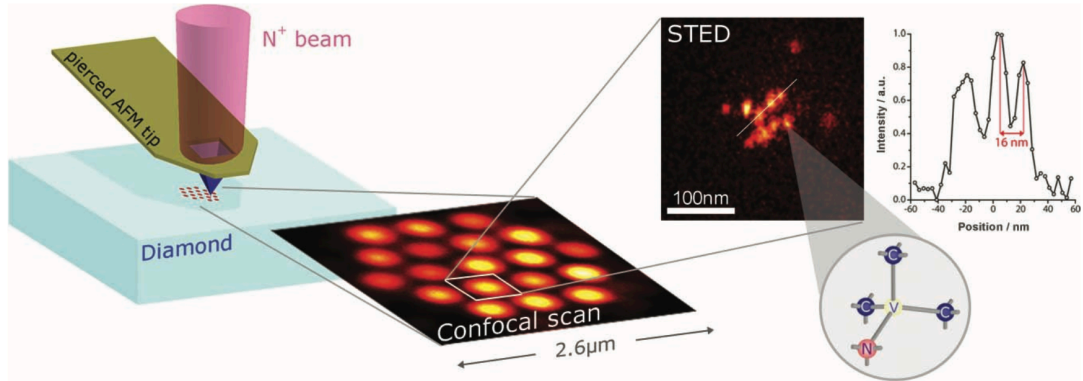


FIGURE 2.2: *Nanoscale engineering and optical addressing of single NV centres in diamond. The nanoscale implantation is realised through the pierced hollow tip of the atomic microscope. A fluorescence image (confocal scan) shows a hexagonal pattern implanted in diamond with N ions at 5 keV and fluence of $1 \times 10^{13} \text{ cm}^{-2}$. A stimulated emission depletion microscopy image of one particular spot reveals an ensemble of about 12 single NV centres. Two NV centres separated by 16 nm are resolved[6]. Reproduced with permission from [6].*

For many NV⁻ applications, single NV⁻ centres must be placed at particular positions with high spatial accuracy. The most common method to achieve this is ion implantation. The concept of the ion implantation method is to use a nitrogen ion beam to bombard diamonds, resulting in introducing nitrogen atoms into diamond lattice and creating neutrally charged vacancies (GR1 centres) when the nitrogen ions collide with the carbon atoms. The GR1 centre becomes mobile when annealing above 600°C, so it could become trapped by the implanted nitrogen atoms to form NV centres[76]. Nanoscale positioning ($\sim 20 \text{ nm}$) using the ion-implantation method was achieved by focusing the ion beam into a pierced AFM tip and reducing the ion beam energy down to 5 keV, as shown in Figure 2.2[6]. However, the yield of NV⁻ centres is only 1~5%.

2.2.1 Annealing

Annealing process is an important procedure to generate colour centres for most engineering methods due to two reasons. The vacancies and/or interstitial carbon atoms can diffuse away and find the impurity atoms to form colour centres during annealing. Secondly, high temperature annealing restores the crystal lattice, reducing the crystal damage caused by the ion implantation.

The diffusion of atoms in diamond during annealing is very complicated and has not yet been fully understood. However, it is believed that the single-interstitial atoms and their aggregates start to move at very low temperature and are completely annealed out by 400°C[77]. Single vacancies are relatively stable and become mobile at around 600°C[78]. The NV⁻ centres are stable up to a temperature of 1400°C[77]. The mobility of the impurity atoms in diamond at high temperature is still under debate. The long-range diffusion of impurity atoms can be ignored at temperatures up to 2000°C[77], whereas it might be possible for these impurity atoms to move within a few interatomic distances in the vicinity of other lattice defects. This short-range diffusion may contribute to the formation of the impurity-related defects[77].

The local environment surrounding the colour centres can greatly influence the characteristics of colour centres. Yamamoto et al suggest that the concentration of multivacancy complexes was minimized at about 1100°C[79]. Naydenov et al demonstrated that the longer coherence time of 50 μ s can be achieved after

annealing at 1200°C[80], compared with the coherence time of 2 μ s after 800°C annealing[81].

2.2.2 Coherence properties of the ion-implanted NV⁻ centre

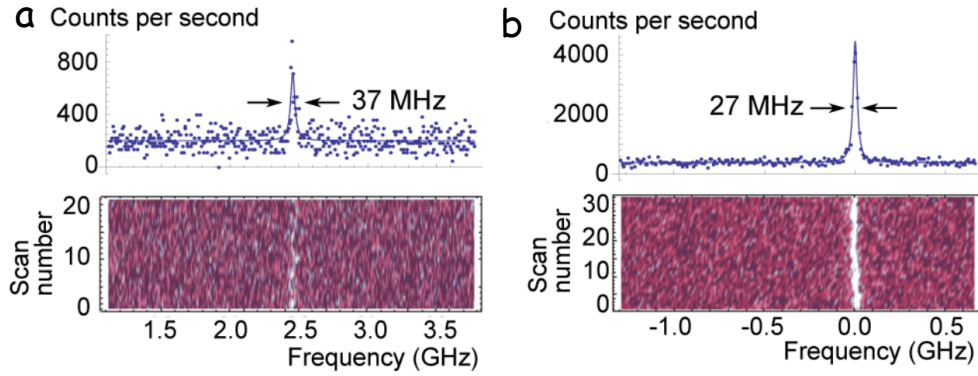


FIGURE 2.3: **a**, PLE spectrum showing the narrowest linewidth (top) obtained by averaging twenty-one successive PLE scans (bottom). **b**, PLE spectrum taken using 575 nm resonant excitation of the NV⁰ state to repump back to NV⁻ [7]. Reproduced with permission from [7].

Staudacher et al demonstrated that the coherence time T_2 of shallow implanted NV⁻ centres can be extended up to 250 μ s by growing an additional diamond layer over the implanted diamond[82] which improves the quality of the surface. However, this T_2 time is still shorter than the T_2 time of single NV⁻ centres produced during the crystal growth, which is about 500~600 μ s.

Chu et al have successfully generated single NV⁻ centres with a ZPL linewidth of 27 MHz by performing proper surface treatments and a three-step annealing process [7], as shown in Figure 2.3. The 27 MHz is close to the Fourier transform limited linewidth of 13 MHz based on the NV⁻ centre's fluorescence relaxation time.

The three-step annealing was optimized to remove residual defects and the surface treatments were introduced to get rid of the surface defects. After prolonged laser illumination, the NV^- centre will be ionized to neutral charged state, so a 532 nm or 575 nm excitation is used to repump the NV centre into negative charge state, as shown in Figure 2.3a and b respectively.

2.2.3 Light-weight ion implantation

Huang et al proposed that using light-weight ion (He) implantation to generate NV^- centres should reduce the level of residual defects, resulting in better coherence properties[83]. The basic concept is that using He ion beam to bombard the type Ib diamond (nitrogen concentration greater than 1ppm) to create vacancies. During annealing, the vacancies can diffuse around to find the native nitrogen atom to form the NV centres. The ZPL linewidth of the He implanted NV^- centre ensemble is about 25 GHz, which is similar to that of native NV^- ensemble in the same sample but much narrower than N implantation (>100 GHz). Fávaro de Oliveira et al observed a 5-fold improvement of the spin coherence time of He implanted NV^- centre, compared with that of N implanted NV^- centre[84].

The He implantation method has a severe disadvantage, the generation of additional fluorescence[85]. The additional emission centres are at about 600 nm and extend to 800 nm, and has photon count rates 100 times greater than that of a single NV^- centre[85]. This additional emission is assigned to He-vacancies complexes[37] and can not be removed.

2.3 Electron irradiation and δ -doped diamond

Although ion-implantation can engineer the NV⁻ centre with high positioning accuracy in xy-plane, the positioning accuracy in depths is greater than 10 nm because of straggling and channeling effects[32]. Ohno et al have proposed a nitrogen δ -doping technique to solve the short T₂ time and wide depth dispersion[86]. The δ -doping means a thin layer (1~2 nm) of diamond with high nitrogen concentration (approximately 20 ppb). They grew a thin isotopically pure diamond layer (~2 nm) with high nitrogen doping on a commercial CVD diamond, and then grew a buffer layer with low nitrogen concentration on top of it. Electron irradiation method is used to generate vacancies and the energy of the electron beam are set to generate most vacancies around the δ -doping layers. During annealing, the vacancies can be captured by the nitrogen in δ -doping layers to form the NV centres. McLellan et al demonstrated the T₂ times of single NV⁻ centre up to 1 ms with yield of approximately 50% using this method[44]. The T₂ time was limited by the spin bath of substitutional nitrogen impurities, so it can be improved by reducing the nitrogen doping level[44]. The lateral positioning accuracy is better than 450 nm[44]. This method can generate NV⁻ centres at greater depth, 60 μ m below the surface, compared with ion-implantation (2 μ m).

2.4 Ultra-fast laser writing

Recently, laser engineering of micro-scale structures on bulk diamond has been established[87], creating an opportunity to generate vacancies and the NV⁻ centres.

Liu et al were the first group to use a femtosecond pulse laser to generate NV⁻ centres[88]. The concept is to use femtosecond pulsed laser to generate vacancies in diamond. During annealing, the vacancies can diffuse around to meet native nitrogen atom to form the NV centres. The femtosecond laser was focused 1 or 2 μm above the surface of a type Ib diamond, generating damage on the surface. After annealing at 680°C in air to oxidize the defects on the surface, an NV⁻ centre ensemble was observed.

They claimed that the NV⁻ centres were created by electrons instead of directly by laser pulse. The intense ultra-short laser pulses induced ionization of O₂ and N₂ molecules in air and created free electrons[89], which in turn generated vacancies. However, the pre-annealing PL spectra did not show any sign of the GR1 centres. The NV⁻ centres may have been generated because the electron beam transfers the charge state of the native NV⁰ centres to negative.

Pimenov et al demonstrated that the fluorescence of NV⁰ and NV⁻ was enhanced after a multipulse picosecond pulsed laser illuminated a type IIa CVD diamond[90]. The laser pulses had not only created vacancies but also raised high temperature in the focal volume to 1600°C, resulting in the diffusion of vacancies and hence the formation of the NV⁻ and NV⁰ centres. However, this method not only generates the NV⁻ and NV⁰ ensemble but also heavy damages in the vicinity of the NV centres, degrading the coherence properties of the NV⁻ centres.

2.5 Summary

After over 5 decades of research, the NV^- centre is believed to be a good candidate for many quantum applications. The spin state of the NV^- centre can be optically initialized and read-out; the spin coherence time is long (~ 1.8 ms in isotopically purified diamond) at room temperature. The NV^- centre also shows good optical coherence properties. In order to realize the quantum application to the fields of quantum sensing and computing, it requires the generation of single NV^- centres with high spatial positioning accuracy.

The ion-implantation is the most common method to generate NV^- centres. It can achieve 20 nm positioning accuracy by reducing implantation energy, but the yield of the NV^- centre is less than 5% due to low implantation energy. The T_2 time of the ion-implanted NV^- centre depends on the annealing temperature and surface properties. After high temperature annealing and proper surface treatments, the T_2 times can be extended to 250 μs . Similarly, the ZPL linewidth of the ion-implanted NV^- centre can be improved to 27 MHz by performing a three-step annealing process and proper surface treatments. However, the T_2 time of the ion-implanted NV^- centre is still shorter than that of the naturally grown NV^- centre. Moreover, the ion-implantation method can not generate the NV^- centres with lifetime-limited optical transitions. These suggest that there are some residual defects after annealing and surface treatments. He ion implantation generally generates the NV^- centres with better spin and optical coherence properties. However, the He ion implantation creates strong additional fluorescence due to He-vacancies complexes.

δ -doped diamond combined with electron irradiation is another alternative method. This method generated the NV^- centres with T_2 time of up to 1 ms. This method also provides high positioning accuracy; the lateral accuracy is estimated to be better than 450 nm. However, the optical coherence properties of the NV^- centre generated by this method are not reported on.

The final alternative method is ultra-fast laser writing. The first attempt used the laser-induced electron beam to damage the diamond surface instead of directly using laser to create vacancies. Pimenov et al demonstrated that the multipulse picosecond pulsed laser can generate NV^0 and NV^- ensemble in type IIa diamond. However, the laser pulses also generate heavy damages around the NV centres, degrading the coherence properties of the NV centres. In addition, the coherence properties of the laser-induced NV^- centres are not included in the papers.

In summary, the lighter particle generates less defects and distortion in diamond lattice, resulting in better spin and optical coherence properties. Thus, ultra-fast laser writing may generate the NV^- centre with better coherence properties than the existing methods.

Chapter 3

Theoretical background

This chapter will discuss the theoretical background required to describe the properties of laser-generated single NV^- centres. Although it has been demonstrated that ultra-fast pulsed laser can generate damages in many transparent materials, including diamond, the mechanism of vacancy generation is not crystal clear. The three proposed models, multi-photon absorption, tunneling breakdown and Avalanche ionization, will be described. The formation of the NV^- centres in laser writing method is dependent on the diffusion of vacancies during annealing. The governing vacancy diffusion equation will then be presented.

The electronic structure of the NV^- centre determines many of its properties, so it will be described in detail. The excited state of the NV^- centre is very sensitive to the local strain field; thus, it can be used to measure the magnitude of local strain. The detail of the spin Hamiltonian of the excited state with transverse strain will be described step-by-step. As the optical coherence properties of the laser-induced

NV⁻ centres are determined by measuring the linewidth of its ZPL, the two ZPL broadening mechanisms, i.e. homogeneously and inhomogeneously broadening, will be presented. The NV⁻ centres become ionized after prolonged excitation, resulting in losing signals. Therefore, it is worth discussing the mechanisms of ionization and repump. The single photon emission property of the NV⁻ centre will also be described. The concept of ODMR and the hyperfine structures of the NV⁻ centre will be presented. A simple model to estimate the probability of generating NV⁻ centres per site will be established.

3.1 Mechanism of laser-induced damage

It has been demonstrated that ultrashort laser pulses (femtosecond or picosecond) can be used to modify the refractive index or generate damage in transparent dielectrics[91, 92]. When a transparent dielectric material is illuminated by intense femtosecond laser, a large amount of excited electrons may be generated[93]. Relaxation channels of these free electrons in wide bandgap materials may produce intrinsic defects, resulting in photoinduced damages. For transparent materials, there is no linear absorption of the incident laser light to excite electrons due to the bandgap greater than photon energy. Thus, a nonlinear mechanism must be responsible for the generation of free electrons. Three models have been proposed to describe the mechanism of free electrons creation[8, 93]. These three models are tunneling ionization (also called Zener breakdown), multiphoton ionization (MPI) and Avalanche ionization. In the former two mechanisms, the electron is directly

excited by laser field; on the other hand, Avalanche ionization needs a free-carrier to occur.

3.1.1 Tunneling ionization and multiphoton ionization

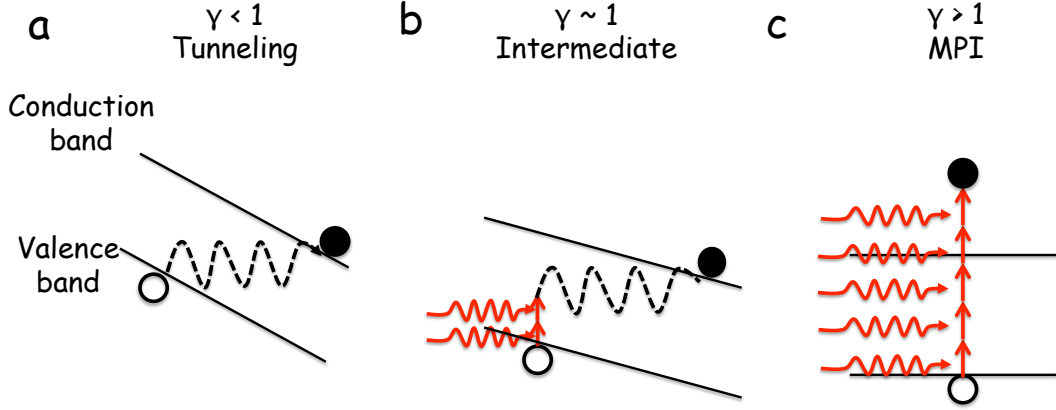


FIGURE 3.1: Schematic graphs of the ionization of an electron in a band structure for different values of the Keldysh parameter[8]. In fact, the electron is excited from the valence band to conduction band, instead of ionized. *a*, Tunneling ionization. *b*, Intermediate. *c*, MPI.

Both the tunneling ionization or the MPI occur in parallel, but which one dominates depends on the laser frequency and intensity. The phase transition between the tunneling ionization and MPI can be described by the Keldysh parameter[94],

$$\gamma = \frac{\omega}{e} \left[\frac{mc n \varepsilon_0 E_g}{I} \right]^{1/2}, \quad (3.1)$$

where ω is the laser frequency, I is the laser intensity at the focus, m and e are the reduced mass and charge of the electron, c is the velocity of light, n is the refractive index of the material, E_g is the direct bandgap of the material and ε_0 is the permittivity of free space. The Keldysh parameter can be interpreted as a ratio of the characteristic atomic momentum $\hbar k = \sqrt{2mI_p}$ to the field induced

momentum $p = \frac{eE}{\omega}$. I_p is ionization potential which is proportional to the bandgap of the material and E is the electric field. When the Keldysh parameter is greater than 1, MPI is the dominant mechanism. On the other hand, when the Keldysh parameter is smaller than 1, tunneling ionization is the dominant mechanism.

Figure 3.1 shows a schematic of tunneling ionization, MPI and intermediate mechanism. In the tunneling ionization (Figure 3.1a), the electric field of the laser biases the band structure, leading to the bending of the conduction band. Then, the electron can tunnel into the conduction band through the short energy barrier, as the conduction band has bent to a low enough energy[8]. This mechanism dominates the laser writing process for a strong laser field, i.e. the Keldysh parameter smaller than 1. I consider the tunneling ionization model and assume the number of GR1 defects created scales as the volume of the diamond in which the field is above the breakdown energy threshold. The point spread function of pulsed laser in diamond is assumed to be a Gaussian beam with cylindrical symmetric intensity distribution

$$E(r, z) = E_0 \cdot \frac{1}{1 + \left(\frac{z}{z_R}\right)^2} \cdot e^{-\frac{2r^2}{w_z^2}}, \quad (3.2)$$

where E_0 is a constant proportional to laser pulse energy, w_z is the beam width at axial displacement z , w_0 is the beam waist at $z = 0$, z_R is the Rayleigh range. The width in radial direction at $z = 0$ when laser pulse energy is equaled to the threshold laser pulse energy to generate vacancy can be expressed as

$$E_{th} = E_0 \cdot e^{-\frac{2r^2}{w_z^2}} \Rightarrow r = w_z \sqrt{\frac{1}{2} \ln \frac{E_0}{E_{th}}}, \quad (3.3)$$

where E_{th} is the threshold laser pulse energy to generate vacancy. The width in axial direction with $r = 0$ when laser pulse energy is equaled to the threshold pulse energy to generate vacancy can be described as

$$E_{th} = E_0 \cdot \frac{1}{1 + (\frac{z}{z_R})^2} \Rightarrow r = z_R \sqrt{\frac{E_0}{E_{th}} - 1}. \quad (3.4)$$

The number of GR1 defects, N_{GR1} , can be expressed as

$$N_{GR1} \propto V_{th} \Rightarrow N_{GR1} = N_0 \ln\left(\frac{E}{E_{th}}\right) \sqrt{\frac{E}{E_{th}} - 1}, \quad (3.5)$$

where V_{th} is the volume in which the laser pulse energy is above the threshold, N_0 is a constant and E is the laser pulse energy.

On the other hand, when the Keldysh parameter is greater than 1, MPI becomes the dominant effect, as shown in Figure 3.1c. In this region, the electron can be promoted to the conduction band via the simultaneous absorbing several photons. The electron must absorb enough photons at once so that the photon energy multiplied by the number of photons absorbed is equal to or greater than the direct bandgap of the material[8]. The photoionization rate of MPI can be expressed as

$$P(I)_{MPI} = \sigma_k I^k, \quad (3.6)$$

where σ_k is the multiphoton absorption coefficient for absorption of k photons[95].

3.1.2 Avalanche ionization

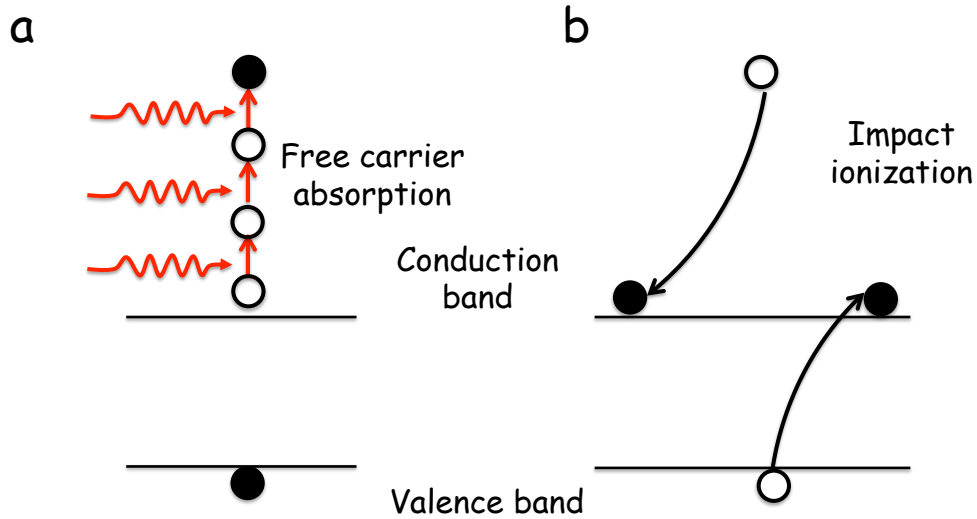


FIGURE 3.2: *Schematic graphs of Avalanche ionization. a, An initial free electron linearly absorbs several photons via free-carrier absorption. b, The free electron in a impacts on another atom, resulting in ionizing another electron.*

Avalanche ionization consists of two steps, free-carrier absorption and impact ionization, as shown in Figure 3.2. A free electron in the conduction band linearly absorbs several photons, which promotes the electron to higher energy levels in the conduction band, depicted in Figure 3.2a. The electron must absorb enough photons so that the energy difference between the electron and the conduction band minimum is greater than bandgap energy of the material[8]. Then, the electron can ionize another electron to the conduction band via collision with another atom, as shown in Figure 3.2b. As a result, two electrons are in the conduction band.

The initial free electrons can be generated by thermally excited carriers, easily ionized impurities or defects, or photoionized electrons via tunneling or multiphoton

ionization[8]. In high purity diamond, the initial free electrons mainly come from tunneling or multiphoton ionization process. Thus, laser writing creates defects in high purity diamond via the generation of energetic seed electrons by MPI and tunneling ionization, combined with Avalanche ionization. Recently, Lagomarsino et al have concluded that MPI is responsible for the generation of damage in high purity diamond under an illumination intensity between 1- 10 TW cm⁻² and it involves 9 photons by measuring the photoionized electron yield as a function of laser pulse intensity[96]. As aforementioned, the laser-induced vacancies is created by the heat of rapid relaxation of free electrons. Thus, there is no direct link between the degree of nonlinearity and the energy needed to dislodge an atom from the lattice. Lagomarsino et al. used a femtosecond pulse laser with wavelength of 790 nm to generate lattice damage. Each photon in the laser pulse carries an energy of 1.57 eV, suggesting that energy is transferred to the diamond in pockets of 14 eV. However, the displacement threshold energy is thought to fall in the region of 35-40 eV[97, 98].

3.2 Vacancy diffusion

After laser writing of vacancies, a high temperature annealing is required to let the vacancies diffuse around to find nitrogen atoms to form the NV⁻ centres. The diffusion of the GR1 centre during annealing is critical in the generation of the NV⁻ centre. The isotopic diffusion function for a cylindrically symmetric vacancy distribution can be expressed as

$$N(r, t) = N_0 \exp\left(\frac{-r^2}{4Dt}\right), \quad (3.7)$$

where $N(r, t)$ is the concentration of the diffusing vacancies at the radius r and time t and N_0 is the normalization constant. The diffusion coefficient is determined by the activation energy of the vacancy and the annealing temperature, and it follows the equation:

$$D = D_0 \exp\left(\frac{-E_a}{kT}\right), \quad (3.8)$$

where E_a is the activation energy for vacancy diffusion, k is the Boltzmann constant, T is the temperature in K and D_0 is a pre-factor. It was recently reported the value of D_0 for vacancy diffusion near the diamond surface is $3.6 \times 10^{-6} \text{ cm}^2 \text{ s}^{-1}$ [99]. The activation energy of the vacancy varies from 1.7 to 4 eV in reports [100–103]. The diffusion distance, d , can be estimated from the equation

$$d \approx \sqrt{Dt}. \quad (3.9)$$

3.3 The NV centre in diamond

3.3.1 The energy level structure

A substitutional nitrogen and an adjacent vacancy form a nitrogen-vacancy pair, the axis of which is in the $[111]$ crystalline direction, as shown in Figure 3.3a. The

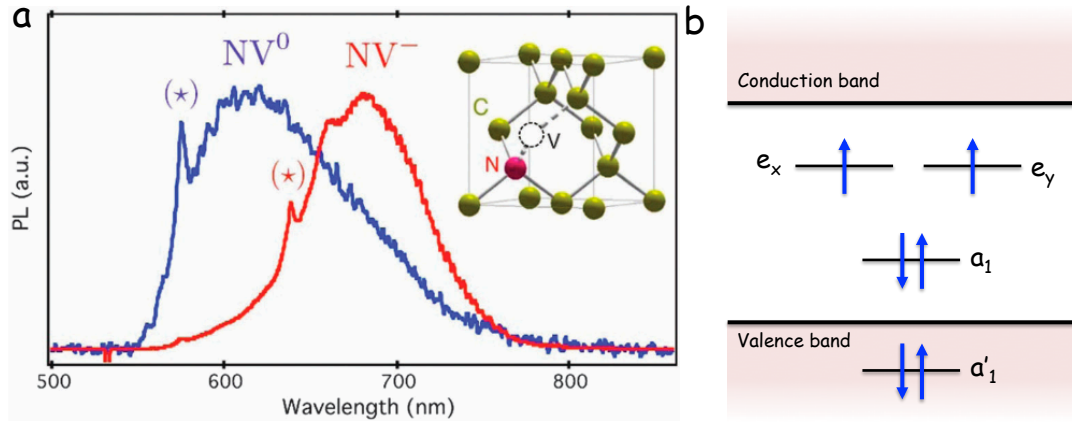


FIGURE 3.3: **a**, Typical spectra of single NV^0 (blue curve) and NV^- (red curve) centre. The ZPLs of them are labelled by asterisk (*). The inset shows schematic representation of the nitrogen vacancy centre structure illustrating the lattice vacancy (open circle), the substitutional nitrogen atom (pink) and the carbon atoms forming diamond matrix (olive)[9]. **b**, The energy position of NV^- ground state relative to the energy band structure of diamond. The electron spins (blue arrow) fill the molecular orbitals following the Hund's rules[4]. Reproduced with permission from [4].

neutrally charged NV (NV^0) centre possesses five dangling bonding electrons, two from the nitrogen atom and one from each of the three carbon atoms surrounding the vacancy[4]. The NV^0 centre is a single photon emitter with ZPL at 575 nm[104] and blue curve in Figure 3.3a shows the typical spectrum of single NV^0 centre.

The NV centre can also exist in a negative charge state with ZPL at 637 nm, trapping a sixth electron, as shown in Figure 3.3a (red curve). Considering the C_{3v} point group and group theory, the NV^- centre has two non-degenerate a_1 orbitals and two doubly degenerate e orbitals[4, 11]. The six electrons of the NV^- centre fill in these orbitals following the Hund's rules, as shown in Figure 3.3b. According to theory calculation, the a'_1 orbital is located within the valence band. The a'_1 orbital will be ignored in the remaining discussion, as it is filled for all observable electronic levels of the NV^- centre[4]. The remaining three orbitals are located deep in the band gap, i.e. well below the conduction band, resulting in that the

NV⁻ centre can be optically read out. Figure 1.1a shows the electronic structure of the NV⁻ centre. The intermediate singlet levels at ¹A₁ and ¹E separated by 1.19 eV and there is an optical transition between them[105].

3.3.2 Photon emission statistics

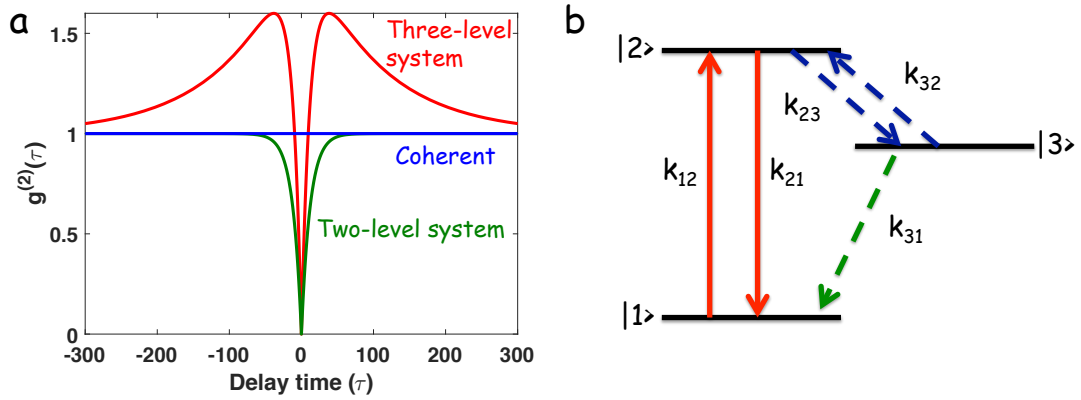


FIGURE 3.4: **a**, Schematically theoretical HBT spectra for coherent light (blue), a two-level quantum system (green) and a three-level quantum system (red). **b**, Schematic three-level system of the NV centre with transition rate constants, k . Level $|1\rangle$ is the ground state, level $|2\rangle$ is the excited state and level $|3\rangle$ is intermediate state. The red solid lines denote optical transition and the blue dash lines indicate the non-radiative transition. Adapted from [10].

The NV centre is a single photon emitter, but its electronic structure is a three-level system instead of a simple two-level system, as shown in Figure 1.1a. Thus, it is worth discussing how the third level will effect the photon-statistics. The single photon emission is determined by measuring the photon autocorrelation function via HBT interferometer. The fundamental principle of HBT measurement is that two detectors at the outputs of a 50:50 beam-splitter (one at each side) cannot be simultaneously triggered by a single photon. The histogram of photon statistics is built up as a function of the delay time τ of the photon events between two detectors. This second order correlation function can be described as

$$g^{(2)}(\tau) = \frac{\langle I(t)I(t+\tau) \rangle}{\langle I(t) \rangle \langle I(t+\tau) \rangle}, \quad (3.10)$$

where $I(t)$ is the intensity at time t and the brackets $\langle \dots \rangle$ denote the time average.

Figure 3.4a depicts theoretical HBT histograms for various light sources, coherent light in blue, a two-level system in green and a three-level system in red. The $g^{(2)}$ value is close to unity for all types of light source as the delay time is approaching to infinity. For single photon emitters, the $g^{(2)}$ value decreases to zero at $\tau = 0$ (Figure 3.4a), called anti-bunching dip. The shape of and the converge rate to unity of the HBT histogram depend on the internal dynamics of the emitter's energy levels. The two-level system is the simplest case, where only the excitation rate (γ_{exc}) and the spontaneous emission rate (γ_{spon}) contribute to the dynamic behaviour. The photon statistic histogram of a two-level system can be described as[106]

$$g^{(2)}(\tau) = 1 - e^{-(\gamma_{exc} + \gamma_{spon})\tau}. \quad (3.11)$$

The NV centre is a three-level system and the intermediate state has great influence on the photon statistics. Figure 3.4b is a schematic three-level system of the NV centre and the transition rates are highlighted. Level 1 is the ground state, level 2 is the excited state and level 3 is the intermediate state. The population dynamics can be described by the rate equations, showed as follow[35]:

$$\begin{bmatrix} \dot{L}_1 \\ \dot{L}_2 \\ \dot{L}_3 \end{bmatrix} = \begin{bmatrix} -k_{12} & k_{21} & 0 \\ k_{12} & -k_{21} - k_{23} & k_{23} \\ 0 & k_{23} & -k_{32} \end{bmatrix} \cdot \begin{bmatrix} L_1 \\ L_2 \\ L_3 \end{bmatrix}$$

where L_i and \dot{L}_i are the electron population of level i and its first order time derivative, and k_{ij} is the transition rate from level i to level j . An analytical expression for the second order correlation function can be obtained by solving the rate equation, and the solution can be expressed as[35]

$$g^{(2)}(\tau) = 1 + c_2 e^{-\frac{\tau}{\tau_2}} + c_3 e^{-\frac{\tau}{\tau_3}}, \quad (3.12)$$

where the decay times and coefficients are given by,

$$\begin{aligned} \tau_{2,3} &= \frac{2}{A \pm \sqrt{A^2 - 4B}}, \\ c_2 &= \frac{1 - \tau_2 k_{32}}{k_{32}(\tau_2 - \tau_3)} = -1 - c_3 \end{aligned} \quad (3.13)$$

$$A = k_{12} + k_{21} + k_{32} + k_{23}, \quad (3.14)$$

$$B = k_{12}k_{23} + k_{12}k_{32} + k_{21}k_{32}.$$

Besides an anti-bunching at $\tau = 0$, photon bunching appears at medium time scales. Note that k_{12} is linearly proportional to excitation power (P) which can be expressed as $k_{12} = \sigma P$, resulting in that $\tau_{2,3}$ and $c_{2,3}$ depend on the power of the optical excitation. In the low excitation power limit, τ_2 tends towards the spontaneous emission lifetime of excited state and c_3 decrease towards 0, resulting

in the vanishing of bunching behaviour. The steady-state population of level 2 is given by[35]

$$L_2(t \rightarrow \infty) = \frac{k_{23}k_{12}}{B} = \frac{k_{23}\sigma P}{(\sigma k_{23} + \sigma k_{32})P + k_{21}k_{32}} = \frac{I_{sat}P}{P + P_{sat}}, \quad (3.15)$$

showing a saturation behaviour as a function of the excitation power (P). I_{sat} is the saturation intensity of the emitter, depending on the quantum efficiency of the emitter and photon collection efficiency of the microscope. P_{sat} is the saturation power, depending on the efficiency of exciting the emitter by pump laser.

3.4 Excited state and strain splitting

3.4.1 Excited state fine structure

Although the first theoretical study of the NV^- excited state was completed by Lenef et al[107], Maze et al's work provides a clearer and correct understanding of the excited state using a group theory approach[11]. The excited state of the NV^- centre is obtained by promoting one electron in the a_1 orbital to the e_x or e_y orbital, as shown in Figure 3.5. According to group theory, the symmetry of this electron configuration is 3E and the six sublevels are A_1 , A_2 , E_x , E_y , E_1 and E_2 .

The spin-orbit interaction splits the degeneracy of multiplets with non-zero angular momentum. The Hamiltonian of spin-orbit interaction can be expressed in the basis of the excited state six sublevels as

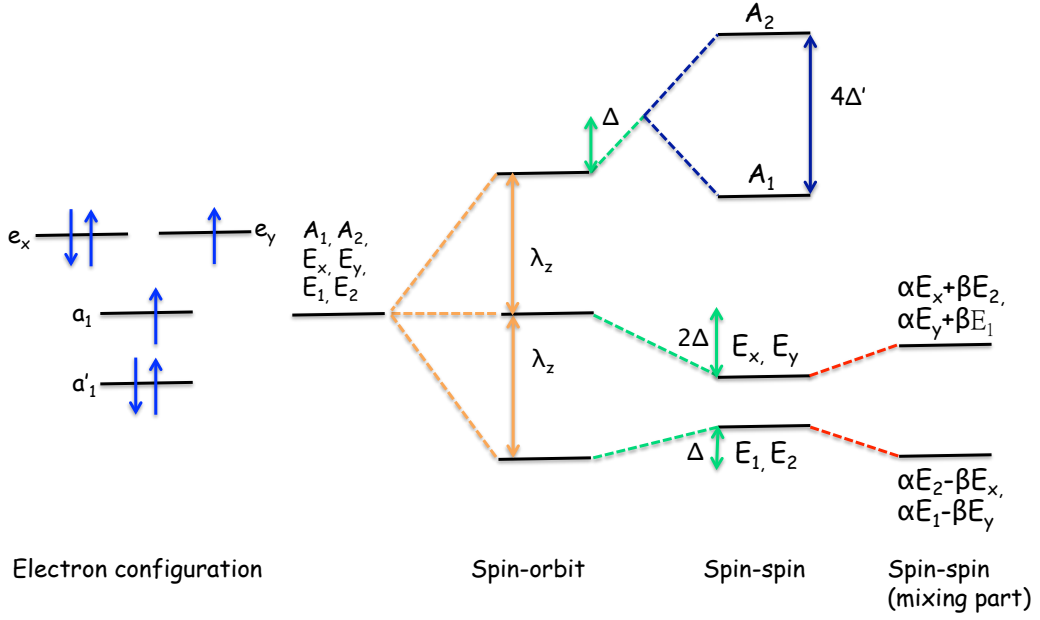


FIGURE 3.5: Schematic picture of the excited state fine structure due to spin-orbit and spin-spin interactions. The electron configuration of the NV⁻ excited state is also shown. The spin-orbit interaction separates the states $\{A_1, A_2\}$, $\{E_x, E_y\}$ and $\{E_1, E_2\}$ by λ_z . The spin-spin interaction further change the energies difference between different spin projections and also splits the A_1 and A_2 states. According to Maze et al's theory, the spin-spin interaction also mixes the $E_{1,2}$ and $E_{x,y}$ states[11]. Figure is adapted from [11].

$$H_{SO} = \lambda_z(|A_1\rangle\langle A_1| + |A_2\rangle\langle A_2| - |E_1\rangle\langle E_1| - |E_2\rangle\langle E_2|), \quad (3.16)$$

where λ_z denotes the axial strength of the spin-orbit interaction[11]. The spin-spin interaction can also be written in the basis of six states above as

$$\begin{aligned} H_{SS} = & \Delta(|A_1\rangle\langle A_1| + |A_2\rangle\langle A_2| + |E_1\rangle\langle E_1| + |E_2\rangle\langle E_2|) \\ & - 2\Delta(|E_x\rangle\langle E_x| + |E_y\rangle\langle E_y|) + 2\Delta'(|A_2\rangle\langle A_2| - |A_1\rangle\langle A_1|) \\ & + \Delta''(|E_1\rangle\langle E_y| + |E_y\rangle\langle E_1| - i|E_2\rangle\langle E_x| + i|E_x\rangle\langle E_2|), \end{aligned} \quad (3.17)$$

where Δ is zero-field splittings, Δ' is the gap between A_1 and A_2 states and Δ'' is the spin mixing term[11]. Figure 3.5 shows the schematic picture of the spin-orbit

and spin-spin induced splitting. The spin-orbit induced splitting was determined to be about 5.5 GHz by both experiment[65, 108] and theory[11, 107]. The spin-spin interaction characteristic parameters are $3\Delta \approx 1.42$ GHz and $\Delta' \approx 1.55$ GHz[11, 65, 107, 108]. This theory first predicts a non-spin preserving cross transition term (Δ'') generated from the spin-spin interaction, leading to the observation of the lambda transition[109].

3.4.2 Strain splitting

Strain is defined by the displacement (Δu) of the atomic positions while the crystal is stretched by Δx [110]. The strain field splits excited state of the NV^- centre, used to measure the local strain. The Hamiltonian of strain field can be described by the following equation

$$H_{str} = \delta_x \hat{V}_x + \delta_y \hat{V}_y + \delta_z \hat{V}_z, \quad (3.18)$$

where δ_i and \hat{V}_i denote the strain parameter and an orbital operator in the i direction respectively[11, 65]. Axial strain, δ_z , linearly shifts all the spin sublevels, so it is not considered here[107]. The transverse strains (δ_x, δ_y) split the excited states into two spin triplets, corresponding to the two orbital branches E_x and E_y [65]. The spin-Hamiltonian of the excited state under transverse strain can be described in the basis of excited state spin sublevels as

$$H = \begin{bmatrix} \lambda_z + \Delta - \Delta' & 0 & 0 & 0 & \delta_x & -i\delta_y \\ 0 & \lambda_z + \Delta + \Delta' & 0 & 0 & i\delta_y & -\delta_x \\ 0 & 0 & -2\Delta + \delta_x & \delta_y & 0 & i\Delta'' \\ 0 & 0 & \delta_y & -2\Delta - \delta_x & \Delta'' & 0 \\ \delta_x & -i\delta_y & 0 & \Delta'' & -\lambda_z + \Delta & 0 \\ i\delta_y & -\delta_x & -i\Delta'' & 0 & 0 & -\lambda_z + \Delta \end{bmatrix} \quad (3.19)$$

Since the δ_x is equivalent to δ_y , only the excited state splitting as a function of δ_x is considered for simplification. Figure 3.6 depicts the energies splittings as a function of uniaxial transverse strain in x direction and the magnitude of the strain is expressed in units of the strain-induced splittings between the E_x and E_y states. The local stress in the vicinity of the measured NV^- centres can be estimated from the splitting between E_x and E_y states. The splitting between E_x and E_y states, ΔE , induced by the stress in $[001]$ crystal direction can be expressed as^[111]

$$\Delta E = 4.15 \times 10^{-12} \text{eV Pa}^{-1}. \quad (3.20)$$

Anti-crossing occurs between E_y and E_1 when the uniaxial transverse strain is approximately 7 GHz. This anti-crossing causes spin mixing between $m_s = 0$ and $m_s = \pm 1$ in E_y state, resulting in the absence of E_y in the PLE spectrum. In fact, the spin mixing happens before the anti-crossing due to the thermal fluctuation. To observe the whole spectra and E_y state under high strain, the application

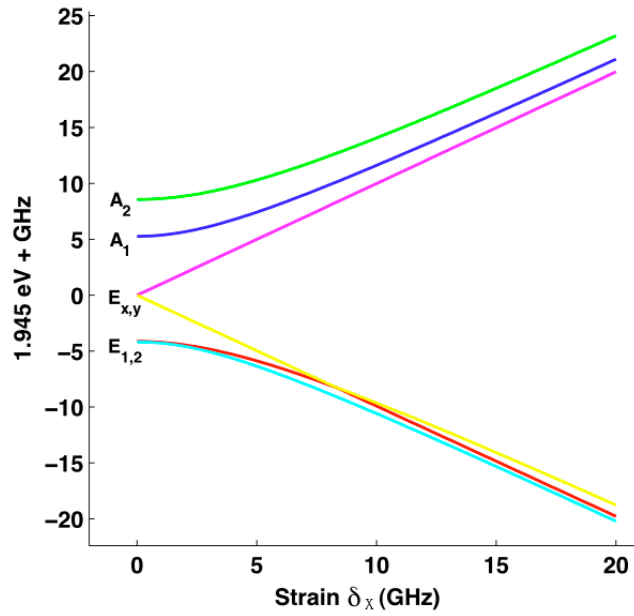


FIGURE 3.6: *Energies of the excited states as a function of uniaxial transverse strain, expressed in the units of the splittings between the E_x and E_y states*[11].
Figure is reproduced from [11].

of a microwave field of frequency 2.88 GHz or lambda transition mechanism are required. Chu et al observed more than 6 PLE lines in the spectra and they were attributed to the Fermi's golden rule forbidden transitions, as shown dash lines in Figure 3.7[136].

According to the selection rules, the polarization of the photons generated from different excited states are different. Table 3.1 shows the summary of the polarization of photons from various optical transitions[11]. In order to observe the whole PLE spectrum of the excited states, it is better to use circularly polarized excitation.

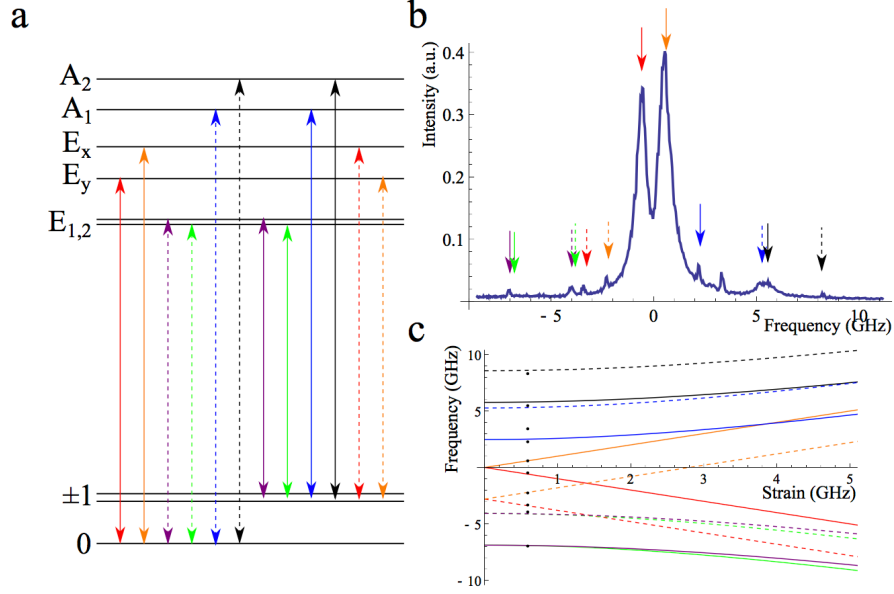


FIGURE 3.7: *Optical transitions of the NV⁻ centre. a, All possible transitions between the ground and excited states, with direct transitions indicated with solid lines, and Fermi's golden rule forbidden transitions indicated with dash lines. b, PLE spectrum. c, Frequencies of all transitions shown in a as a function of strain[136].*

\hat{e}	A ₁	A ₂	E ₁	E ₂	E _x	E _y
³ A ₂₋	$\hat{\sigma}_+$	$\hat{\sigma}_+$	$\hat{\sigma}_-$	$\hat{\sigma}_-$		
³ A ₂₀					\hat{y}	\hat{x}
³ A ₂₊	$\hat{\sigma}_-$	$\hat{\sigma}_-$	$\hat{\sigma}_+$	$\hat{\sigma}_+$		

TABLE 3.1: *Photon polarization for the optical transitions between the excited states and ground state. Linear polarizations are denoted by \hat{x} and \hat{y} , while circular polarizations are represented by $\hat{\sigma}_{\pm} = \hat{x} + i\hat{y}$ [11]. Reproduced with permission from [11].*

3.4.3 The ionization and repump of the NV⁻ centre

The excited state six sublevels can be measured by photoluminescence excitation (PLE) method. However, after prolonged laser excitation, the NV⁻ centre becomes ionized to NV⁰ centre, resulting in the lose of signal[112, 113]. The mechanism of ionization was established by Siyushev et al[12]. Figure 3.8 shows a schematic of the ionization and recovery process of the NV⁻ centre.

The ionization process consists of only two steps; two-photon absorption followed

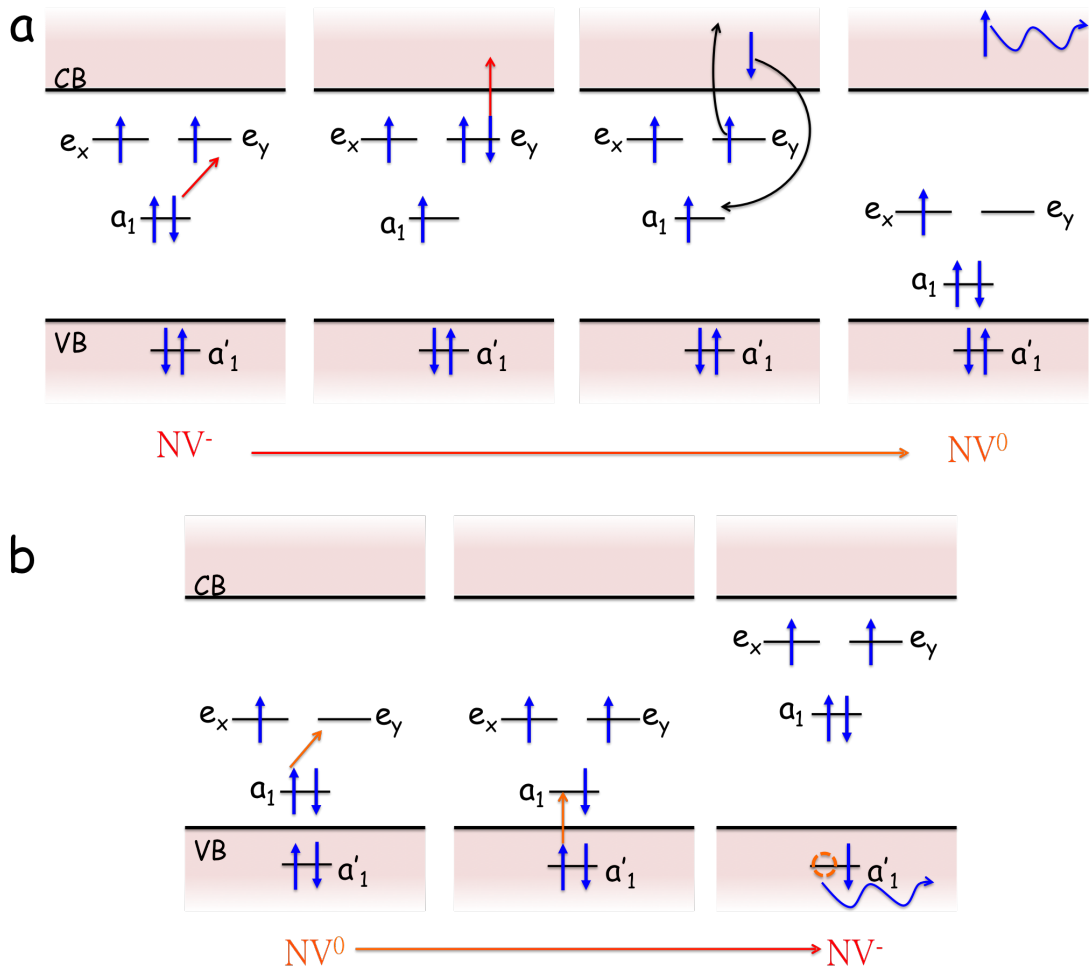


FIGURE 3.8: Schematic picture of the charge transfer process for the NV⁻ and NV⁰ centre. **a**, Ionization process from NV⁻ to NV⁰ includes two-photon absorption and an Auger process that releases enough energy to detach an electron from the defect. **b**, NV⁻ restoring process includes two electrons excited by laser and migration of deep hole[12]. Figures are adapted from [12].

by an Auger process, as shown in Figure 3.8a [12]. The NV⁻ centre simultaneously absorbs two photons, exciting one electron from the a_1 orbital to the conduction band through one of the e levels [12]. After the Auger process via the intermediate e level, the NV centre relaxes to the ground state of the neutral charge state (NV⁰) [12].

Figure 3.8b depicts the recovery process of the NV⁻ centre and it involves the excitation of two electrons and migration of a deep hole. First, one electron is

excited from the a_1 orbital to the empty e level and then the second electron is promoted from the a'_1 orbital band to the a_1 orbital [12]. The energy gap between the a'_1 orbital and the a_1 orbital is comparable to the transition energy of the ZPL of NV^0 centre, implying that the lowest energy needed to restore the negative charge state is comparable to the transition energy of the ZPL of NV^0 centre [12]. The electron hole at the a'_1 orbital migrates away from the NV^0 centre and it relaxes back to the NV^- centre [12].

3.4.4 Broadening of the zero-phonon line

3.4.4.1 Homogeneous broadening mechanism

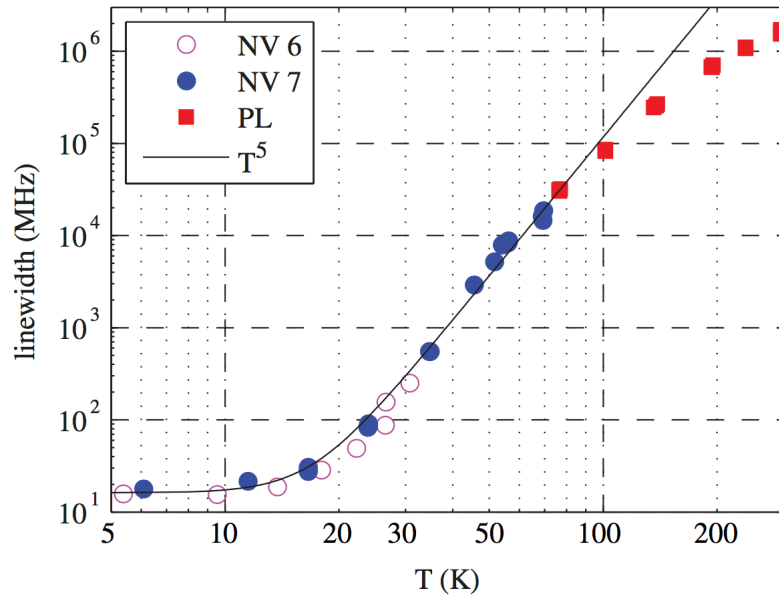


FIGURE 3.9: *Log-log scatter plot of the PLE linewidths as a function of temperature from two single NV^- centres and the PL linewidths from other three NV^- centres. The solid line is the best fit to Equation 3.21[13].*

Reproduced with permission from [13].

The ZPL linewidth of the NV^- centre depends on temperature due to the interaction between the excited state electrons and phonon modes of the diamond

lattice, called homogeneously broadening of the ZPL. Fu et al have investigated the linewidth of the ZPL as a function of temperature (T) and found a systematic trend which can be expressed as[13],

$$\gamma(T) = \gamma_0 + c_2 r T^5, \quad (3.21)$$

where $\gamma_0 = 2\pi \times 16.2$ MHz, $c_2 = (9.2 \pm 0.5) \times 10^{-7} K^{-5}$ and $r = (12.5 \text{ ns})^{-1}$, as shown in Figure 3.9. The T^5 dependence suggests that the dynamic Jahn-Teller effect is the dominant mechanism causing homogeneously broadening below 100 K[13]. However, the linewidth of ZPL does not follow the T^5 dependence above 100 K, indicating there are other mechanism present at higher temperature. Plakhotnik et al proposed that it may be due to the interaction between the electrons and symmetric phonon modes[114]. In order to find out if the ZPLs are transform-limited, the PLE measurements have to be performed below 5 K.

Below 5 K, the linewidth of ZPL is limited by the lifetime of excited state. According to Heisenberg uncertainty principle, the uncertainty in energy of the excited state can be expressed as

$$\Delta E = h\Delta\nu_N = \frac{h}{2\pi\tau}, \Delta\nu_N = \frac{1}{2\pi\tau}, \quad (3.22)$$

where $\Delta\nu_N$ is the uncertainty of the emission photons' wavelength and τ is the lifetime of the excited state. This effect is called natural broadening and the measured homogeneous lineshape of ZPL, ϕ , can be expressed as

$$\phi(\nu) = \frac{\Delta\nu_N/2}{\pi(\nu - \nu_0)^2 + (\Delta\nu_N/2)^2} \quad (3.23)$$

where ν is the wavelength and ν_0 is the central position of the spectral.

3.4.4.2 Inhomogeneous broadening mechanism

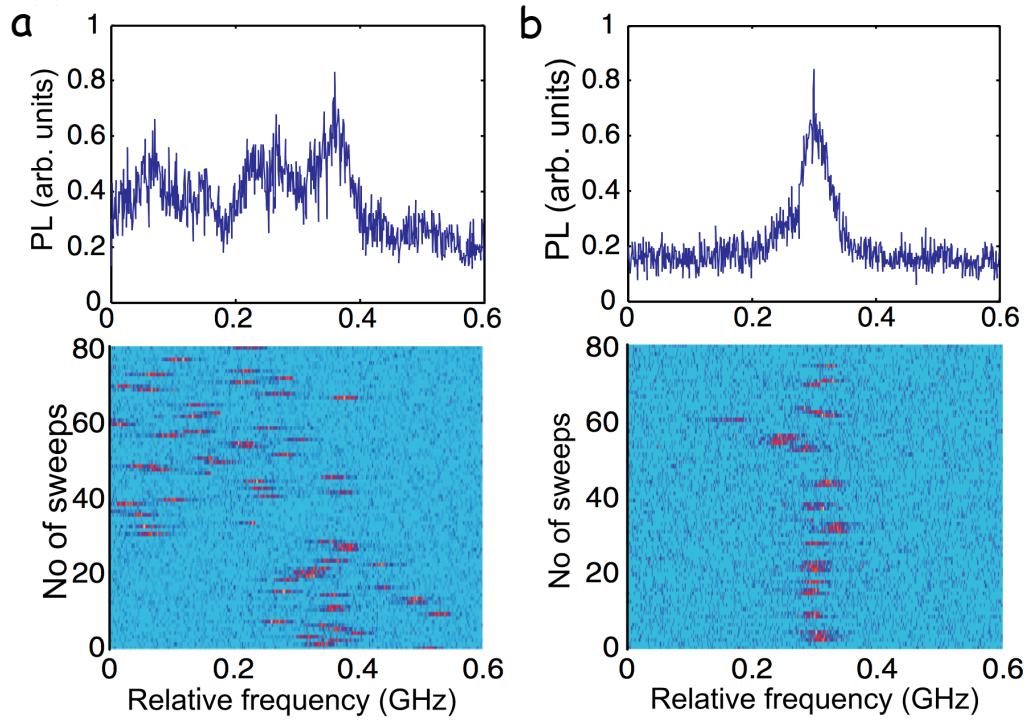


FIGURE 3.10: *Spectral jumping of the NV^- centre with two to different types of repump, **a**, 532 nm repump and **b**, 575 nm repump[12]. Reproduced with permission from [12].*

In most cases, the linewidths of ZPL are observed to be significantly broader than the homogeneous linewidth, called as inhomogeneous broadening. The spectral jumping of the ZPL is responsible for the inhomogeneous broadening, as shown in Figure 3.10. This spectral jumping is generated from the variations in the strain and electric fields in the vicinity of the NV^- centre, due to both impurities and structural defects via the Stark effect[63, 115]. The spectral jumping can

be observed by the repeated PLE scans of the ZPL, as shown in Figure 3.10. The substitutional nitrogen impurity has been believed to be one of the causes of inhomogeneous broadening, because the ionization energy of the substitutional nitrogen is about 1.7 eV below the conduction band. 532 nm (2.34 eV) repump can easily ionize the substitutional nitrogen and Figure 3.10a shows the repeated PLE scans with 532 nm repump[12]. 575 nm laser can also restore the NV^- centre and requires far less power due to resonant with NV^0 , reducing spectral jumping, as shown in Figure 3.10.

3.5 Optically detected magnetic resonance

The NV^- centre can also be identified by the ground state zero-field splitting at 2.87 \sim 2.88 GHz and this splitting originates from the spin-spin interaction[116]. The magnetic resonance between $m_s = 0$ and $m_s = \pm 1$ of ground state can be detected by ODMR at room temperature[54]. The zero-field splitting of the excited state (\sim 1.42 GHz) can also be detected by ODMR at room temperature[117].

The origin of the ODMR signal is the spin-dependent fluorescence because the transition rates of excited state spin sublevels ($m_s = 0$ and $m_s = \pm 1$) to the intermediate state are different[54]. When the electrons are optically pumped to the excited states, the $m_s = \pm 1$ sublevel electrons have a higher chance of relaxing to the intermediate state via a non-radiative transition than the electrons at $m_s = 0$ sublevel do, as shown in Figure 1.1a.

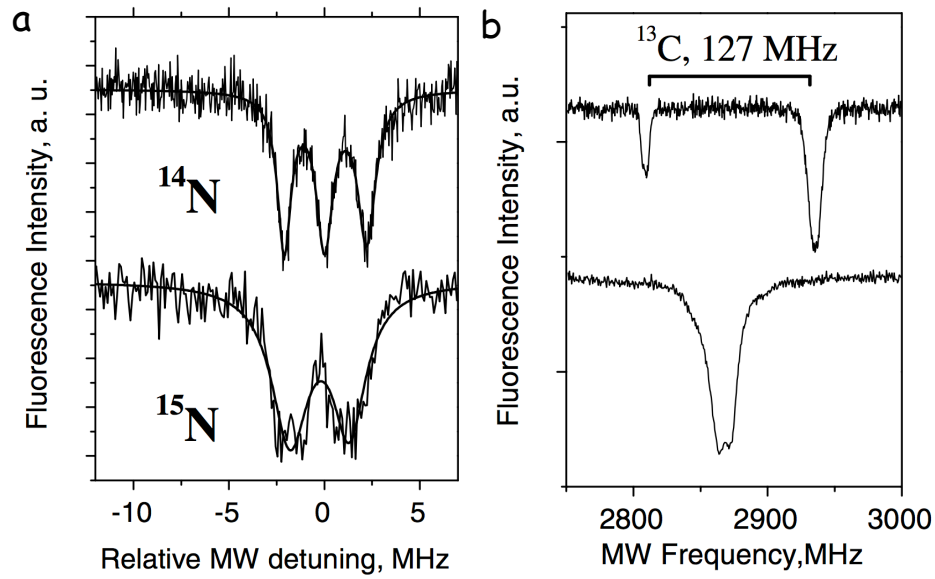


FIGURE 3.11: ODMR spectra of the **a**, ^{14}N and ^{15}N hyperfine structure and **b**, ^{13}C hyperfine structure. The spectra were obtained at ambient temperature without applied external magnetic field[14]. Reproduced with permission from [14].

On the contrary, the intermediate state couples more strongly to the ground state $m_s = 0$ spin sublevel than to the ground state $m_s = \pm 1$ sublevels, resulting in most electrons populating the ground state $m_s = 0$ sublevel[4]. After a couple of optical cycles, the electron spin of the NV^- centre will be polarized to $m_s = 0$ and this spin-polarization effect can be used to prepare an initial state for spin manipulation.

The hyperfine structure, the coupling of the NV^- centres' electrons to the nuclear spins of neighbouring atoms, can be resolved by the ODMR measurements due to the long coherence times of the nuclear spins, which is at least on the order of milliseconds. For the NV^- centre, the most common hyperfine structure originates from the coupling of ^{14}N , ^{15}N or ^{13}C to the NV^- centre. The nuclear spin of ^{14}N is spin-1 and the nuclear spin of ^{15}N and ^{13}C are spin-1/2. Therefore, the ^{14}N hyperfine interaction splits each $m_s = \pm 1$ into three states and there are

two states in ^{15}N and ^{13}C hyperfine structures, as shown in Figure 3.11. The hyperfine splittings of the ^{14}N and ^{15}N have been identified at about 2.2[118, 119] and 3 MHz[120, 121], respectively. The hyperfine splitting of ^{13}C depends on the distance between ^{13}C atom and the NV^- centre and the splitting from nearest neighbour ^{13}C is seen at 130 MHz[14].

The nuclear spin bath causes local magnetic field fluctuation, resulting in the degradation of the spin coherence time[122, 123]. Note that the nuclear spin of ^{12}C is spin-0, so it does not contribute to any hyperfine structure nor spin dephasing. Thus, the longer T_2 time was observed in isotopically pure type IIa diamond.

3.6 Theory for estimating the probability of generating NV^- centres

To get more insight into the NV^- generation, I have built up a simple model to calculate the success probability of creating the NV^- centres per laser damage site, based on the vacancy diffusion equation. This simple model will be used to estimate the probability of the NV^- centres generation per site in Section 5.7. The time dependent vacancy density can be expressed as

$$\frac{dC_V}{dt} = G(t) - C_V C_i V_{diff} \sigma_i - C_V C_N V_{diff} \sigma_N - \sqrt{2} C_V^2 V_{diff} \sigma_V + D \nabla^2 C_V, \quad (3.24)$$

where C_V , C_i and C_N are the density of vacancy, interstitial carbon and nitrogen respectively and V_{diff} is the vacancy diffusion velocity. The first term in the right hand side of Equation 3.24 is the vacancy generation term. The second term is the recombination of vacancy and interstitial carbon term and σ_i is the cross section of recombination. The third term is the NV centre formation term and σ_N is the cross section of the NV centre formation. The fourth term is the divacancy formation term and σ_V is the cross section of di-vacancy formation. The fifth term is the vacancy diffusion term and D is the diffusion coefficient. During annealing, no vacancies are generated, so $G(t) = 0$. Antonov et al use Monte Carlo methods to calculate the number of vacancy as a function of annealing time and suggest that the number of vacancies dramatically drops lower than 20% within a few seconds and then slowly decreases[124] from 20% to a few % in 3 hours. To simplify the model, the second term is neglected, assuming that the number of vacancy is a constant to about 10% of the initial vacancy number[124]. The third term can be neglected because the concentration of nitrogen is much lower than the vacancies. The fourth term is dropped because the di-vacancy is not stable at 1000°C[79], so the concentration of di-vacancy is far more lower than the concentration of single vacancy. Then, the equation can be rewritten to be

$$\frac{dC_V}{dt} = D \nabla^2 C_V, \quad (3.25)$$

which is a classical diffusion equation. Since the shape of laser damage is elongated in z direction (see Section 6.2), only the diffusion in x - y plane is considered and

the diffusion of vacancy in z-axis is averaged out. The cylindrically symmetrical solution of vacancy diffusion equation can be expressed as[125]:

$$C_V = \frac{N_V}{4\pi DtL} e^{-\frac{r^2}{4Dt}}, \quad (3.26)$$

where N_V is the initial number of vacancy, r is the radial distance from the centre of the laser damage and L is the length of the damage in z-direction.

The time dependent concentration of the NV^- centres can be described as

$$\frac{dC_{NV}}{dt} = C_V C_N V_{diff} \sigma_N = \frac{\sigma_N D}{d_{hop}} C_N C_V, \quad (3.27)$$

where d_{hop} is the hopping distance of the vacancy each time. Here, I assume that the vacancy only hops to the nearest neighbor carbon site each time, so $d_{hop} = 0.15 \text{ nm}$ [124]. In addition, assuming that the radius of the cross section is the nearest neighbor distance. The concentration of nitrogen of electronic grade CVD diamond is specified to be less than 5 ppb, corresponding to the detection limit of the EPR methods for nitrogen concentration. As a consequence the NV^- concentration obtained from this calculation is also a upper limit, as well. The value of D is obtained from the fitting of the displacement histogram of laser-generated NV^- centres, described in Section 6.3.2. Thus, the Equation 3.27 can be rewritten as

$$\frac{dC_{NV}}{dt} = \frac{\pi \times 0.15^2 \times 3.7}{0.15} \times 8.81 \times 10^{-7} C_V = 1.58 \times 10^{-6} C_V. \quad (3.28)$$

The concentration of NV centres can be obtained by combining Equation 3.26 and Equation 3.28 and then integrating over the size of the laser-induced feature and annealing period.

$$\begin{aligned}
 N_{NV} &= \int_{time} \int_0^L \int_0^{2\pi} \int_0^\infty 1.58 \times 10^{-6} \frac{N_V}{4\pi DtL} e^{-\frac{r^2}{4Dt}} r dr d\theta dz dt \\
 &= \int_{time} 1.58 \times 10^{-6} \times N_V dt \\
 &= 1.58 \times 10^{-6} \times N_V \times T
 \end{aligned} \tag{3.29}$$

where T is the annealing duration.

3.7 Summary

This chapter has discussed the theoretical framework within laser writing for damage and the characterization of NV⁻ properties, including optical and spin properties. The three models, tunneling ionization, MPI and Avalanche ionization, proposed to describe the mechanism of laser-induced damage, have been discussed. The vacancy generation mechanisms will be used to analyze the results of the laser-generated GR1 in Chapter 5. In addition, the diffusion function of vacancy has been presented, which will be used in Chapter 6 to analyze the results of the laser-generated NV⁻ centres after annealing.

The electronic structure of the NV⁻ centre was presented. The theory of the photon statistics of a three-level system has been presented and it will be used to fit the HBT results in Chapter 5. The spin Hamiltonian of the NV⁻ centre's excited

state under transverse strain has been presented and the strain-induced excited state splitting has also provided. The theory of the strain-induced splitting will be used to analyze the results of PLE strain measurements in Chapter 8. The mechanism responsible for the ionization of the NV^- centre has been discussed to explain why the repump excitation is required. In addition, this section has also discussed two mechanisms broadening the ZPL, the homogeneous and inhomogeneous mechanism. The homogeneously broadening mechanism explains the temperature dependence of the linewidth of the ZPL and inhomogeneously broadening suggests that defects and impurities in the vicinity of the NV^- centre cause spectral jumping; hence it is difficult to artificially generate the NV^- centre with a transform-limited optical transition.

The spin-dependent fluorescence has been discussed, enabling the spin state of NV^- centre to be read out via ODMR. The hyperfine structures of the NV^- centre has been presented. I have built a simple model based on the vacancy diffusion equation to estimate the probability of generating the NV^- centres per site. A cylindrically symmetric diffusion function is considered due to the elongated shape of the features. To include the recombination mechanism in the calculation, the initial number of vacancy is scaled by factor of 0.1. The formation of divacancy is ignored because the divacancy is not stable at 1000°C . The nitrogen concentration is assumed to be 5 ppb, but it is overestimated. This model will be used to analyze the probability of generating the NV^- centres per site in Section [5.7](#).

Chapter 4

Experimental Methods

This chapter is going to describe all the experimental set-up and methods used to generate and characterize the laser-created NV^- centres. First, the laser writing apparatus which was used to generate laser-induced damage is described. The importance of the aberration correction in the laser writing process is also discussed. All the effects and mechanisms which can minimize the size of laser damage will be discussed. The detail of the diamond samples which were used in this thesis will be presented. In addition, the equipment and the experimental method, used to anneal the samples, will be also presented.

After the laser writing process and annealing, investigations of the optical and coherence properties of the laser-generated NV^- centres are the backbone of this work, relying heavily on the experimental apparatus and methods. They will be described as three parts:

1. Custom-built confocal microscope apparatus and the experimental methods of the HBT and lifetime measurements.
2. Continuous wave ODMR and Hahn echo experimental apparatus and methods.
3. PLE spectroscopy and strain measurements at low temperature.

4.1 Laser writing

4.1.1 Experimental set-up

Direct laser writing (DLW) was performed by using a regeneratively amplified Ti:Sapphire laser (Spectra Physics Solstice). Figure 4.1a shows the layout of the laser processing optical set-up. The laser beam was first expanded onto a liquid crystal phase-only spatial light modulator (SLM) (Hamamatsu X10468-02), which was imaged in a 4f system onto the back aperture of a $\times 60$ 1.4NA oil immersion objective lens (Olympus PlanApo). The diamond sample was mounted on precision translation sample stages (Aerotech x-y: ABL10100; z: ANT95-3-V) which provide three axis movements. A LED transmission microscope was built as a side arm to monitor the sample during the laser processing. Before the objective lens the laser pulse was linearly polarised and the duration of the pulse is about 250 fs which was measured by an intensity autocorrelator (APE Pulsecheck). The pulse duration at focus will be slightly longer because of the dispersion in the objective lens.

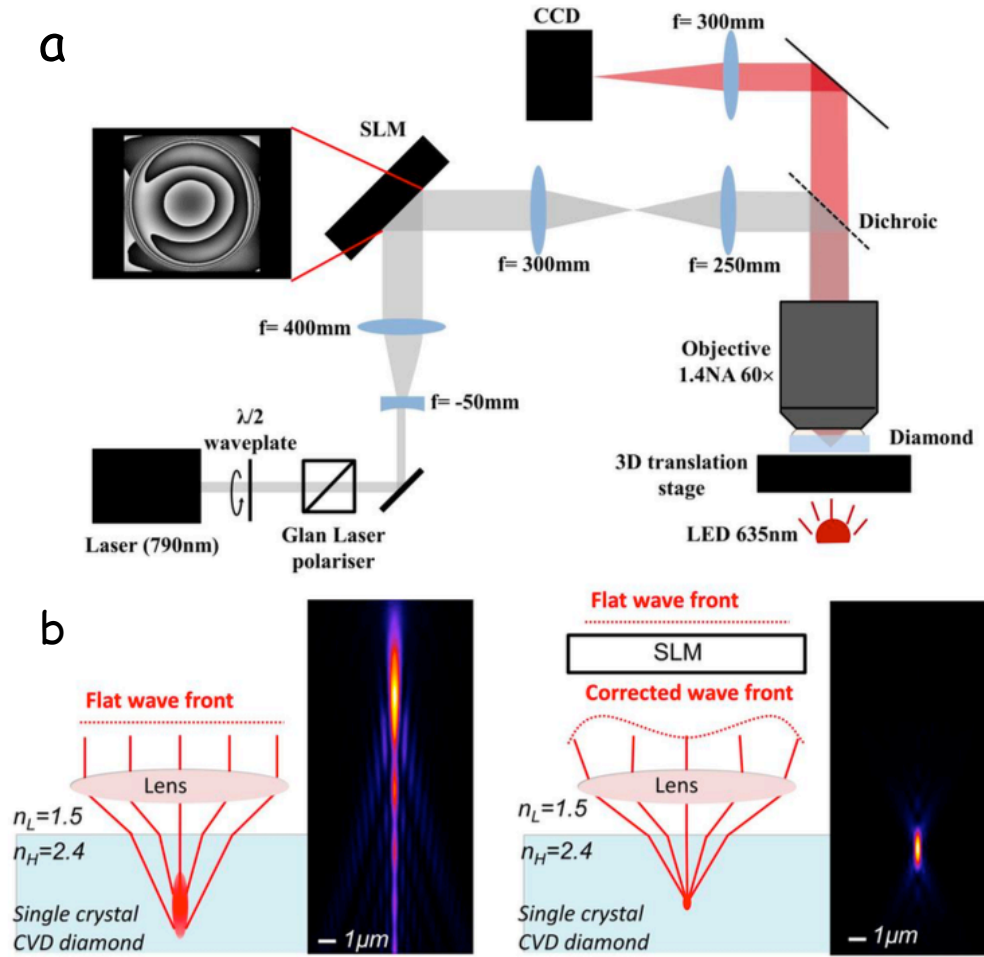


FIGURE 4.1: **a**, Schematic of laser processing optical set-up. The phase pattern of the laser beam is modified by the liquid crystal phase-only spatial light modulator (SLM) to correct the aberrations in the system and those introduced by focussing into the diamond. **b**, The effect of the aberration correction on the laser focal intensity distribution when focused through the interface between the immersion oil and diamond to a depth of $50\mu\text{m}$. Left graph shows that the focus is significantly elongated in z axis by spherical aberration without aberration correction. Right graph presents that a good z axis focus is achieved with the SLM. Figure courtesy of Patrick Salter.

4.1.2 Aberration correction and size of focal spot

The high numerical aperture objective lens is necessary to minimize the size of the laser focus and move into the regime appropriate for the creation of single localized NV centres as opposed to NV centre ensembles which are usually created around the area of laser induced graphitisation[90]. However, focusing the laser beam deep

into a diamond by high numerical aperture optics introduces remarkable amount of spherical aberration due to the mismatch of the refractive indices between the immersion oil and diamond, causing strong refraction. Thus, it is very important to correct the spherical aberration to recover the optimum optical performance, which has already been demonstrated to enhance the light matter interaction while laser writing sub-surface graphitic patterns[126]. Therefore, the phase pattern displayed on the SLM was modified to remove any system and sample induced aberrations by experimentally minimizing the required laser pulse energy to create visible damages in diamond sample. Figure 4.1b shows that introducing the SLM significantly reduces the size of the pulsed laser focal spot. The left graph of Figure 4.1b shows that the size of the pulsed laser focal spot is much larger than $2\mu\text{m}$ in z axis without the SLM, whereas the size of the focal spot in z-axis is reduced to about $2\mu\text{m}$ after aberration correction (the right graph in Figure 4.1b). This significant improvement in the size of the focus in axial direction is because the spherical aberration at the diamond/immersion oil interface is the dominant aberration source. Martin Booth's group have demonstrated that with adaptive optics, they can accurately fabricate damage patterns in diamond at the depth of at least $220\mu\text{m}$ [87]. In general, the laser writing method does not have a limitation on fabrication in z-direction, and the depth of fabrication is only limited by the working distance of the objective lens.

Thanks to the aberration correction, the focal spot of the pulsed laser is expected to be near the diffraction-limit of the objective lens, which is 350 nm and $2\mu\text{m}$ in the transverse and axial dimension (full width half maximum) respectively, giving

a focal volume of about $0.12 \mu\text{m}^3$. The laser fabrication is highly non-linear because the vacancies and interstitial carbon pairs are created via multi-photon absorption processing as aforementioned in Section 3.1. The pulsed laser intensity is strong enough only within the focal volume, so that there is a sufficient probability of a multi-photon absorption process. The MPI model suggests that the distribution of vacancies generation with y -photons absorption depends on the y^{th} power of the laser intensity distribution. Therefore, the vacancies are expected to be generated within a volume considerably smaller than diffraction-limited focal volume due to nonlinearity.

The duration of the laser pulse has a significant affect on the size of the damage spot. For nanosecond or longer laser pulses, thermal processes dominate the damage generation mechanism because the pulse duration is comparable with the characteristics time of thermal diffusion (ns)[3]. The diffused heat will melt the material and generate damage outside the focal volume of laser. Moreover, the temperature in the focal spot is high enough to make the vacancy diffuse, increasing the distribution of vacancies. In contrast, the duration of ultrafast lasers (with picosecond or femtosecond pulse length) is shorter than the characteristics timescale of thermal diffusion. Thus, most of the laser pulse energy is delivered to the focal volume before it can diffuse away as heat, leading to a limit the feature size within the focal volume of the pulsed laser beam. Moreover, only the laser pulses with femtosecond or picosecond durations are possible to fabricate features beneath the diamond surface[3, 127]. As the laser pulse length is much longer than picosecond, only surface damage would be generated.

4.2 Diamond samples and annealing

This work contains two data sets recorded from two diamond samples, labelled as sample A and sample B. Both diamond samples are 'electronic grade' single crystal chemical vapor deposition (CVD) plates from Element Six Ltd with $\{100\}$ orientation faces and the edges of the samples are along $\langle 110 \rangle \pm 3^\circ$ crystallographic orientation. The electronic grade means that the nitrogen concentration is less than 5 ppb and the boron concentration is less than 1 ppb, which are lower than the detection limit of electron paramagnetic resonance (EPR) measurements. The electronic grade CVD diamond has very low density of the NV centres ($1 \sim 2$ per $100 \times 100 \mu\text{m}^2$). In addition, there are almost no NV centres generated after high temperature annealing, because the level of intrinsic vacancies is very low. Thus, it is a perfect material to demonstrate the generation of single NV centres. Moreover, the low level of nitrogen atoms and defects should result in that the NV^- centre has good coherent properties, because they disturb the NV's electron spin and generate electric field fluctuation. The 5 ppb native nitrogen atom is the source to form the laser-generated NV centres. Although it seems that 5 ppb nitrogen concentration is too low to generate NV centres, there are about 880 native nitrogen atoms per μm^3 .

The annealing was performed in a tube furnace (Elite Thermal System TSH16/50/180-2416). The diamond samples were loaded in an alumina boat and buried in a sacrificial diamond grit (Element Six Micron+). The furnace was purged with dry nitrogen boil-off to minimize oxidization and graphitization of the diamond surface. The dry nitrogen gas can prevent the diamond from oxidation and graphitization

up to 900°C. However, in this work the diamonds were needed to be annealed over 900°C and the dry nitrogen gas is no longer sufficient to protect the diamond surface. The diamond grit has larger surface-area-to-volume ratio, so the diamond grit is easier to be oxidized and graphitized, consuming all oxygen and moisture. Thus, the diamond grit is essential for annealing at temperature above 900°C.

4.3 Confocal microscope

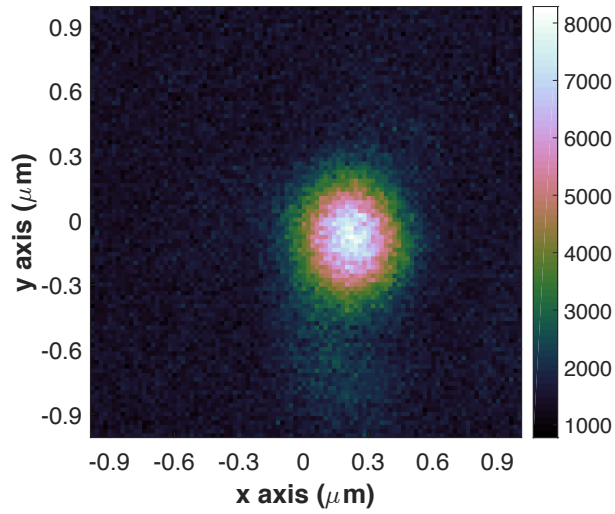


FIGURE 4.2: *Typical PL image of single NV⁻ centre.*

All the optical characterizations in this project were carried out by using a custom-built scanning confocal microscope. The significant advantage of this is the high resolution in depth, which reduces the background fluorescence and enables to investigate single point defects. To achieve that, the excitation illumination is first focused on the interested feature and the photoluminescence (PL) is focused into a pinhole before the detector. If carefully tuning the aperture of the pinhole to match the image plane of the microscope, it will become confocal with the focal plane of the excitation illumination. Thus, the pinhole blocks out all the

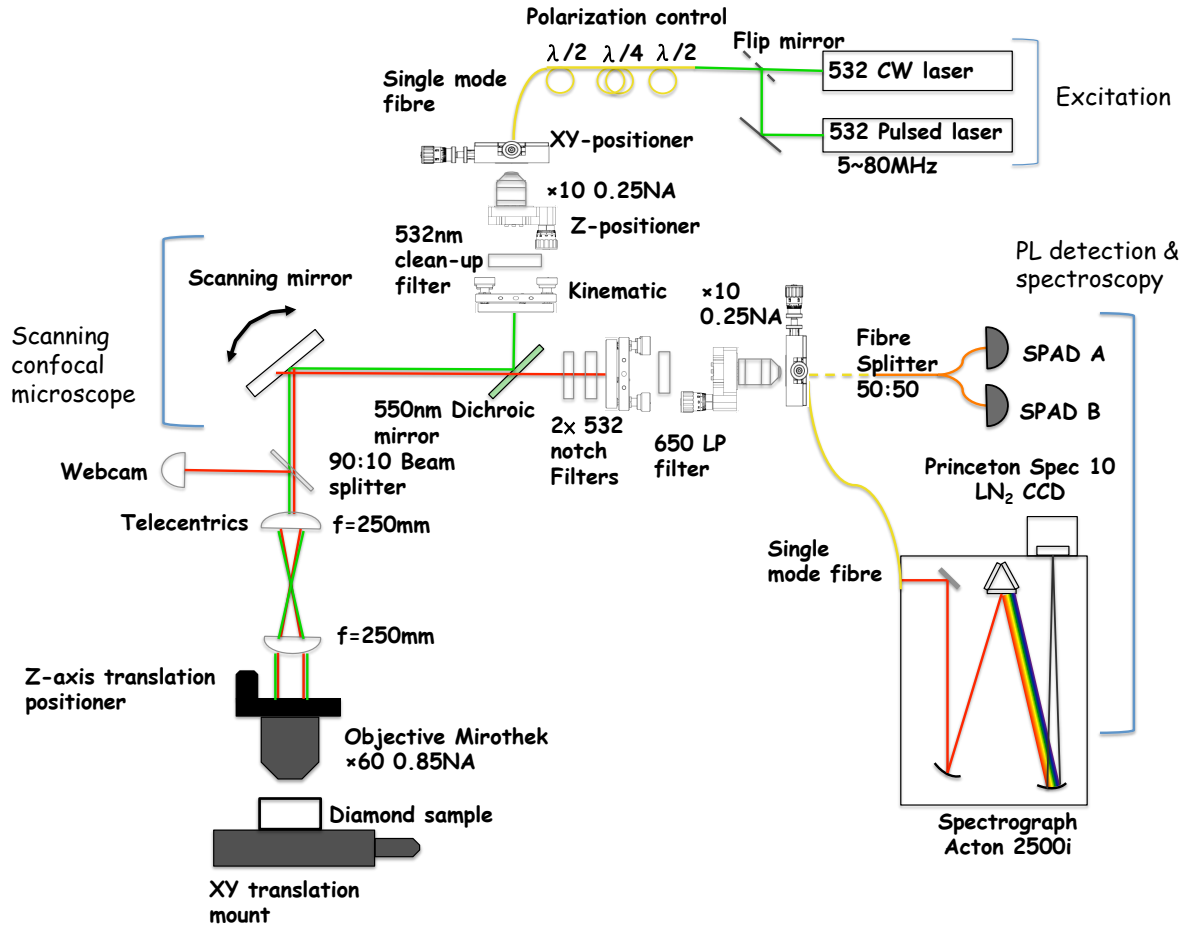


FIGURE 4.3: *Schematic layout of the optical components for room temperature operation and the custom-built confocal microscope set-up, including all actuators to align the system. All optics are mounted onto an optical table. The output end of the excitation single mode fibre is mounted on a XY-positioner to align the position of the laser beam and the laser beam is collimated by using a $\times 10$ 0.25 NA objective lens. A 550 nm dichroic mirror is used to separate the excitation and photoluminescence to different direction.*

scattered light and fluorescence from the outside of the focal plane, leading to a higher resolution in depth. The resolution of the confocal microscope can achieve diffraction limited. For all room temperature measurements, a objective lens with numerical aperture (NA) of 0.85 was used, giving the diffraction limited resolution of about 300 nm. Figure 4.2 shows a typical PL image of single NV⁻, indicating that the resolution of the confocal microscope is about 300 nm, enabling to measure the displacement of the laser-generated NV⁻ centres in Chapter 6.

The schematic graph of the optical set-up of optical characterizations is shown in Figure 4.3. A 532 nm laser was used to excite the NV^- centres and the laser-induced damages in cw [CNI MGL-III-532, 200mW] or pulsed mode [PicoQuant LDH-P-FA-530B] using a pulsed driver [PDL 800-B, 5~80MHz]. The 532 nm excitation is coupled into the excitation arm of the confocal microscope via a single mode fibre (Thorlabs SM460HP) with a 3-paddle polarization controller (Thorlabs FPC030). The polarization controller is based on the stress-induced birefringence of the optical fibre to create quarter waveplate, half waveplate and quarter waveplate ($\lambda/4$, $\lambda/2$, $\lambda/4$) in sequence. In theory, this 3-paddle polarization controller can generate any kind of polarization, including linear and circular polarization, enabling perfect excitation of the NV^- centre. The other end of the optical fibre is mounted on a XY-positioner (Thorlabs ST1XY) in the excitation arm of the confocal microscope, as shown in Figure 4.3.

Figure 4.3 also shows the schematic picture of the confocal microscope. The excitation laser beam is collimated by using a $\times 10$ 0.25NA objective lens. The excitation and photoluminescence propagate in the system as collimated beam. A 532 nm clean-up filter is placed in the excitation arm to prevent the Raman emission generated by the optical fibre from reaching the sample. A kinematic mount (Thorlab KC1 T/M) is used to adjust the launch angle of the excitation beam which enables to align the excitation focal spot to fluorescence focal spot. There is a similar set-up in the collection arm and the PL is coupled into a single mode fibre and the single mode fibre works as the pinhole. After the excitation arm, there is a 550 nm dichroic mirror to separate the excitation and PL to different

directions. Although the dichroic mirror prevents most excitation light from going to the collection arm, two 532 nm notch filters are placed before collection arm to filter out the leakage of the excitation to protect the detectors. A 650 nm long pass filter is installed in collection arm to get rid of the first order and second order Raman lines from diamond in most measurements, but it is removed when taking spectra.

A fast steering mirror (Newport FSM300) enables the excitation focal spot to rapidly scan across the sample to get a 2D image. A 4f configuration is built after the fast steering mirror by two opposing telecentric lenses ($f=250\text{mm}$). The fast steering mirror and objective lens are located at the image plane of each side of the 4f configuration. Thus, the 4f system ensures that the collimated excitation beam goes into the objective lens through the centre of the back aperture. In between the 4f configuration and the fast steering mirror, a 90:10 beam splitter is introduced to direct a small amount of LED light reflected by sample surface into a webcam to search the location of the damage array. The excitation is focused into the sample by a $\times 60$ 0.85NA objective lens (Microthek). The fluorescence is collected by the same objective and coupled into a single mode fibre (Thorlabs SM460HP) via the collection arm and the fibre is plugged into a single photon avalanche detector (Perkin-Elmer SPCM-AQRH) for imaging. A time-correlation single photon counting card (Edinburgh Instruments TCC900) is used to record the time-correlation photoluminescence (TRPL) measurements and photon autocorrelation function measurements. When performing photon autocorrelation function measurements, the single mode fibre is coupled into a 50:50 fibre beam

splitter. The single mode fibre can also be coupled into the spectrometer (Acton 2500i) with a liquid nitrogen cooled CCD (Princeton Spec10). The spectrometer equips two gratings (300 and 1200 lines/nm), providing 0.13 nm and 0.03 nm spectral resolution respectively. The confocal microscope controlling software was written by Matthew Wincott and Philip Dolan added more functions to it, such as auto spectra sequence.

4.4 Hanbury-Brown and Twiss and lifetime

The photon autocorrelation function measurements are able to identify if a feature is single photon emitter and they were carried out by using the Hanbury-Brown and Twiss (HBT) interferometer. A 1×2 50:50 fibre splitter (Thorlabs FCMM50-50A) is used to split the PL emission evenly into two single photon detectors. One of the detector serves as a start channel and the other is stop channel. When the start channel receives a photon, the measurement is started at time $t=0$. When the stop channel detects a photon, the measurement is ended at time $t=\tau$. A histogram of correlation intensity is built up as the function of the delay time (τ) between the photon detection events of the two channels.

For a single photon emitter, it is not possible that both detectors receive a photon at the same time, resulting in a anti-bunching dip at time $t = 0$. In theory, the anti-bunching dip goes down to absolutely zero. However, there is always some background emission in reality, leading to the minimum of the dip being above zero. The Fock state of ideal two single photon emitters is $|n = 2\rangle$, resulting in

$g^{(2)}(0) = 0.5$. Thus, in general, if $g^{(2)}(0)$ is lower than 0.5, it can be recognized as a single photon emitter.

The normalization of the resulting histogram is important to obtain correct depth of anti-bunching dip. The normalization is accomplished through dividing by $I_1 \times I_2 \times t_{\text{bin}} \times T_{\text{tot}}$. I_1 and I_2 mean the PL count rates of both detectors respectively, t_{bin} is the bin width of the measurement and T_{tot} is the total integration time period. After this normalization, the $g^{(2)}$ function at infinity should be equaled to 1.0.

The excitation is swapped to a pulsed laser to measure the PL lifetime of the NV⁻ centre. The lifetime of the NV⁻ centre in bulk diamond is around 12 ns, so the repetition rate of the pulsed laser is usually set as 10 MHz to allow a large enough time window for the PL intensity to decay to the background level. The background emission contributes a short decay time component to the measurement, so in order to remove the fast component a lifetime measurement is taken off-centre with the same laser power and integration time. After subtracting the background lifetime measurement, the time-related PL result usually appears as a single exponential decay. This single exponential decay is fitted by the Equation [4.1](#)

$$I(t) = I_0 + Ae^{-\frac{t-t_0}{\tau}}, \quad (4.1)$$

where I_0 is the baseline, A is the amplitude of the fit, t_0 is the start of the decay and τ is the lifetime of measured feature.

4.5 Optically Detected Magnetic Resonance

4.5.1 Continuous wave optically detected magnetic resonance

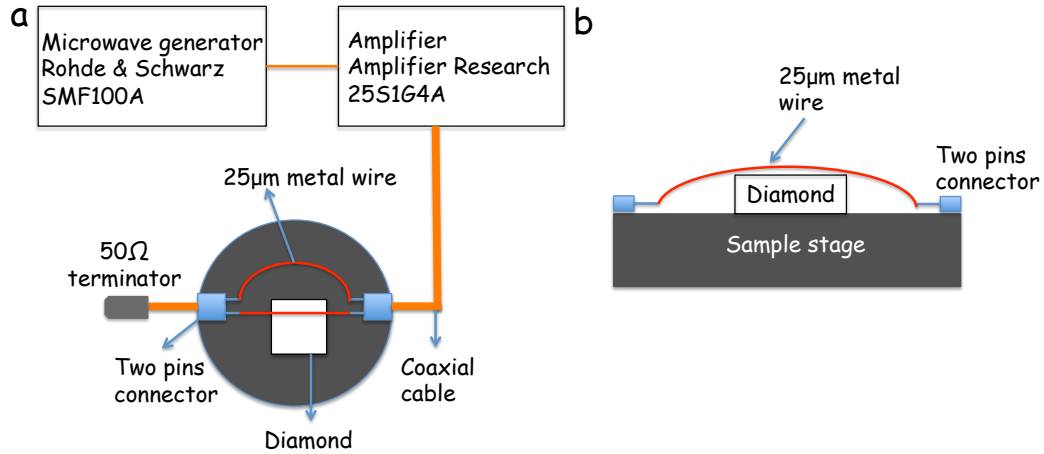


FIGURE 4.4: *a*, Schematic layout of the cw ODMR experimental apparatus. *b*, Schematic layout of the metal wire and diamond sample.

The cw ODMR measurements were carried out by applying microwaves on the target NV^- centre and recording the change of the PL intensity as a function of the microwave frequency. Figure 4.4 shows the schematic graphs of the layout of the ODMR experimental apparatus and the layout of mounting the 25 µm metal wire. The microwaves are provided by a microwave generator (Rohde & Schwarz SMF100A) and the power of microwaves are increased by an amplifier (Amplifier Research 25S1G4A). The microwaves are output from the amplifier by a coaxial cable and the other end of the coaxial cable is connected to a two pin connector. The microwaves are delivered to the diamond sample by a gold wire with diameter of 25 µm which spans above the diamond sample, as shown in Figure 4.4b. The 25 µm gold wire is soldered onto the pin which connects to the fire wire of the

coaxial cable. The other end of the gold wire is soldered onto the second two pin connector and connected to a 50Ω terminator via a coaxial cable. The ground pins of both pin connectors are connected by the second $25\mu\text{m}$ gold wire to form a circuit loop.

The microwave power was normally set between -8 and -5 dBm depending on the distance between the measured NV^- centre and the $25\mu\text{m}$ gold wire and the gain of the amplifier was set to be 4dB. The laser power was set lower than 1 mW since strong excitation power would broaden the ODMR signal and decrease the contrast. The scan bin width was usually set to be 1 MHz and the time per scan was 3~4s, depending on the scan frequency range. In order to get clear ODMR spectra, it needed to accumulate at least 300 scans. The linewidth of the ODMR signal depends on laser and microwave power. Thus, in order to resolve the hyperfine structure, the laser and microwave power were further reduced and the scan bin width was decreased to 50 kHz. The microwave power was set below -11 dBm and the laser power was set below 0.7 mW. To observe hyperfine structure, it required to accumulate at least 2000 scans due to low count rates. The software for cw ODMR measurements was also written by Matthew Wincott.

4.5.2 Hahn echo measurements

The Hahn echo measurements were carried out by Sebastian Knauer in University of Bristol and he also developed the method. The spin coherence times, T_2 , of the laser-generated NV^- centres were measured by the Hahn Echo method. The Hahn echo pulse sequence includes $\pi/2 - \tau_0 - \pi - \tau_1 - \text{echo}$, as shown in the Figure

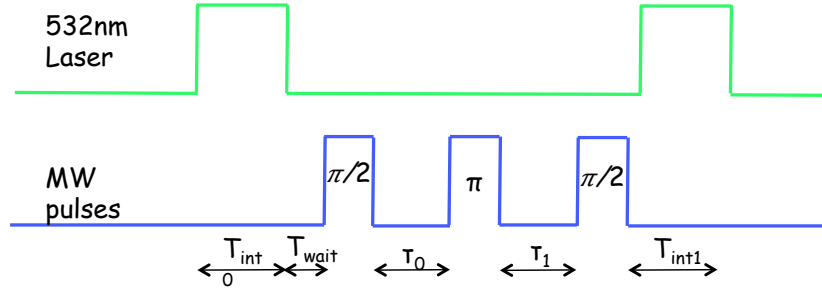


FIGURE 4.5: *Pulse sequence for the Hahn echo measurements. Laser gating is indicated in green and microwave gating in blue.*

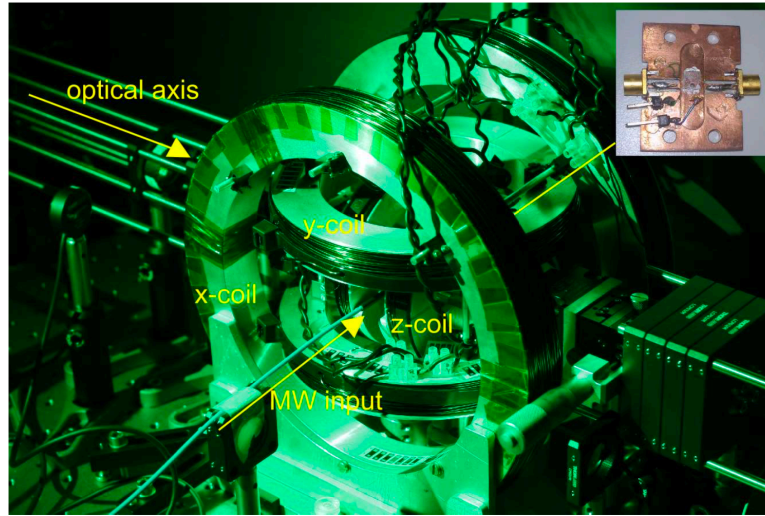


FIGURE 4.6: *Image of Helmholtz coil in the Hahn echo setup. The optical axis and the microwave input is shown. Inset: example of a sample holder. The image is taken by Sebastian Knauer.*

4.5. Figure 4.6 shows the image of the sample stage of the Hahn echo setup. The microwave was delivered to the NV^- centre by a gold wire spanning above the diamond sample and the apparatus is similar to Figure 4.4b and the inset of Figure 4.6 shows the image of the sample holder. An external magnetic field of 6.7 mT was applied and carefully aligned parallel to the NV^- centre axis. The magnetic field is generated from three Helmholtz coil pairs, as shown in Figure 4.6. The Zeeman splitting between the -1 and +1 ground state spin sublevels was large enough to ensure the individual driving of the $m_s = -1$ transition. The amplitude of the fluorescent echo signal was measured as a function of the pulse separation,

τ_1 .

The time duration of the $\pi/2$ -pulse was chosen to be 20 ns (40 ns for π -pulse), determined by Rabi oscillation measurements on the $0 \leftrightarrow -1$ transition. Thus, the bandwidth was larger than the splitting, allowing full excitation of the $0 \leftrightarrow -1$ transition. A single Hahn echo measurement, i.e. iteration of τ_1 around the set value of τ_0 , consisted of a few million iterations of the pulse sequence and corresponding to about 3500 photon detection events. The signal was normalized to the equilibrium between the -1 and 0 spin sublevels of the optical pulse. The Hahn echo decay was measured over the first decay and on the revival.

4.6 Low temperature

4.6.1 Photoluminescence excitation measurements

The linewidth of the laser-generated NV^- centre's ZPL was investigated by the photoluminescence excitation (PLE) method, since the resolution of the normal spectrometer is not high enough to resolve it. Figure 4.7a shows the schematic apparatus of PLE experiment. The PLE spectrum is recorded by using an external cavity diode laser (Toptica DLC pro) to scan across the ZPL at wavelength of 637 nm and collecting all phonon sideband photons. The linewidth of the resonance excitation, which limits the PLE spectrum resolution, is less than 300 kHz. Thus, this laser is able to resolve the transformed-limited ZPL (13 MHz) of the NV^-

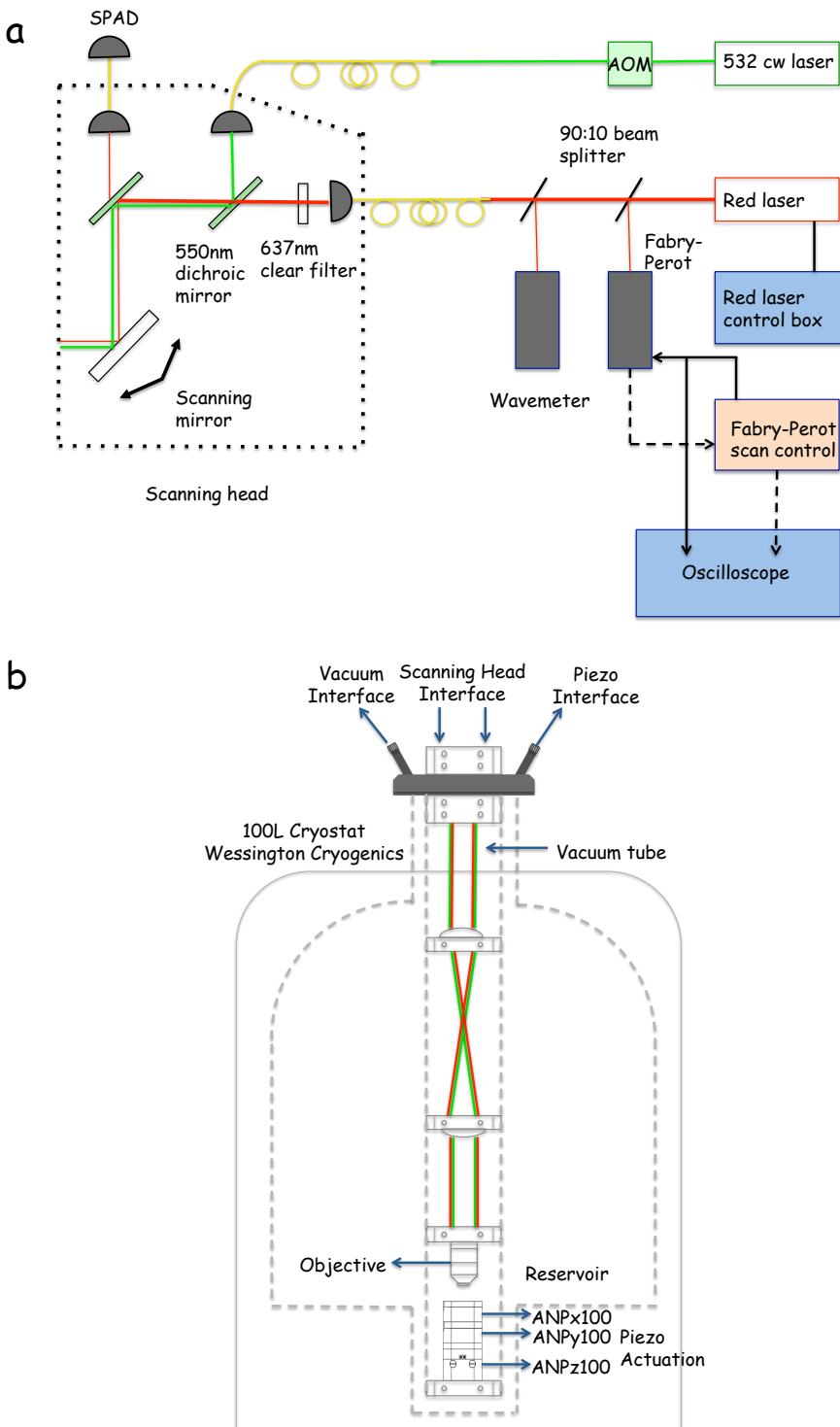


FIGURE 4.7: **a**, Schematic detail layout of the PLE experimental apparatus and the reconfiguration of the scanning head for PLE measurements. **b**, Schematic diagram of the low temperature apparatus.

centres. The wavelength of the resonance excitation was measured directly using a wavemeter (High Finesse WSU-30).

In order to obtain a good PLE result, the resonance excitation must be set up to provide single mode lineshape. Therefore, a scanning Fabry-Perot interferometer (Thorlab SA200-5B) with control box (Thorlab SA201) was used to monitor the mode shape of the resonance excitation. The mode of the resonance excitation was lively displayed by an oscilloscope (Rohde & Schwarz RTM2104) and the single modes are obtained by tuning the current and feed forward settings of the diode laser. After prolonged excitation, the NV^- could be ionized to be NV^0 , as discussed in Section 3.4.3. A short 532 nm pulse is needed to pump the NV^0 back to NV^- . The repump pulses were delivered from a frequency doubled diode-pumped solid state laser at 532 nm (CNI MGL-III-532), gated into 200 ms pulses using an acousto-optic modulator (AOM) (Isomet IMDD-P80L-1.5). The repump pulses were applied in the next sweep only when no PLE signals had been detected.

Laiyi Weng set up the resonance excitation and wrote the software for PLE measurements. 40 GHz resonance excitation frequency range have been performed on each NV^- centre in two runs (20 GHz for each run) to search the PLE signals. The power of the resonance excitation was set to be 1 mW and one sweep takes 2~3 s. It requires to accumulate at least 100 sweeps to measure the inhomogeneous broadening linewidth. The starting excitation frequencies are slightly different from sweep to sweep, so colourscale map of the repeated PLE spectra was built up by aligning each sweep to a new frequency axis. The new frequency axis are established by

the frequency maximum and minimum among all sweeps measured by wavemeter with bin width equal to the frequency increment of setting.

The linewidth of the NV^- centre's ZPL depends on the temperature due to the phonon interaction[13], so the PLE experiment was carried out at 4.2 K to minimize the phonon interaction. Our custom-built confocal microscope has the capability to reconfigure for low temperature experiments. The whole scanning head of the confocal microscope in Figure 4.7 can be detached from the optical bench and installed onto the top of a bath cryostat (100L Wessington Cryogenics).

Figure 4.7b shows the schematic graph of low temperature system. The sample stage is needed to be put inside of the bath cryostat, so the sample stage must be remotely controllable. Therefore, a set of piezo stacks were used to control the position of the sample, including three piezo nanopositioners (Attocube ANPz100, ANPx100, ANPx100) to have three translational degrees of freedom. The piezo nanopositioners were controlled by control modules (ANC300 Controller, 3×ANM150 Modules). The Microthek lens is not designed for the low temperature operation, so a $\times 50$ 0.82 NA objective lens (Attocube LT-APO/VISIR/0.82) was used for all low temperature measurements. The vacuum tube underwent three cycle of pumping down to 5×10^{-5} mbar and filling with Helium gas to get rid of all moisture and air. Then the tube was filled with 50 mbar Helium gas for heat exchange.

4.6.2 Methods of full zero-phonon line spectra measurements

Normal PLE spectra only show two optical transition lines, E_x and E_y , because the spin projection quantum number of $A_{1,2}$ and $E_{1,2}$ states are $m_s = \pm 1$. After couple cycles of optical excitation, the electron of the NV^- centre is pumped into the $m_s = 0$ spin sublevel of ground state; thus according to Fermi's golden rule no electron can be promoted to $A_{1,2}$ and $E_{1,2}$ states by an excitation laser. In general, the optical transition lines from these four excited states are never been observed. On the other hand, the spin projection quantum numbers of the E_x and E_y states are zero, so the optical transition lines from them should be seen. The anti-crossing between E_y and E_2 at a transverse strain of 7 GHz causes spin mixing, resulting in the absent of the E_y transition line. In fact, the spin mixing happens before this anti-crossing, so the E_y transition line is not observed at a lower strain filed than 7 GHz.

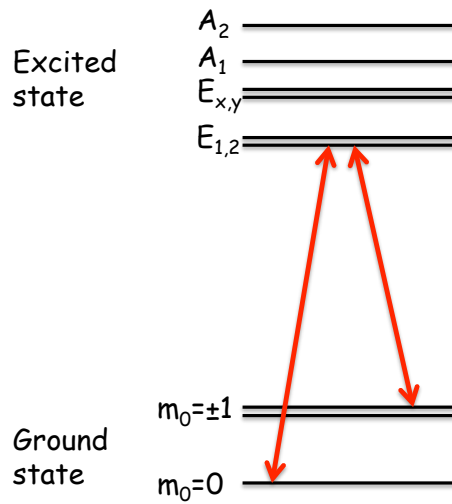


FIGURE 4.8: A schematic graph of lambda transition.

The four absent optical transition lines can be obtained by applying two laser lines via lambda transitions, as shown in Figure 4.8, when the separation between two excitation lines matches with the zero-field splitting of ground state. An electro-optic amplitude modulator (Jenoptik AM635) was used to modulate the resonance excitation, resulting in the generation of two extra satellite laser lines, one higher and one lower in frequency. The separation between the satellite lines and main laser line can be tuned by the frequency of input microwave.

Figure 4.9a and b show the PLE spectra with EOM modulation and without EOM modulation respectively. The electron can be promoted to $E_{x,y}$ states by single laser line, so both of them have three PLE lines in the PLE spectrum, excited by the main laser line and two satellite lines. The $E_{x,y}$ signals excited by satellite lines are labeled as $E_{x,y}$ side in this thesis. On the other hand, obtaining the optical transition line of the $A_{1,2}$ and $E_{1,2}$ states needs the main laser line and one satellite line at the same time, so these four states only have 2 PLE signals. For the case of two PLE signals, the lower energy PLE signal is activated by the combination of the main laser line and the satellite line with higher energy, while the higher energy one is activated by the combination of the main laser line and the satellite line with lower energy.

The polarizations of the NV^- centre's optical transitions from various excited state spin sublevels are different which has been discussed in Chapter 3 and shown in Table 3.1. Thus, the polarization of the resonance excitation was changed to circular polarization by placing a quarter wave plate in the resonance excitation arm. To get absolutely circular polarization, a linear polarization was inserted before

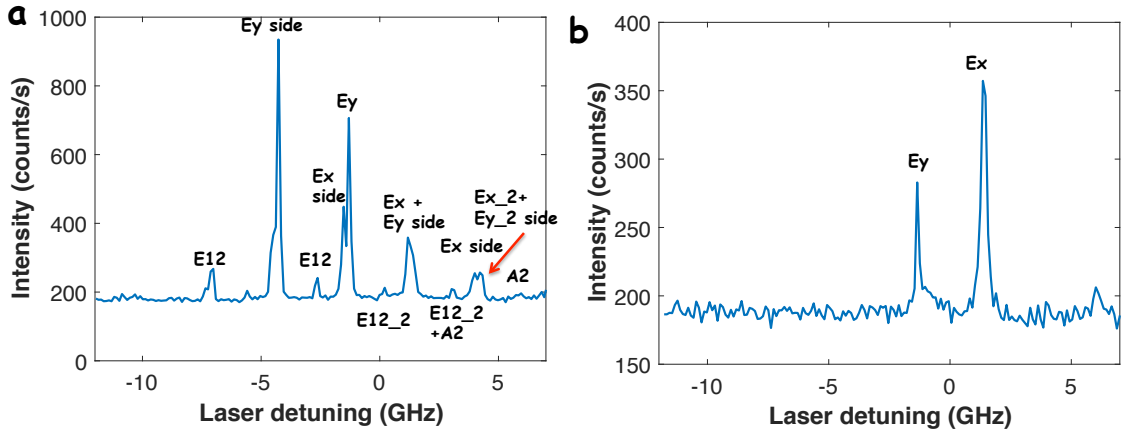


FIGURE 4.9: An example of the PLE spectrum **a**, with EOM modulation and **b**, without EOM modulation. The labels with ₂ indicate the PLE signals of the second NV^- centre in the same site.

the quarter wave plate to clear up the polarization of the resonance excitation. The scan range of the laser frequency were set around 11 GHz. If the scan range of the laser frequency are much greater than 11 GHz, the mode of the laser is hard to be stabilized after tuning the laser frequency. Thus, the full PLE spectra were recorded by three scan runs with different laser frequency ranges. These three scans had at least 2 GHz overlap with the adjacent frequency range scans and the full PLE spectrum was obtained by stitching the three scan runs together. The intensities of $A_{1,2}$ and $E_{1,2}$ PLE signals are weak, so each scan was obtained by accumulating at least 500 sweeps.

The intensity of satellite laser lines depends on the power of input microwave. In order to maximize the intensity of satellite laser lines, the laser lines were measured by Fabry-Perot interferometer and displayed on an oscilloscope with various microwave input powers. The highest intensity of satellite lines occurs with microwave input power of 20 dBm. The frequency of the input microwave has to match with the zero-field splitting of ground state. The intensity of the $E_{1,2}$

lines with microwave frequency of 2.87 GHz is greater than their intensity with a microwave frequency of 2.88 GHz, indicating that 2.87 GHz is closer to the value of the zero-field splitting of ground state. Thus, the frequency of input microwave was set to be 2.87 GHz for all NV⁻ centres.

4.7 Summary

The experimental methods and the apparatus involved in this work have been presented in this chapter. The laser writing apparatus has been fully described and the aberration correction method in the laser writing apparatus has been presented. The size of the laser damage significantly influences the position accuracy of this method, so all aspects minimizing the size of the laser damages have been discussed. Detailed information of the diamond samples used in this works has been presented. Maintaining the quality of diamond surface during the annealing is critical for optical investigations, so the methods used to protect the diamond from oxidization and graphitization have been described.

The experimental set-up of the custom-built confocal microscope which was used to investigate the optical properties of the laser-generated damage and NV⁻ centres has been presented. An overview of the experimental methods of HBT and lifetime measurements is provided. The reconfigurations of the confocal microscope to perform cw ODMR has be introduced. The method of Hahn echo measurements is described. Finally, the configuration of equipments to conduct PLE measurements including PLE strain measurements at 4.2 K has been presented.

Chapter 5

Laser Fabrication and Nitrogen-Vacancy Generation

5.1 Introduction

Chapter 2 has discussed various methods to generate NV centres in bulk diamond and every method has its own advantages and disadvantages. Although a few groups recently have used the femtosecond pulsed laser to generate NV centre ensembles around laser-induced graphitization, they have not yet successfully generated single NV centres without residual defects near-by, as aforementioned in [Section 2.4](#).

The aim of this work is to develop and prove that the femtosecond laser writing method has the 3D fabrication capability of generating single NV centres without residual defects. This chapter presents a procedure to create vacancies and

NV centres by the laser writing method, including various trials of annealing conditions. There are some theoretical frameworks which have been developed to explain the mechanism of the optical breakdown of ultrafast laser pulse in transparent materials, as mentioned in Section 3.1. This chapter will discuss which theory is best to describe the mechanism of the laser writing in diamond based on the experimental results. This chapter also shows the optical investigation results to demonstrate that this method can successfully generate single NV centres with very low level of residual defects.

The basic idea of the laser writing of NV centres is to use a femtosecond pulsed laser to generate a few vacancies in the diamond. The laser writing apparatus was described in Section 4.1.1. During high temperature annealing the vacancies become mobile and they can be captured by the native nitrogen atoms to form NV centres. Note that there is no artificially introduced nitrogen atoms in diamond such as ion-implantation and the the generation of the NV centres completely relies on the native nitrogen atoms. The probability of NV^- centre generation depends on the number of vacancies, but vacancies and multi-vacancy defects degrade the properties of NV^- centres. The best scenario is that only one of the laser-induced vacancies form the NV^- centre and the other vacancies are completely annealed out. Thus, controlling the number of vacancies generated by laser writing and the annealing conditions are very critical for creating single NV centres with optimal properties. A simple model established in Section 3.6 will be used to calculate the probability of generating the NV^- centres per site.

All the laser writing works in this work were performed by Dr. Patrick Salter in

Professor Martin Booth's group in the Department of Engineering in University of Oxford. All the anneals were carried out by Angelo C. Frangeskou and Colin J. Stephen under supervision of Professor Gavin Morley in the Department of Physics in University of Warwick. All the optical characterizations of the samples before and after annealing were conducted by myself.

5.2 Laser fabrication

5.2.1 Damage array and pulsed laser energy

Two commercial electronic grade CVD diamonds (labeled as sample A and sample B) were used to demonstrate the laser writing of the NV⁻ centres and the detail information of them are provided in Section 4.2. The laser damage was created by single femtosecond laser pulses of wavelength 790 nm and duration 300 fs, in order to gain better control of the pulsed laser energies and number of vacancies than the nanosecond pulsed laser, discussed in Section 4.1.2. The laser writing apparatus was described in Section 4.1.1. The laser beam was focused at a depth of 50 μm to demonstrate the capability of a deeper fabrication than other existing fabrication methods, such as ion implantation. In order to determine the best pulsed laser energy to generate single NV centres, the pulsed laser energy was varied from 16.0 nJ to 61.8 nJ in 24 increments with an even separation. The exact number of the laser pulse energies were listed in Table 5.1. Every laser pulse energy has 20 repeats to build up the statistics of NV generation, forming a 25 \times 20 square array with a separation of 5 μm , as shown in Figure 5.1.

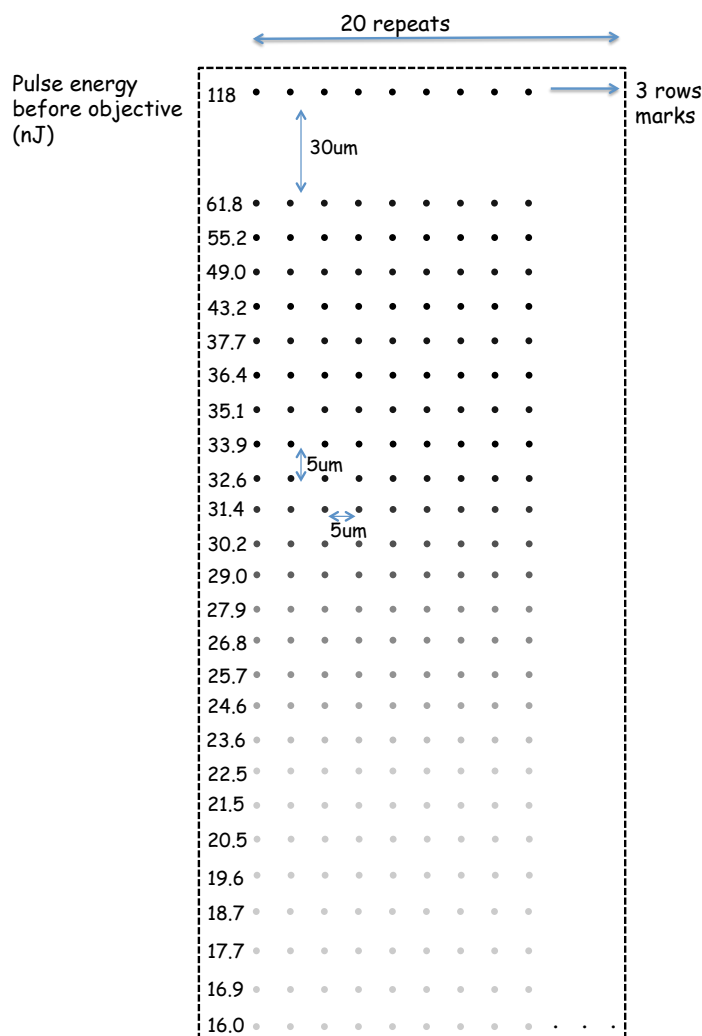


FIGURE 5.1: *Schematic picture of the damage array.*

The laser pulse energy was accurately controlled by rotating half waveplate before a Glan-Taylor polariser. Table 5.1 shows the 25 different waveplate settings (first column) and the corresponding laser pulse energies measured before objective lens (second column). The third column in Table 5.1, pulse energy after objective, is obtained by reducing the pulse energies by a factor of 0.7 due to the transmission loss of the objective lens, based on the manufacturers specifications. Note that the term "pulse energy" in this thesis refers to the laser pulse energy measured before objective lens. Three rows above the laser fabrication array was generated at sufficient pulse energy (118 nJ) to induce graphitization and these features are easily

Angle of $\lambda/2$ waveplate (degree)	Pulse energy before objective (nJ)	Pulse energy after objective (nJ)
5	118.0	82.6
30μm gap		
3.6	61.8	43.2
3.4	55.2	38.6
3.2	49.0	34.3
3	43.2	30.2
2.8	37.7	26.4
2.75	36.4	25.5
2.7	35.1	24.6
2.65	33.9	23.7
2.6	32.6	22.8
2.55	31.4	22.0
2.5	30.2	21.1
2.45	29.0	20.3
2.4	27.9	19.5
2.35	26.8	18.7
2.3	25.7	18.0
2.25	24.6	17.2
2.2	23.6	16.5
2.15	22.5	15.8
2.1	21.5	15.1
2.05	20.5	14.4
2	19.6	13.7
1.95	18.7	13.1
1.9	17.7	12.4
1.85	16.9	11.8
1.8	16.0	11.2

TABLE 5.1: *Laser pulse energies used for the generation of vacancies. The energies measured before the objective lens are the values quoted in this work. The first row is the parameters of the graphitization features and there is a 30 μ m gap between the graphitization features and the actual array.*

observed under the wide field imaging of the custom-built confocal microscope. The waveplate setting and the laser pulse energies of graphitization features were shown in the first row of Table 5.1 and there is 30 μ m gap between the graphitization features and the laser writing array. These graphitization features were used to locate the array since the rest of the array was almost invisible with LED illumination under confocal microscope because the laser pulse only generate a little

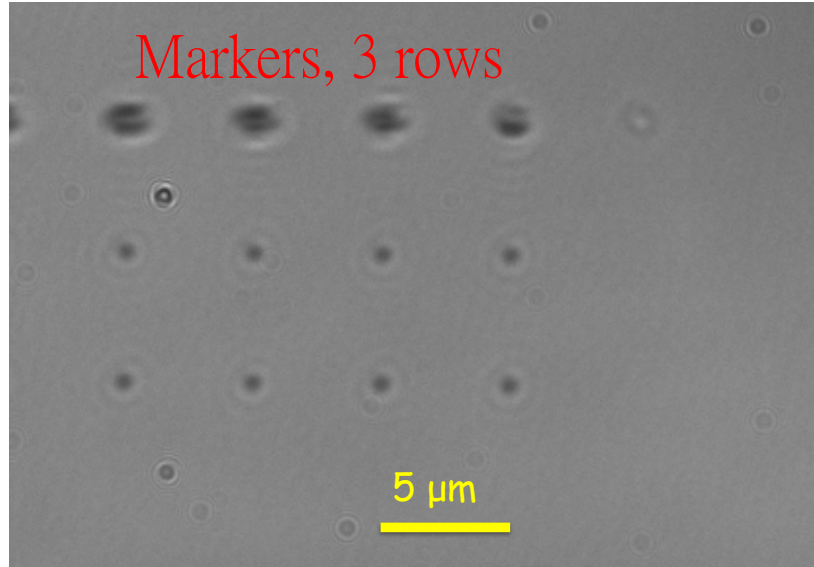


FIGURE 5.2: *Transmission microscope image of three graphitization marker rows.*

defects in the diamond. Figure 5.2 shows the transmission microscope image of the graphitization mark rows. The first row was generated by higher laser energies than 118 nJ for pulse laser energy calibration.

Although I have presented the values of the laser pulse energies of the damage array, these pulse energies can not guarantee to generate similar damage level in next iteration because of three uncertainties. Each diamond sample has different energy threshold to generate modifications and even in the same sample different area also need different pulse energy to generate damage. This sample or area dependence may be due to the concentration of impurity and defects, and they lower the pulse energy threshold because they can provide initial seed electron for avalanche process[8]. Secondly, the alignment of the laser writing apparatus can vary the values of pulse energy a lot. In addition, the strain in the diamond causes birefringence and it may defocus the laser beam in z axis, leading to decreasing the intensity of the laser pulse at focus.

5.3 Characterization of laser written array pre-annealing

The laser fabricated array was invisible under the standard transmission microscope and a custom-built scanning confocal microscope was used to investigate the PL of the laser fabricated array. The layout of the custom-built confocal microscope was described in Section 4.3.

5.3.1 Photoluminescence Image

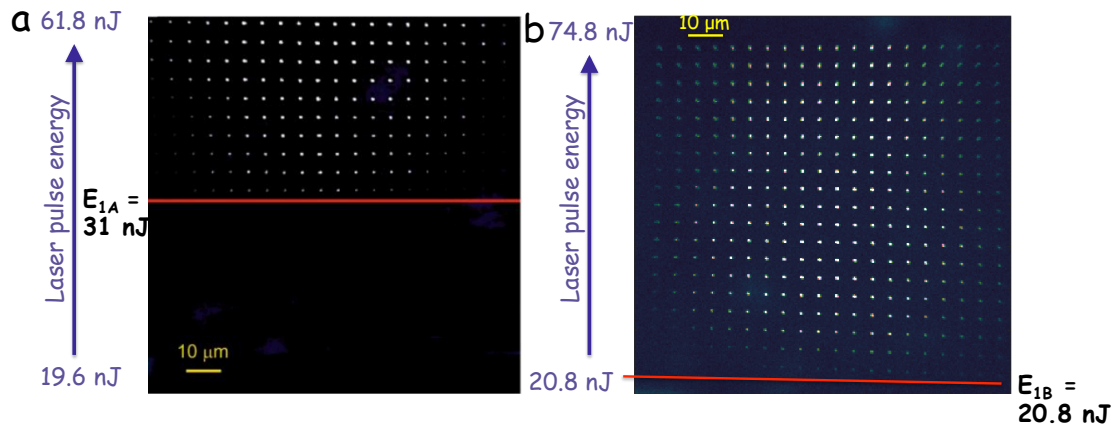


FIGURE 5.3: Photoluminescence image of the laser-fabricated array immediately after laser processing (before annealing) of **a**, sample A and **b**, sample B. The laser pulse energy increase from the bottom to the top of both images and there are 20 repeats for each energy distribute along the other axis. The red solid lines indicate the lowest laser pulse energy to generate visible fluorescence.

The confocal microscope described in Section 4.3 was used to investigate the PL of the damage array with 532 nm laser excitation. Figure 5.3 shows the PL images of sample A and sample B, immediately taken after laser fabrication and before annealing. The laser pulse energy increases from the bottom to the top of the

images. The laser pulse energies are slightly different in the two samples, but they generally cover similar energy range. The repeats of every energy are distributed in horizontal direction. The damage features become dimmer toward the edge of the array due to the aberrations away from the optical axis of the confocal microscope. Only the first 10 rows, generated by laser pulse energies from 61.8 to 31 nJ, were visible under confocal in sample A, but there were 19 rows in sample B (74.8 to 20.8 nJ) which were observed under confocal microscope. The lowest laser pulse energies which can produce visible fluorescence were labelled by a red solid line and called E_{1A} and E_{1B} in both images. The E_{1A} is 31 nJ and the E_{1B} is 20.8 nJ. The difference in visibility threshold may be because the two sample have slightly different defect or impurity concentrations.

5.3.2 Spectroscopy

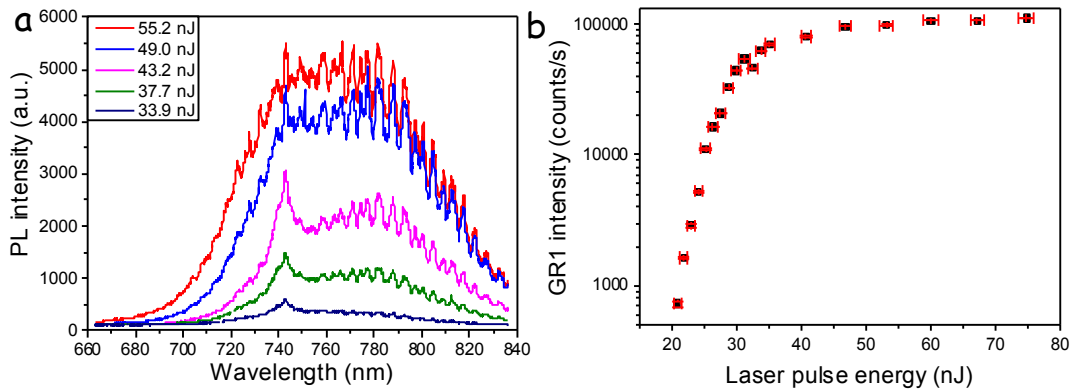


FIGURE 5.4: **a**, Fluorescence spectra from laser-induced features (pre-annealing) of sample A at different laser pulse energies. **b**, Power saturation measurement of the PL intensity of the GR1 centre.

The fluorescence of some laser-induced features can be clearly observed by the confocal microscope and the fluorescence spectra were recorded from multiple sites

in sample A prior to annealing. Figure 5.4a shows the recorded spectra of laser-damaged features as a function of the laser writing pulse energy from sample A. The spectra consist of a sharp peak at 740 nm and broad sideband, indicating that the laser-induced features are the neutrally charged vacancy centres, also called GR1 centres[45]. The intensity of the broad sideband increases faster than the sharp peak with laser energy and the extra increase of the broad sideband region may be attributed to the emission of B-band[37]. The B-band is usually attributed to the dislocations or sp^2 carbon in diamond[37, 45]. The total PL intensity of the laser-induced features can be controlled by tuning the laser pulse energy. This is an crucial point as it implies that the number of the GR1 centres can be controlled by tuning the laser pulse energy. Figure 5.4b shows the scatter plot of PL intensity of laser-induced features as a function of laser pulse energy and the PL intensity shows a saturate behaviour after 30 nJ, indicating that the number of the GR1 centres generated per unit energy decrease as it saturates. The PL intensity values in Figure 5.4b were obtained by fitting the PL images of the features with 2D gaussian function to extract the peak height. The error bars of the GR1 intensity were obtained from the 2D gaussian fitting. The error bars of the pulse laser energies were estimated from the resolution of the rotation mount of the half waveplate in the laser writing apparatus (Section 4.1.1) which is specified by the manufacturer as 0.03 degree. The saturation behaviour should be relative to the vacancy generation mechanisms, so next section is going to discuss the vacancy generation mechanism.

5.4 Vacancy generation mechanism

5.4.1 Models

Three models have widely agreed to be the most possible mechanisms for vacancy generation by ultrashort laser pulses in transparent materials. These models are multi-photon ionization (MPI), tunneling ionization (also called Zener breakdown) and Avalanche ionization, which are described in Section 3.1. In this work, the laser pulse (300 fs) is shorter than the characteristic timescales of thermal diffusion (ns)[3], so the heat dissipation mechanism can be neglected in this scenario. Vacancy generation in saturation regime in Figure 5.4b will not be discussed as this is a regime whereby many residual defects were created per sites after annealing (see Section 5.6). Thus, the Avalanche ionization will not be discussed because it happens under high laser pulse energy illumination[93, 96]. As mentioned in Section 3.1, the phase transition between MPI and tunneling ionization is typically described by the Keldysh parameter, Equation 3.1[94]. MPI is dominant over tunneling ionization when $\gamma > 1$ corresponding to

$$I < \frac{mcn\epsilon_0 E_g \omega^2}{e^2}. \quad (5.1)$$

In diamond, m is $0.4 m_e$, n is 2.4, the direct band gap is 7.1 eV, and the laser frequency is $2.4 \times 10^{15} \text{ s}^{-1}$. Here assuming a pulse duration of 300 fs, a beam waist of 350 nm, and allowing Fresnel reflection at the oil/diamond interface and

losses in the objective, Equation 5.1 predicts the MPI will dominate the tunneling ionization for pulse energies below about 25 nJ.

5.4.2 Experimental results and fits

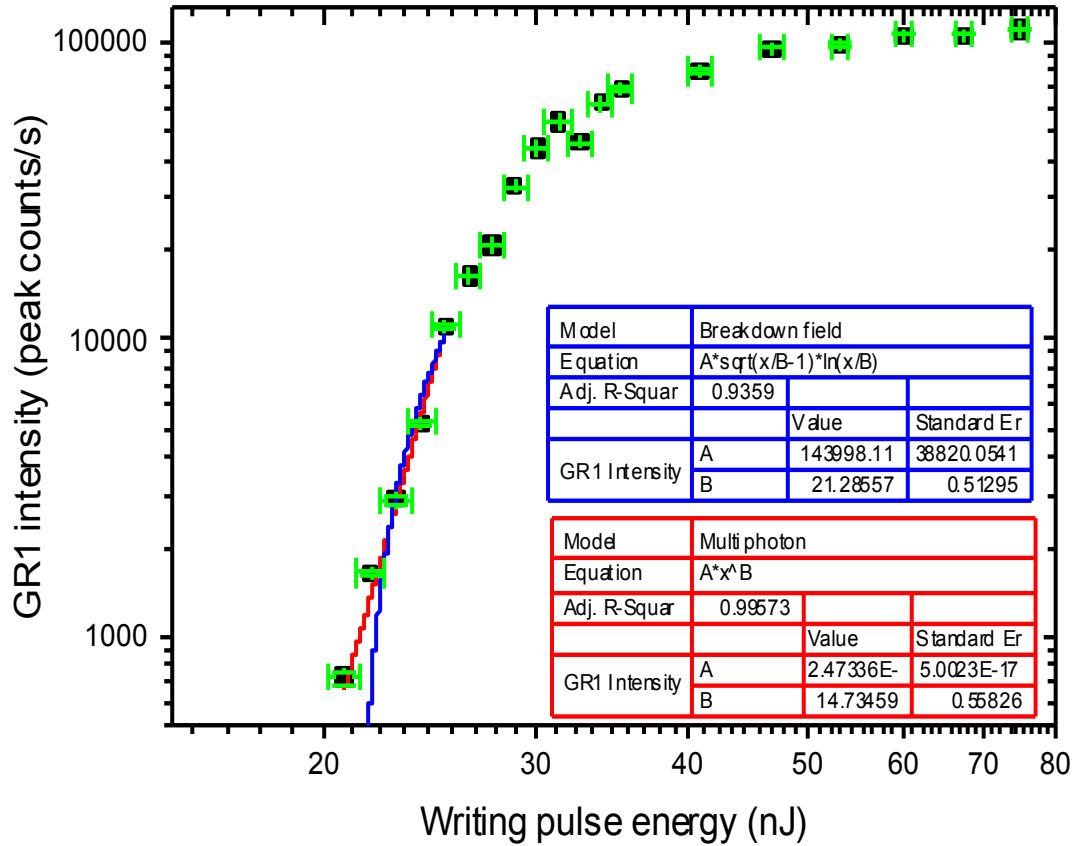


FIGURE 5.5: *Logarithmic plot of measured GR1 photoluminescence intensity as a function of laser pulse energy (black squares). The red line is the least-square fit of a power-law relationship corresponding to multi-photon ionization, and provides a much better fit to the five data points below 25 nJ than does the blue line, the best fit to a simple Zener breakdown field model.*

To confirm that MPI is the dominant mechanism in the laser writing process, the dependence of the GR1 fluorescence intensity on the laser pulse energy has been measured. I assume that the measured fluorescence intensity at laser-induced features before annealing is proportional to the number of GR1 centres present, meaning that the fluorescence of GR1 centres are not influenced each other. This

assumption is most likely to hold at the lowest laser pulse energy region because fewest defects are generated and they should be well separated within the damage region. The black squares in Figure 5.5 show the GR1 fluorescence intensity as a function of laser pulse energy in a logarithmic plot. The GR1 fluorescence intensity starts to saturate after 25 nJ. It agrees extremely well with the estimation of the laser pulse energy from the Keldysh parameter and the Keldysh parameter predicts that the MPI is no longer dominant effect if the laser pulse energy is greater than 25 nJ. Also, it is highly likely that some of the defects are in vacancy complexes (divacancy, dislocation, etc.) forms above 25 nJ, because the density of defects is very high.

The saturation behaviour in Figure 5.5 may be due to phase transition the dominant mechanism from the MPI to tunneling ionization combined with Avalanche ionization. In addition, the density of GR1 centres approaches to the graphitization threshold when the laser energy above 37.7 nJ (see Section 5.6). Near and above this threshold, the laser pulses generate not only the GR1 centres but also multi-vacancy complexes and sp^2 structure which may be dimmer or not fluorescent[37]. When the laser energy is greater than 25 nJ, the mechanism of defect generation is too complicate to analysis. Thus, curve of the GR1 intensity above 25 nJ was not fitted.

In the multi-photon ionization model the number of GR1 defects generated depends on the y^{th} power of the laser pulse energy[8, 93, 96]:

$$I_{GR1}(E) = AE^y \quad (5.2)$$

$$\Rightarrow \log(I_{GR1}) = y \cdot \log(E) + const, \quad (5.3)$$

where I_{GR1} and E are the fluorescence intensity of measured site and laser pulse energy respectively and A is a pre-factor of the power law. On the other hand, for the Zener breakdown model the number of GR1 defects created by laser pulsed can be expressed as Equation 3.5 and the intensity of GR1 defects can be described as:

$$I_{GR1}(E) = I_0 \ln\left(\frac{E}{E_{th}}\right) \sqrt{\frac{E}{E_{th}} - 1}. \quad (5.4)$$

where I_0 is a constant and E_{th} is the threshold laser pulse energy to generate vacancy. The least-square fits of the two model are shown in Figure 5.5. The MPI model (red solid line) fits the five lowest laser pulse energies data points very well (R-square = 0.996), while the the quality of fit for the Zener breakdown model (blue solid line) is relatively poor (R-square = 0.936). The experimental results suggest that the MPI model is the dominant mechanism if the laser pulse energy lower than 25 nJ. The MPI model fit indicates that the number of photon involved in the GR1 generation process is $y = 14.7 \pm 0.6$. Each photon in the $\lambda = 790$ nm laser pulse possesses an energy of 1.57 eV, implying that energy is transferred to diamond lattice in packets of 23.1 ± 0.9 eV. This value is near to the lowest theoretical values for the displacement threshold energy of carbon atom with 28 eV[128], but much lower than other recent studies which fall in the region

of 35-40 eV[97, 98]. As explained in Section 3.1.2, the degree of nonlinearity is not necessary to match with the displacement threshold energy.

5.5 Characterization of post-annealing array

The PL spectra of the laser-induced features have shown that the laser fabrication can generate vacancies, so after annealing some of features may well result in NV formation. In Section 2.2.1, the annealing conditions to generate NV centre for the ion implantation method has been briefly discussed. Annealing at higher temperature and longer duration should generate more NV centres per laser damage site, because the vacancies can diffuse farther and have higher probability to find a nitrogen atom. The annealing equipment and methodology are described in Section 4.2.

I have tried six different annealing conditions which are presented as follow

Step1 Anneal at 800°C for an hour (Section 5.5.1).

Step2 Anneal at 900°C for an hour (Section 5.5.2).

Step3 Anneal at 900°C for 3 hours (Section 5.5.2).

Step4 Anneal at 1000°C for 3 hours (Section 5.5.3).

Step5 Anneal at 1200°C for 24 hours (Section 5.5.4).

Step6 Anneal with a three-step process following Chu et al's work[7]. Table 5.2 shows the recipe of the three-step annealing (Section 5.5.4).

Temperature	400°C	800°C	1200°C
Duration	4 hours	2 hours	2 hours
3°C/minute ramping rate between steps			

TABLE 5.2: *The temperature and duration of the three-step annealing recipe following Chu et al's works[7]. Adapted from [7].*

The two samples, which were used in this thesis, experienced different annealing history. Sample B was used to test various annealing conditions and find out the best condition to generate single NV⁻ centres. Sample A was mainly used to reproduce the best results of sample B to demonstrate the reproducibility of laser writing method. The results will be discussed in the following sections. Before some annealing steps, fresh arrays were made to compare with the existing arrays, enabling to gain more understanding about the annealing conditions. Thus, there are four arrays in sample B and two arrays in sample A, and they experienced different annealing history. Table 5.3 shows the summary of the annealing history of each array in sample A and sample B.

Annealing condition	Step1	Step2	Step3	Step4	Step5	Step6	1000°C (3 hours)
Array 5 Sample A						✓	✓
Array 6 Sample A							✓
Array 1 Sample B	✓	✓	✓	✓	✓		✓
Array 2 Sample B				✓	✓		✓
Array 3 Sample B					✓		✓
Array 4 Sample B							✓

TABLE 5.3: *The summary of the annealing history of the arrays in sample A and B.*

5.5.1 Annealing at 800°C

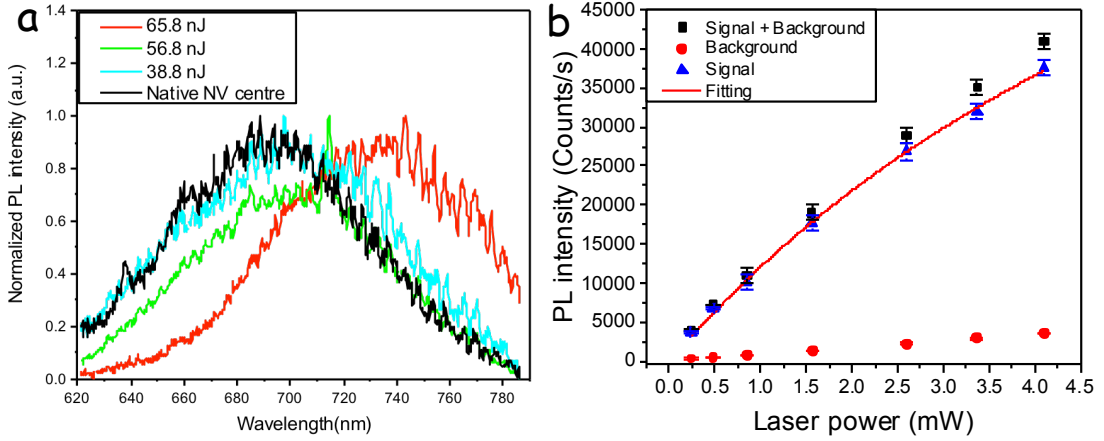


FIGURE 5.6: **a**, Room temperature fluorescence spectra of the Array 1 in sample B after annealing at 800°C. **b**, The scatter plots of the PL intensity of laser-induced damage in Array 1, generated with laser pulse energy of 38.8 nJ as a function of excitation power. The scatter graphs show the photon count rates measured when aligned to the damage feature (squares), off the feature (circles) and the difference between the two (triangles) which present only PL from the feature. The red solid line is the least-squares fit of the saturation Equation 3.15 to the PL intensity.

First, the Array 1 in sample B (Table 5.3) was annealed at 800°C for an hour in pure nitrogen gas. After annealing, only the features which were generated by the laser pulse energies from 74.8 to 38.8 nJ, can be observed. Room temperature spectra are shown in Figure 5.6a. The features which were created by the laser pulse energy lower than 38.8 nJ were completely annealed out. The spectra of the feature generated by laser pulse energy of around 74.8 nJ still shows a mixture of GR1 and B-band features. However, the spectra of features generated by lower laser pulse energies (green and blue curves) shifted towards 690 nm suggestive of NV⁻ emission (black curve), but the spectra still did not show the ZPL of the NV⁻ centres as shown in Figure 5.6a. The PL intensities of GR1 centre and B-band emission are linearly proportional to excitation power. On the other hand, the excitation power dependence measurement of a typical NV⁻ PL intensity shows a

saturation behaviour, which can be described by Equation 3.15 in Section 3.3.2, and the saturation power is around 1 mW[35]. The power dependence measurements can be used to identify if the NV⁻ centres were generated after annealing.

The excitation power dependence measurement was performed on the feature, generated by 38.8 nJ, as shown in Figure 5.6b. Figure 5.6b shows the scatter graphs for the combined PL and background intensity (black squares) when aligned optimally to the laser-induced feature, the background intensity (red circles) aligned away from the feature, and the difference between the two signals, PL only (blue triangles). The result shows a weak saturation behaviour and the red solid line is the least-squares fit of Equation 3.15. P_{sat} is 8.3 ± 0.85 mW which is much higher than the saturation power of the native NV⁻ centre in the sample (1 mW). Moreover, the HBT histogram, not shown here, did not show a dip at $\delta t = 0$. These results may suggest the generation of the NV⁻ centres with poor quality due to a lot of residual defects and the optical properties of these NV⁻ centres should be improved after higher temperature annealing. Therefore, most of the features generated by laser pulse energy of 38.8 nJ should show a saturation behaviour in power dependence measurement and a dip at $\delta t = 0$ in HBT histogram after higher temperature annealing. However, only two features out of 20 repeats generated by laser pulse energy of 38.8 nJ showed the improvements of their optical properties after 900°C annealing (see Section 5.5.2). Moreover, the three-step annealing recipe including a 800°C step and a 1200°C step (see Table 5.2) can not generate the NV⁻ centres, discussed in Section 5.5.4. It is difficult to determine if the NV⁻ centres were generated after annealing only based on the spectra without

observing ZPL, because the shift of spectra to 690 nm may be due to the formation of multi-vacancy complexes or other defects[37]. Thus, the features may not be transformed into the NV centres after annealing at 800°C and this annealing condition may not be able to generate NV centre. The reason why this annealing condition can not generate the NV centres may be due to the low annealing temperature, resulting in short diffusion length. By using Equation 3.9, the diffusion length of vacancies at this annealing conditions is calculated to be approximately 23 nm. The reason that no NV centre was generated after an hour annealing at 800°C may be because the probability of the vacancies to meet native nitrogen atoms is too low with this diffusion length. Therefore, the same sample was annealed again, this time at 900°C, to increase the diffusion length and subsequently the probability of generation NV centres. Note that an hour annealing at 800°C works for ion implantation because the vacancies are generated very near to the implanted nitrogen atoms.

5.5.2 Annealing at 900°C

After annealing Array 1 of sample B at 900°C, the first clear evidence of the NV centres was observed and three features have been found in NV formation. This section presents detailed optical characterizations of these three NV centres.

The sample B was annealed at 900°C in pure nitrogen gas for an hour again without any further laser fabrication (Table 5.3). Three laser-induced features in Array 1 have been successfully transformed into the NV centres and they are labelled as 4P1R, 5P7R and 5P10R. 4P1R was created at the laser pulse energy of

Label	4P1R	5P7R	5P10R
Laser pulse energy (nJ)	47.8	38.8	38.8

TABLE 5.4: *Summary of the laser pulse energy of the three laser-induced NV⁻ centres in Array 1 sample B.*

47.8 nJ and 5P7R and 5P10R were generated at the laser pulse energy of 38.8 nJ, as shown in Table 5.4.

The spectra, power dependence and HBT measurements of 4P1R, 5P7R and 5P10R are shown in Figure 5.7a, b and c respectively. The black curve in Figure 5.7a shows the spectrum of 4P1R. The spectrum of 4P1R shows relatively high PL intensity between 620 nm and 660 nm than typical single NV⁻ centre's spectrum, indicating a mixture of the NV⁻ and NV⁰ (see Figure 3.3a). The GR1 centres will compete with the NV⁻ centres for electrons, resulting in changing the NV⁻ to NV⁰. Therefore, the present of the NV⁰ emission implying that there are some residual GR1 centres. The power dependence measurements of the PL intensity presents a saturation behavior (Figure 5.7b) and the result is well fitted by the Equation 3.15. The saturation power of 4P1R is 4.7 ± 0.50 mW. The other repeat features, generated by the same laser pulse energy, show bright B-band emission, so the 4P1R must have residual defects. The residual defects emission is much weaker compared with the NV⁻ centre, so the B-band did not show in the spectrum. The fluorescence intensity of residual defects is linearly proportional to the excitation power. Thus, the power dependence results of the mixture of NV⁻ centres and residual defects should be described by Equation 3.15 plus a linear function and this linear component will increase the P_{sat} values. The P_{sat} of the 4R1R is higher than that of the native single NV⁻ centres due to the residual defects. The HBT

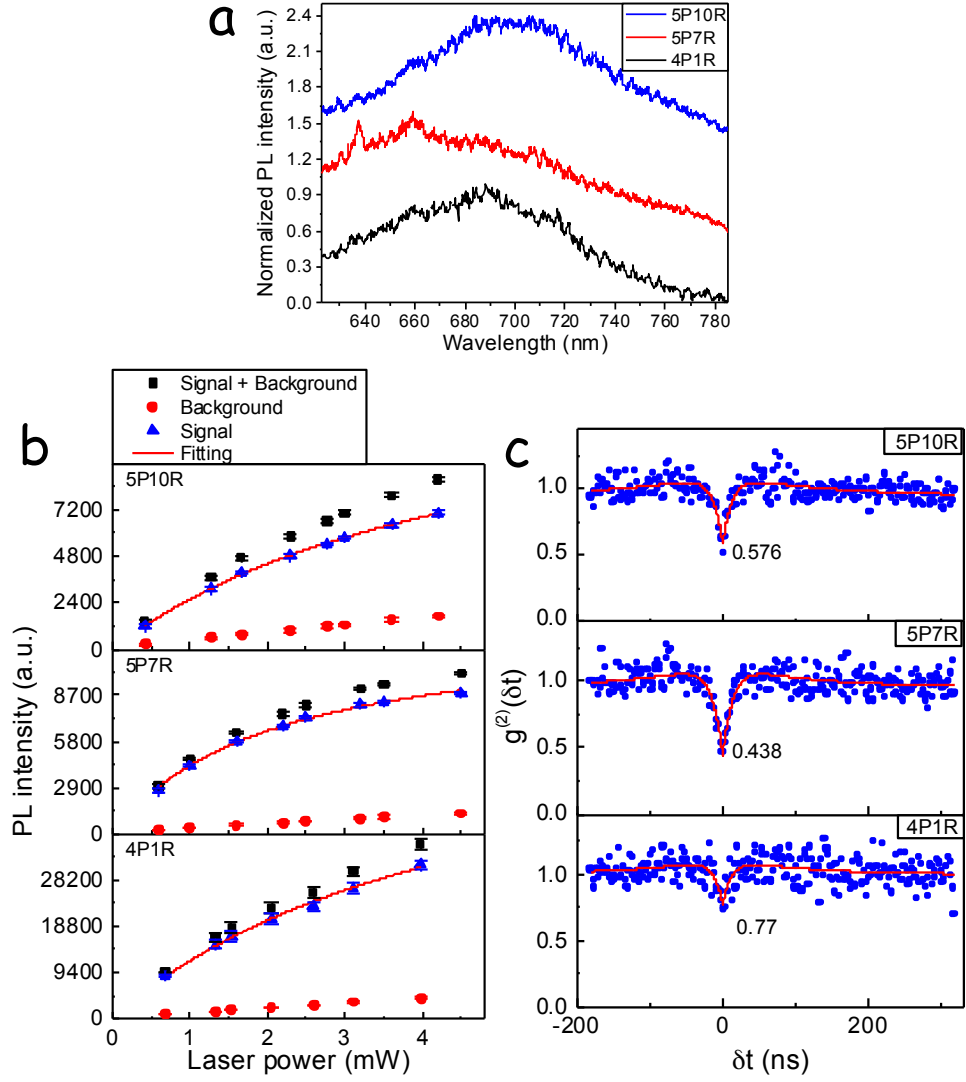


FIGURE 5.7: The optical characterization results of 4P1R, 5P7R and 5P10R in Array 1 sample B after an hour annealing at 900°C. **a**, Spectra. **b**, The scatter plots of power dependence measurements of the PL intensity. The red solid lines are the best fits to Equation 3.15. **c**, HBT measurements of the photon correlation function ($g^{(2)}(\delta t)$). The red lines are the best fits to Equation 3.12 and the depths of the anti-bunching dips are given.

measurement was performed to confirm the 4P1R is the NV centre instead of residual defects. The bottom panel in Figure 5.7c shows the HBT result of 4P1R and the red line in Figure 5.7c is the least-squares fits of Equation 3.12. The depth of the characteristic dip of 4P1R is measured to be 0.77 ± 0.03 , implying the generation of multiple single NV centres. The shallow characteristic dip of

4P1R (greater than 0.5) may be due to residual defects or multi NV centres, so it is difficult to identify whether the 4P1R is a double or triple NV centres.

The spectrum of 5P7R also shows a combination of NV^- and NV^0 (red line in Figure 5.7a); however, the ZPL of the NV^- centre is clearly observed, which confirms the generation of the NV^- centre. Similarly, the NV^0 emission suggests that GR1 centres were not completely annealed out. The P_{sat} of 5P7R is $2.0 \pm 0.15\text{mW}$, as shown in the middle panel in Figure 5.7b. This value is much near to the P_{sat} of native single NV^- compared with 4P1R, indicating the linear component from residual defects is smaller. The smaller P_{sat} value implies that there is less residual defects in 5P7R compared with the 4P1R. Thus, if there are fewer vacancies generated by laser pulse, there would be fewer residual defects after annealing. The middle panel in Figure 5.7c shows the HBT spectrum of 5P7R and the depth of the HBT characteristic dip is 0.438 ± 0.03 , implying the generation of the single NV centre. The characteristic dip above zero is due to the emission of residual defects. The power dependent and HBT results of 4P1R and 5P7R prove that the higher P_{sat} and shallower HBT dip are due to the residual defects which can be reduced by decreasing the laser pulse energy.

The spectrum of the 5P10R is similar to the spectrum of the NV^- centre, but the ZPL is absent (see the blue line in Figure 5.7a). The P_{sat} of 5P10R is $4.8 \pm 0.24\text{mW}$, indicating that there is a significant linear component, as shown in the top panel in Figure 5.7b. This significant linear component suggests that there are a lot of residual defects. The higher residual defect level may be the reason of the absence of the ZPL. The depth of the HBT characteristic dip of 5P10R is 0.576

± 0.03 , as shown in the top panel in Figure 5.7c. Although the characteristic dip is above 0.5, the 5P10R may be a single NV^- centre if considering the existing of residual defects.

One hour annealing at 900°C can successfully generate the single NV^- centres, but the laser-induced damages can not be completely annealed out. That may be due to the short annealing period, because some literature reports that the annealing duration needs to be longer than 2 hours[86, 129]. The sample B was annealed at 900°C for 3 hours without further treatment, as shown in Table 5.3. After the 3 hours annealing, there are still only three NV centres (4P1R, 5P7R and 5P10R) and no more NV^- centre was formed in the Array 1. This probably means that most of the GR1 centres were annealed out after the previous annealing stage (900°C for an hour).

Figure 5.8a, b and c show the spectra, power dependence and HBT results of 4P1R, 5P7R and 5P10R after 3 hours annealing at 900°C respectively. The spectrum of 4P1R shifts from mixture of NV^- and NV^0 to pure NV^- emission, as shown as black line in the Figure 5.8a. The depth of the HBT characteristic dip of 4P1R is measured to be 0.61 ± 0.03 which is slightly lower than after 1 hour annealing, as shown in the bottom panel in Figure 5.8c. These suggest that some residual defects and most of the residual GR1 centres were annealed out after longer annealing duration.

After 3 hours annealing the ZPL of the NV^- centres is still observed in the spectrum of 5P7R, but the PL intensity increase in the spectral range from 740 nm to 790 nm which is due to the B-band emission (red line in Figure 5.8a). In addition, the

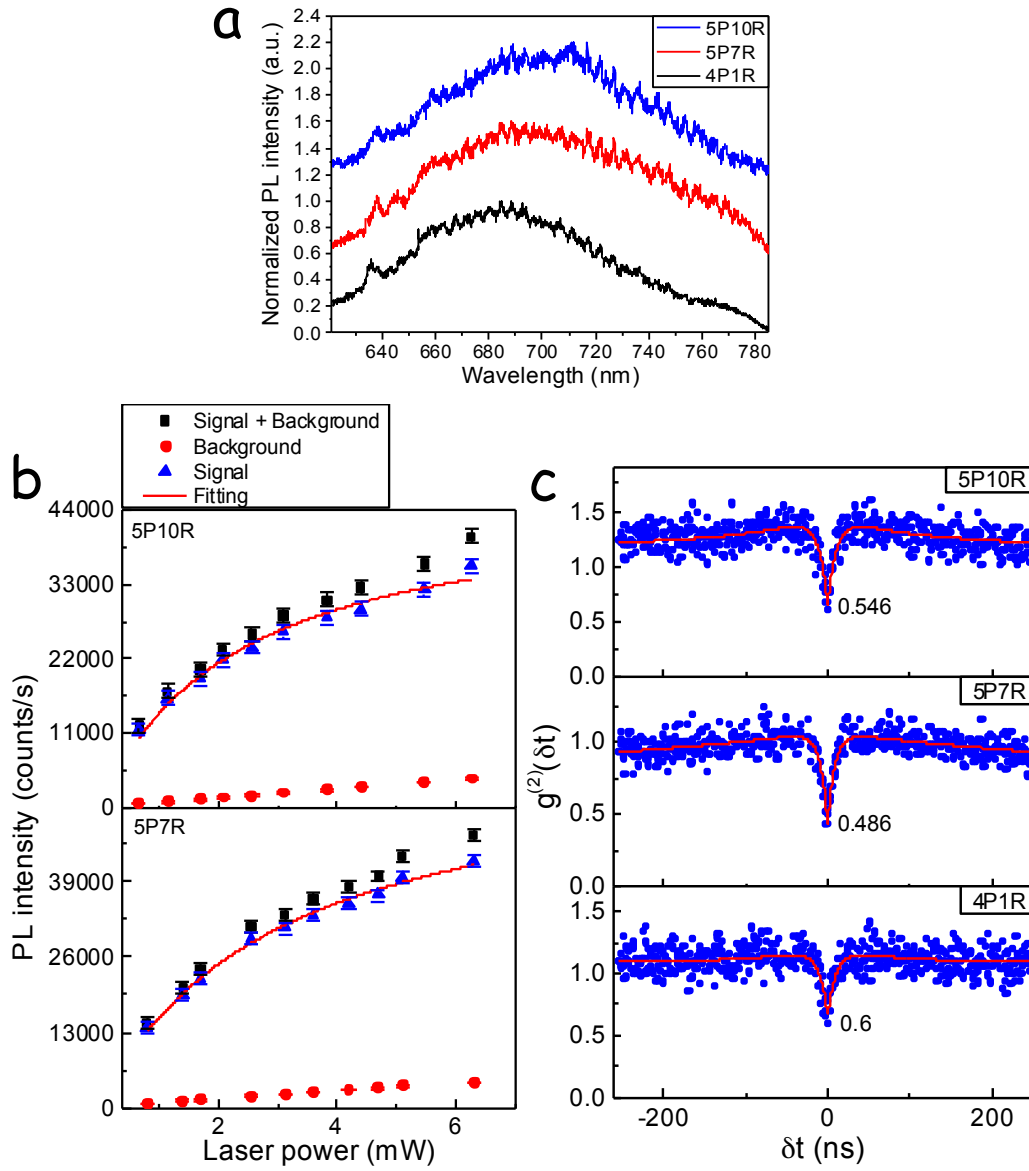


FIGURE 5.8: The optical characterization results of 4P1R, 5P7R and 5P10R in Array 1 sample B after three hours annealing at 900°C. **a**, Spectra of the features. **b**, The scatter plots of power dependence measurements of the PL intensity. The red solid lines are the best fits to Equation 3.15. **c**, HBT measurements of the photon correlation function ($g^{(2)}(\delta t)$). The red lines are the best fits to Equation 3.12 and the depths of the anti-bunching dips are given.

NV^0 emission disappears. The bottom panel of Figure 5.8b shows the power dependence measurements of 5P7R after 3 hours annealing at 900°C and the P_{sat} of 5P7R increases to $3.0 \pm 0.22\text{mW}$. The depth of the HBT characteristic dip of 5P7R is slightly lifted to 0.486 ± 0.05 , as shown in the middle panel of Figure

Label	4P1R	5P7R	5P10R
Laser pulse energy (nJ)	47.8	38.8	38.8
Spectra (an hour annealing)	NV ⁻ + NV ⁰	NV ⁻ with ZPL + NV ⁰	NV ⁻
Spectra (3 hours annealing)	NV ⁻ with ZPL	NV ⁻ with ZPL + B-Band	NV ⁻ with ZPL
P _{sat} (an hour annealing)	4.7 mW	2.0 mW	4.8 mW
P _{sat} (3 hours annealing)	- -	3.0 mW	2.3 mW
HBT dip (an hour annealing)	0.77	0.438	0.576
HBT dip (3 hours annealing)	0.61	0.486	0.546

TABLE 5.5: *Summary of the optical properties of 4P1R, 5P7R and 5P10R after an hour and 3 hours annealing at 900°C.*

5.8c. These results suggest the residual GR1 centres were transformed into sp² structure after 3 hours annealing.

After 3 hours annealing, the optical properties of 5P10R become slightly better, as shown in Figure 5.8. The ZPL of the NV⁻ centre can be seen in Figure 5.8a and no B-band emission is observed. The top panel of Figure 5.8b shows the power dependence results of 5P10R and the P_{sat} of 5P10R decreases to 2.3 ± 0.25 mW. The depth of the HBT characteristic dip becomes deeper down to 0.546 ± 0.04 , as shown in the top panel of Figure 5.8c.

Table 5.5 shows the summary of the optical properties of 4P1R, 5P7R and 5P10R after an hour and 3 hours annealing at 900°C. Although the 3 hours annealing at 900°C improves the optical properties of the 4P1R and 5P10R, it degrades the optical properties of the 5P7R towards the levels similar to the 4P1R and 5P10R. The increase of the B-band emission in the 5P7R suggests that the residual

defects are sp^2 carbon form or amorphous structure, because these forms are stable at higher temperature[130]. No more new NV centre generated after 3 hours annealing at 900°C , suggesting that most of the GR1 centres should be annealed out or transferred to sp^2 structure after an hour annealing at 800 and 900°C . However, there are still some residual GR1 centres after an hour annealing at 800 and 900°C , because the spectra of the 4P1R and 5P7R show a mixture of NV^0 and NV^- . The spectra of the 4P1R and 5P7R were shifted from the mixture of NV^- and NV^0 to pure NV^- emission after 3 hours annealing at 900°C , indicating that this anneal removed the residual GR1 centres. The 3 hours annealing at 900°C is served to remove the residual defects.

The diffusion length of vacancies after an hour annealing at 900°C is estimated to be 57.5 nm, according to Equation 3.9. The first sign of NV centres creation occurs after annealing at 800°C for an hour plus at 900°C for an hour, suggesting that the vacancies need to diffuse at least 80.5 nm ($23\text{ nm} + 57.5\text{ nm}$) to meet nitrogen atoms and form NV centres. Although annealing at 900°C can generate single NV^- centres, it can not completely anneal out the residual defects even for three hours annealing. The higher temperature annealing is necessary to remove the residual defects. Thus, a three hours annealing at 1000°C was performed to removed the residual defects.

5.5.3 Annealing at 1000°C

After annealing the sample B at 1000°C for three hours, no more NV^- centre was created in Array 1, which is consistent with the results of 3 hours annealing

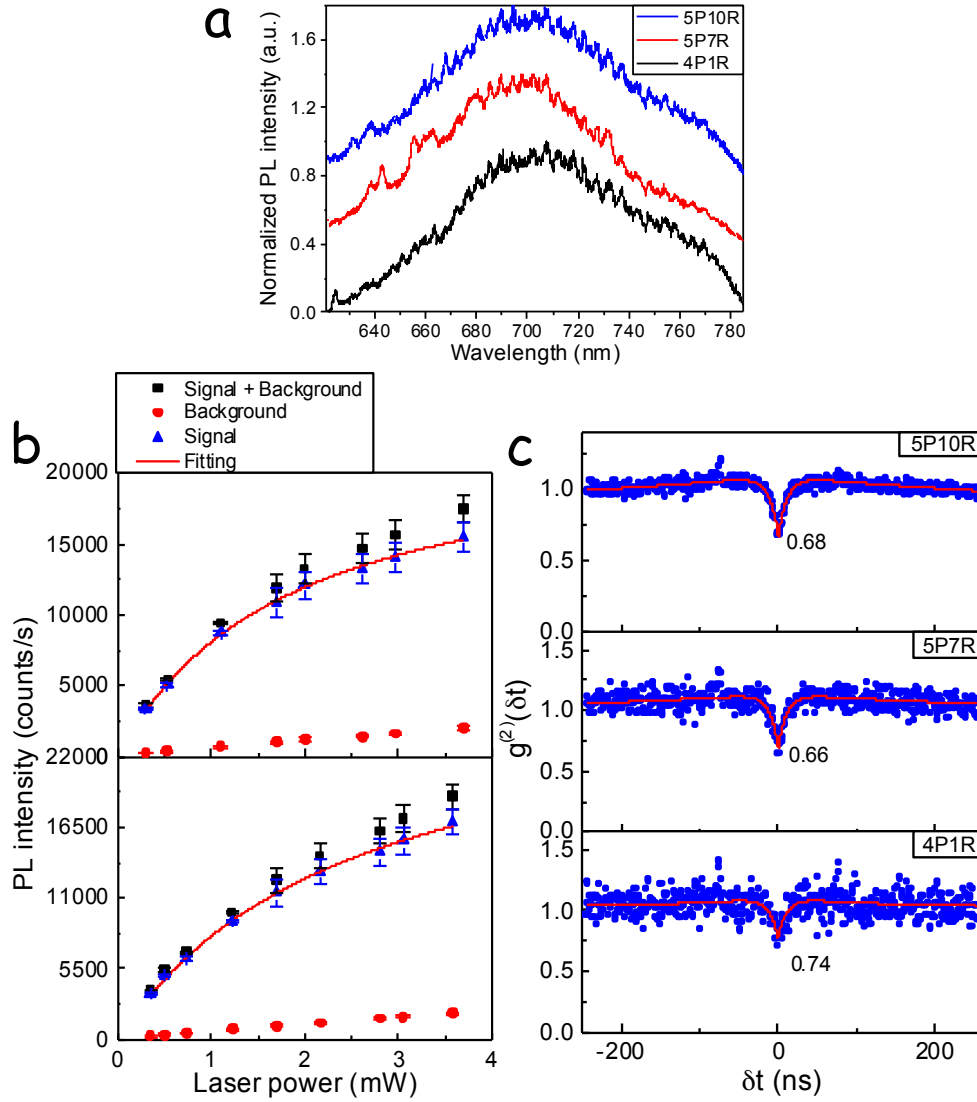


FIGURE 5.9: The optical characterization results of 4P1R, 5P7R and 5P10R in Array 1 sample B after three hours annealing at 1000°C. **a**, Spectra of the features. **b**, The scatter plots of power dependence measurements of the PL intensity. The red solid lines are the best fits to Equation 3.15. **c**, HBT measurements of the photon correlation function ($g^{(2)}(\delta t)$). The red lines are the best fits to Equation 3.12 and the depths of the anti-bunching dips are given.

at 900°C. Thus, the characterization and analyses are focused on the three NV⁻ centres, 4P1R, 5P7R and 5P10R. Figure 5.9a, b and c show the spectra, power dependence and HBT results of 4P1R, 5P7R and 5P10R after 3 hours at 1000°C respectively.

The spectrum of 4P1R shows a combination of NV^- centre and B-band, and the ZPL of the NV^- centre disappears, as shown in Figure 5.9a (black line). Similar to the previous analysis, the presence of the B-band emission after 1000°C indicates that the residual defects are in sp^2 structure, which is stable at high temperature. The depth of the HBT dip of 4P1R is measured to be 0.74 ± 0.06 , as shown in the bottom panel of Figure 5.9c. The shallower anti-bunching dip compared with that after 3 hours annealing at 900°C may be due to the residual defects or generation of new NV^- centres.

After 1000°C annealing, the optical properties of 5P7R have been further improved. The B-band emission in the spectrum of 5P7R is significantly reduced and the ZPL is still observed, as shown in Figure 5.9a (red line). The bottom panel of Figure 5.9b shows the power dependence result of 5P7R. The P_{sat} value decreases from 3.0 mW (3 hours at 900°C) to 2.5 mW (3 hours at 1000°C), suggesting that some residual defects have been removed. However, the P_{sat} is still higher than that of the native NV^- centres in the same material, indicating that there are some optically detectable residual defects. The depth of anti-bunching dip of 5P7R is measured to be about 0.66 ± 0.07 , as shown in the middle panel of Figure 5.9c.

Similar to 5P7R, the optical properties of 5P10R have been slightly improved. The intensity of B-band emission increases after 1000°C annealing and the ZPL of NV^- centres is observed, as shown in Figure 5.9a (blue line). The top panel of Figure 5.9b shows the power dependence result of 5P10R. The P_{sat} of 5P10R decreases from 2.3 mW (3 hours at 900°C) to 1.8 mW (3 hours at 1000°C), implying

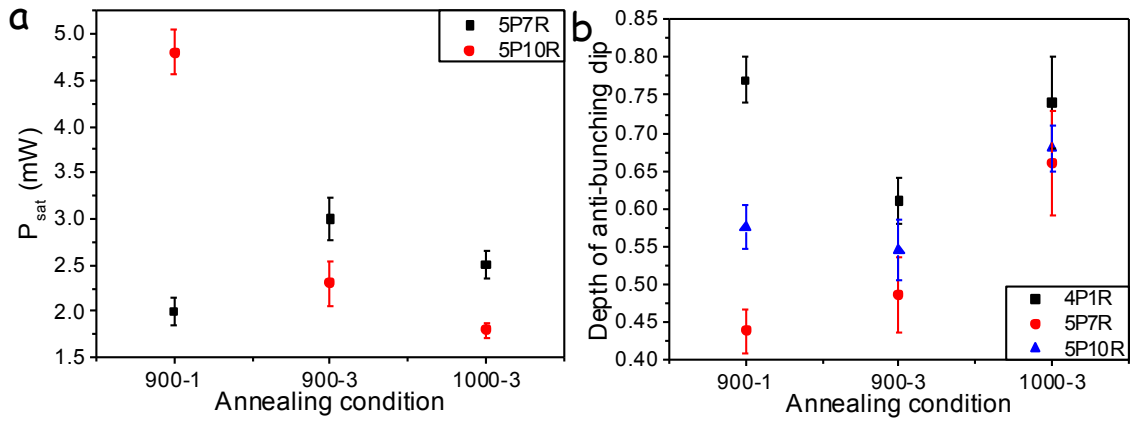


FIGURE 5.10: The summary of the optical properties of 4P1R, 5P7R and 5P10R as a function of annealing conditions. 900-1, 900-3 and 1000-3 indicate the annealing at 900°C for an hour, at 900°C for three hours and at 1000°C for three hours, respectively. **a**, A scatter plot of the P_{sat} values. **b**, A scatter plot of the depth of anti-bunching dips.

that some residual defects have been removed. The depth of anti-bunching dip of 5P10R is measured to be about 0.68 ± 0.03 , as shown in the top panel of Figure 5.9c.

The optical properties of the laser-generated NV^- centres can be measured based on the P_{sat} values and depths of anti-bunching dip. Figure 5.10a and b show the scatter plots of the P_{sat} values and depths of anti-bunching dip of 4P1R, 5P7R and 5P10R as a function of annealing conditions. The P_{sat} values of 5P10R decrease as function of annealing conditions, as shown in Figure 5.10a. Although the P_{sat} of 5P7R increases after annealing at 900°C for three hours, it decreases after annealing at 1000°C for three hours. The one hour annealing at 900°C may be too short to reach an equilibrium state of the species and number of residual defects, so the difference of the P_{sat} values between 5P7R and 5P10R is large. In addition, the presence of NV^0 emission in 5P7R spectrum and absence of the NV^0 emission in 5P10R spectrum also suggest that the species of residual defects are

different in them after an hour annealing at 900°C (see Figure 5.7a). After 3 hours annealing at 900°C, the P_{sat} values of both 5P7R and 5P10R shift towards 2.7 mW, suggesting that the species and number of residual defects reach an equilibrium state. The depths of anti-bunching dip also show this tendency between 1 hour and 3 hours annealing at 900°C, as shown in Figure 5.10b. The depths of anti-bunching dip show a wide distribution among three NV^- centres after an hour annealing at 900°C, but the depths move towards 0.55 after 3 hours annealing at 900°C. These suggest that the duration of annealing need to be about 3 hours to reach the equilibrium state of residual defects at 900°C.

After annealing 1000°C for three hours, the P_{sat} of both 5P7R and 5P10R decrease with similar among, indicating that this higher annealing can remove more residual defects. On the other hand, the depths of anti-bunching dips of these three NV^- centres increase to approximately 0.7. The increase of the depth of anti-bunching dip but decrease of P_{sat} suggest the generation of new NV^- centres in the laser damage site. Thus, the 5P7R and 5P10R should be double NV^- centres per site. But, it is difficult to determine that 4P1R is double or triple NV^- centres per site due to higher level of residual defects. In general, three hours annealing at 1000°C can generate the NV^- centres with less residual defects, resulting in better optical properties.

The results of 3 hours annealing at 900°C suggest that most of the GR1 centres were annealed out or transformed to sp^2 structure. Thus, a fresh array (Array 2) was created next to the Array 1 in sample B to investigate optical properties of the NV^- centres generated by only annealing at 1000°C for three hours, as shown

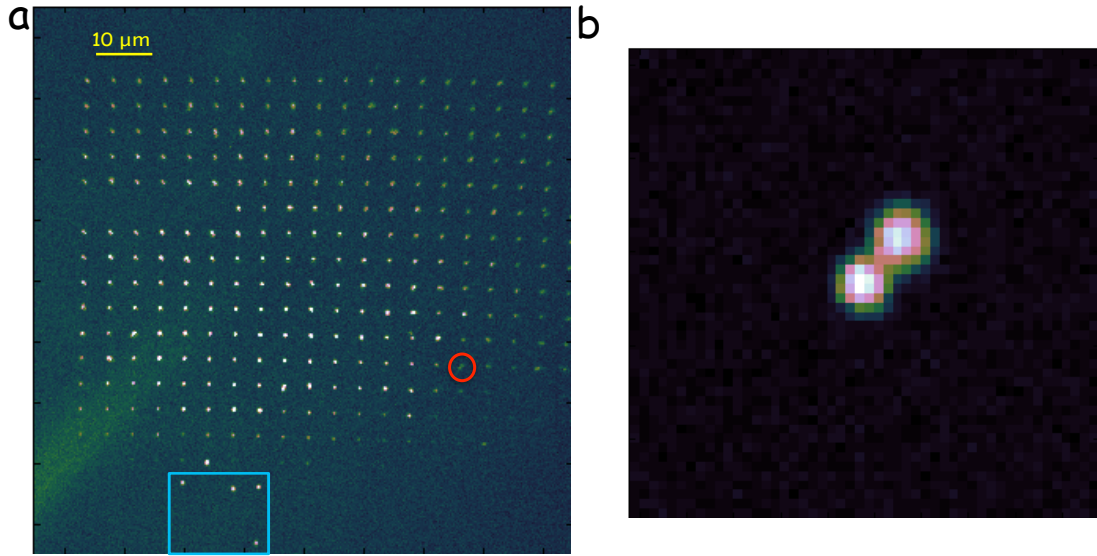


FIGURE 5.11: **a**, The PL image of Array 2 in sample B after annealing 1000°C for 3 hours. The blue square labels four laser-generated NV^- centres without optically detectable residual defects and the red circle labels 'NV pair'. **b**, The PL image of the 'NV pair', circled in **a**.

in Table 5.3. Figure 5.11 shows the PL image of the Array 2 in sample B after 3 hours annealing at 1000°C. Many NV^- centres were generated across the damage array. Many NV^- centres were generated on the damage sites, overlapping with the residual defects. Some NV^- centres were created away from the laser damage sites. In some damage sites the NV^- centres were generated both on and away from the damage sites, forming 'NV pair'. One of the 'NV pair' is labelled by a red circle in Figure 5.11a and a zoom-in image of it is shown in Figure 5.11b.

Similar to the results of array 1, the optical properties of the NV^- centres overlapping with the optically detectable residual defects is not as good as the native single NV^- centres. Figure 5.12 shows the power dependence and HBT measurements results of three selected NV^- centres (12P4R, 14P7R and 15P4R) generated by different laser pulse energies. Table 5.6 shows the laser pulse energies used to generate these three NV^- centres. The P_{sat} and depth of the anti-bunching dip of

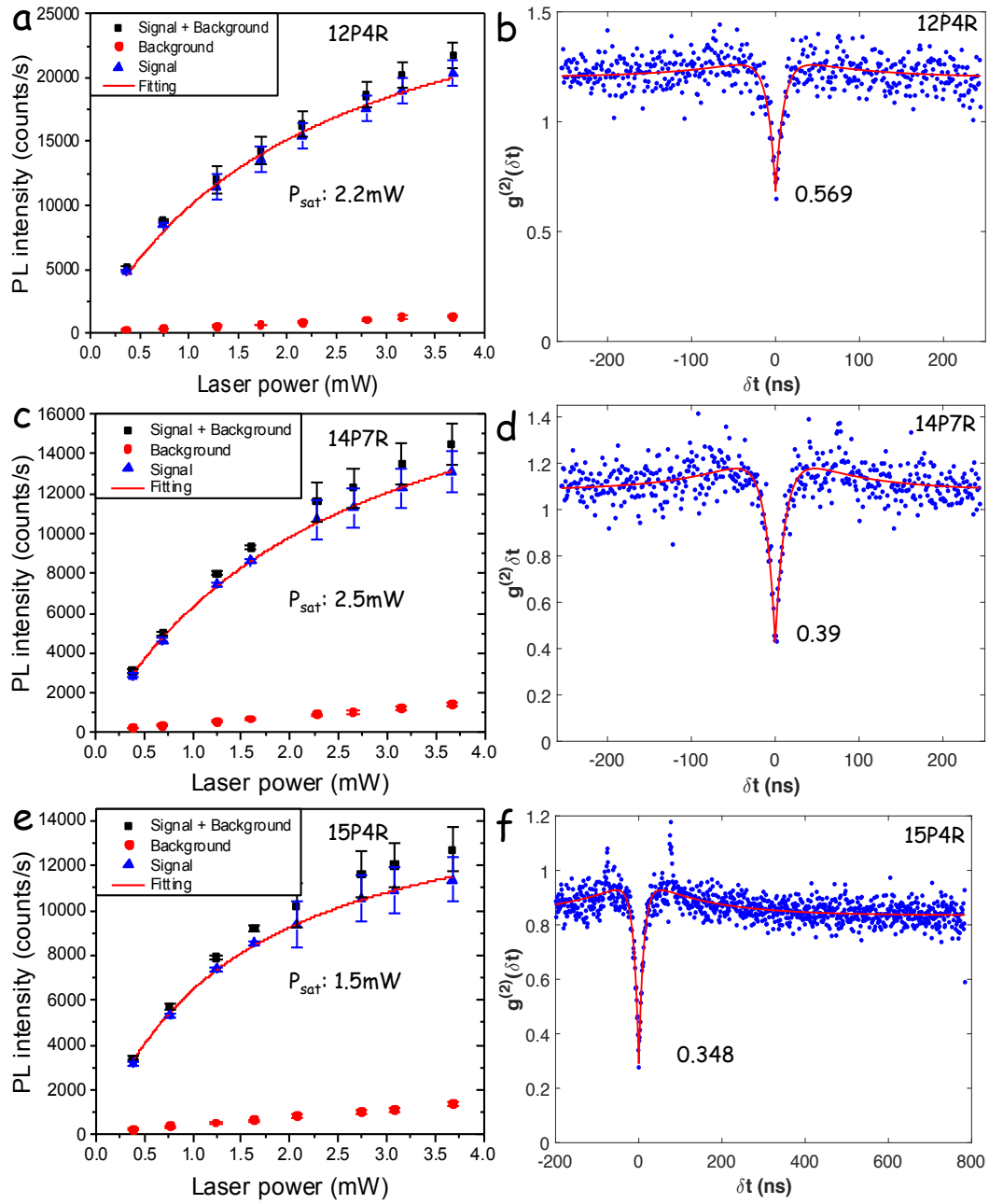


FIGURE 5.12: Summary of the optical properties of the NV⁻ centres generated by various laser pulse energies. **a**, **c**, and **e**, Power dependence measurements of 12P4R, 14P7R and 15P4R, respectively. The solid red lines are the best fits to Equation 3.15. **b**, **d** and **f**, HBT measurements of 12P4R, 14P7R and 15P4R respectively. The red lines are the best fits to Equation 3.12. The P_{sat} values and depths of anti-bunching dips are given in each graph.

12P4R were measured to be 2.2 ± 0.2 mW and 0.569 ± 0.03 respectively, as shown in

Label	12P4R	14P7R	15P4R
Laser pulse energy (nJ)	28.7	26.3	25.2
P_{sat} (mW)	2.2 ± 0.2	2.5 ± 0.1	1.5 ± 0.06
Depth of HBT dip	0.569 ± 0.03	0.39 ± 0.03	0.348 ± 0.01

TABLE 5.6: *Summary of the laser pulse energy and optical properties of the three selected NV⁻ centres in Array 2.*

Figure 5.12a and b. The P_{sat} and depth of the anti-bunching dip of 14P7R were measured to be 2.5 ± 0.1 mW and 0.39 ± 0.03 respectively (see Figure 5.12c and d). The P_{sat} and depth of the anti-bunching dip of 15P4R were measured to be 1.5 ± 0.06 mW and 0.348 ± 0.01 respectively, as shown in Figure 5.12e and f. The optical properties of these NV⁻ centres are summarized in Table 5.6. When the laser pulse energy is decreased from 28.7 nJ to 26.3 nJ, although the P_{sat} values are comparable within the error bars, the depths of anti-bunching dips improve remarkably from 0.569 to 0.39. When the laser pulse energy is further decreased to 25.2 nJ, the P_{sat} values significantly decrease to 1.5 mW and the depths of anti-bunching dips decrease slightly. These results suggest that the higher laser pulse energies generate more residual defects after annealing.

The significant difference between the results of Array 2 and Array 1 is that four NV⁻ centres were generated without optically detectable residual defects, labelled by blue square in Figure 5.11a. Three of the four NV⁻ centres were generated by laser pulse energy of 23 nJ and the other one was generated by laser pulse energy of 20.8 nJ. The other repeats generated by the same laser pulse energies as the four NV⁻ centres are invisible in PL image, implying that most of the damage was healed after annealing and the level of residual defects is too low to be detected by confocal microscope. Figure 5.13 shows the typical optical properties of these four

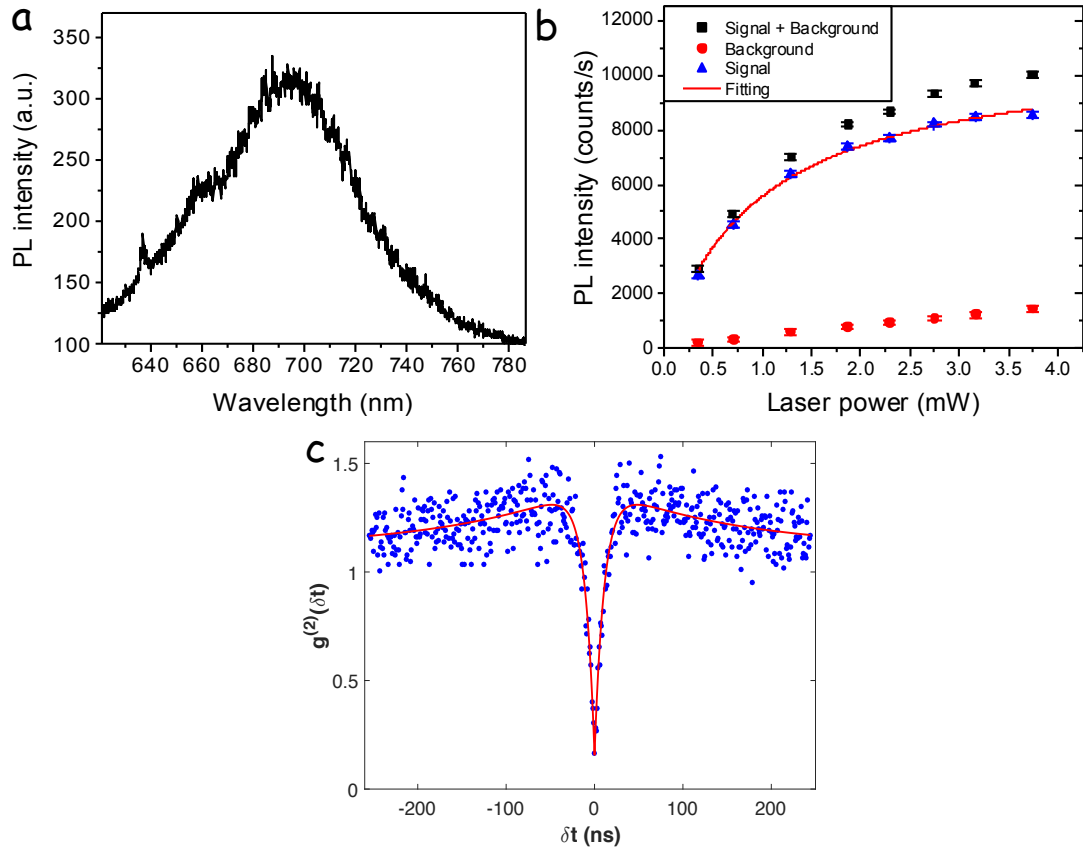


FIGURE 5.13: Typical optical properties of the four NV^- centres labelled by blue square in Figure 5.11a. **a**, Spectrum. **b**, The scatter plots of power dependence measurements of the PL intensity. The red solid line are the best fit to Equation 3.15. **c**, HBT measurements of the photon correlation function ($g^{(2)}(\delta t)$). The red line is the best fit to Equation 3.12.

NV^- centres. The spectrum shows the pure NV^- emission and the ZPL is observed (see Figure 5.13a). The power dependence measurement is presented in Figure 5.13b and the P_{sat} is measured to be 0.99 ± 0.07 mW, which is almost same as the P_{sat} value of the native single NV^- centre (1 mW). Figure 5.13c shows the typical HBT result and the depth of the anti-bunching dip is determined to be 0.142 ± 0.07 . The optical properties of these four laser-generated NV^- centres are as good as the native single NV^- centres which further confirms the generation of the NV^- centres without optically detectable residual defects.

All the NV^- centres in Array 2 disappeared after annealing at 1200°C for 24 hours,

which will be discussed in Section 5.5.4. Therefore, the coherence properties of the NV^- centres in Array 2 were not measured. In addition, the probability of the NV^- centres generation in Array 2 in sample B is relatively lower than the Array 4 in sample B and Array 6 in sample A. Thus, the results of Array 2 will not be further analyzed in the rest of this thesis. The lower probability of the NV^- centres generation in the Array 2 may be due to the lower nitrogen concentration in this region.

5.5.4 Annealing at 1200° C

There are still some optically detectable residual defects which can not be completely annealed out at 1000°C and also the successful probability of generating the single NV^- centre could be improved. The probability of creating NV^- centre increases with the diffusion length depending on annealing temperature, so the higher temperature annealing may solve both problems. First, sample B was annealed at 1200°C for 24 hours with a fresh array (Array 3, see Table 5.3) alongside the old arrays (Array 1 and Array 2). There was no NV centre generated in the Array 3. All the laser-generated NV^- centres in Array 1 and Array 2 were completely annealed out, and some native NV^- centres were annealed out as well. Yamamoto et al annealed their ion-implanted sample up to 1200°C for three hours and they observed the decreases of defects number and generation of the NV^- centres[79]. The evidence suggests that the 1200°C is not a very stable condition to form the NV centres. As the annealing time is much longer than 3 hours, there

is sufficient probability to break the nitrogen-vacancy bond even though the thermal kinematic energy is slightly lower than the nitrogen-vacancy binding energy. In addition to the failure of generating NV^- centres, the surface of sample B was damaged and some holes were created on the surface even though the sample was buried in diamond grit. The damage holes scatter the excitation laser and PL, resulting in that the laser-induced features and NV^- centres beneath the holes are unable to be observed by confocal microscope.

Chu et al proposed a multi-step annealing protocol for the ion-implantation method to generate the NV^- centres with good optical and coherent properties[7]. The multi-step annealing involves 4 hours at 400°C, 2 hours at 800°C and 2 hours at 1200°C, with 3 degrees Celsius per minute ramping rate between steps[7]. The 400°C step is used to get rid of the surface graphitization and defects, the 800°C is the actual NV^- centre formation step, and the 1200°C annealing is introduced to remove the residual defects. Since the surface of sample B was damage by 24 hours annealing at 1200°C, another annealing at such high temperature may further damage the surface. A fresh array, Array 5, was fabricated in sample A for this multi-step annealing (see Table 5.3) and no any NV centre was generated after this anneal. This recipe was unsuccessful because 800°C may be too low to create the NV centre in the laser writing method. In ion-implantation method, the vacancies are generated near to the implanted nitrogen atoms. In contrast, in laser writing scenario the native nitrogen atoms randomly distribute in the 3D space, so the vacancies need to diffuse a certain distance to find the native nitrogen atoms. The failure of this annealing implies the diffusion length of 2 hours at

800°C (32.5 nm) is too short to generate the NV centre. Although the 2 hours at 1200°C annealing should provide long enough diffusion length, most of the vacancies recombined with interstitial carbon sites or formed multi-defects chain during the 800°C step, so the density of single vacancy was too low to have sufficient probability of the NV centre formation. This thesis will give more detail analysis and discussion of the sufficient diffusion length to generate the NV centre in laser writing method in the next chapter.

5.6 Optical properties and statistics analyses of the laser-generated NV⁻ centres

The optical properties results of various annealing conditions suggest that annealing at 1000°C for 3 hours not only generates the NV⁻ centres but also minimizes the number of residual defects. A fresh laser-induced arrays were generated in sample A (Array 6) and sample B (Array 4) with similar pulse laser energy range and both samples were annealed with this condition to gain more insights and statistics. Figure 5.14a and c show the PL images of Array 6 in sample A before annealing and after 3 hours of 1000°C annealing, respectively. The red lines at laser pulse energy $E_{1A} = 31$ nJ in Figure 5.14a and c indicate the lowest laser pulse energy that generates visible vacancy fluorescence. A lot of new features appeared at several sites below the red line in Figure 5.14c, implying the formation of new colour centres. The pre-annealing and post-annealing PL images of the Array 4 in sample B are shown in Figure 5.14d and e, respectively. Similarly, many new

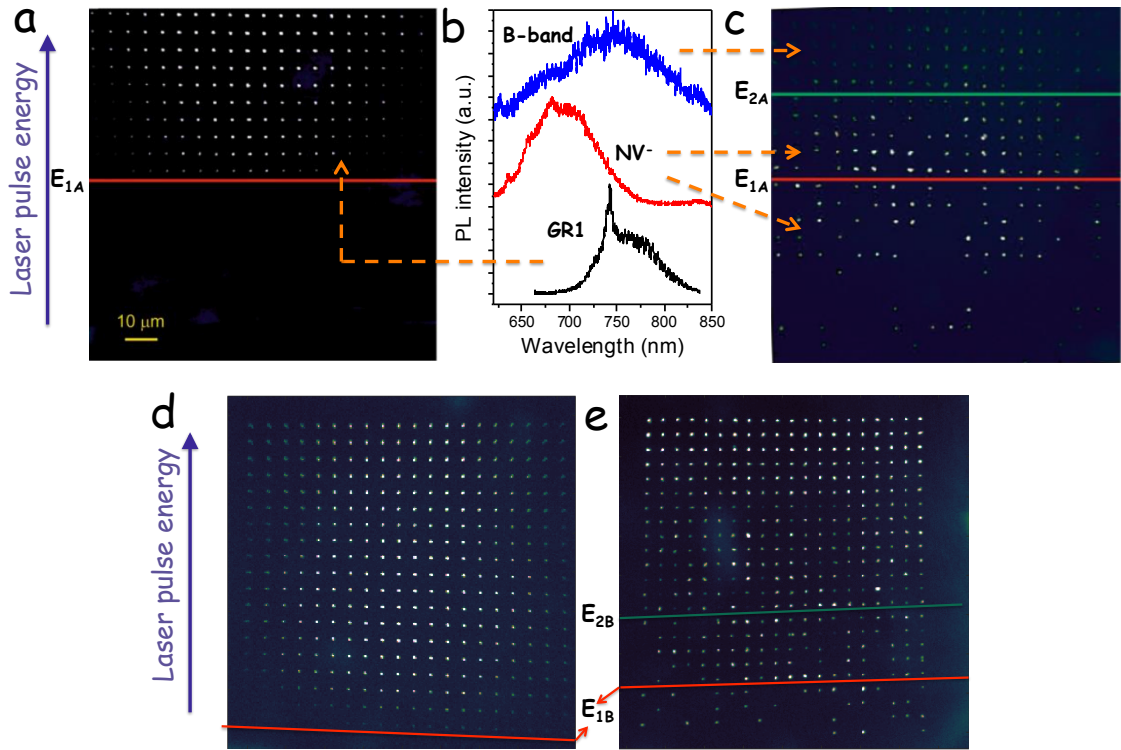


FIGURE 5.14: **a**, The PL image of the Array 6 of sample A before annealing. The laser pulse energy increases from the bottom to the top of the the image. The red solid line at laser pulse energy E_{1A} indicates the lowest energy laser pulse that produces visible fluorescence. The decrease in intensity of the features toward the edge of the array is due to off axis aberrations in the confocal microscope. **b**, Typical spectra measured from points in **a** (lower plot) characteristic of GR1 defects, from **c** below energy E_{2A} (middle plot) characteristic of the negatively charged nitrogen-vacancy (NV^-) centre, and **c** above energy E_{2A} (upper plot) characteristic of the radiation B-band. **c**, PL image of the Array 6 of sample A after 1000°C annealing for 3 hours, showing the NV^- centre emission from multiple sites processed with laser pulse energies both above and below E_{1A} . The green line at pulse energy E_{2A} indicates the graphitization threshold. **d** and **e**, The PL image of Array 4 in sample B before annealing and after annealing at 1000°C for 3 hours. The red line at laser pulse energy E_{1B} indicates the lowest energy laser pulse that generates visible fluorescence. The green solid line at laser pulse energy E_{2B} indicates the graphitization threshold.

features appeared below red line in Array 4 sample B after annealing, as well.

The red lines at pulse energy $E_{1B} = 20.8 \text{ nJ}$ in Figure 5.14d and e represent the lowest laser pulse energy that generate visible vacancy fluorescence. A typical PL spectrum of these new features are shown in Figure 5.14b (red curve) and Figure 5.15a, indicating that all new features are the NV^- centres. The strong sharp peaks

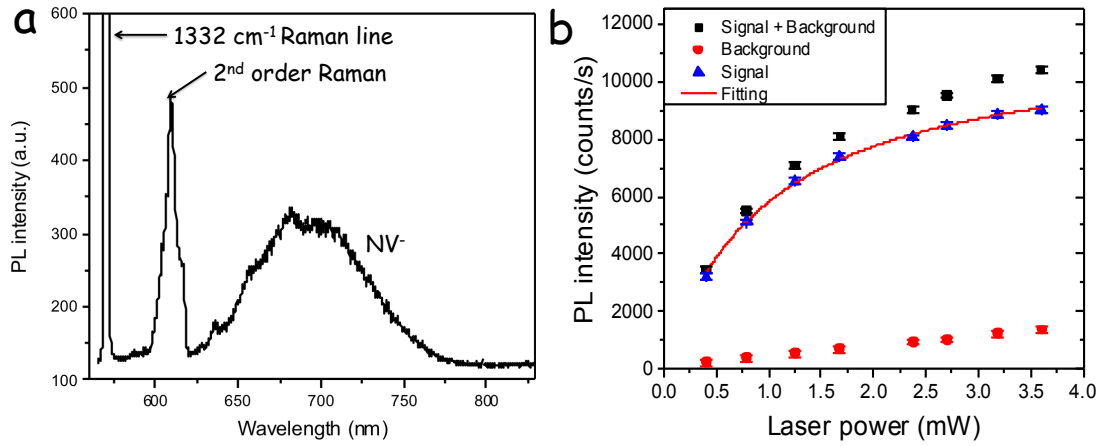


FIGURE 5.15: **a**, A typical PL spectrum of the new features below red line in Figure 5.14, indicating they are NV⁻ centres. **b**, A typical scatter plot of saturation curve for the PL intensity from the laser-generated NV⁻ centres below the red line. The red solid line is the least square fit of the saturation equation.

at 572 and 610 nm in Figure 5.15a are the first and second order Raman lines of diamond, respectively. The ZPL of the NV⁻ centre is clearly observed in the spectra of all the new features. There is no sign of the NV⁰ emission, implying that the concentration of the vacancies and other electron traps is very low after the anneal. Figure 5.15b is a typical power dependence measurement of PL intensity and the P_{sat} is about 0.99 ± 0.04 mW which perfectly matches with the P_{sat} of the native NV⁻ centre in bulk (1 mW) measured in the same confocal microscope. That is another evidence for the low concentration of fluorescence defects.

All 20 repeats are still visible after annealing if the laser pulse energy is greater than $E_{2A} = 36.4$ nJ ($E_{2B} = 25.2$ nJ) in sample A (B) which is indicated by green line in Figure 5.14c (e). There is no feature completely annealing out above the green line, suggesting that the vacancies generated at these sites exceeded the threshold for graphitization during annealing[130]. When the number of the vacancy is more than the threshold for graphitization, most of the vacancies will form amorphous

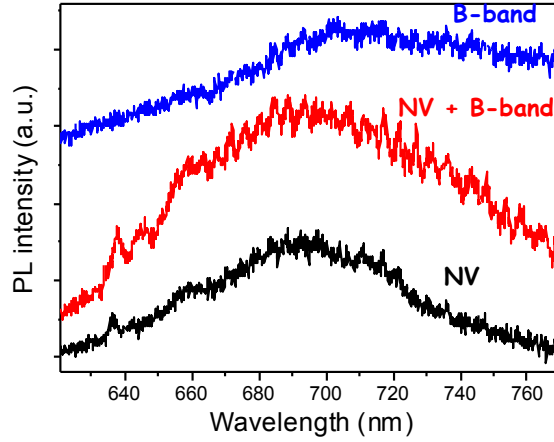


FIGURE 5.16: *Spectra from the sites with laser pulse energy greater than E_{2A} . B-band emission is observed (top plot), and spectra in which B-band and the NV^- centre emission are both present (middle plot). The spectra are offset in the vertical direction for clarity.*

sp^2 structure and the sp^2 structure can not be annealed out since it is more stable at high temperature. Some of sites above the green line are dimmer and the spectra of them show a broad band centring at 740 nm, as shown in Figure 5.14b (top plot). This broad band can be assigned as radiation B-band[37]. The middle plot of Figure 5.16 is a typical spectrum of the rest sites above green line and the PL intensity above 720 nm is higher than the spectrum of the native NV^- centres, indicating they are the combination of B-band and NV^- emission. I suggest that the difference of the graphitization threshold between sample A and sample B is due to the different alignment of the laser writing setup between two fabrication run and the strength of strain in the two samples. The strain in the diamond cause the birefringence and it will defocus the laser beam in z axis, resulting in decreasing the intensity of the laser pulse at focus. In addition, the difference of native defect or impurity concentrations between these two sample may also cause the difference of the graphitization threshold.

The HBT measurements of photon autocorrelation function measurement, $g^{(2)}(\delta t)$,

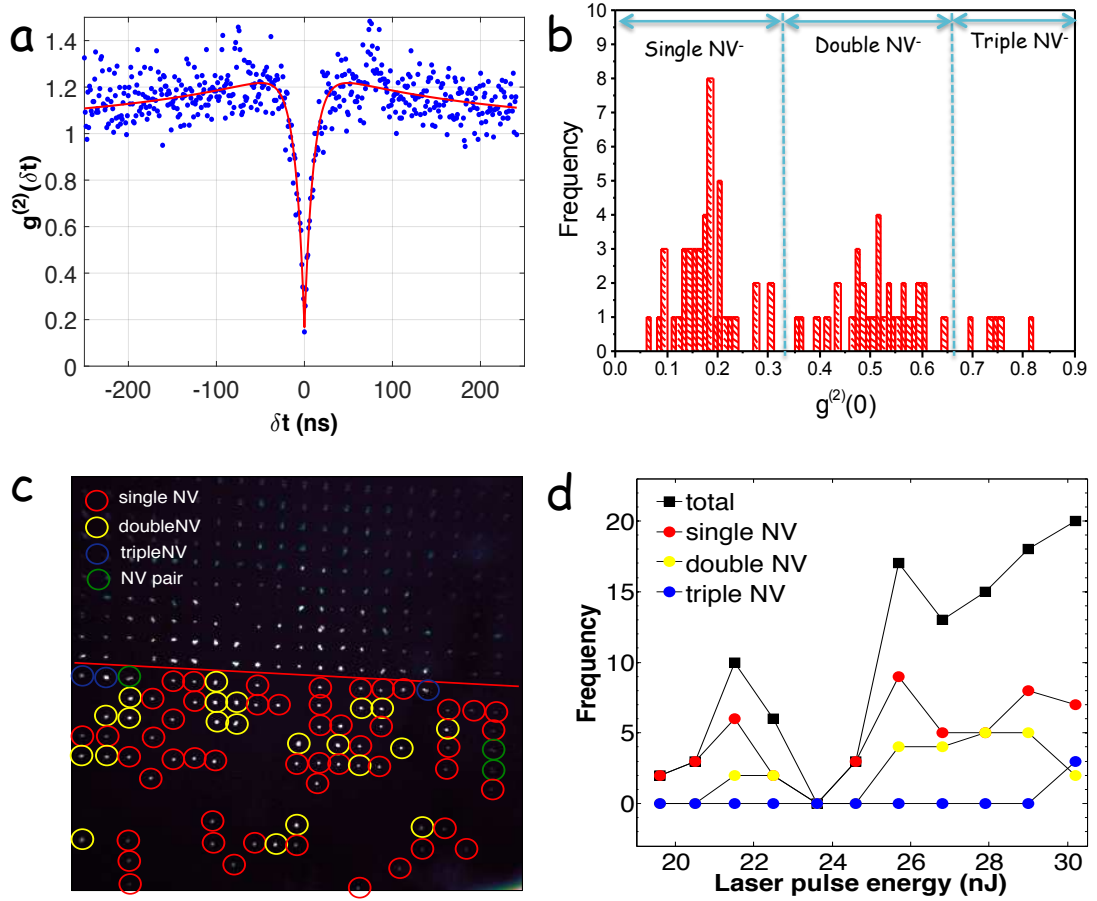


FIGURE 5.17: **a**, A typical histogram showing photon autocorrelation function $g^{(2)}(\delta t)$ from a single NV^- centre. Fits to Equation 3.12 is shown as solid red line. **b**, Histogram of $g^{(2)}(0)$ for the different laser processing sites, allowing identification of sites of single, double, and triple NV^- centres generation. **c**, Map of the number of NV centres generated at different sites. 'NV pair' refers to a double NV where the two defects are spatially resolved. **d**, Plot of the number of single (red), double or 'pair' (yellow), and triple (blue) NV^- centres generated in each row of 20 sites as a function of laser pulse energy measured before the objective lens in the writing apparatus. The total number generated per row is shown in black.

were performed on each of the laser-generated NV^- centres below red line in Figure 5.14c to determine the number of NV^- centres per site. A typical HBT result from a site with a single NV^- centre is shown in Figure 5.17a, showing a characteristic dip well below 0.5 at $\delta t = 0$. No background correction has been applied to the data, so the dip does not reach zero. Some of the sites show much shallower characteristic dip, indicating they are multiple NV^- centres. All the $g^{(2)}(0)$ values are plotted as

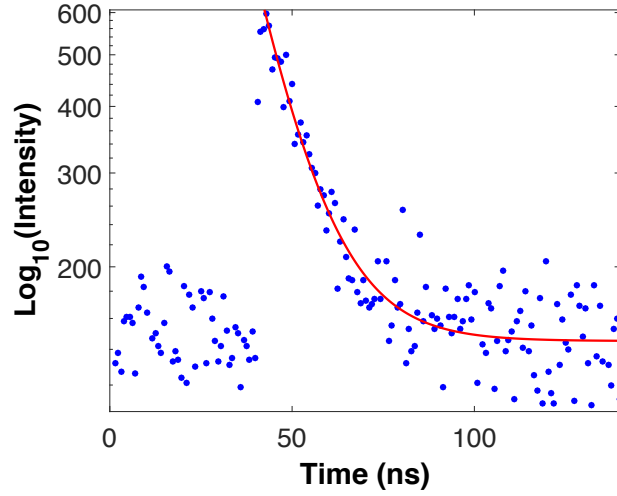


FIGURE 5.18: *A typical semilogarithmic plot of time-resolved PL for the laser-generated NV^- centre. The data are corrected for background and shown as scatter graphs. Fits to single exponential decays are shown as red line.*

a histogram as shown in Figure 5.17b. Two populations emerge, one with $g^{(2)}(0) < 0.32$ and another with $0.32 < g^{(2)}(0) < 0.65$, which are attributed to the existing of single and double NV^- centres respectively. A few features showed $g^{(2)}(0)$ between 0.65 and 0.85, which is assigned to be triple NV^- centres. The $g^{(2)}(0)$ should be between 0.1 and 0.2 for single NV^- centres in bulk diamond with perfect excitation polarization alignment, if including the background emission. However, the HBT measurements was conducted in automatic multi-sites sequence, so the polarization of excitation can not be tuned to perfectly excite each NV^- centre. That causes less emission from the NV^- centre and higher fraction background emission, leading to shallower characteristic dip. Also, the confocal may slightly misalign due to the temperature change during a long sequence. For double NV^- centres, some of the two NV^- centres do not orient along the same direction, so they can not perfectly excite at the same time, resulting in $g^{(2)}(0)$ lower than 0.5.

Figure 5.17c shows a spatial map of the NV^- centres number per site. The multiple NVs seem to generate at particular region and there is no NV^- centres generated in

17th row. These indicate that the concentration of nitrogen is not uniform across the fabrication region. The laser fabrication method may be used to determine the concentration of nitrogen at such low concentration in the future, which is lower than the detection limit of the current technology. Figure 5.17d shows the row statistics as a function of laser pulse energy. The total number of the NV⁻ centre per row reveals a systematic trend for more NVs to be created at higher laser pulse energies, but continued five rows deviate from the general trend due to the non-uniformity of the nitrogen distribution in the sample. To some extent, the number of and the ratio between the single and multiple NV⁻ centres can be controlled by tuning the laser pulse energy. At the laser energy of 25.7 nJ 9 single NV⁻ centres were found out of 20 corresponding to a probability of 45% which is the highest success rate of generating single NV⁻ centres.

Figure 5.18 shows a typical time-resolved photoluminescence decay with background removal and the data set fit well to signal exponential decay function. The excited state decay lifetime at 300K is measured to be $\tau = 12.1 \pm 1.1$ ns, which matches well with the value in literature[27].

5.7 Estimation of the probability of generating NV⁻ centres

In order to gain more insights into the mechanism of the NV⁻ centres generation, a simple model is established to estimate the probability of the NV⁻ centres generated per site, described in Section 3.6. Although the experimental result of GR1

intensity suggest that the vacancy generation mechanism is 15-photons absorption process, Lagomarsino et al. suggest that it involves 9 photons. Thus, both cases were considered in this section. The probability of NV⁻ centres can be obtained by using Equation 3.29. The number of initial vacancies for 9-photons and 15-photons absorption cases are calculated in Section 6.2.

First, the NV⁻ concentration for the 9-photon absorption process case is considered. The initial number of vacancy at the first row below the GR1 visibility threshold is 7.1×10^6 , as shown in Table 6.1. As mentioned in Section 3.6, in order to consider the recombination of the vacancies and interstitial carbon the number of vacancy is scaled by factor of 0.1. The number of NV centre can be obtained by putting the values of initial vacancy and annealing duration into Equation 3.29, giving about 12000 NV⁻ centres per damage site.

For 15 photons process, the initial number of vacancy is 8.5×10^5 at the first row below the GR1 visibility threshold, as shown in Table 6.1. The number of vacancy is 8.5×10^4 with consideration of recombination process. The number of the NV⁻ centre is calculated to be about 1450 per laser damage site on average.

For sample A, 8 sites have no NV⁻ generated, 7 sites have single NV⁻ centres, 2 sites have double NV⁻ centres and 3 sites have triple NV⁻ centres in the first row below the GR1 visibility threshold. 20 NV⁻ centres have been generated in this row, so the average number of NV⁻ centres generated per site is 1.0. Figure 5.19a shows the probability of how many the NV⁻ centres per laser damage site can be found in sample A. The black squares are obtained from the Poisson distribution with the mean value equal to 1 and the red circles are the experimental data set for

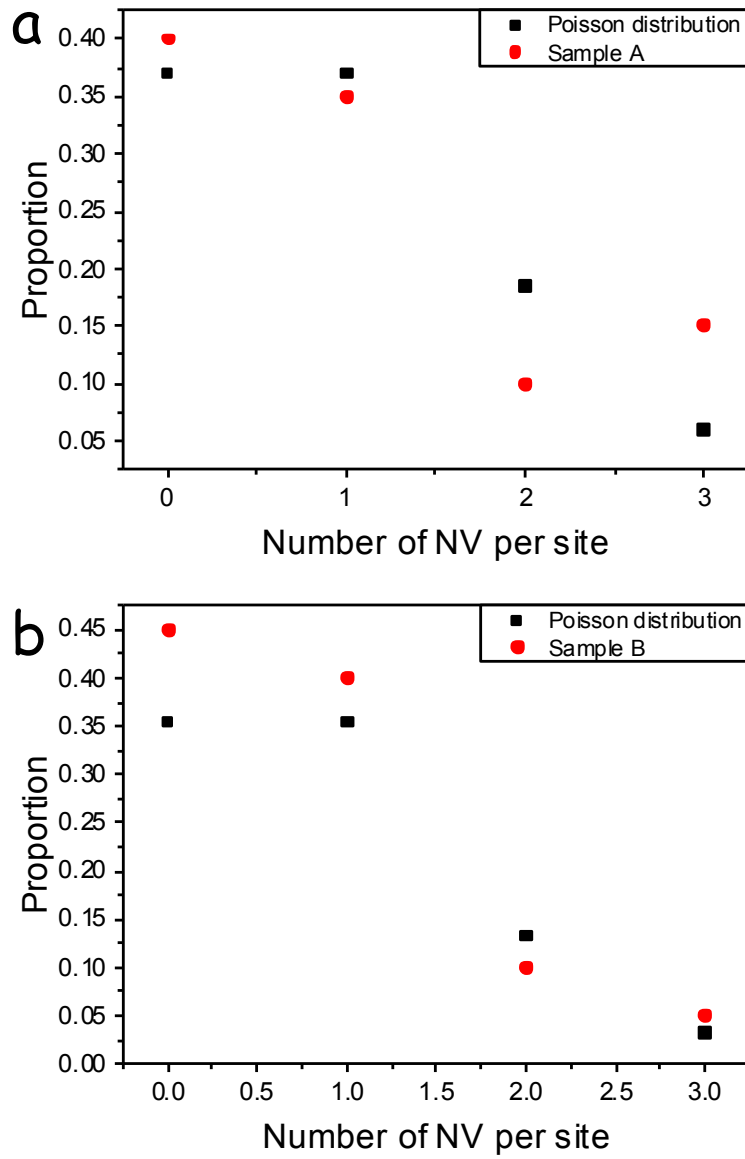


FIGURE 5.19: A scatter plot of the probability of the number of NV centres per laser damage site for **a** sample A and **b** sample B. The black squares are calculated from the Poisson distribution with mean value equal to 1 for sample A and with mean value equal to 0.75 for sample B. The red circles are the experimental data set from the first row below the GR1 visibility threshold.

the first row below the GR1 visibility threshold. The experimental data matches well with the poisson distribution, indicating the generation of the NV⁻ centres follows Poisson distribution.

For sample B, 9 sites have no NV⁻ centre generated, 8 sites have single NV⁻ centres, 2 sites have double NV⁻ centres and 1 site has triple NV⁻ centres in the first row

below the GR1 visibility threshold. Thus, the number of the NV^- centres generated per site is 0.75. Figure 5.19b depicts the number distribution of NV^- centres per site in the first row below the GR1 visibility threshold of sample B. The experimental data (red circles) follows the Poisson distribution with mean value of 0.75 (black squares).

The theoretical expectation values of NV^- centres generation for both 9-photon and 15-photon process are a lot more than the experimental data of the sample A and sample B. However, the 15-photon process is almost a order of magnitude near to the experimental results. The mismatch between the experimental and theoretical results may be due to three reasons. The recombination rate of the vacancies and interstitial carbon defects may be greater than 90%, which is obtained from the Monte Carlo calculation of ion-implantation method. The vacancies are created along the path of the implanted ions for ion-implantation method; in contrast, the laser-induced vacancies are generated within the focal volume for laser writing method. The vacancies generated by laser writing method are relatively near to the other interstitial carbon defects, compared with the ion-implantation method. Thus, the recombination rate for laser writing method may be greater than that of ion-implantation method.

The second issue is that the concentration of nitrogen is undetermined. The detection limit of current technique for nitrogen concentration is about 5 ppb, so the nitrogen concentration of 5 ppb used in the calculation is overestimated. In fact, the nitrogen concentration is much lower than 5 ppb and the nitrogen concentration may be lower than 0.5 ppb. Finally, although the number of the initial

vacancies is estimated from the volume of the focal spot, the value may be not accurate. Therefore, it requires other experiments to measure the number of vacancies.

5.8 Summary

This chapter has described the idea of laser writing, the detail of laser writing and the optical characterization results of the laser-generated array before anneal and after six different annealing recipes. The basic idea of generation of the NV centres is that using a single femtosecond laser pulse to create a few single vacancies in the diamond via multi-photon absorption mechanism. Single laser pulses were delivered to two commercial electronic grade CVD diamond at a depth of 50 μm to demonstrate the 3D fabrication capability of vacancies and the NV⁻ centres generation. The pulse energy was varied from 16.0 nJ to 61.8 nJ in 24 increments to generate different degree of damage to the lattice. Each energy has 20 repeats to build up the statistics.

The laser-induced array was characterized by the confocal microscope immediately after fabrication (before anneal). The PL intensities of the laser-induced features decrease with laser pulse energy and the features became invisible when the laser pulse energy lower than certain energy threshold. This energy threshold depends on the concentration of the impurity and defect in the sample and alignments of the laser writing apparatus. The spectra show that the laser damage features are

the GR1 centres in low laser pulse energy region and they are the combination of the GR1 and B-band in the high laser pulse energy region.

The MPI and Zener breakdown are considered to be possible mechanisms of vacancy generation in the low laser energy region. The Keldysh parameter predicts the MPI is the dominant mechanism when the laser pulse energy below 25 nJ. The experimental result may also suggest the MPI is the dominant mechanism if the laser pulse energy below 25 nJ and it also suggests that 15 photons are involved in the multi-photon absorption process.

Above 800°C the GR1 centre become mobile and the vacancy can be caught by substitutional nitrogen atom to form the NV centre. Six annealing recipes have tried on the samples. 1 hour 800 degrees annealing may not be able to generate NV centre due to the low temperature. Annealing at 900°C for an hour successfully generates three NV centres, but the residual defects were not completely annealed out. The following anneal at 900 degrees for three hours improves the optical properties of the three NV centres but still could not completely anneal out all residual defects. This means that the higher temperature annealing can remove more residual defects, so higher temperature annealing is necessary to generate the single NV⁻ centre without residual defects. After an hour annealing at 900°C, the spectra of the two laser-generated NV centres show a mixture of NV⁰ and NV⁻ emission, indicating that some residual GR1 centres did not completely anneal out. After 3 hours annealing at 900°C, the spectra of them were transformed to the pure NV⁻ centre emission, implying that the residual GR1 centres have been annealed out or transformed to sp² structure. The optical properties of the three

NV⁻ centres was further improved after 3 hours annealing at 1000°C. The B-band emissions in the spectra of 5P7R and 5P10R were reduced and the P_{sat} values of them also decreased. These suggest that the 1000°C annealing can remove more residual defects. On the other hand, the depths of anti-bunching increase more than 0.66, suggesting that a new NV⁻ centre may be generated after 1000°C annealing in each site. The optical properties of 4P1R, 5P7R and 5P10R as a function of annealing conditions were presented. The P_{sat} values and depths of anti-bunching dip show wide distribution for each site after an hour annealing at 900°C, but they were shifted to similar levels after three hours anneal at same temperature. This indicates that one hour annealing duration is too short to reach the equilibrium state of residual defects, but after 3 hours annealing the state of residual defects are stable.

The sample was also annealed at 1200°C for 24 hours, but no NV centre has been generated and the NV⁻ centres which were created by 1000 degrees annealing were completely annealed out. A multi-step annealing recipe has been tried, but it could not generate any NV centre, as well. In conclusion, three hours annealing at 1000 degrees Celsius is the best condition for the laser writing method. The diffusion length of the vacancy is a critical issue for generation of the NV centre, so it will be discussed it in the next chapter.

Fresh arrays annealed at 1000 degrees for three hours generate many single NV⁻ centres without optically detectable residual defects. Some of the laser-induced sites were transformed to multiple NV⁻ centres after annealing and the multiple NV⁻ centres seem to appear at certain area and form some clusters, implying that

the concentration of nitrogen is not uniform across the array. The laser writing method may be used to map out the distribution of nitrogen concentration even though it is lower than 5 ppb. The spectra of all the laser-generated NV^- centre show pure NV^- emission and no any sign of NV^0 emission. This indicates that the 3 hours annealing at 1000°C can remove most GR1 centres and other electron trap defects. The total number of the NV^- centres per row shows a systematic trend for more NV^- centres to be generated at higher laser pulse energy. The highest probability of generating single NV^- centres with 45% happens at the leaser energy of 25.7 nJ. The excite state decay lifetime of the laser-generated NV^- centre is measured to be about 12.1 ns which is similar to the native NV^- centre in bulk.

A simple model was established to estimate the probability of generating NV^- centres per site for both 9-photons and 15-photons absorption processes. For 9-photons process, the expectation value of the number of the NV^- centres per site is about 12000 and in the 15-photons case the expectation value is 1450, which are much higher than the experimental results (1 for sample A and 0.75 for sample B). More accurate experiments are needed to determine the number of vacancy and concentration of nitrogen to get more accurate calculation. The probability of the distribution of the NV^- centres' number per site can be found in the first row below the GR1 visibility threshold in sample A and B were presented. They match well with the Poisson distribution, indicating the generation of NV^- centres follows Poisson distribution.

Chapter 6

Positioning Accuracy of Laser Written NV Centres

6.1 Introduction

In Chapter 5, it has demonstrated that the laser writing method can successfully generate single NV⁻ centres. The positioning accuracy is very critical for a NV⁻ centres generation methods and it includes two factors, size of the laser-induced features and diffusion length of vacancies. This chapter will give an estimation of the size of laser-induced features and the estimated number of vacancies which are generated by laser pulse can be calculated. The displacement of the laser-generated NV⁻ centres will be calculated and the results will be fitted by a diffusion equation, which is introduced in Section [3.2](#), to determine the diffusion constant. The discussion and analysis in this chapter are all based on the results of annealing

at 1000°C for three hours which is best annealing condition to generate the single NV⁻ centre.

6.2 Size of laser-induced features and number of vacancies

The aberration of the laser writing apparatus has been optimally corrected by SLM and the vacancy generation mechanism is highly non-linear, so the size of the laser-induced features should be smaller than the focal volume. The point spread function can be used to estimate the size of the laser-induced features, but it only provides the upper limit of the sizes. The point spread function in the diamond is assumed to be a Gaussian beam with cylindrical symmetric intensity distribution

$$I(r, z) = I_0 \cdot \frac{1}{1 + \left(\frac{z}{z_R}\right)^2} \cdot e^{-\frac{2r^2}{w_z^2}}, \quad (6.1)$$

$$d_1 = w_0 \sqrt{2 \ln 2}, \quad (6.2)$$

$$L_1 = 2z_R, \quad (6.3)$$

where $w_z = w_0 \sqrt{1 + (\frac{z}{z_R})^2}$ is the beam width at axial displacement z , w_0 is the beam waist at $z = 0$, z_R is the Rayleigh range and d_1 and L_1 are the full width half maximum (FWHM) of the photon intensity in radial and axial directions respectively. The w_0 and z_R are estimated to be 297 nm and 852 nm respectively, based on the numerical aperture of the objective lens, giving $d_1 = 350$ nm and $L_1 = 1704$ nm respectively. The estimated focal volume is $\frac{\pi}{4} d_1^2 L_1 = 0.16 \mu\text{m}^3$.

Both the theory and experimental results suggest MPI is the dominant mechanism in laser writing process, as discussed in Section 5.4. The nonlinearity of the multi-photon absorption process is expected to result in vacancy creation within a region smaller than the focal volume estimated by the field intensity $I(r,z)$. According to the MPI model, the distribution function for vacancy generation with y -photons absorption is dependent on $I^y(r,z)$ and the corresponding FWHM in radial and axial directions are given by

$$d_y = w_0 \sqrt{\frac{2 \ln 2}{y}}, L_y = 2z_R \sqrt{2^{\frac{1}{y}} - 1}. \quad (6.4)$$

Label	d (nm)	L (nm)	Volume (μm^3)	$N_{37.7}$	N_{GR1}	N_{single}
9- photons	117	482	5.2×10^{-3}	5.2×10^7	7.1×10^6	1.4×10^5
15- photons	90	371	2.37×10^{-3}	2.37×10^7	8.5×10^5	1.3×10^3

TABLE 6.1: Summary of the size of the laser-induced damage and the numbers of vacancy for 9-photons and 15-photons absorption cases. Here, $N_{37.7}$ denotes the number of vacancies created at graphitization threshold, N_{GR1} denotes the number of vacancies created at the first row below the GR1 visibility threshold and N_{single} is the number of vacancies at the lowest pulse energy to produce single NV⁻ centres.

Lagomarsino et al suggest that the multi-photon absorption process in diamond involves 9 photons[96] and I suggest that it is 15 photons absorption process based on the experimental result (see Section 5.4.2). The 15 photons absorption process may describe the vacancy generation mechanism better than 9-photon process, because the 15-photon process is obtained from the measurements of GR1 intensity. In the contrast, the 9-photons absorption process was obtained by measuring the density of photo-induced free electron. Although 9-photon process can generate free electrons, the energy of these free electrons may be not high enough to generate lattice damage. The 15-photon process only considers the generation of the free electrons which possess enough energy to generate lattice damage. Here, both cases are considered to further confirm which process can describe the vacancy generation process better. For the 9-photons case, the estimated FWHM are $d_9 = 117 \text{ nm}$ and $L_9 = 482 \text{ nm}$, corresponding to a volume of $\frac{\pi}{4}d_9^2L_9 = 5.2 \times 10^{-3} \mu\text{m}^3$. The vacancy density is about 10^{22} cm^{-3} at the graphitization threshold[130, 131] and this threshold is determined to be at the laser pulse energy of 37.7 nJ in Chapter 5. Thus, 5.2×10^7 vacancies are created over the volume calculated above with the 37.7 nJ pulse energy. In the MPI model, the number of the vacancies is proportional to the 9th power of pulse energy (E^9), providing an estimation of 7.1×10^6 vacancies at the first row below the GR1 visibility threshold and about 1.4×10^5 vacancies at the lowest pulse energies to produce the NV^- centres. All the parameters are summarized in Table 6.1.

For 15-photons process, the estimated FWHM are $d_{15} = 90 \text{ nm}$ and $L_{15} = 371 \text{ nm}$,

providing a volume of $2.37 \times 10^{-3} \mu\text{m}^3$. Therefore, 2.37×10^7 vacancies were generated at graphitization threshold (37.7 nJ). Following the MPI model, the estimated number of vacancies is 8.5×10^5 at the first row below the GR1 visibility threshold and 1.3×10^3 at the lowest pulse energies to produce the NV⁻ centres. All the values above are concluded in Table 7.1 alongside with those values of the 9-photons case for comparison.

6.3 Displacement of the laser-generated NV⁻ centre

The displacement of the laser-generated NV⁻ centre from the original laser damage position defines the positioning accuracy of the laser writing method. In addition, the displacement distribution can give some insight of the diffusion mechanism of the vacancy during annealing. This section is going to describe how the displacement of the laser-generated NV centres was obtained and will then estimate the position accuracy.

6.3.1 Distortion of the PL image and recovery

The location of each NV⁻ centre in the image plane can be extracted from the PL image by fitting with a 2D Gaussian surface to the measured intensity distribution. The spatial resolution of the microscope ($\sim 500 \text{ nm}$) combined with the intensity of the single NV⁻ fluorescence images (~ 10000 counts) allows Gaussian fitting

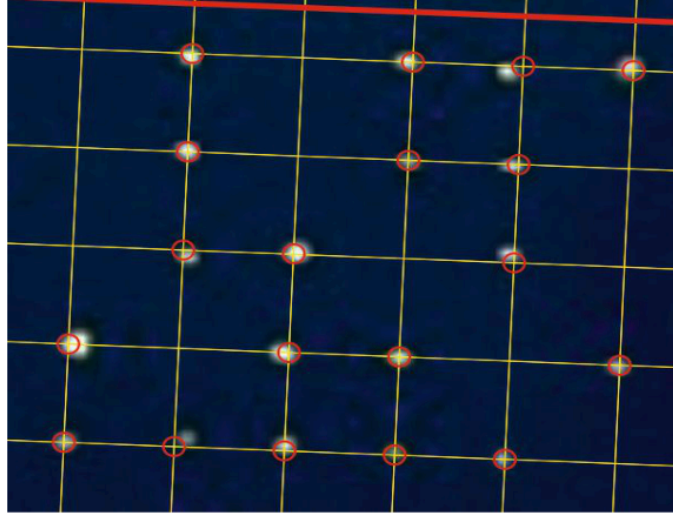


FIGURE 6.1: *Magnified image of the NV^- centre fluorescence relative to the laser processing grid. Red circles centre on the grid points are $1\ \mu\text{m}$ in diameter.*

with a standard error in the position of the NV centres of between 50 and 100 nm. The positioning accuracy of the sample stage in laser writing apparatus is about 30 nm, according to the manufacturer's specification. The positioning accuracy of the sample stage is smaller than the standard error of Gaussian fitting, so it is neglected. Figure 6.1 shows a magnified image of the central region of the array below E_{1A} with a superimposed grid showing the nominal target position. The red circles centred on the grid points are $1\ \mu\text{m}$ in diameter. The displacements of most NV^- centres from the grid points in Figure 6.1 are less than $0.5\ \mu\text{m}$. However, the displacements increase toward the edge of array due to the field distortion in the confocal microscope.

The previous chapter has mentioned that there is a field distortion in the confocal microscope, reducing the intensity of features toward the edge of the image. This optical aberration also cause a spatial distortion in the image, resulting in the increase in the separation of features toward the edge of the array. This distortion

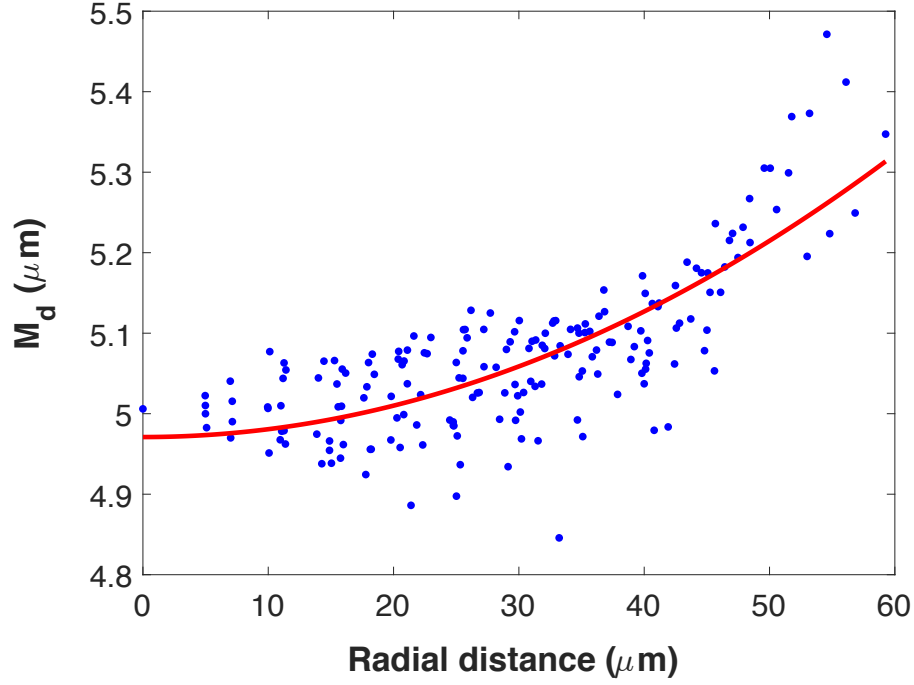


FIGURE 6.2: Scatter plot of the mean value of the nearest neighbor distance (M_d) as a function of the radial distance from the centre of field of view. The red solid line is the least-square fit of Equation 6.5.

mainly comes from the non-plan objective lens used in the confocal microscope, leading to spherical aberration. The distortion is quadratic proportional to the distance from the centre of field of view. In order to correct the distortion in the post-annealing PL image, I extract the function expression of the distortion in term of radial distance from the pre-annealing PL image. The separation of laser-induced array grids is $5\mu\text{m}$ with high accuracy because the SLM in the laser writing apparatus corrects all optical aberrations.

The position coordinate of each laser-induced feature in the pre-annealing PL image was obtained by a 2D Gaussian fit. The nearest neighbor distances of every feature were calculated. The mean value of the nearest neighbor distance, M_d , of each feature was plot as a function of radial distance from the centre of field of view as shown in Figure 6.1. The distortion takes a quadratic form as:

$$M_d = Ar^2 + B, \quad (6.5)$$

where M_d is the the mean value of the nearest neighbor distance, r is the radial distance from the centre of field of view, and A and B are constants. The red solid line in Figure 6.2 is the best fit of Equation 6.5, giving $A = 1.35 \times 10^{-4} \pm 1.5 \times 10^{-5}$ and $B = 4.965 \pm 0.014$. Equation 6.5 fit well to the data points with radial distance less than $30 \mu\text{m}$. However, it did not fit well to the data points with radial distance greater than $45 \mu\text{m}$. The radial distance of most of the NV^- centres which were considered in Section 6.3.2 are within $30 \mu\text{m}$, so the fitting results are good enough. Note that the intensity of some features in the pre-annealing array image are low and the 2D Gaussian fitting of them have greater error bars in position. As a result, there is a wide distribution of the data points with radial distance between 20 and $40 \mu\text{m}$ in Figure 6.2.

6.3.2 Displacement of the NV^- centres after annealing

The 3-hour anneal at 1000°C gives the best results for generating the single NV^- centres, so I will only calculate the displacement of the NV^- centres after this annealing condition. The position coordinates of each NV^- centre was extracted by fitting a 2D Gaussian function. In sample A only the NV^- centres below E_{1A} were considered, but in sample B 4 more rows above E_{1B} were also considered because there are less NV^- sites below E_{1B} . Also, some features near the edge of the array in sample B are too dim to get a good fit, so they are not considered.

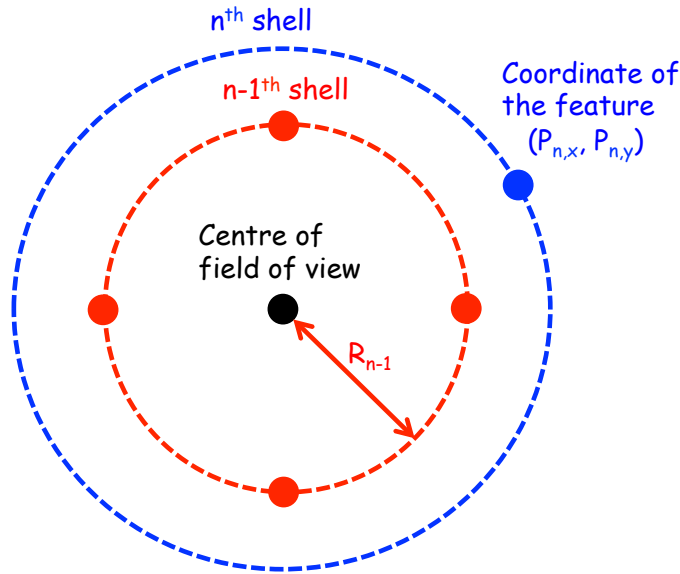


FIGURE 6.3: Schematic graph of the geometry of the $n-1^{th}$ and n^{th} shell points.

In order to build up a theoretical grid for comparison, the coordinates of the starting point is critical. The features above graphitization threshold should be near to the original laser damage position, because the graphitization structure do not diffuse during annealing. However, the laser-generated NV^- centres can still cause a slight displacement, so in each x and y direction a linear function is fitted to 5 points above graphitization threshold to average out the displacement. The intersection point of the two lines is the starting point. The theoretical grid with quadratic field distortion was created by using the following formula:

$$P_{n,x} = P_{n-1,x} \pm (1.35 \times 10^{-4} \times R_{n-1} + 4.965) \quad (6.6)$$

$$P_{n,y} = P_{n-1,y} \pm (1.35 \times 10^{-4} \times R_{n-1} + 4.965), \quad (6.7)$$

where $P_{n,x}$ ($P_{n,y}$) is the x (y) coordinate of the n^{th} shell point from the starting

position, and R_{n-1} is the radial distance between the $n-1^{\text{th}}$ shell point and centre of field of view, as shown in Figure 6.3. The centre of field of view is treated as the centre of the theoretical grid where is no spherical aberration because the laser light delivered to there propagates through the centre of all optics in confocal microscope.

The displacement between the laser-generated NV^- centres and their theoretical grid points with quadratic field aberration represents the position accuracy of each site. The displacements of each NV^- centre in sample A(B) are labeled in Figure 6.4a(b) and the labels are colour-coded four magnitude groups to reveal the systematic trends that would indicate further uncompensated field distortion. The displacements in sample A show a oscillation pattern. The displacement in the central region is minimum, it increases when going away from the central region, but it drop to smallest group when going further out side. This oscillation pattern indicates that there is some other distortion than spherical aberration which was not observed in the pre-annealing and post-annealing sample B images. Because the extra distortion did not present in the pre-annealing image, the magnitude and formula of it are hard to be determined. The displacement result of sample A will not be considered in the further analysis. Figure 6.4b shows the displacement results of sample B. It shows that there is little evidence of systematic order in the displacements, suggesting that the dominant field distortions have been corrected. Thus, the remaining displacements represent the random location of the NV^- centres about the original laser damage position. Figure 6.5 shows the histogram of the displacements of the NV^- centres in sample B, measured after

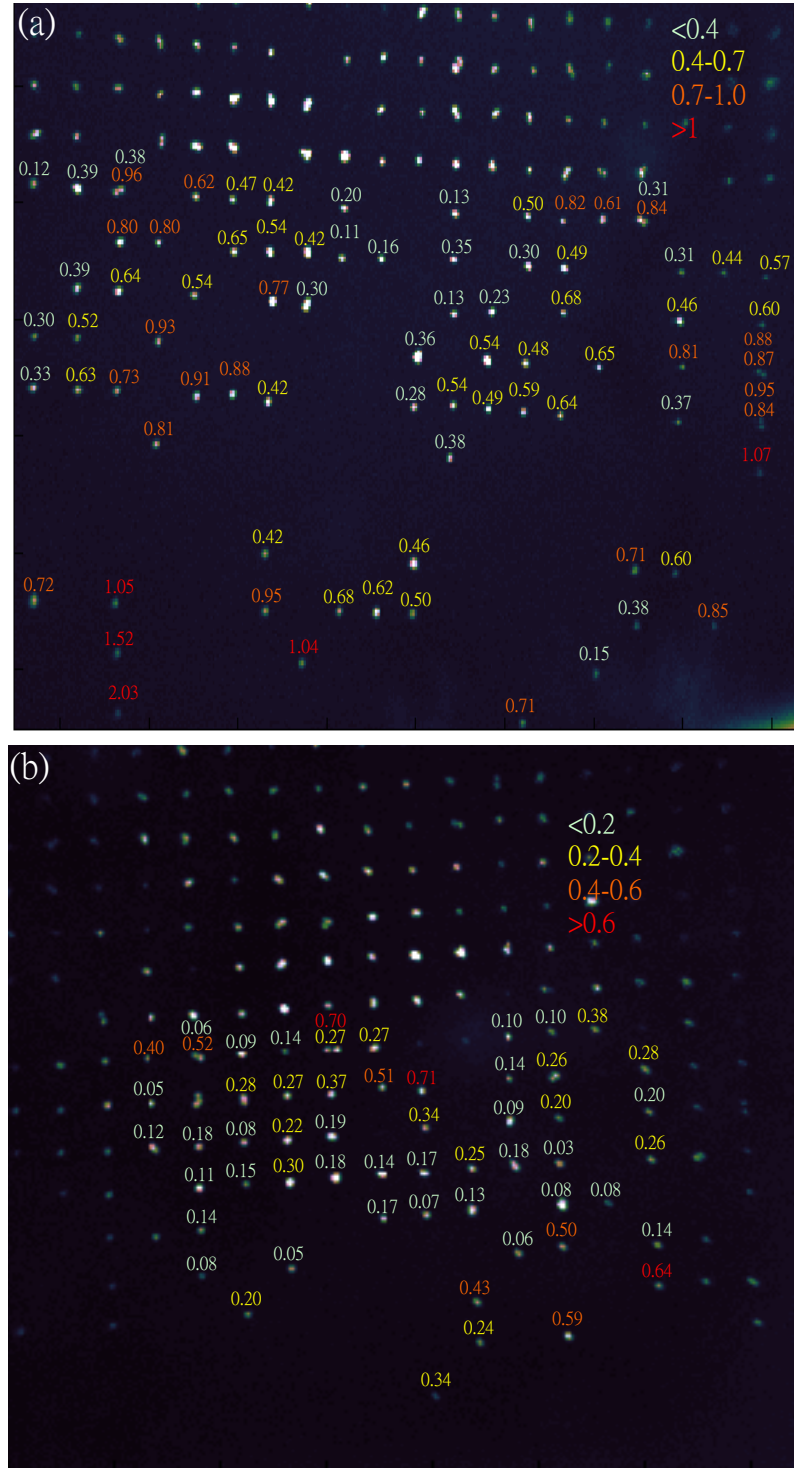


FIGURE 6.4: Positional accuracy of the NV^- centres generation in **a** sample A and **b** sample B. Labels show the displacement of NV centres from their theoretical grid positions (in μm), after removal of a quadratic field distortion. The labels are colour-coded into four magnitude groups to reveal systematic trends that would indicate further uncompensated field distortion.

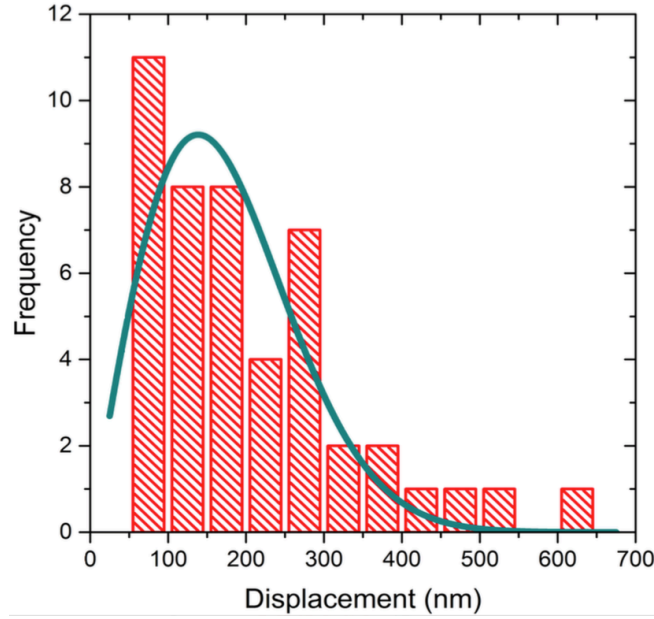


FIGURE 6.5: *Histogram of the displacement in the image plane for the NV-centres in sample B measured after correction for field distortion in the confocal microscope. The data are fitted with a cylindrical distribution function, Equation 6.9.*

field distortion correction. The measured displacements are remarkably larger than the predicted radial distribution of laser-induced vacancies in xy-plane, implying that diffusion of vacancies during annealing determines the spatial distribution of the NV⁻ in the image plane.

During the annealing the vacancies diffuse outward isotropically, and the process can be described by the vacancy diffusion equation. The substitutional nitrogen atoms are assumed to distribute randomly in the lattice. In the Section 6.2, the estimated size of the laser damage spot in xy plane (90 nm) is much smaller than in z (371 nm). Therefore, I make the assumption that the vacancy distribution in $z \gg r$, so the distribution of the NV⁻ centres displacements from their initial laser writing position after an annealing period t can be described by the cylindrically symmetric vacancy diffusion:

$$n_{NV}(r) = A r e^{-r^2/4Dt} \quad (6.8)$$

where A is a constant and the D is the diffusivity. The solid line in Figure 6.5 is a best fit of the 2D distribution function

$$f(r) = A r e^{-r^2/r_0^2} \quad (6.9)$$

where r is the radial displacement and A and r_0 are the fitting parameters, corresponding to the isotropic diffusion of vacancies, r_0 was found to be 196 ± 20 nm. Based on the distribution, the displacement of 61% the NV^- centres are within r_0 of the original laser damage position in the image plane. However, the positioning accuracy in z direction is expected to be lower, around 700 nm, because of the elongated shape of the laser-induced features generation volume. Comparing the fit result and Equation 6.8 provides $\sqrt{Dt} = r_0/2 = 98 \pm 1$ nm, giving a value of $D = 3.7 \times 10^{-14} \text{ cm}^2 \text{ s}^{-1}$. The diffusion of vacancies in diamond is a thermally activated hopping process the activation energy (Δ) for which can be expressed as

$$\Delta = -kT \ln\left(\frac{D}{D_0}\right), \quad (6.10)$$

where kT is the thermal energy and D_0 is a constant. Using the $D_0 = 3.6 \times 10^{-6} \text{ cm}^2 \text{ s}^{-1}$ in the work of Hu et al.[99] the activated energy of vacancy hopping is found to be $\Delta = 2.0$ eV, which is consistent with values presented in other reports (see Section 3.2)[100, 102, 103]. The comparable Δ value with the reported values and the good

fit to the histogram imply that the cylindrically symmetric diffusion function can describe the generation of the NV^- centres during annealing.

6.4 Summary

In this chapter, some models were used and built to calculate the displacement of laser-generated NV^- centres based on the experimental results in Chapter 5. The damage volume depends on the number of photon involved in the vacancy generation. The initial number of vacancies can be obtained based on the focal volume and MPI model. The initial number of vacancies at the first row below GR1 visibility threshold are 7.1×10^6 and 8.5×10^5 for 9-photons and 15-photons process respectively.

In order to determine the positioning accuracy of laser writing method, the displacements of NV^- centres are calculated by comparing the position of the each site in PL image with their theoretical grid point with aberration correction. The positions of the laser-induced sites are extracted by fitting a 2D gaussian function. The function of distortion is obtained by fitting a quadratic polynomial to the positions of laser-induced features in pre-annealing PL image. The histogram of the displacements can be fitted well by the cylindrically symmetrical diffusion function, giving the mean value to be 196 nm. Thus, the positioning accuracy in image plane is determined as 200 nm, but the position accuracy in z direction is expected to be around 700 nm due to the elongated shape of the laser-induced features. Also, the diffusivity, D , provided by the fitting is $3.7 \times 10^{-14} \text{ cm}^2 \text{ s}^{-1}$.

Still some works could be done in the future to increase the positioning accuracy.

A diamond with higher nitrogen concentration and lower annealing temperature may reduce the displacement of the NV⁻ centres.

Chapter 7

Coherent Properties of Laser Written NV Centres

7.1 Introduction

Chapter 5 has demonstrated that laser writing can successfully generate single NV⁻ centres without any optically detectable residual defects, indicating they are good candidates for quantum applications. The coherent properties of NV⁻ centres are critical for most quantum applications, so this chapter will present the spin and optical coherence properties of the laser-generated NV⁻ centres.

Continuous wave optically detected magnetic resonance (cw ODMR) was used to preliminarily probe the spin properties of the laser-generated NV⁻ centres. Pulsed ODMR measurements were conducted to measure their spin coherence time (T_2)

by applying Hahn echo pulse sequence. Photoluminescence excitation (PLE) spectroscopy has been used to measure linewidths and spectral stability of the ZPL of the laser-generated NV^- centres at 4.2 K. The linewidth of ZPL indicates the coherent properties of the optical transition of the NV^- centre.

The cw ODMR and PLE measurements were performed by myself and the pulsed ODMR measurements were carried out by Sebastian Knauer who is a DPhil student in Professor John Rarity's group in University of Bristol.

7.2 Spin properties of the NV^- centres

7.2.1 Continuous wave optically detected magnetic resonance measurements

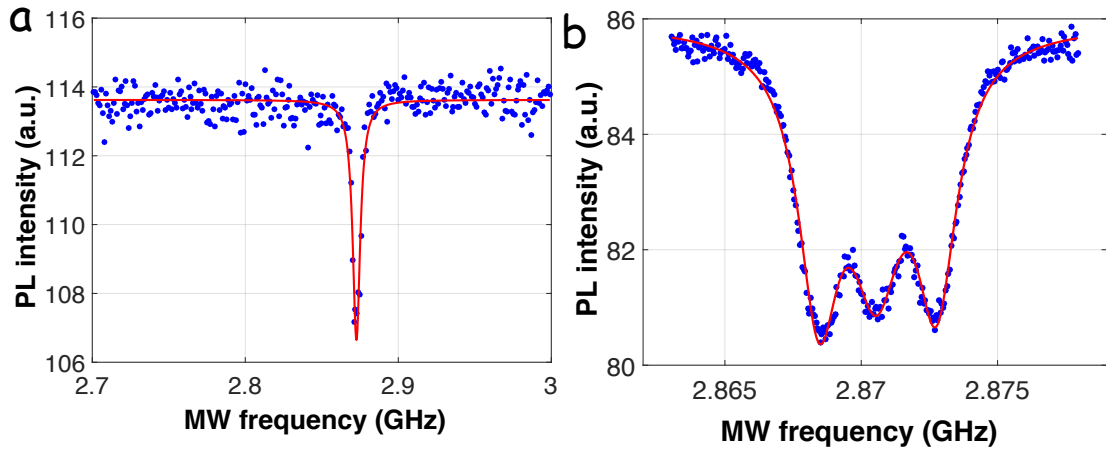


FIGURE 7.1: *a*, A typical scatter plot of cw ODMR spectrum of a laser-generated NV^- centre well below the GR1 visibility threshold. The red line is the least square fit of a Lorentzian function. *b*, A typical scatter plot of the hyperfine structure of the laser-generated NV^- centres. The red line is the least square fit of 3 Lorentzian functions.

The spin properties of the laser-generated NV^- centres were initially investigated by ODMR spectroscopy. Most quantum applications require single NV^- centres; hence only single NV^- centres in the low laser pulse energy region were measured. The cw ODMR apparatus and methodology are described in Section 4.5.1. Figure 7.1a shows the typical cw ODMR spectrum of the laser-generated NV^- centres below the GR1 visibility threshold and the data set fits well to a single Lorentzian function (red solid line in Figure 7.1a). The position of the ODMR signal is at 2.873 GHz and has a linewidth of 6 MHz.

Figure 7.1b shows a typical high resolution cw ODMR spectrum of the laser-generated NV^- centres and the ODMR signal splits into three dips due to the ^{14}N hyperfine interaction. The hyperfine structure data set is well fitted by three Lorentzian functions (red solid line in Figure 7.1b) and the positions of the three dips are at 2868.44 ± 0.01 , 2870.55 ± 0.02 and 2872.76 ± 0.01 MHz. The separations of them are approximately 2.2 MHz, which is comparable to the value of the ^{14}N hyperfine splitting in Doherty et al's paper[4]. However, the hyperfine structure of a few single NV^- centres can not be resolved because of strong strain field, which is not shown here. The strain field splits the ODMR signal into two branches and the resolution of the cw ODMR is not high enough to resolve the hyperfine splitting with strain splitting. 6 NV^- centres in sample A were measured and the hyperfine structure of two of them can not be measured due to the strong splitting.

The NV^- centres above GR1 visibility threshold may be of interest for some quantum applications, because the probability of generating multiple NV^- centres per

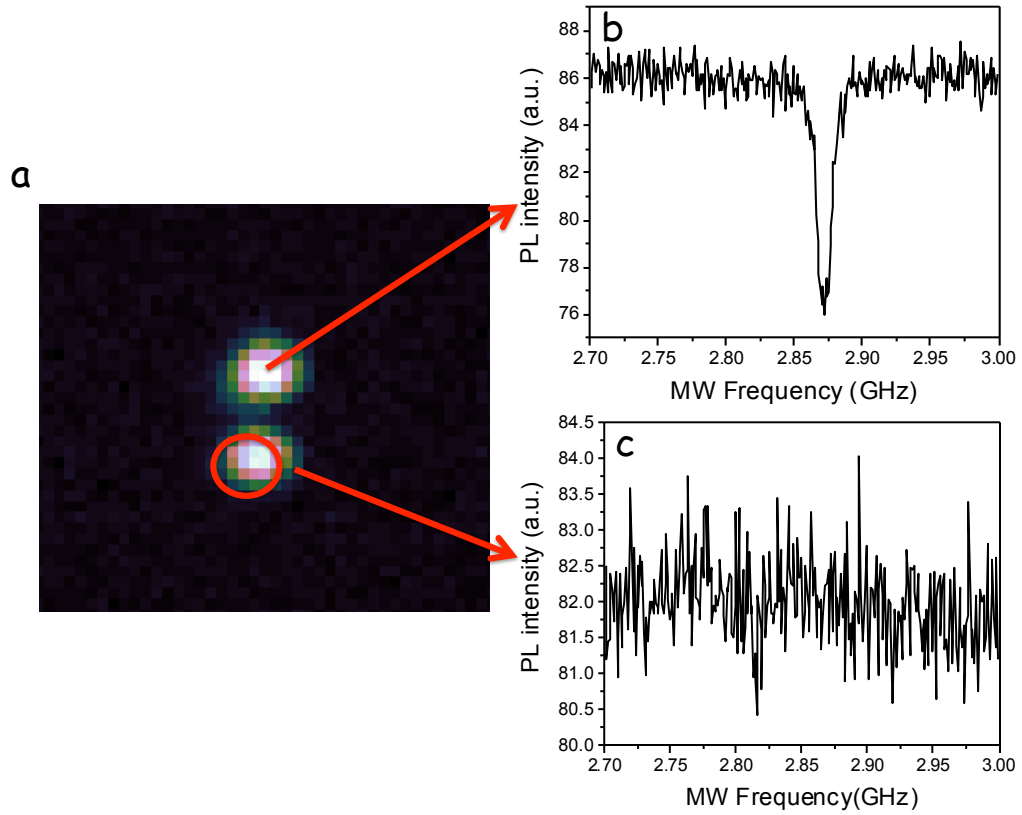


FIGURE 7.2: Typical ODMR results of the NV^- centers above the GR1 visibility threshold. **a**, A PL image of an 'NV pair'. **b** and **c**, ODMR spectra from the top and bottom NV^- in **a**, indicated by red arrows. The red circle is a illustrated label of the initial laser writing position.

site is much higher and there are no optically detectable residual defects. Figure 7.2a shows a PL image of 'NV pair' and the HBT measurements prove that they are both single NV^- centres, indicating no optically detectable residual defects. Figure 7.2b and c are their ODMR spectra and the red circle is a schematic label of the initial laser writing position. The NV^- centre further away from the initial laser writing position has a clear dip in the ODMR spectrum around 2.875 GHz, but the other one does not show any ODMR signal. The absence of the ODMR signal indicates a strong local strain around the initial laser writing position but the local strain fast decreases with distance. The fast decrease of the local strain suggests that the local strain should be attributed to the residual defects generated

by laser writing pulse. Although the NV^- centres generated by the pulse energy above GR1 visibility still possess good optical properties without any optically detectable residual defects, there is a strong local strain which degrades the spin properties of the NV^- centres.

7.2.2 T_2 coherence time

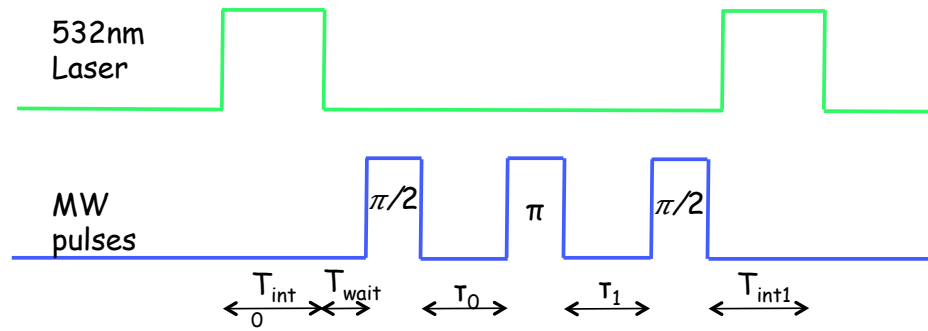


FIGURE 7.3: Pulse sequence for Hahn echo measurements. Laser gating indicated in green and microwave gating in blue.

Label	21P7R	20P5R	20P18R	15P1R	NV3	NV18
Laser pulse energy (nJ)	19.6	20.5	20.5	25.7	19.8	20.8

TABLE 7.1: Summary of the laser pulse energy of the NV^- centres which T_2 times measurements were carried on. 21P7R, 20P5R, 20P18R and 15P1R are in sample A. NV3 and NV18 are in sample B.

Pulsed ODMR measurements with the Hahn echo pulses sequence ($\frac{\pi}{2} - \tau_0 - \pi - \tau_1$ —echo, see Figure 7.3) were carried out on 4 NV^- centres in sample A and 2 NV^- centres in sample B to measure the spin coherence time (T_2). The apparatus and methodology of the T_2 coherence time measurements are presented in Section 4.5.2. The four measured NV^- centres in sample A are labeled as 21P7R, 20P5R, 20P18R and 15P1R. 21P7R was generated with laser pulse energy of 19.6 nJ, 20P5R and 20P18R were generated with laser pulse energy of 20.5 nJ and 15P1R

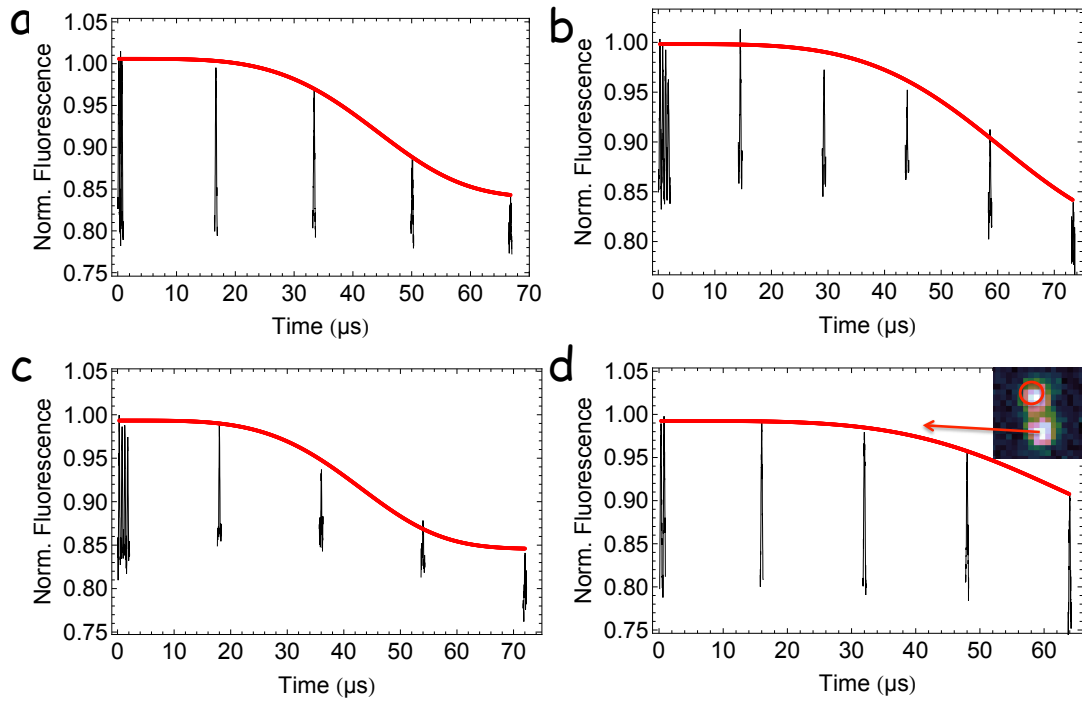


FIGURE 7.4: *Hahn echo data for **a** 21P7R, **b** 20P5R, **c** 20P18R and **d** 15P1R in sample A. The red lines are the best fits to Equation 7.1. The inset in d is the PL image of 15P1R, showing that it is an 'NV pair' and the red circle is a schematic label of the position of original laser damage. The Hahn echo measurement was carried out on the bottom NV⁻ centre.*

was generated with laser pulse energy of 25.7 nJ. Table 7.1 shows the summary of the pulse energy of these four NV⁻ centres. Figure 7.4 shows the T_2 results of the four NV⁻ centres in sample A and the red lines are the best fits to the function

$$I(\tau) = y_1 e^{-\left(\frac{\tau}{T_2}\right)^n} + y_0, \quad (7.1)$$

where the exponent n is a free parameter and y_0 , y_1 and T_2 are fitting parameters. The T_2 times of 21P7R, 20P5R and 20P18R are measured to be 47.6 ± 1.6 , 65.3 ± 9.8 and $46.2 \pm 3.4 \mu\text{s}$ respectively. The inset of Figure 7.4d is the PL image of 15P1R, showing that it is an 'NV pair'. The red circle is a illustrated label of the position of initial laser damage instead of actual position and the T_2 measurement

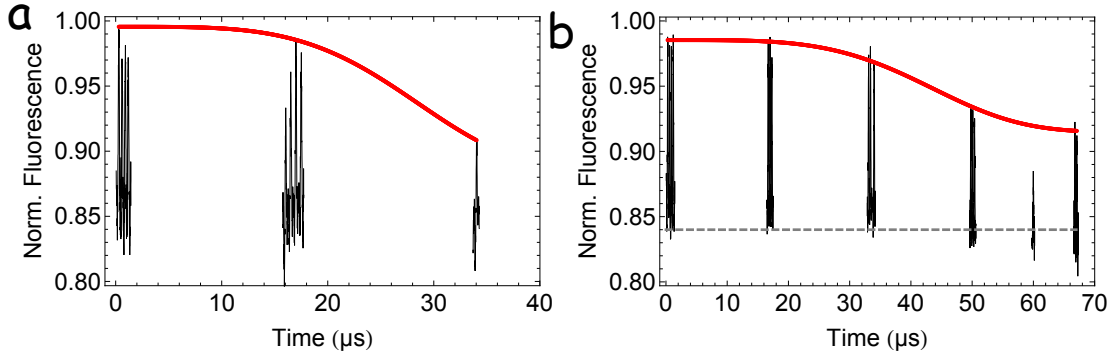


FIGURE 7.5: Hahn echo data for **a** NV3 and **b** NV22 in sample B. The red lines are the best fits to Equation 7.1.

was conducted on the bottom NV⁻ centre, as shown in Figure 7.4d. The photon counts of the T₂ measurement are too low when the delay time is longer than 70 ns, because the apparatus does not have enough laser power to saturate the NV⁻ centre at the depth of 50 μm. The data set of 15P1R does not reach $\frac{1}{e}$ value of the starting fluoresce counts, so we can only say the T₂ is longer than 100 ns. The longer T₂ time of 15P1R may be due to the larger displacement from the initial laser writing position. This may indicate that the residual defects generated by laser writing and subsequent annealing degrade the spin properties of the NV⁻ centres and those residual defects may be divacancy and multivacancy complexes[79, 80].

The two measured NV⁻ centres in sample B are referred to as NV3 and NV22, generated with a laser pulse energy of 19.8 nJ and 20.8 nJ respectively, as shown in Table 7.1. Figure 7.5 shows the Hahn echo results of NV3 and NV22. The T₂ time of NV3 is about 34 μs and the T₂ time of NV22 is greater than 100 μs. Similar to 15P1R, we can not give a exact T₂ value for NV22. The displacements of NV3 and NV22 are 70 and 150 nm. This may show a relationship between the coherence time and displacement. However, there are not enough data points to

draw a full conclusion.

The T_2 times of the laser-generated NV^- centres are typically between 30 and 80 μs , while two exhibit coherence times longer than 100 μs . Rodin et al reported that the longest T_2 times of the ion-implanted NV^- centres in diamond with natural isotopic abundance ($[^{13}C] = 1.1\%$) is about 300 μs [29]. Although the T_2 times of the laser-generated NV^- centres are slightly shorter than the value of ion-implantation method, the values of the laser-generated NV^- centres are still long enough to be of interest. Moreover, further optimizations can be done in the future to improve the T_2 time. Although the annealing at 1000 degrees Celsius should remove most multi-vacancy complexes, there may still be a few divacancies generated after annealing. Furthermore, there may be still a small number of residual single vacancies, degrading the spin coherence properties. These two kind of residual defects can be removed by annealing the sample at higher temperature for a short period (less than 3 hours). The multi-vacancy complexes and single vacancy can be quantitatively measured by ensemble EPR; however, the feature sizes and the number of the defects are too small to be measured by EPR method. Thus, the number of the GR1 and divacancy were not measured, so there is no experimental evidence to prove which kind of residual defect is responsible for the short T_2 times.

The other reason for the short T_2 times are the limitations imposed by the experimental method. The power of the 532 nm excitation laser is not high enough to saturate the laser-generated NV^- centres, so the count rate of the revival peaks were low. This setup can not measure the revival peaks greater than 60 μs , resulting

in the fitting results were pessimistic. Thus, it needs to improve the experimental apparatus to get more accurate results.

7.3 Optical coherent properties

The linewidth of the NV^- ZPL indicates the coherent properties of the optical transition and the linewidth of ZPL strongly depends on the temperature due to dynamic Jahn Teller effect[13]. As described in Section 3.4.4.1, the dynamic Jahn Teller effect is responsible for the homogeneous broadening of the ZPL. In order to remove the homogeneously broadening effect, all of the experiments in this section were performed at 4.2 K.

7.3.1 Spectroscopy in 4.2 K

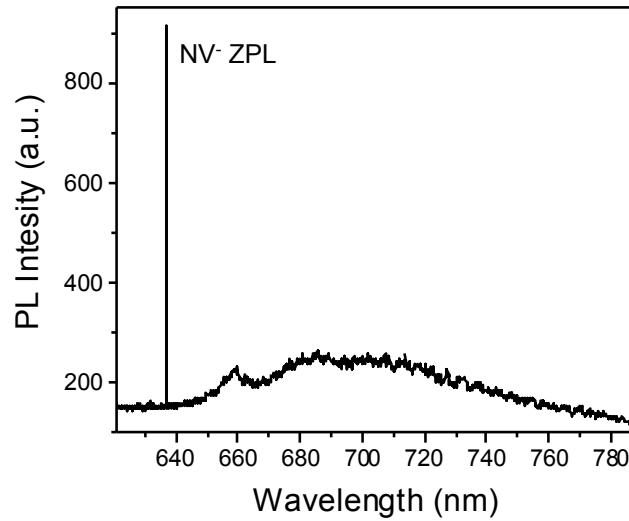


FIGURE 7.6: A typical spectrum of the laser-generated NV^- centre at 4.2 K. The sharp line is the ZPL of the NV^- centre.

Figure 7.6 shows a typical spectrum of the laser-generated NV^- centres at 4.2 K and the sharp peak seen at 637 nm is the ZPL of the NV^- centre. The linewidth is much narrower at 4.2 K than that at room temperature and the phonon sideband has been suppressed. These indicate that the phonon interaction has been reduced at 4.2 K. The resolution of the spectrometer is not high enough to resolve the ZPL, so the PLE method is essential to measure the linewidth of ZPL. The spectra still provides a rough wavelength range of each NV^- centres' ZPL, which makes the PLE measurements easier.

7.3.2 Photoluminescence excitation measurements

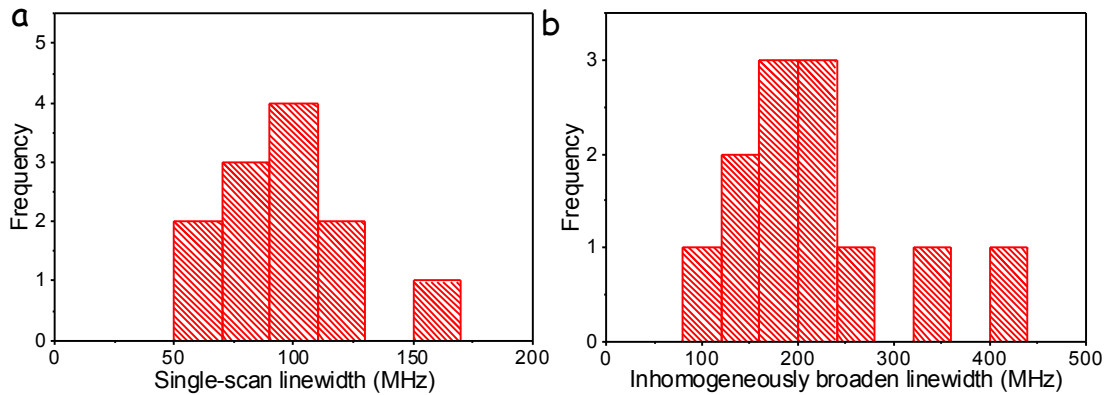


FIGURE 7.7: **a**, Histogram of the single-scan linewidths from sample A. **b**, Histogram of linewidths including spectral jumping from sample A.

The concept of the PLE is to use a wavelength tunable excitation laser to scan through the ZPL of the NV^- centre at wavelength of 637 nm and collect all phonon sideband photons. The experimental setup and methodology are described in Section 4.6.1. 16 NV^- centres and 34 NV^- centres were investigated in sample A and sample B respectively. Although the scanning range of excitation frequency covered 40 GHz, the ZPLs of some NV^- centres were not observed in both samples.

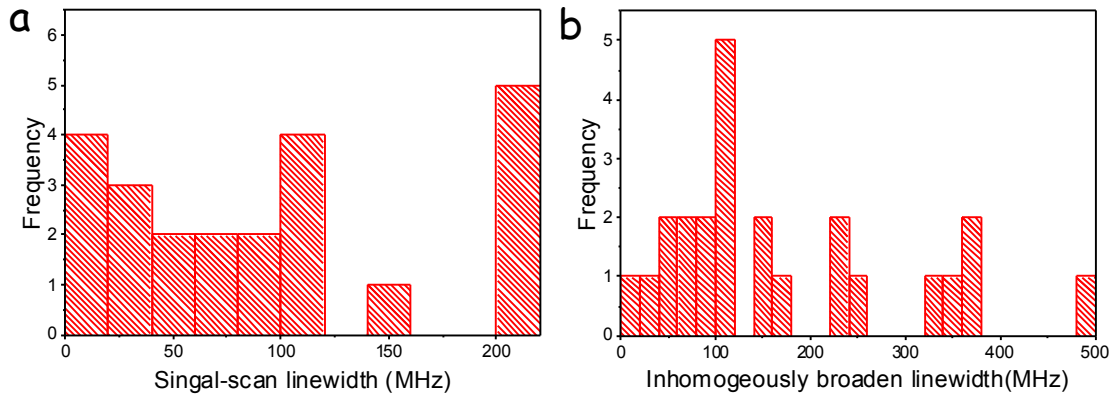


FIGURE 7.8: **a**, Histogram of the single-scan linewidths from sample B. **b**, Histogram of linewidths including spectral jumping from sample B.

That may be because the ZPLs are outside the scanning range or the intensity of the ZPLs is too weak to be seen due to strong local strain.

Figure 7.7 displays the histograms of the single-scan and inhomogeneously broaden linewidths (including spectral jumping) from sample A. The single-scan linewidths of the ZPLs in sample A vary from 60 to 165 MHz and inhomogeneously broaden linewidths of the ZPLs in sample A vary from 118 to 410 MHz. Although these values are much narrower than the values (500 MHz-2 GHz) in some reports[132, 133], they are much broader than the values (27 MHz-50 MHz) in other reports, including the best recodes of the ion-implanted NV^- centres[7, 13].

In sample B, the single-scan linewidths of the ZPLs vary from 12 to 200 MHz. Figure 7.8a shows the histogram of the single-scan linewidths from sample B. Half of the measured NV^- centres possess single-scan linewidths narrower than 100 MHz and almost one third of all measured NV^- centres have single-scan linewidths narrower than 30 MHz. There are couple of NV^- centres with single-scan linewidths greater than 200 MHz. Figure 7.8b shows the histogram of the inhomogeneously

broaden linewidths (including spectral jumping) from sample B. Half of the measured NV^- centres show the inhomogeneously broaden linewidth narrower than 120 MHz. A couple of the NV^- centres show the inhomogeneously broaden linewidth greater than 300 MHz.

Figure 7.9a shows a selection of PLE single-scan results from three NV^- centres, showing linewidths of 13.5 ± 0.3 MHz, 12.0 ± 0.7 MHz and 27.5 ± 1.2 MHz. The linewidths are obtained by fitting a Lorentzian function. A good fit to a Lorentzian function confirms that the homogeneous broadening mechanism is the dominant effect. The two narrowest lines are consistent with the Fourier transform limit of 12.4 ± 0.1 MHz for an NV^- centre in bulk diamond based on a excited state lifetime of about 13 ns. In order to further confirm this, the time-resolved photoluminescence decay (TRPL) of NV3 was measured at 4.2 K. In order to get a good fit to the high resolution lifetime result, the instrumental response function has to be considered. The instrumental response function was recorded by removing the laser blocking filter and inserting a neutral density filter to measure attenuated reflection of the laser. The instrumental response function was then convoluted with single exponential decay function and fitted to the TRPL data set. Figure 7.10 shows the TRPL results of NV3 after background removal and the best fit to the single exponential decay function convoluted with the instrumental response, giving the lifetime of 12.8 ± 0.1 ns. The Fourier inverse linewidth based on the 12.8 ± 0.1 ns lifetime is calculated to be 12.4 ± 0.1 MHz by using Equation 3.22. Comparison of this lifetime-limited linewidth with the measured linewidths of NV3 and NV8 shows that they possess a transform-limited optical transition, i.e.

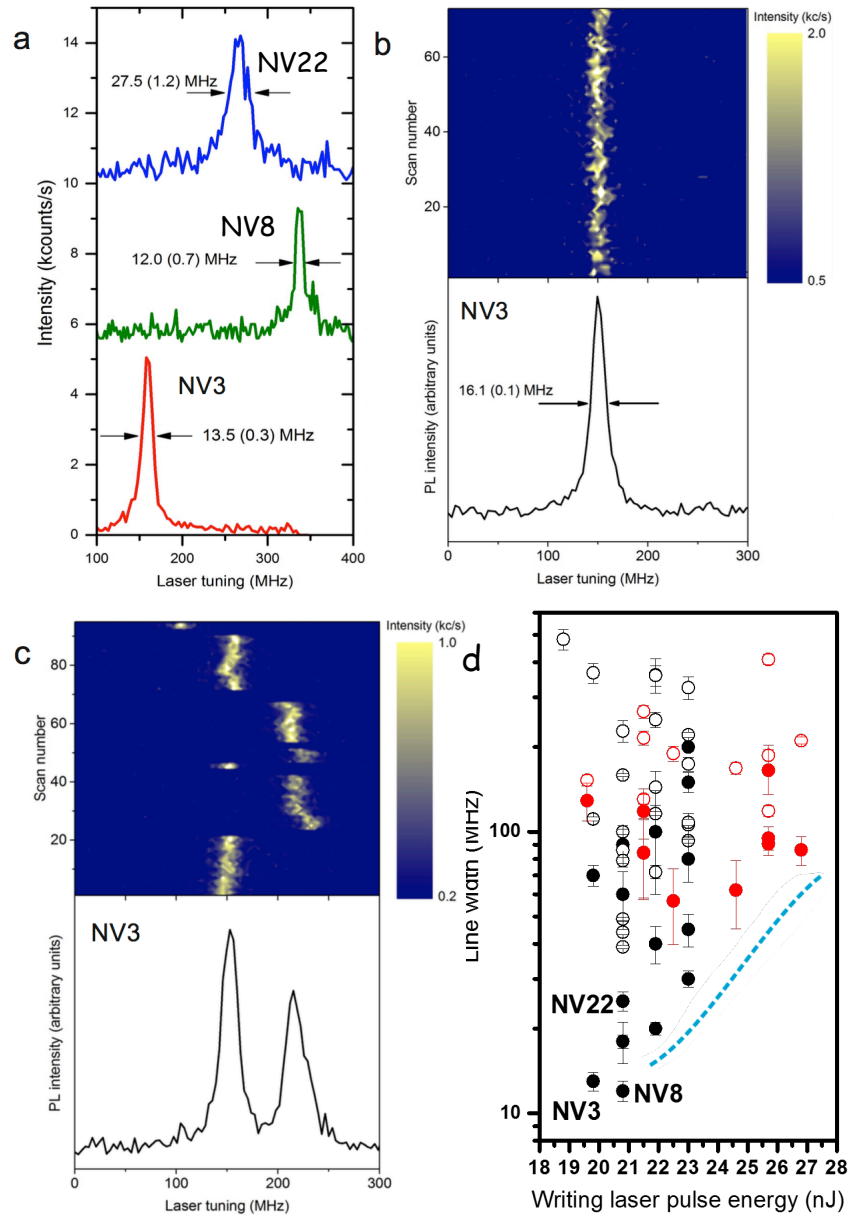


FIGURE 7.9: **a**, Photoluminescence excitation (single sweep) of three different NV⁻ centres, with two showing Lorentzian peaks below 14 MHz in width. Full-width-at-half-maximum values from Lorentzian peak fits are given, with errors in parentheses. **b**, Colourscale map of repeated PLE spectra of NV3, showing a stable line over 70 laser sweeps with an inhomogeneous line width of 16.1 MHz. **c**, Spectral jumping as a result of a 532 nm repump pulse required to restore the negative charge state upon ionization. Lower plots in **b** and **c** are aggregates of the consecutive sweeps in the colourscale images. **d**, Scatter plot of the single-scan linewidth (solid circles) and repump-broadened linewidth (open circles) for different energies of laser writing pulse. Data from sample A and B are shown as red and black circles respectively. The dashed blue line is a guide showing a trend to larger single-scan linewidths with higher pulse energies.

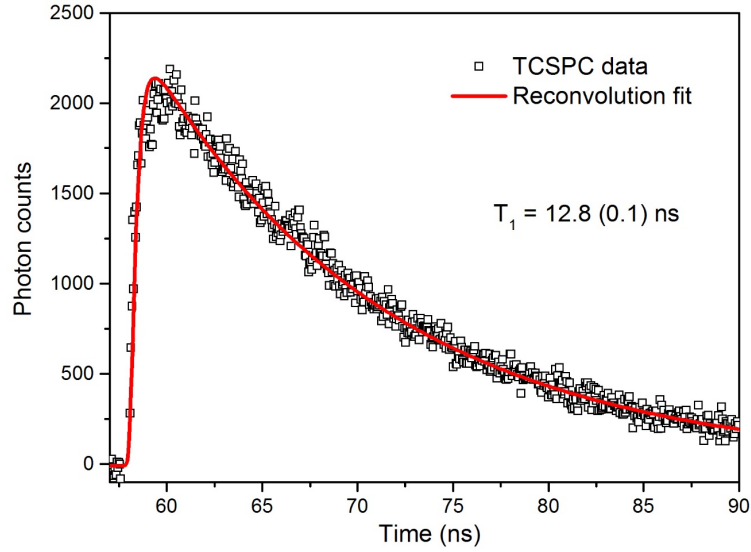


FIGURE 7.10: *Time-resolved photoluminescence result of NV3 in sample B at 4.2 K, fitted with a single exponential decay convoluted with the instrument response of the TCSPC apparatus.*

coherent optical transition.

Figure 7.9b shows the repeated scans of NV3 and it shows only small fluctuations in peak position over 70 scans resulting in an inhomogeneously broaden line of width 16.1 MHz. The PLE signal of NV3 can be very stable with little spectral diffusion for a few minutes. In general, the NV^- can be ionized to NV^0 after prolonged excitation (~ 30 s) and an optical repump was required to recover the negative charged state. Here, a 532 nm laser was used for repump and an acousto-optic modulator was introduced to gate the cw laser. Figure 7.9c shows the repeated PLE spectra with repump and the repump pulses were applied only when no PLE signal detected. The repump pulses not only restored the NV^- centres' charged state but also ionized the other defects in the vicinity of the NV^- centre, leading to change the local electric field and shift the transition energy of the NV^- centre by about 70 MHz via the Stark effect in Figure 7.9c[63]. Such spectral jumping can be reduced by using 575 nm laser for repump[7, 12], or corrected using dynamic

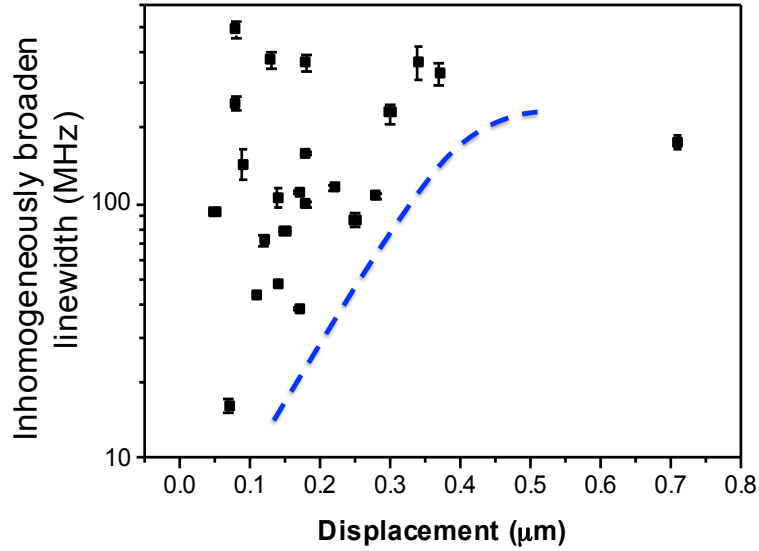


FIGURE 7.11: A semilogarithmic scatter plot of the inhomogeneously broadened linewidths from sample B as a function of their displacements from the initial laser writing position. The dashed blue line is a guide showing a trend to larger inhomogeneously broadened linewidth with larger displacement.

stabilization techniques[134].

Figure 7.9d shows the linewidths of all measured NV^- centres as a function of laser pulse energy. Although the linewidths distribute across a wide range for each laser energy setting, the narrowest single-scan linewidth measured for each laser pulse energy increases systematically with laser pulse energy, indicated by the dashed blue lines in Figure 7.9d. This systematic trend suggests that the residual defects degrade the coherent properties of the optical transition, resulting in broadening the homogeneous linewidth at progressively higher laser pulse energy. Although the ZPL linewidths of the measured NV^- centres in sample A are much broader than those in sample B, Figure 7.9d shows that the linewidths from sample A follow the systemic trend inferred from sample B, implying that the data set of sample A is just a subset of sample B.

Figure 7.11 shows a scatter plot of the inhomogeneously broaden linewidths (including spectral jumping) from sample B as a function of their displacements. According to the model described in Section 6.2, the greatest lattice damage should occur near to the centre of the laser focus, suggesting that the inhomogeneously broaden linewidths should decrease as the displacements increase. However, Figure 7.11 shows a weak positive correlation between the inhomogeneously broaden linewidths and their displacements. It is surprising that the weak correlation in experimental results is not consistent with the simple model. This trend may be because the local structure in the centre of the laser damage may be restored by introducing vacancies and subsequent annealing. In the centre of the laser-induced damage, the local structure is modified due to the creation of vacancies. During annealing, those vacancies recombine with interstitial carbon defects and hence the local structure is recovered to the pristine diamond structure. Therefore, there is an opportunity for a better lattice structure to form and reducing the local strain in the starting materials.

On the other hand, away from the centre of damage, little damage was generated, so the degree of reshuffling the local structure is much smaller. Thus, stronger local strain in the starting materials will be left after annealing. The local strain in the starting materials has to be considered and should be the dominant effect of linewidth broadening for the NV^- centres with displacement greater than 100 nm, which is the estimated size of damage (see Section 6.2). Thus, the wide range of the linewidth for each displacement may be due to the local strain in the starting materials. The broader linewidths in sample A can be explained by the strain field

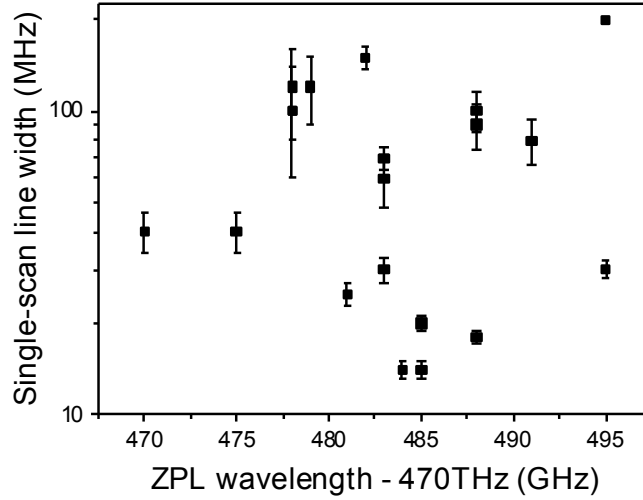


FIGURE 7.12: A semilogarithmic scatter plot of the single-scan linewidths from sample B as a function of their ZPL wavelength.

in the starting material being stronger in sample A than it is in sample B.

The longitudinal strain field shifts and broadens the wavelength of the ZPL[11], so the relative strength of the longitudinal strain may be worked out by investigating the correlation between the ZPL wavelength and the linewidth. Figure 7.12 shows a semilogarithmic scatter plot of the single-scan linewidths of the NV^- centres from sample B as a function of their ZPL wavelength. Note that the values of ZPL wavelength in Figure 7.12 have been subtracted by 470 THz for simplification and all the ZPL wavelength values mentioned in the rest of this thesis also follow this convention. The ZPL wavelength of narrowest single-scan linewidth (NV3) is at around 485 GHz. There is a trend that the single-scan linewidths increase as the ZPL wavelengths are either longer or shorter than 485 GHz. The trend suggests that the longitudinal strain field broadens the linewidth and shifts the wavelength of ZPL, which agrees with the theoretical calculation in [11]. The NV^- centres with transform-limited linewidth should experience very little longitudinal strain field (see Section 3.4.4.2), suggesting that the unshifted ZPL wavelength should

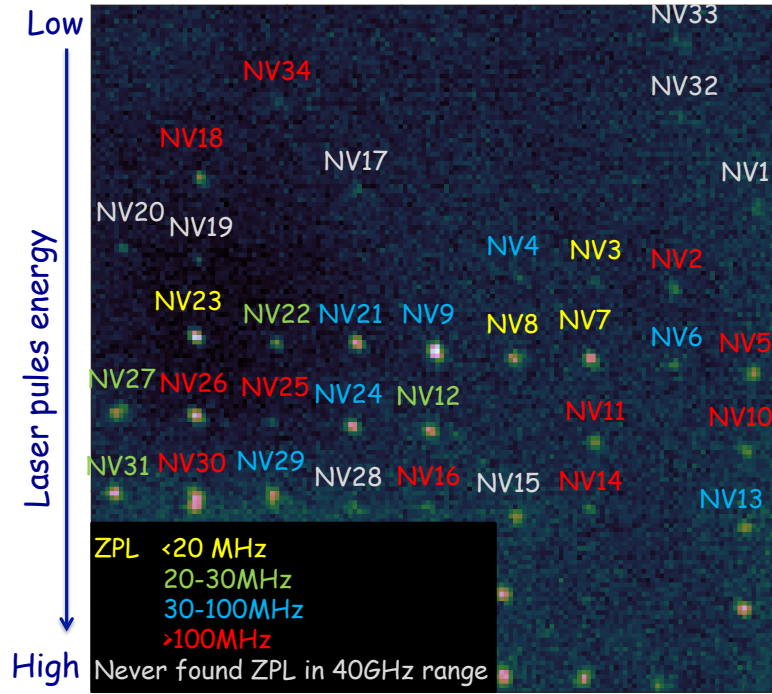


FIGURE 7.13: Map of the single-scan linewidths of the measured NV^- centres in sample B. The laser pulse energy decreases from the bottom to the top of the image.

be at around 485 GHz. The wide range distribution of single-scan linewidths for each ZPL position may be due to the transverse strain field, but it needs more experiments to prove the hypothesis.

The other evidence which suggests that the strain field in starting material is dominant effect is the spatial distribution of the single-scan linewidths. Figure 7.13 shows a map of the single-scan linewidths of the measured NV^- centres in sample B. The yellow labels indicate the NV^- centres with linewidths narrower than 20 MHz, the green labels indicate the NV^- centres with linewidths between 20 and 30 MHz, the blue labels indicate the NV^- centres with linewidths between 30 and 100 MHz and the red labels indicate the NV^- centres with linewidths greater than 100 MHz. The ZPLs of some measured NV^- centres were not observed within 40 GHz resonance excitation scanning range, labeled in grey. The ZPLs of them

may be outside the 40 GHz, or they may be too weak to be detected. Note that the laser writing energy decrease from the bottom to the top in Figure 7.13. Three of the NV^- centres with linewidths narrower than 20 MHz appear next to each other and most of the NV^- centres with linewidths between 30 and 100 MHz line up as straight line. The single-scan linewidths show some degrees of area dependence. This area dependence may indicate that the broadening of ZPL linewidth is because of the strain field in starting material. However, the possibility of the laser-induced strain is not completely ruled out; therefore, further strain investigations are needed.

The broader homogeneous linewidth implies dephasing in the excited state. NV^- centres with transform-limited optical transitions are important for quantum computing, as the transform-limited optical transition is required to generate indistinguishable photons with highest efficiency. To the best of my knowledge, there is only one natural diamond sample that has native NV^- centres with transform-limited ZPL (13 MHz)[63] and the NV^- centres with nearly transform-limited ZPL linewidth of 16 MHz were found in a single diamond nanocrystal[135]. However, for many quantum applications generating the NV^- centres with transform-limited optical transition at particular position with high spatial accuracy is essential. Although many groups have made great efforts to artificially create the NV^- centres with coherent optical transition by ion-implantation, the narrowest inhomogeneously broaden linewidth from repeated scans reported is still twofold larger (27 MHz) than transform-limited linewidth[7]. We are the first group who artificially generate the NV^- centres with transform-limited linewidth.

The residual defects are widely believed to be the reason for both shortening T_2 coherence time and broadening ZPL linewidth. Electrons may be trapped by the residual defects such as vacancies. These electrons in trap site not only generate fluctuating electric fields which increase the ZPL linewidths but also have spins which flip randomly and increasing spin dephasing rate of the NV^- centres via flip-flop mechanism. Thus, the NV^- centre with long T_2 time is expected to have narrow ZPL linewidth. However, no experimental or theoretical studies report the correlation between the T_2 coherence time and ZPL linewidth. The T_2 time of NV22 (greater than 100 μs) is much longer than the value of NV3 (34 μs), but the line width of NV22 (25 MHz) is broader than the line width of NV3 (13 MHz). In general, no correlation between the ZPL linewidth and T_2 coherence time is observed in this work. The shortening of T_2 coherence time is due to the spin coupling between the NV^- centre and defects, while the broadening of the ZPL linewidth is because of the electric fluctuation generated by the defects. Thus, it is not necessary that T_2 times of NV^- centres is strong correlated to their ZPL linewidth. As mentioned before, the T_2 measurements require very long time to complete due to the low counts rate, so only a few laser-generated NV^- centres were performed T_2 measurements. In addition, for those NV^- centres experience strong strain, the T_2 coherence times can not be measured, because the hyperfine structure can not be resolved (see Section 7.2.1). Therefore, only a few NV^- centres were performed both T_2 and PLE measurements.

7.4 Summary

This chapter discusses the coherent properties of the laser-generated NV^- centres to demonstrate that the laser writing could be a good method to generate the NV^- centres for most quantum applications. First, cw ODMR was used to investigate the spin coherence properties of the laser-generated NV^- centres. The hyperfine structure of most NV^- centres can be resolved and the hyperfine structure of them contains three dips with separation of 2.2 MHz, indicating that it is due to ^{14}N hyperfine interaction. The cw ODMR measurements show that the NV^- centres above GR1 visibility threshold experience strong localized strain field. The local strain field is highly likely to be generated by the laser writing pulse. Thus, the NV^- centres above the GR1 visibility threshold is not of interest for many quantum applications.

Hahn echo measurements were conducted on four NV^- centres in sample A and two NV^- centres in sample B at the laser writing energy well below the GR1 visibility threshold. The T_2 times vary from 30 to 80 μs and two NV^- centres possess relatively long T_2 times, longer than 100 μs . These T_2 times are shorter than the value of the ion-implanted NV^- centres in literature. The short T_2 may be due to the residual defects.

PLE was used to measure the linewidth of ZPL at 4.2 K because the resolution of our spectrometer is not high enough to resolve the linewidth of ZPL. The single-scan linewidths in sample A are between 60 and 165 MHz and the single-scan linewidths in sample B vary from 12 to 200 MHz. The single-scan linewidths of

NV3 and NV8 in sample B are 13.5 MHz and 12 MHz and the lifetime measurement at 4.2 K proves that these narrow linewidths are transform-limited. The inhomogeneously broadened linewidth of NV3 without repump is measured to be 16.1 MHz and the spectral jumping of NV3 due to repump is about 70 MHz. We are the first group who artificially generate the NV^- centres with transform-limited linewidth in the world.

The narrowest linewidth for each laser writing energy setting increases as the laser writing energy increases, indicating that the laser writing pulses and subsequent annealing generate local strain. This laser-induced local strain broadens the linewidths of the NV^- centre. Thus, for laser writing energy lower than 21 nJ which was used to generate NV8, there should not be any laser-induced strain field. However, the wide range distribution of the linewidths for a given laser writing energy and the correlation between displacement and inhomogeneously broadened linewidth may suggest that the strain field existing in the starting materials contributes more to the broadening of ZPL linewidths. The correlation between the ZPL wavelength and the linewidth supports the theory that the longitudinal strain broadens the linewidth, and wide range distribution of the linewidths for a given ZPL wavelength may be due to the transverse strain field. More information about transverse strain field is required. The linewidths of the measured NV^- centres show some degree of area dependence and this area dependence may be the other evidence that the strain field in starting material is the dominant effect.

Chapter 8

Strain Environment of Laser Written NV Centres

The previous chapter has investigated the coherent properties of the laser-generated NV⁻ centres. Although a few NV⁻ centres show transform-limited optical transition, the linewidths of half of the measured NV⁻ centres are greater than 100 MHz. The broad linewidths of the ZPL are due to a local strain field. However, local strain could either be generated by laser writing pulses or exist in the starting material. In order to determine which is the dominant effect, a detailed strain investigation is needed. This chapter will discuss three different methods used to measure the strain field, which are cross polarization, Raman mapping and photoluminescence excitation (PLE) strain measurements.

The cross polarization and Raman mapping measurements were performed by

Shazeaa Ishmael and Ben Green in University of Warwick. The PLE strain measurements were conducted by myself.

8.1 Cross polarization

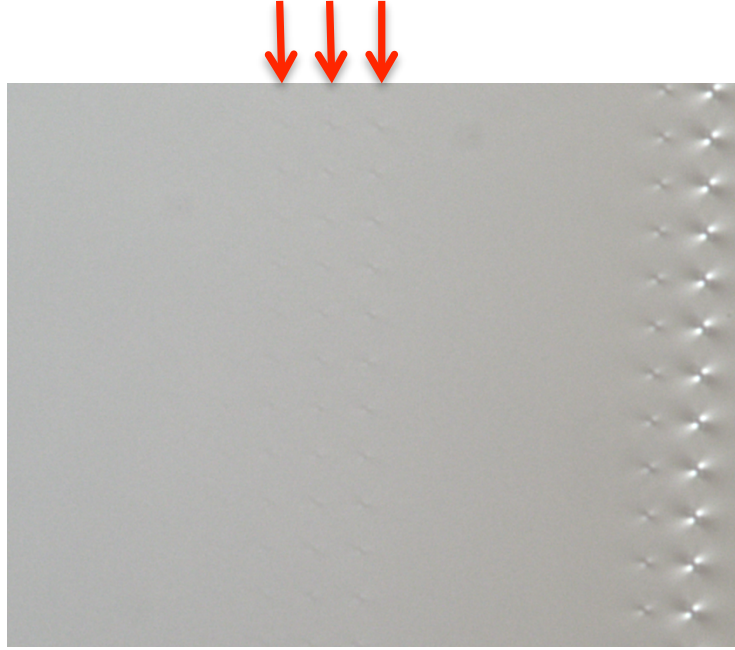


FIGURE 8.1: *Birefringence image of sample B measured using orthogonal linear polarizers. Red arrows indicate the locations of the rows of features created by the three highest writing pulse energies in the main array.*

Cross polarization is the simplest method to measure the strain map in the diamond. The cross polarization method records an optical birefringence image by sandwiching the diamond sample with orthogonal linear polarizers and measuring the transmitted broadband light. Figure 8.1 shows the birefringence image of sample B. Two test rows on the right hand side of Figure 8.1, which were generated with laser writing pulse energies in excess of 100 nJ, are clearly seen. Toward the centre of the image, three rows in the main array are visible, corresponding to the highest laser pulse energies of 60 ~ 75 nJ. No birefringence is observed at the

sites fabricated with laser energies lower than 60 nJ. In addition, no background birefringence pattern is observed within the array region, indicating that the strain field in the starting material is weak.

Although the cross polarization method is a good starting approach of strain measurements, the sensitivity of this method is poor. The magnitude of the birefringence along the light propagation direction needs to be large enough to generate a visible difference in transmitted brightness. Thus, even though the local strain is strong, the birefringence may not be observed due to the small size of the features. Considering that the size of the laser-induced features are smaller than 500 nm, the cross polarization method may not be a good method to measure the local strain. Therefore, Raman mapping was used to investigate the sample B, because it should provide a higher sensitivity to the local strain.

8.2 Raman mapping

The Raman mapping method is to record the first order Raman line of every scanning point and plot the differences of the peak width, position and magnitude between the Raman spectra of the measured points and bare diamond. The Raman spectra of the first order line at around 1332 cm^{-1} were obtained by shining a 532 nm excitation source and dispersing with a 2400 lines/mm grating. Figure 8.2 shows the Raman mapping results of sample B. Figures 8.2a, c and d show the colourscale maps of the width, position and height of the first order Raman peak

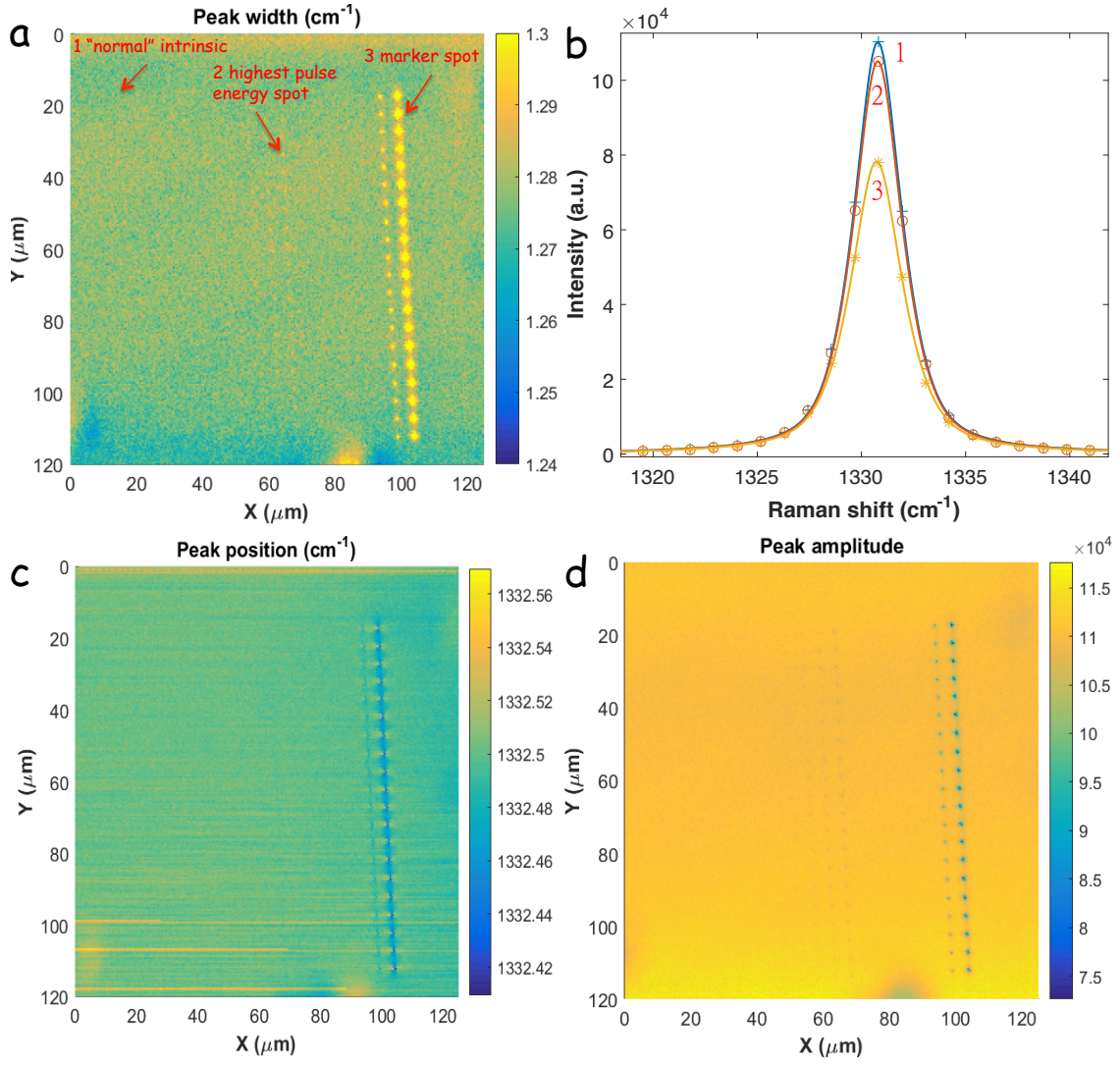


FIGURE 8.2: **a**, Colourscale map of the width of the first order Raman peak. **b**, Example fits of the pseudo-Voigt function for the three points labelled in plot **a**. **c** and **d** are maps of the Raman peak position and peak amplitude obtained from the fits.

and Figure 8.2b shows the examples of the Raman peak for three different points labelled in Figure 8.2a. The peaks were fitted with a pseudo-Voigt function

$$y(x) = A\left\{(1 - \eta)\exp(-\ln(2)\left(\frac{x - x_0}{\sigma}\right)^2) + \frac{\eta}{1 + \left(\frac{x - x_0}{\sigma}\right)^2}\right\} + c, \quad (8.1)$$

where η is the degree of Lorentzian-Gaussian character, x_0 is the peak position and σ is the linewidth. The blue Raman spectrum in Figure 8.2b was taken from

the bare diamond (outside the laser fabrication region), indicating the first order Raman line of pristine diamond. The red Raman spectrum in Figure 8.2b was obtained from the laser-induced feature generated by laser energy of 75 nJ and the yellow Raman spectrum in Figure 8.2b was taken from the laser-induced feature generated by laser energy in excess of 100 nJ. The height of the Raman peak decreases with an increase of the laser writing energy and the width of the Raman line increases with the laser writing energy. Although the high laser writing energy causes blue shift, the shift of the peak position of the Raman line is not significant. Therefore, the first three rows in the main array were not observed in Figure 8.2c.

The Raman results are similar to the cross polarization results and only the first three rows in the main array show changes in their Raman peaks due to the laser-induced strain field. Note that the positional shift of the Raman line is not obvious, but on the other hand the changes in peak height and width are more sensitive to the strain field. The measured broadening in peak linewidth can be used to estimate the local stress induced by the laser writing pulses. A conservative assumption was made that the change in linewidth is due to the slowest-splitting component ([001], upper bound) for which $\Delta\omega = 0.73 \pm 0.1 \text{ cm}^{-1} \text{ GPa}^{-1}$. The broadening of the linewidth was observed to be about 0.01 cm^{-1} for pulse energies of 60 - 75 nJ, suggesting that the residual strain field is about 13.7 MPa. This value is a conservative upper limit of the laser-induced strain field after an anneal at 1000°C for three hours. Based on the fluorescence intensity of the GR1 centres, the residual strain field could be two orders of magnitude smaller at the laser pulse energy below 20 nJ.

Although the cross polarization and Raman mapping methods show that local strain was observed in the first three rows in the main array due to the laser writing pulse, the magnitude and origin of the strain at the laser writing energies which generate single NV^- centres can not be measured by these two methods. Such laser writing energies are much lower than 60 nJ, so the upper limit of the local strain does not provide too much information. Thus, another approach which is much more sensitive to local strain field is needed.

8.3 Photoluminescence excitation

The cross polarization and Raman mapping methods are not sensitive enough to measure the strain field at the laser pulse energies generating single NV^- centres. However, the degenerate electronic states of the NV^- centre will be split due to the transverse strain field which can be used to measure local strain. The excited states of the NV^- centre are more sensitive to strain field than the ground states. Recording the strain-induced splitting of the ZPL is the best approach to measure the local strain in the vicinity of the NV^- centres. The theory of the electronic structure and strain-induced splitting of the NV^- centre excited state have been discussed in Section [3.4.2](#).

8.3.1 PLE strain measurement results

In order to identify the origin of local strain, the PLE strain measurements were carried out on a selection of NV^- centres the linewidths of which had been measured. The detail of the PLE experiments are found in Section 4.6.2. Figure 8.3 shows the full PLE spectra of five NV^- centres without detectable strain splitting and Figure 8.4 shows the full PLE spectra of six NV^- centres with strain splitting. The positions of the PLE lines were obtained by fitting with a Gaussian function. In order to assign the corresponding excited states to each of the PLE lines, the transition lines of E_x and E_y were firstly identified. The transition lines of E_x and E_y were identified by taking a PLE spectrum without laser modulation, because the PLE lines of $E_{1,2}$, $A_{1,2}$ and the $E_{x,y}$ side peaks disappeared after switching off the EOM, as described in Section 4.6.2. Then, the E_x and E_y side peaks can be easily assigned by adding or subtracting 2.87 GHz to the main E_x and E_y peak positions. The rest of the PLE lines were labelled by comparing their separations from the main E_x PLE line with theoretical predictions, described in Section 3.4.2. The A_2 transitions are not observed in all measured NV^- centres and it may be because these transitions are relatively weaker than other transitions.

The theory predicts that the energy difference between E_x and $E_{1,2}$ states is about 4.1 GHz[11, 65]. In the PLE spectrum, the separation between the main E_x line and the $E_{1,2}$ line with higher energy represents the energy gap between these two states. The separations between E_x and $E_{1,2}$ lines in the PLE spectra of NV3 (Figure 8.3a) and NV31 (Figure 8.3e) are very similar to the theoretical value, whereas the two PLE lines with lowest energies in the spectra of NV4 (Figure

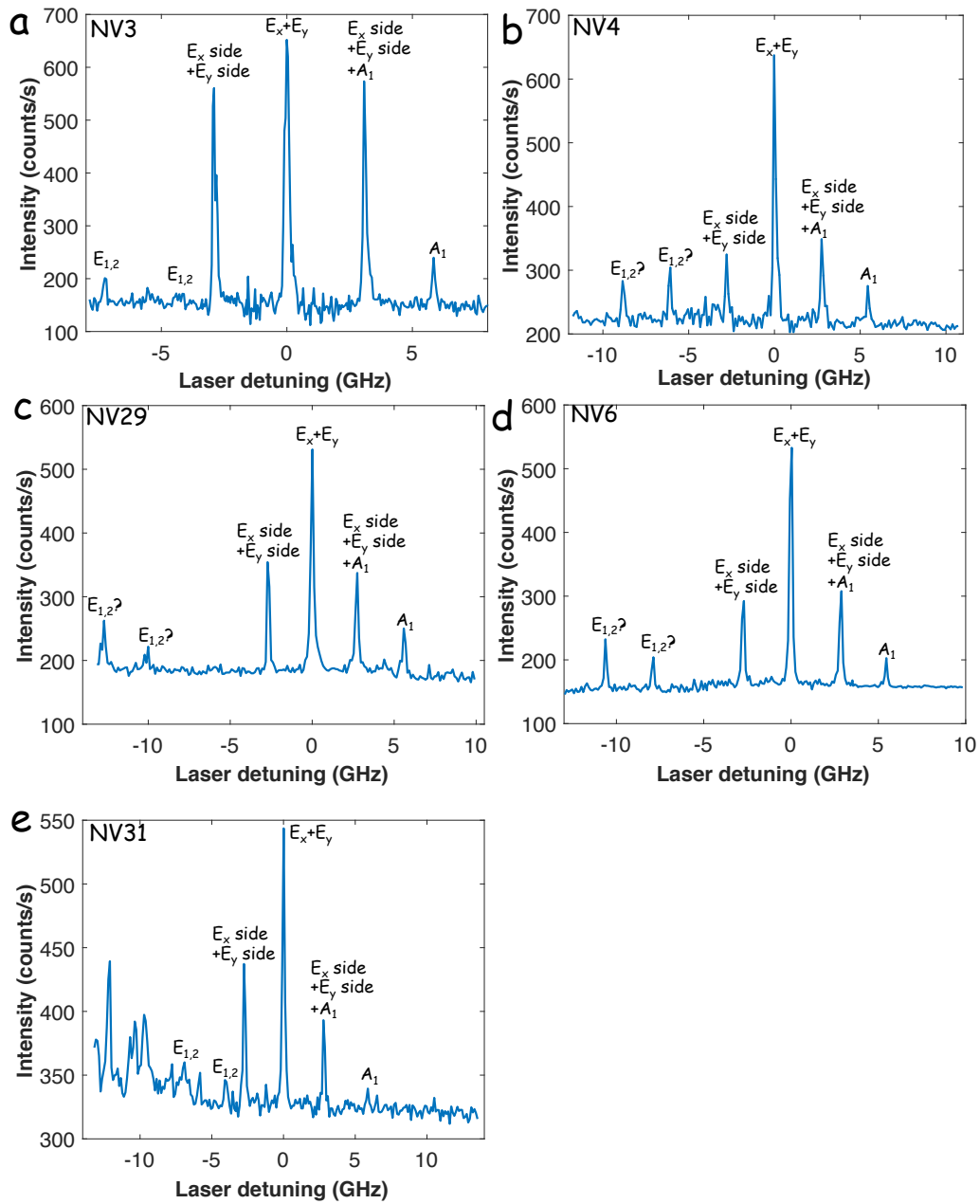


FIGURE 8.3: *Full PLE spectra of the NV^- centres without detectable strain field. a, NV3. b, NV4. c, NV29. d, NV6. e, NV31. NV31 is a double NV^- site and the PLE lines without labels in the low energy region are from the second NV^- centres. The question marks of the $E_{1,2}$ lines in b, c and d indicate that they are too far away from the theoretical value.*

8.3b), NV29 (Figure 8.3c) and NV6 (Figure 8.3d) have an too low energy to be considered as $E_{1,2}$ transitions, according to theory. The background noise is very low, so the $E_{1,2}$ lines should be observed. These two PLE lines with lowest energies in the spectra of NV4 and NV29 and NV6 should be the transitions of their $E_{1,2}$

Label	NV3	NV4	NV29	NV6	NV31
Linewidth (MHz)	13	70	80	60	30

TABLE 8.1: *The single-scan linewidths of the E_x transitions of NV3, NV4, NV29, NV6 and NV31.*

states.

Table 8.1 shows the summary of the single-scan linewidths of NV3, NV4, NV29, NV6 and NV31. The single-scan linewidths of NV4, NV29 and NV6 are about 70 MHz, whereas the single-scan linewidths of NV3 and NV31 are 13 MHz and 30 MHz respectively. The broader linewidths may suggest that the longitudinal strain causes the farther shift of the $E_{1,2}$ states transitions. However, Maze et al's calculation of excited state structure in the presence of strain using a group theory approach suggests that the longitudinal strain shift all excited states equally[11]. It is worth mentioning that the small splitting of main PLE lines of E_x and E_y states in NV3 and NV4 are due to the spectral jumping, caused by the 532 nm repump. The unlabelled PLE lines in the low energy region of NV31 spectrum (Figure 8.3e) belong to the second NV^- centres in this laser damage site. Although these 5 PLE spectra do not show any strain-induced splitting, it does not mean that these NV^- centres do not experience any transverse strain at all. The detection limit of this method depends on the linewidth of the measured transition line. Thus, if the strain-induced splitting is less than half of the linewidth, the splitting would not be resolved.

Figure 8.4 shows the PLE spectra of the NV^- centres with strain-induced splitting and the splitting between E_x and E_y states are given in the inset of each graph.

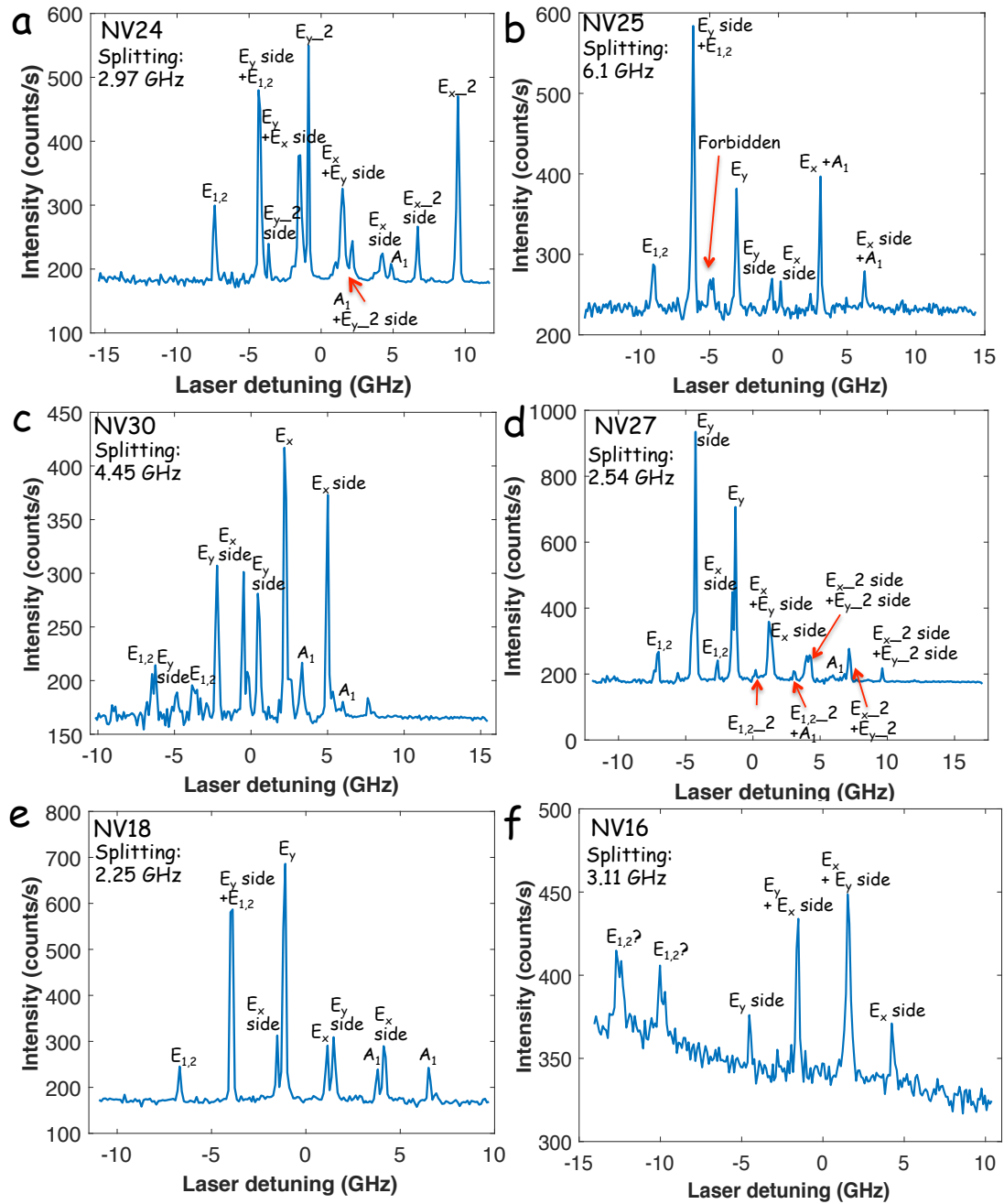


FIGURE 8.4: Full PLE spectra of the NV^- centres with detectable strain field and the splitting between E_x and E_y states are given in each graph. The PLE lines from the second NV^- centre are labelled with $_2$. **a**, NV24. **b**, NV25.

Forbidden means that the transition lines are from Fermi's golden rule forbidden transition. **c**, NV30. **d**, NV27. **e**, NV18. **f**, NV16.

According to theory, the magnitude of the transverse strain is equal to half of the splitting between E_x and E_y states. There are two NV^- centres per site at NV24 (Figure 8.4a) and NV27 (Figure 8.4d), so there are two sets of PLE lines and

the second set of PLE lines are labelled with adding $_2$ after the excited states' names. The strain-induced splittings are all greater than 2 GHz and NV25 (Figure 8.4e) experiences the strongest transverse strain, with a splitting of 6.1 GHz. In the spectrum of NV25 (Figure 8.4e), there are a few extra PLE lines between E_y and $E_{1,2}$ states and they may be attributed to the Fermi's golden rule forbidden transitions, compared with Figure 3.7. That means that they are the optical transition lines from the E_y to $m_s = \pm 1$ ground states or from the $E_{1,2}$ to $m_s = 0$ ground state[136]. It is not clear why the forbidden transition lines were observed only in the spectra of NV25. One suggestion is that the forbidden transition lines can only be seen under strong transverse strain. The strong transverse strain may break the NV centres' symmetry and the overlapping of electron wave functions between $m_s = 0$ and ± 1 states may increase, resulting in higher probability of forbidden transitions.

8.3.2 Comparison of the strain splitting with theory

The theory of the electronic structure and strain-induced splitting of the NV^- centre excited state have been outlined in detail in the Section 3.4.2. The Hamiltonian of the excited state under strain can be expressed as Equation 3.19. The eigenvalues of the excited state triplet as a function of δ_x strain can be reproduced by diagonalizing Equation 3.19, shown as solid lines in Figure 8.5.

The PLE lines positions of all measured NV^- centres are compared with the theory to gain more insight into the local strain. Figure 8.5 shows the excited state structure as a function of the transverse strain for 7 measured NV^- centres. Here, 6

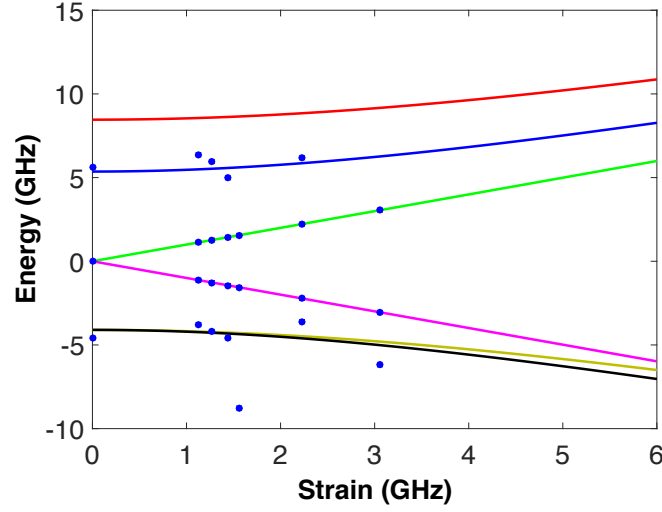


FIGURE 8.5: *Excited state energy structure as a function of the transverse strain for 7 measured NV⁻ centres. The data sets of the 7 NV⁻ centres were labelled by blue circles. The solid lines are the eigenvalues of excited states from theory. The red line is A_2 state, the blue line is A_1 state, the green line is E_x state, the pink line is the E_y state, the yellow line is E_1 state and the black line is E_2 state.*

NV⁻ centres with strain-induced splitting and the NV3 (without detectable strain-induced splitting) are plotted in the Figure 8.5. The errors of the PLE peaks positions, given by the Gaussian function fitting, are all smaller than 50 MHz, but the data bin of the PLE scan is about 110 MHz. Thus, the error of the data set is mainly from the data bin of the PLE scan (110 MHz) which is similar to the size of the data point in Figure 8.5. Because the values of transverse strain were obtained from the splitting between E_x and E_y states, so all E_x and E_y PLE signals perfectly match with the theoretical lines.

Most of the measured NV⁻ centres match well with the theoretical predictions, apart from the $E_{1,2}$ state of NV16 (strain = 1.55 GHz). Here, the linewidth of NV16 is broadest (~ 200 MHz) amongst all of the measured NV⁻ centres, so the big deviation of the $E_{1,2}$ state from the theoretical value may be due to the strong longitudinal strain.

Label	NV24	NV25	NV30	NV27	NV18	NV16
Splitting (GHz)	2.97	6.1	4.45	2.54	2.25	3.11
Stress (MPa)	2.96	6.06	4.43	2.53	2.24	3.1

TABLE 8.2: *The strain-induced splitting and local stress of NV24, NV25, NV30, NV27, NV18 and NV16. The local stresses are estimated using Equation 3.20.*

The local stress in the vicinity of the measured NV^- centres can be estimated from the splitting between E_x and E_y states by using Equation 3.20. In order to compare the magnitude of residual stress estimated from Raman mapping results in Section 8.2, assuming that the strain splitting is generated by the stress along [001] crystal direction. Table 8.2 shows the summary of the estimated local stress of NV24, NV25, NV30, NV27, NV18 and NV16. The magnitude of this stress is, in general, three to four times lower than in the first three high-damage rows of the array (13.7 MPa), as shown in Section 8.2.

8.3.3 Linewidth and strain splitting

In the PLE spectrum of NV27 there are two sets of PLE lines attributed to two different NV^- centres in the focus as shown in Figure 8.4d. The first NV^- centre has the strain-induced splitting of 2.54 GHz and the linewidth of the main E_x transition is about 150 MHz. On the other hand, the second NV^- centre does not show any splitting and the linewidth of the E_x state is about 20 MHz. These show an interesting correlation between the magnitude of the transverse strain and the linewidth of the E_x state. Thus, it is worth investigating the correlations between the strain-induced splitting and all other parameters for all measured NV^- centres.

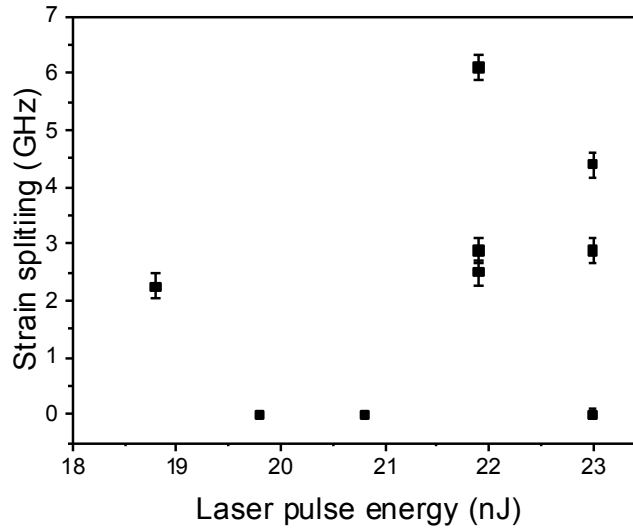


FIGURE 8.6: *Scatter plot of the strain-induced PLE splitting as a function of the laser writing pulse energy.*

First of all, the influence of the laser writing energy on the strain-induced splitting was investigated. Figure 8.6 shows a scatter plot of the strain-induced splitting between E_x and E_y states as a function of laser writing pulse energy. Although the NV^- centres generated by higher laser pulse energies tend to experience stronger strain, the NV^- centre generated by laser pulse energy of 18.8 nJ also has strain-induced splitting of 2.24 GHz. The splittings show a wide distribution for a given laser pulse energy. The laser pulses with high energy can generate stronger transverse strain fields, but there are other effects contributing to the transverse strain field, as well.

Figure 8.7 shows a scatter plot of the strain-induced splitting as a function of their linewidths. It is clear that if the linewidth is broader than 100 MHz, the strain-induced splitting seems to be greater than 2 GHz. Most of the NV^- centres with linewidth less than 100 MHz do not show any detectable strain-induced splitting in the PLE spectra, except NV30. This correlation indicates that the transverse strain field causes the broadening of the linewidth of the ZPL. The linewidth is not

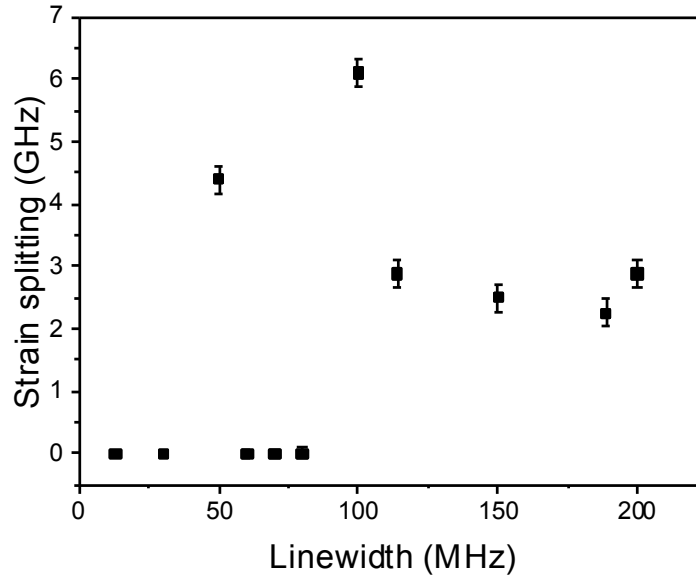


FIGURE 8.7: *Scatter plot of the strain-induced PLE splitting as a function of the linewidth of E_x PLE line.*

linearly proportional to the transverse strain because the NV^- centres may experience different magnitudes of longitudinal strain field. To have a full understanding of the broadening of the ZPL, the longitudinal and transverse strains need to be considered together.

Figure 8.8a shows the scatter plot of the strain-induced splitting as a function of the ZPL position. Here, I assume that the shift of the ZPL wavelength is purely due to the longitudinal strain field and NV3 experiences the weakest longitudinal strain because of the lifetime-limited linewidth. The ZPL position of NV3 is at 485 GHz. When the ZPL positions of the NV^- centres are farther away from 485 GHz, their strain-induced splittings are more likely to be greater than 2 GHz. Therefore, if the NV^- centres experience strong longitudinal strain, they are likely to experience strong transverse strain, as well. In Section 7.3.2, it has been mentioned that the longitudinal strain can not explain why the linewidths span a wide range for a given ZPL position. Figure 8.8b shows a scatter plot of the linewidth as a function

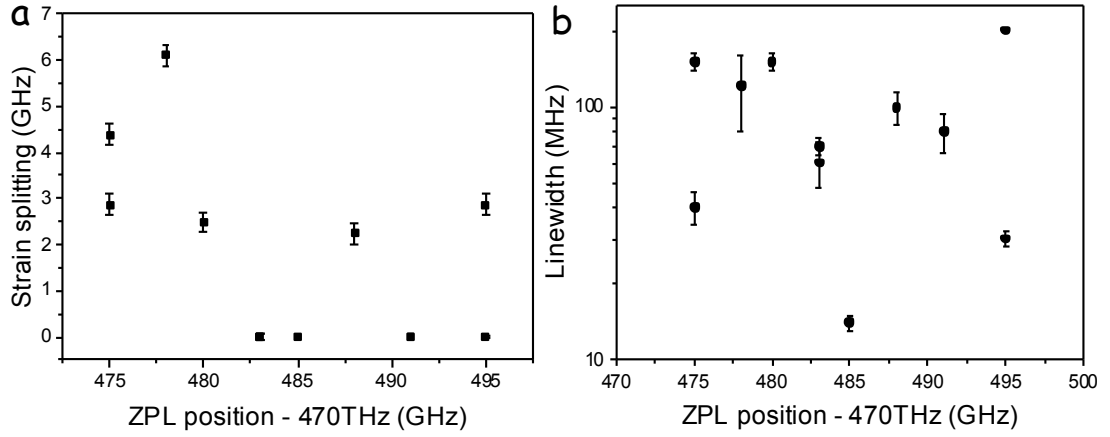


FIGURE 8.8: **a**, Scatter plot of the strain-induced splitting as a function of the ZPL position. **b**, Scatter plot of the line width of ZPL as a function of the ZPL position.

of the ZPL position for each of the 11 NV^- centres in the strain measurements. Comparing Figure 8.8a and b, the possible explanation for the wide distribution of ZPL linewidth for a given ZPL position (same longitudinal strain) may be because they experience different magnitudes of transverse strain field (strain-induced splittings).

Although a correlation between the longitudinal and transverse strains is observed, it does not give more insight about the origin of the strain. However, as mentioned in Section 7.3.2, the spatial distribution of the linewidth of the ZPL shows an area dependence, indicating that the strain in the starting materials is the dominant effect.

8.4 Summary

This chapter has discussed three different approaches to measure the strain around the laser-generated NV^- centres. First, the cross polarization method was used to

record the 2D birefringence image of the laser-induced array after annealing. Only the damage features, generated with laser writing pulse energies of greater than 60 nJ, showed detectable birefringence. These suggest that the laser writing pulses with high energy generates localized strain in the diamond and the magnitude of the strain decrease with laser energy. The Raman mapping method was introduced to measure the magnitude of the strain and the results are similar to that of the cross polarization method. The estimated upper limit of the residual stress in the rows generated with laser writing pulse energy above 60 nJ is 13.7 MPa.

The cross polarization and Raman mapping methods are not sensitive enough to measure the strain in the low laser writing energy region. Thus, PLE strain measurements were carried out on the NV^- centres the linewidths of which were measured. Half of the measured NV^- centres do not show detectable strain-induced splitting in the PLE spectra and the other half of them show splittings greater than 2 GHz in their PLE spectra, corresponding to the stress of greater than 2 MPa. The energies of the PLE lines of most of the measured NV^- centres can be well described by the theory. However, the $E_{1,2}$ transition lines of some NV^- centres shift further to lower energy, which may be due to larger longitudinal strain field.

The scatter plot of the strain splitting as a function of the laser writing pulse energy shows a trend that the strain-induced splitting increases with the laser writing pulse energy. In addition, the NV^- centres generated with the lowest laser pulse energy shows large strain-induced splitting, suggesting that the strain in the starting material can not be neglected. There is a correlation between the strain splitting and linewidth of the E_x PLE lines. If the linewidth is greater

than 100 MHz, over 2 GHz splitting is likely to be observed in the PLE spectra. On the contrary, if the linewidth is smaller than 100 MHz, there is no detectable strain-induced splitting in PLE spectra of most NV^- centres, except NV30.

A correlation is seen by comparing the transverse strain (strain splitting) with the longitudinal strain (ZPL position) for each of the measured NV^- centres. If both transverse and longitudinal strains are considered, the wide range distribution of the linewidth for a given ZPL wavelength can be explained, suggesting both transverse and longitudinal strains broaden the linewidth. Although there are some strong correlations between the strain-induced splitting and other parameters, they do not provide more insight to the origin of the strain. However, the area dependence of the linewidth suggests that the strain field in the starting materials is the dominant effect which is consistent with the results of strain measurements.

Chapter 9

Conclusion & Outlook

This section will summarize the important experimental and theoretical results, and the future prospects for this works.

9.1 Conclusion

This thesis has demonstrated that the femtosecond laser writing of vacancies into diamond can be used to produce optically coherent NV^- colour centres at desired locations. The laser writing apparatus has been presented. Aberration correction is achieved using an adaptive optics, and has been shown to be important for high positioning accuracy. The PL spectra show that the laser-induced damage is GR1 centres. Various annealing conditions have been applied on the samples to generate the NV^- centres. Among all of the annealing conditions, three hours annealing at 1000°C was found to be the best condition to generate single NV^- centres without optically detectable residual defects when the laser writing energy is below GR1

visibility. All the laser-generated NV centres are in negative charged state. The total number of the NV⁻ centres among 20 repeats increases with the laser pulse energy, implying that the number of the NV⁻ centres can be controlled by adjusting the laser pulse energy. The spatial map of the NV⁻ centres number per site shows some area dependence, indicating that the concentration of nitrogen is not uniform across the laser fabrication regime. The highest probability of generating single NV⁻ centres is found to be 45% at a laser energy of 25.7 nJ. Similar laser writing energy ranges and annealing have been performed on a second diamond sample, with similar results to the first sample, showing the reproducibility of the method. The lifetime of the laser-generated NV⁻ centre is measured to be about 12.1 ns which is comparable to the lifetime of the native NV⁻ centre in the same diamond.

Some theoretical analyses have been performed on the experimental results to gain more insights into the mechanism of the generation of vacancies and the subsequent NV⁻ centres. The Keldysh parameter[94] predicts that the Multiphoton Ionization (MPI) is the dominant mechanism as the laser pulse energy is below 25 nJ. Both MPI and tunneling ionization models have been used to fit the experimental results. The MPI model provides a better fit than the tunneling ionization model does, implying that MPI dominates the mechanism of laser writing of vacancies. The fit result of MPI also suggests that 15 photons are involved in vacancy creation; however, the recent work of Lagomarsino[96] concludes that the laser writing of vacancies in diamond is 9-photon absorption process. Both 9-photon and 15-photon absorption processes were considered in the rest analyses. For a 9-photon process, an estimate of 7.1×10^6 vacancies were generated at the GR1 visibility

threshold and about 10^5 were created at the lowest laser energies required to generate the NV^- centres. For the 15-photon case, 8.5×10^5 vacancies were created at GR1 visibility threshold and approximately 10^3 were produced at the lowest laser energies needed to generate the NV^- centres. The positioning accuracy of the laser-generated NV^- on the image plane is measured to be about 200 nm, giving a diffusivity value of $3.7 \times 10^{-14} \text{ cm}^2 \text{ s}^{-1}$. A simple model was established to estimate the probability of generating the NV^- centres per site. The probability of generating the NV^- centre per site is measured to be 1 in sample A and 0.75 in sample B. For the 9-photon absorption process, the theoretical expectation value of the number of the NV^- centres per site is 12000 which is much higher than the experimental results. On the other hand, the theoretical expectation value for 15-photon process is 1450 which is still higher than the experimental results.

The ^{14}N hyperfine structure of the most NV^- centres can be resolved in cw ODMR spectra. The T_2 times of the laser-generated NV^- centres vary between 30 and 80 μs . Two centres show a T_2 time greater than 100 μs . The ZPL linewidths were measured to be from 12 to 200 MHz. Three NV^- centres show narrow single-scan linewidth of about 12 MHz, which is the transform-limited linewidth for an NV^- centre in bulk diamond based on its lifetime. The NV^- centres with transform-limited optical transition have never been generated by current NV^- engineering methodologies. The narrowest single-scan linewidth measured for each laser pulse energy increases systematically with laser pulse energy, implying that the progressively higher laser pulse energy broadens the linewidth. The wide distribution of linewidth for a given laser pulse energy may indicate that the strain field in starting

material also contributes to the broadening of linewidths. The spatial distribution of linewidths shows some area dependence, which also suggests that the strain in starting material has significant affect on the linewidth of NV⁻ centre's ZPL.

Cross polarization and Raman mapping can only measure the strain in the first three rows of the array due to low sensitivity. The Raman mapping method provides an estimated upper limit of the local stress in the rows generated with laser writing pulse above 60 nJ. The local stress was determined to be 13.7 MPa. The strain fields surrounding the NV⁻ centres at the laser pulse energy below GR1 visibility were measured by the PLE method. Out of 11 measured NV⁻ centres, 5 centres did not show a detectable strain-induced splitting and 6 centres showed large strain-induced splitting of greater than 2 GHz. The local stresses estimated from the PLE measurements vary from 2 to 6 MPa. These strain-induced splittings can be well described by the spin-Hamiltonian with transverse strain. The NV⁻ centres with ZPL linewidth broader than 100 MHz is likely to show large splittings in their PLE spectra. On the other hand, most of the NV⁻ centres with linewidth narrower than 100 MHz do not show detectable splitting, except one centre. This correlation indicates that the transverse strain also broadens the linewidth of ZPL. The wide distribution of the linewidths can be explained by considering both longitudinal and transverse strains.

9.2 Future prospects

The submicrometre positioning accuracy achieved in this work reaches the requirement for coupling NV⁻ centres to optical structures such as multimode waveguides and whispering gallery resonators[42], or place under solid immersion lenses[67]. However, the 200 nm and 1 μ m positioning accuracy in the image plane and longitudinal direction respectively are not sufficient for photonic crystal structures[32, 41, 43]. The presented in-plane accuracy is limited by the diffusion of the vacancies during annealing. Lower annealing temperature (800 \sim 900°C) can reduce the diffusion length of vacancies, but this temperature can not completely anneal out residual defects. Thus, high temperature anneal (1100 \sim 1200°C) following the lower temperature anneal is needed. In addition, this two-step annealing process needs to be applied on diamond with a higher nitrogen concentration, because the short diffusion length results in low probability of NV⁻ centres generation. The high positioning accuracy in depth may be achieved by performing laser writing of vacancies on the diamond with delta-doping of a thin nitrogen-rich layer[44, 86].

This recipe may also improve the T_2 time of the laser-generated NV⁻ centres, because the recipe may be able to create NV⁻ with lower laser pulse energy due to higher nitrogen concentration. In addition, the 1100 \sim 1200°C anneal may reduce the number of residual defects. Growing a thin boron-doped layer on top of the diamond sample can suppress the generation of divacancy during annealing, resulting in a longer T_2 time[137]. Although the laser writing method can generate the NV⁻ centres with coherent optical transition, the probability of success is not

high due to the strain in the starting material. Performing laser writing on the low strain diamond may increase this probability.

The adaptive optics used for aberration correction would also allow colour centres to be placed under a microstructure surface. The laser writing method can be used to generate NV^- centres with coherent optical transitions in diamond membranes, which can be coupled to open-cavity[71]. Beyond quantum photonic devices, the ability to write large and detailed 2D or 3D arrays of NV^- centres may be useful for the applications in magnetic field, electric field or temperature imaging systems[138]. The laser writing technique for NV^- centres could be readily applied in conjunction with the writing of subsurface waveguides[139, 140] and electrodes[141]. The laser writing technique can be used to generate other colour centres and point defects in other wide bandgap materials. For example, SiV and GeV show great potential in QIP applications[16, 142, 143], but SiV and GeV centres with transform-limited optical transitions are yet to be produced during diamond growth process or ion-implantation[142–144]. This laser writing technique may be able to create these colour centres with coherent optical transitions.

Bibliography

- [1] JR Weber, WF Koehl, JB Varley, A Janotti, BB Buckley, CG Van de Walle, and David D Awschalom. Quantum computing with defects. *Proceedings of the National Academy of Sciences*, 107(19):8513–8518, 2010.
- [2] Andrew Dzurak. Quantum computing: Diamond and silicon converge. *Nature*, 479(7371):47–48, 2011.
- [3] Rafael R Gattass and Eric Mazur. Femtosecond laser micromachining in transparent materials. *Nature photonics*, 2(4):219–225, 2008.
- [4] M. W. Doherty, N. B. Manson, P. Delaney, F. Jelezko, J. Wrachtrup, and L. C. L. Hollenberg. The nitrogen-vacancy colour centre in diamond. *Physics Reports*, 528(1):1–45, 2013.
- [5] Igor haronovich and Elke Neu. Diamond nanophotonics. *Advanced Optical Materials*, 2(10):911–928, 2014.
- [6] Sébastien Pezzagna, Dominik Wildanger, Paul Mazarov, Andreas D Wieck, Yanko Sarov, Ivo Rangelow, Boris Naydenov, Fedor Jelezko, Stefan W Hell, and Jan Meijer. Nanoscale engineering and optical addressing of single spins in diamond. *Small*, 6(19):2117–2121, 2010.

-
- [7] Y Chu, NP De Leon, BJ Shields, B Hausmann, R Evans, E Togan, MJ Burek, M Markham, A Stacey, AS Zibrov, A Yacoby, DJ Twitchen, M Loncar, H Park, P Maletinsky, and MD Lukin. Coherent optical transitions in implanted nitrogen vacancy centers. *Nano letters*, 14(4):1982–1986, 2014.
- [8] Chris B Schaffer, Andre Brodeur, and Eric Mazur. Laser-induced breakdown and damage in bulk transparent materials induced by tightly focused femtosecond laser pulses. *Measurement Science and Technology*, 12(11):1784, 2001.
- [9] L Rondin, G Dantelle, A Slablab, F Grosshans, F Treussart, P Bergonzo, S Perruchas, T Gacoin, M Chaigneau, H-C Chang, V Jacques, and J-F Roch. Surface-induced charge state conversion of nitrogen-vacancy defects in nanodiamonds. *Physical Review B*, 82(11):115449, 2010.
- [10] Sam Johnson. *The coupling of nitrogen-vacancy centres in diamond to tunable open-microcavities*. PhD thesis, University of Oxford, 2015.
- [11] JR Maze, Adam Gali, Emre Togan, Yiwen Chu, Alexei Trifonov, Efthimios Kaxiras, and MD Lukin. Properties of nitrogen-vacancy centers in diamond: the group theoretic approach. *New Journal of Physics*, 13(2):025025, 2011.
- [12] P Siyushev, H Pinto, M Vörös, A Gali, F Jelezko, and J Wrachtrup. Optically controlled switching of the charge state of a single nitrogen-vacancy center in diamond at cryogenic temperatures. *Physical review letters*, 110(16):167402, 2013.

-
- [13] K-MC Fu, Charles Santori, Paul E Barclay, Lachlan J Rogers, Neil B Manson, and Raymond G Beausoleil. Observation of the dynamic jahn-teller effect in the excited states of nitrogen-vacancy centers in diamond. *Phys. Rev. Lett.*, 103(25):256404, 2009.
- [14] F Jelezko and J Wrachtrup. Single defect centres in diamond: A review. *physica status solidi (a)*, 203(13):3207–3225, 2006.
- [15] D Riedel, F Fuchs, H Kraus, S V  th, A Sperlich, V Dyakonov, AA Solta-mova, PG Baranov, VA Ilyin, and GV Astakhov. Resonant addressing and manipulation of silicon vacancy qubits in silicon carbide. *Physical review letters*, 109(22):226402, 2012.
- [16] Jonas Nils Becker, Johannes G  rlitz, Carsten Arend, Matthew Markham, and Christoph Becher. Ultrafast all-optical coherent control of single silicon vacancy colour centres in diamond. *Nature Communications*, 7:13512, 2016.
- [17] HJ von Bardeleben, JL Cantin, E Rauls, and U Gerstmann. Identification and magneto-optical properties of the nv center in 4 h- sic. *Physical Review B*, 92(6):064104, 2015.
- [18] David J Christle, Abram L Falk, Paolo Andrich, Paul V Klimov, Jawad Ul Hassan, Nguyen T Son, Erik Janz  n, Takeshi Ohshima, and David D Awschalom. Isolated electron spins in silicon carbide with millisecond coherence times. *Nature materials*, 14(2):160–163, 2015.
- [19] Matthias Widmann, Sang-Yun Lee, Torsten Rendler, Nguyen Tien Son, Helmut Fedder, Seoyoung Paik, Li-Ping Yang, Nan Zhao, Sen Yang, Ian Booker,

- Andrej Denisenko, Mohammad Jamali, S Ali Momenzadeh, Ilija Gerhardt, Takeshi Ohshima, Adam Gali, Erik Janzén, and Jörg Wrachtrup. Coherent control of single spins in silicon carbide at room temperature. *Nature materials*, 14(2):164–168, 2015.
- [20] Igor Aharonovich, Dirk Englund, and Milos Toth. Solid-state single-photon emitters. *Nature Photonics*, 10(10):631–641, 2016.
- [21] Nicolas Gisin, Grégoire Ribordy, Wolfgang Tittel, and Hugo Zbinden. Quantum cryptography. *Reviews of modern physics*, 74(1):145, 2002.
- [22] Matthias Leifgen, Tim Schröder, Friedemann Gädeke, Robert Riemann, Valentin Métilon, Elke Neu, Christian Hepp, Carsten Arend, Christoph Becher, Kristian Lauritsen, and Oliver Benson. Evaluation of nitrogen-and silicon-vacancy defect centres as single photon sources in quantum key distribution. *New Journal of Physics*, 16(2):023021, 2014.
- [23] Alexios Beveratos, Rosa Brouri, Thierry Gacoin, André Villing, Jean-Philippe Poizat, and Philippe Grangier. Single photon quantum cryptography. *Physical review letters*, 89(18):187901, 2002.
- [24] Romain Alléaume, François Treussart, Gaëtan Messin, Yannick Dumeige, Jean-François Roch, Alexios Beveratos, Rosa Brouri-Tualle, Jean-Philippe Poizat, and Philippe Grangier. Experimental open-air quantum key distribution with a single-photon source. *New Journal of physics*, 6(1):92, 2004.
- [25] Sean D Barrett and Pieter Kok. Efficient high-fidelity quantum computation using matter qubits and linear optics. *Physical Review A*, 71(6):060310, 2005.

- [26] Simon C Benjamin, Brendon W Lovett, and Jason M Smith. Prospects for measurement-based quantum computing with solid state spins. *Laser & Photonics Reviews*, 3(6):556–574, 2009.
- [27] A. Batalov, C. Zierl, T. Gaebel, P. Neumann, I-Y Chan, G. Balasubramanian, P. R. Hemmer, F. Jelezko, and J. Wrachtrup. Temporal coherence of photons emitted by single nitrogen-vacancy defect centers in diamond using optical rabi-oscillations. *Physical review letters*, 100(7):077401, 2008.
- [28] Alp Sipahigil, Kay D Jahnke, Lachlan J Rogers, T Teraji, J Isoya, Alexander S Zibrov, Fedor Jelezko, and Mikhail D Lukin. Indistinguishable photons from separated silicon-vacancy centers in diamond. *Physical review letters*, 113(11):113602, 2014.
- [29] L Rondin, JP Tetienne, T Hingant, JF Roch, P Maletinsky, and V Jacques. Magnetometry with nitrogen-vacancy defects in diamond. *Reports on Progress in Physics*, 77(5):056503, 2014.
- [30] Florian Dolde, Helmut Fedder, Marcus W Doherty, Tobias Nöbauer, Florian Rempp, Gopalakrishnan Balasubramanian, Thomas Wolf, Friedemann Reinhard, Lloyd CL Hollenberg, Fedor Jelezko, and Jörg Wrachtrup. Electric-field sensing using single diamond spins. *Nature Physics*, 7(6):459–463, 2011.
- [31] VM Acosta, E Bauch, MP Ledbetter, A Waxman, L-S Bouchard, and D Budker. Temperature dependence of the nitrogen-vacancy magnetic resonance in diamond. *Physical review letters*, 104(7):070801, 2010.

- [32] David M Toyli, Christoph D Weis, Gregory D Fuchs, Thomas Schenkel, and David D Awschalom. Chip-scale nanofabrication of single spins and spin arrays in diamond. *Nano letters*, 10(8):3168–3172, 2010.
- [33] Syuto Tamura, Godai Koike, Akira Komatsubara, Tokuyuki Teraji, Shinobu Onoda, Liam P McGuinness, Lachlan Rogers, Boris Naydenov, E Wu, Liu Yan, Fedor Jelezko, Takeshi Ohshima, Junichi Isoya, Takahiro Shinada, and Takashi Tani. Array of bright silicon-vacancy centers in diamond fabricated by low-energy focused ion beam implantation. *Applied Physics Express*, 7(11):115201, 2014.
- [34] Steffen Steinert, Florian Dolde, Philipp Neumann, Andrew Aird, Boris Naydenov, Gopalakrishnan Balasubramanian, Fedor Jelezko, and Joerg Wrachtrup. High sensitivity magnetic imaging using an array of spins in diamond. *Review of scientific instruments*, 81(4):043705, 2010.
- [35] Christian Kurtsiefer, Sonja Mayer, Patrick Zarda, and Harald Weinfurter. Stable solid-state source of single photons. *Physical review letters*, 85(2):290, 2000.
- [36] Alexios Beveratos, Sergei Kühn, Rosa Brouri, Thierry Gacoin, J-P Poizat, and Philippe Grangier. Room temperature stable single-photon source. *The European Physical Journal D-Atomic, Molecular, Optical and Plasma Physics*, 18(2):191–196, 2002.
- [37] Alexander M Zaitsev. *Optical properties of diamond: a data handbook*. Springer Science & Business Media, 2013.

-
- [38] Alp Sipahigil, Michael Lurie Goldman, Emre Togan, Yiwen Chu, Matthew Markham, Daniel J Twitchen, Alexander S Zibrov, Alexander Kubanek, and Mikhail D Lukin. Quantum interference of single photons from remote nitrogen-vacancy centers in diamond. *Physical review letters*, 108(14):143601, 2012.
- [39] Hannes Bernien, Bas Hensen, Wolfgang Pfaff, Gerwin Koolstra, MS Blok, Lucio Robledo, TH Taminiau, Matthew Markham, DJ Twitchen, Lilian Childress, and Ronald Hanson. Heralded entanglement between solid-state qubits separated by three metres. *Nature*, 497(7447):86–90, 2013.
- [40] Gopalakrishnan Balasubramanian, IY Chan, Roman Kolesov, Mohannad Al-Hmoud, Julia Tisler, Chang Shin, Changdong Kim, Aleksander Wojcik, Philip R Hemmer, Anke Krueger, Tobias Hanke, Alfred Leitenstorfer, Rudolf Bratschitsch, Fedor Jelezko, and Jörg Wrachtrup. Nanoscale imaging magnetometry with diamond spins under ambient conditions. *Nature*, 455(7213):648–651, 2008.
- [41] Dirk Englund, Brendan Shields, Kelley Rivoire, Fariba Hatami, Jelena Vuckovic, Hongkun Park, and Mikhail D Lukin. Deterministic coupling of a single nitrogen vacancy center to a photonic crystal cavity. *Nano letters*, 10(10):3922–3926, 2010.
- [42] Andrei Faraon, Paul E Barclay, Charles Santori, Kai-Mei C Fu, and Raymond G Beausoleil. Resonant enhancement of the zero-phonon emission from a colour centre in a diamond cavity. *Nature Photonics*, 5(5):301–305, 2011.

- [43] Janine Riedrich-Möller, Laura Kipfstuhl, Christian Hepp, Elke Neu, Christoph Pauly, Frank Mücklich, Armin Baur, Michael Wandt, Sandra Wolff, Martin Fischer, Stefan Gsell, Matthias Schreck, and Christoph Becher. One-and two-dimensional photonic crystal microcavities in single crystal diamond. *Nature nanotechnology*, 7(1):69–74, 2012.
- [44] Claire A McLellan, Bryan A Myers, Stephan Kraemer, Kenichi Ohno, David D Awschalom, and Ania C Bleszynski Jayich. Patterned formation of highly coherent nitrogen-vacancy centers using a focused electron irradiation technique. *Nano letters*, 16(4):2450–2454, 2016.
- [45] J. Meijer, B. Burchard, M. Domhan, C. Wittmann, Torsten Gaebel, I. Popa, F. Jelezko, and J. Wrachtrup. Generation of single color centers by focused nitrogen implantation. *Applied Physics Letters*, 87(26):261909, 2005.
- [46] Alan T. Collins, Lars Allers, Christopher J.H. Wort, and Geoffrey A. Scarsbrook. The annealing of radiation damage in de beers colourless cvd diamond. *Diamond and Related Materials*, 3(4-6):932–935, 1994.
- [47] Elke Neu, David Steinmetz, Janine Riedrich-Möller, Stefan Gsell, Martin Fischer, Matthias Schreck, and Christoph Becher. Single photon emission from silicon-vacancy colour centres in chemical vapour deposition nano-diamonds on iridium. *New Journal of Physics*, 13(2):025012, 2011.
- [48] Uwe Jantzen, Andrea B Kurz, Daniel S Rudnicki, Clemens Schäfermeier,

- Kay D Jahnke, Ulrik L Andersen, Valery A Davydov, Viatcheslav N Agafonov, Alexander Kubanek, Lachlan J Rogers, and Fedor Jelezko. Nanodiamonds carrying silicon-vacancy quantum emitters with almost lifetime-limited linewidths. *New Journal of Physics*, 18(7):073036, 2016.
- [49] Carsten Arend, Jonas Nils Becker, Hadwig Sternschulte, Doris Steinmüller-Nethl, and Christoph Becher. Photoluminescence excitation and spectral hole burning spectroscopy of silicon vacancy centers in diamond. *Physical Review B*, 94(4):045203, 2016.
- [50] Ke Li, Yu Zhou, A Rasmita, I Aharonovich, and WB Gao. Nonblinking emitters with nearly lifetime-limited linewidths in cvd nanodiamonds. *Physical Review Applied*, 6(2):024010, 2016.
- [51] L. Du Preez. Electron paramagnetic resonance and optical investigations of defect centres in diamond. *University of Witwatersrand*, PhD thesis, 1965.
- [52] J.H.N. Loubser and J.A. Van Wyk. Electron spin resonance in annealed type 1b diamond. *Diamond Res*, 11:4–7, 1977.
- [53] J.H.N. Loubser and J.A. Van Wyk. Electron spin resonance in the study of diamond. *Reports on Progress in Physics*, 41(8):1201, 1978.
- [54] E Van Oort, NB Manson, and M Glasbeek. Optically detected spin coherence of the diamond nv centre in its triplet ground state. *Journal of Physics C: Solid State Physics*, 21(23):4385, 1988.

- [55] Neil B Manson, Xing-Fei He, and Peter TH Fisk. Raman heterodyne detected electron-nuclear-double-resonance measurements of the nitrogen-vacancy center in diamond. *Optics letters*, 15(19):1094–1096, 1990.
- [56] Xing-Fei He, Peter TH Fisk, and Neil B Manson. Autler–townes effect of the photoexcited diamond nitrogen-vacancy center in its triplet ground state. *Journal of applied physics*, 72(1):211–217, 1992.
- [57] Neil B Manson, Xing-Fei He, and Peter TH Fisk. Raman heterodyne studies of the nitrogen-vacancy centre in diamond. *Journal of luminescence*, 53(1-6):49–54, 1992.
- [58] Xing-Fei He, Neil B Manson, and Peter TH Fisk. Paramagnetic resonance of photoexcited n-v defects in diamond. i. level anticrossing in the 3 a ground state. *Physical Review B*, 47(14):8809, 1993.
- [59] David P. DiVincenzo. The physical implementation of quantum computation. *Fortschritte der Physik*, 48(9-11):771–783, 2000.
- [60] A Gruber, A Dräbenstedt, C Tietz, L Fleury, J Wrachtrup, and C Von Borczyskowski. Scanning confocal optical microscopy and magnetic resonance on single defect centers. *Science*, 276(5321):2012–2014, 1997.
- [61] Fedor Jelezko, T Gaebel, I Popa, A Gruber, and Jorg Wrachtrup. Observation of coherent oscillations in a single electron spin. *Physical review letters*, 92(7):076401, 2004.

- [62] I Popa, T Gaebel, M Domhan, C Wittmann, F Jelezko, and J Wrachtrup. Energy levels and decoherence properties of single electron and nuclear spins in a defect center in diamond. *Physical Review B*, 70(20):201203, 2004.
- [63] Ph Tamarat, T Gaebel, JR Rabeau, M Khan, AD Greentree, H Wilson, LCL Hollenberg, S Prawer, P Hemmer, F Jelezko, and J Wrachtrup. Stark shift control of single optical centers in diamond. *Physical review letters*, 97(8):083002, 2006.
- [64] Gopalakrishnan Balasubramanian, Philipp Neumann, Daniel Twitchen, Matthew Markham, Roman Kolesov, Norikazu Mizuochi, Junichi Isoya, Jocelyn Achard, Johannes Beck, Julia Tissler, Vincent Jacques, Philip R. Hemmer, Fedor Jelezko, and Jorg Wrachtrup. Ultralong spin coherence time in isotopically engineered diamond. *Nature materials*, 8(5):383–387, 2009.
- [65] A Batalov, V Jacques, F Kaiser, P Siyushev, P Neumann, LJ Rogers, RL McMurtrie, NB Manson, F Jelezko, and J Wrachtrup. Low temperature studies of the excited-state structure of negatively charged nitrogen-vacancy color centers in diamond. *Physical Review Letters*, 102(19):195506, 2009.
- [66] JP Hadden, JP Harrison, AC Stanley-Clarke, L Marseglia, Y-LD Ho, BR Patton, JL O’Brien, and JG Rarity. Strongly enhanced photon collection from diamond defect centers under microfabricated integrated solid immersion lenses. *Applied Physics Letters*, 97(24):241901, 2010.
- [67] Bas Hensen, H Bernien, AE Dréau, A Reiserer, N Kalb, MS Blok, J Ruitenbergh, RFL Vermeulen, RN Schouten, C Abellán, W Amaya,

- V Pruneri, MW Mitchell, M Markham, DJ Twitchen, D Elkouss, S Wehner, TH Taminiau, and R Hanson. Loophole-free bell inequality violation using electron spins separated by 1.3 kilometres. *Nature*, 526(7575):682–686, 2015.
- [68] Florian Dolde, Ingmar Jakobi, Boris Naydenov, Nan Zhao, Sebastien Pezzagna, Christina Trautmann, Jan Meijer, Philipp Neumann, Fedor Jelezko, and Jörg Wrachtrup. Room-temperature entanglement between single defect spins in diamond. *Nature Physics*, 9(3):139–143, 2013.
- [69] Andrei Faraon, Charles Santori, Zhihong Huang, Victor M Acosta, and Raymond G Beausoleil. Coupling of nitrogen-vacancy centers to photonic crystal cavities in monocrystalline diamond. *Physical review letters*, 109(3):033604, 2012.
- [70] Luozhou Li, Edward H Chen, Jiabao Zheng, Sara L Mouradian, Florian Dolde, Tim Schröder, Sinan Karaveli, Matthew L Markham, Daniel J Twitchen, and Dirk Englund. Efficient photon collection from a nitrogen vacancy center in a circular bullseye grating. *Nano letters*, 15(3):1493–1497, 2015.
- [71] Sam Johnson, PR Dolan, Thomas Grange, AAP Trichet, Gaston Hornecker, Yu-Chen Chen, Laiyi Weng, GM Hughes, AAR Watt, A Auffèves, and Jason M Smith. Tunable cavity coupling of the zero phonon line of a nitrogen-vacancy defect in diamond. *New Journal of Physics*, 17(12):122003, 2015.

- [72] Boris M Chernobrod and Gennady P Berman. Spin microscope based on optically detected magnetic resonance. *Journal of applied physics*, 97(1):014903, 2005.
- [73] Florian Dolde, Marcus W Doherty, Julia Michl, Ingmar Jakobi, Boris Naydenov, Sebastien Pezzagna, Jan Meijer, Philipp Neumann, Fedor Jelezko, Neil B Manson, and Jörg Wrachtrup. Nanoscale detection of a single fundamental charge in ambient conditions using the nv- center in diamond. *Physical review letters*, 112(9):097603, 2014.
- [74] HJ Mamin, M Kim, MH Sherwood, CT Rettner, K Ohno, DD Awschalom, and D Rugar. Nanoscale nuclear magnetic resonance with a nitrogen-vacancy spin sensor. *Science*, 339(6119):557–560, 2013.
- [75] Tobias Staudacher, Fazhan Shi, S Pezzagna, Jan Meijer, Jiangfeng Du, Carlos A Meriles, Friedemann Reinhard, and Joerg Wrachtrup. Nuclear magnetic resonance spectroscopy on a (5-nanometer) 3 sample volume. *Science*, 339(6119):561–563, 2013.
- [76] AG Alekseev, VN Amosov, AV Krasil’nikov, SN Tugarinov, VV Frunze, and A Yu Tsutskikh. Transformation of gr1 defects in annealed natural type iia diamonds. *Technical Physics Letters*, 26(6):496–498, 2000.
- [77] Sébastien Pezzagna, Detlef Rogalla, Dominik Wildanger, Jan Meijer, and Alexander Zaitsev. Creation and nature of optical centres in diamond for single-photon emission—overview and critical remarks. *New Journal of Physics*, 13(3):035024, 2011.

- [78] Lars Allers, Alan T Collins, and Jonathan Hiscock. The annealing of interstitial-related optical centres in type ii natural and cvd diamond. *Diamond and related materials*, 7(2):228–232, 1998.
- [79] T. Yamamoto, T. Umeda, K. Watanabe, S. Onoda, M. L. Markham, D. J. Twitchen, B. Naydenov, L. P. McGuinness, T. Teraji, S. Koizumi, F. Dolde, H. Fedder, J. Honert, J. Wrachtrup, T. Ohshima, F. Jelezko, and J. Isoya. Extending spin coherence times of diamond qubits by high-temperature annealing. *Physical Review B*, 88(7):075206, 2013.
- [80] Boris Naydenov, Friedemann Reinhard, Anke Lämmle, V Richter, Rafi Kalish, Ulrika FS D’Haenens-Johansson, Mark Newton, Fedor Jelezko, and Jörg Wrachtrup. Increasing the coherence time of single electron spins in diamond by high temperature annealing. *Applied Physics Letters*, 97(24):242511, 2010.
- [81] P Neumann, R Kolesov, B Naydenov, J Beck, F Rempp, M Steiner, V Jacques, G Balasubramanian, ML Markham, DJ Twitchen, S Pezzagna, J Meijer, J Twamley, F Jelezko, and J Wrachtrup. Quantum register based on coupled electron spins in a room-temperature solid. *Nature Physics*, 6(4):249–253, 2010.
- [82] T Staudacher, F Ziem, L Häussler, R Stöhr, S Steinert, F Reinhard, J Scharpf, A Denisenko, and J Wrachtrup. Enhancing the spin properties of shallow implanted nitrogen vacancy centers in diamond by epitaxial overgrowth. *Applied Physics Letters*, 101(21):212401, 2012.

- [83] Z Huang, W-D Li, C Santori, VM Acosta, A Faraon, T Ishikawa, W Wu, D Winston, RS Williams, and RG Beausoleil. Diamond nitrogen-vacancy centers created by scanning focused helium ion beam and annealing. *Applied Physics Letters*, 103(8):2013, 2013.
- [84] Felipe Fávaro de Oliveira, S Ali Momenzadeh, Denis Antonov, Jochen Scharpf, Christian Osterkamp, Boris Naydenov, Fedor Jelezko, Andrej Denisenko, and Jörg Wrachtrup. Toward optimized surface δ -profiles of nitrogen-vacancy centers activated by helium irradiation in diamond. *Nano letters*, 16(4):2228–2233, 2016.
- [85] Felipe Fávaro de Oliveira, Seyed Ali Momenzadeh, Denis Antonov, Helmut Fedder, Andrej Denisenko, and Jörg Wrachtrup. On the efficiency of combined ion implantation for the creation of near-surface nitrogen-vacancy centers in diamond. *Physica Status Solidi (a)*, 213(8):1862–6319, 2016.
- [86] Kenichi Ohno, F Joseph Heremans, Lee C Bassett, Bryan A Myers, David M Toyli, Ania C Bleszynski Jayich, Christopher J Palmstrøm, and David D Awschalom. Engineering shallow spins in diamond with nitrogen delta-doping. *Applied Physics Letters*, 101(8):082413, 2012.
- [87] Richard D Simmonds, Patrick S Salter, Alexander Jesacher, and Martin J Booth. Three dimensional laser microfabrication in diamond using a dual adaptive optics system. *Optics express*, 19(24):24122–24128, 2011.

- [88] Yan Liu, Gengxu Chen, Min Song, Xueting Ci, Botao Wu, E Wu, and Heping Zeng. Fabrication of nitrogen vacancy color centers by femtosecond pulse laser illumination. *Optics express*, 21(10):12843–12848, 2013.
- [89] Phillip Sprangle, JR Penano, and Bahman Hafizi. Propagation of intense short laser pulses in the atmosphere. *Physical Review E*, 66(4):046418, 2002.
- [90] Sergei M Pimenov, Andrey A Khomich, Beat Neuenschwander, Beat Jäggi, and Valerio Romano. Picosecond-laser bulk modification induced enhancement of nitrogen-vacancy luminescence in diamond. *JOSA b*, 33(3):B49–B55, 2016.
- [91] M Watanabe, S Juodkazis, H-B Sun, S Matsuo, and H Misawa. Two-photon readout of three-dimensional memory in silica. *Applied Physics Letters*, 77(1):13–15, 2000.
- [92] EN Glezer, M Milosavljevic, L Huang, RJ Finlay, T-H Her, J Paul Callan, and Eric Mazur. Three-dimensional optical storage inside transparent materials. *Optics Letters*, 21(24):2023–2025, 1996.
- [93] SS Mao, Fabien Quéré, Stéphane Guizard, X Mao, RE Russo, Guillaume Petite, and Philippe Martin. Dynamics of femtosecond laser interactions with dielectrics. *Applied Physics A*, 79(7):1695–1709, 2004.
- [94] LV Keldysh. Ionization in the field of a strong electromagnetic wave. *Sov. Phys. JETP*, 20(5):1307–1314, 1965.
- [95] Scott C Jones, Peter Braunlich, R Thomas Casper, Xiao-An Shen, and Paul Kelly. Recent progress on laser-induced modifications and intrinsic bulk

- damage of wide-gap optical materials. *Optical Engineering*, 28(10):281039, 1989.
- [96] Stefano Lagomarsino, Silvio Sciortino, Boyan Obreshkov, Tzveta Apostolova, Chiara Corsi, Marco Bellini, Eleni Berdermann, and Christian J Schmidt. Photoionization of monocrystalline cvd diamond irradiated with ultrashort intense laser pulse. *Physical Review B*, 93(8):085128, 2016.
- [97] J Koike, DM Parkin, and TE Mitchell. Displacement threshold energy for type iia diamond. *Applied physics letters*, 60(12):1450–1452, 1992.
- [98] Diego Delgado and Rafael Vila. Statistical molecular dynamics study of displacement energies in diamond. *Journal of Nuclear Materials*, 419(1):32–38, 2011.
- [99] X. J. Hu, Y. B. Dai, R. B. Li, H. S. Shen, and X. C. He. The diffusion of vacancies near a diamond (001) surface. *Solid state communications*, 122(1):45–48, 2002.
- [100] A. Mainwood. Point defects in natural and synthetic diamond: What they can tell us about cvd diamond. *physica status solidi (a)*, 172(1):25–35, 1999.
- [101] S. J. Breuer and P. R. Briddon. Ab initio investigation of the native defects in diamond and self-diffusion. *Physical Review B*, 51(11):6984, 1995.
- [102] J. Bernholc, A. Antonelli, T. M. Del Sole, Y. Bar-Yam, and S. T. Pantelides. Mechanism of self-diffusion in diamond. *Physical review letters*, 61(23):2689, 1988.

-
- [103] J. O. Orwa, K. W. Nugent, D. N. Jamieson, and S. Prawer. Raman investigation of damage caused by deep ion implantation in diamond. *Physical Review B*, 62(9):5461, 2000.
- [104] I Aharonovich, S Castelletto, DA Simpson, CH Su, AD Greentree, and S Prawer. Diamond-based single-photon emitters. *Reports on progress in Physics*, 74(7):076501, 2011.
- [105] LJ Rogers, S Armstrong, MJ Sellars, and NB Manson. Infrared emission of the nv centre in diamond: Zeeman and uniaxial stress studies. *New Journal of Physics*, 10(10):103024, 2008.
- [106] Janik Wolters. *Integrated quantum hybrid systems*. CRC Press, 2015.
- [107] A Lenef and SC Rand. Electronic structure of the n-v center in diamond: Theory. *Physical Review B*, 53(20):13441, 1996.
- [108] LJ Rogers, RL McMurtrie, MJ Sellars, and NB Manson. Time-averaging within the excited state of the nitrogen-vacancy centre in diamond. *New Journal of Physics*, 11(6):063007, 2009.
- [109] Charles Santori, Philippe Tamarat, Philipp Neumann, Jörg Wrachtrup, David Fattal, Raymond G Beausoleil, James Rabeau, Paolo Olivero, Andrew D Greentree, Steven Prawer, Fedor Jelezko, and Philip Hemmer. Coherent population trapping of single spins in diamond under optical excitation. *Physical review letters*, 97(24):247401, 2006.
- [110] Manuel Cardona and Y Yu Peter. *Fundamentals of semiconductors: Physics and materials properties*. Springer, 2005.

- [111] Gordon Davies and MF Hamer. Optical studies of the 1.945 eV vibronic band in diamond. In *Proceedings of the Royal Society of London A: Mathematical, Physical and Engineering Sciences*, volume 348, pages 285–298. The Royal Society, 1976.
- [112] T Gaebel, M Domhan, C Wittmann, I Popa, F Jelezko, J Rabeau, A Greentree, S Prawer, E Trajkov, Philip R Hemmer, and J Wrachtrup. Photochromism in single nitrogen-vacancy defect in diamond. *Applied Physics B*, 82(2):243–246, 2006.
- [113] G Waldherr, J Beck, M Steiner, P Neumann, A Gali, Th Frauenheim, F Jelezko, and J Wrachtrup. Dark states of single nitrogen-vacancy centers in diamond unraveled by single shot nmr. *Physical review letters*, 106(15):157601, 2011.
- [114] Taras Plakhotnik, Marcus W Doherty, and Neil B Manson. Electron-phonon processes of the nitrogen-vacancy center in diamond. *Physical Review B*, 92(8):081203, 2015.
- [115] Andrew D Greentree, Paolo Olivero, Martin Draganski, Elizabeth Trajkov, James R Rabeau, Patrick Reichart, Brant C Gibson, Sergey Rubanov, Shane T Huntington, David N Jamieson, and Steven Prawer. Critical components for diamond-based quantum coherent devices. *Journal of Physics: Condensed Matter*, 18(21):S825, 2006.

- [116] NB Manson, JP Harrison, and MJ Sellars. Nitrogen-vacancy center in diamond: Model of the electronic structure and associated dynamics. *Physical Review B*, 74(10):104303, 2006.
- [117] P Neumann, R Kolesov, V Jacques, J Beck, J Tisler, A Batalov, Lachlan Rogers, NB Manson, G Balasubramanian, F Jelezko, and J Wrachtrup. Excited-state spectroscopy of single nv defects in diamond using optically detected magnetic resonance. *New Journal of Physics*, 11(1):013017, 2009.
- [118] Solveig Felton, AM Edmonds, Mark E Newton, PM Martineau, D Fisher, and DJ Twitchen. Electron paramagnetic resonance studies of the neutral nitrogen vacancy in diamond. *Physical Review B*, 77(8):081201, 2008.
- [119] M Steiner, P Neumann, J Beck, F Jelezko, and J Wrachtrup. Universal enhancement of the optical readout fidelity of single electron spins at nitrogen-vacancy centers in diamond. *Physical Review B*, 81(3):035205, 2010.
- [120] GD Fuchs, VV Dobrovitski, R Hanson, A Batra, CD Weis, T Schenkel, and DD Awschalom. Excited-state spectroscopy using single spin manipulation in diamond. *Physical review letters*, 101(11):117601, 2008.
- [121] S Felton, AM Edmonds, ME Newton, PM Martineau, D Fisher, DJ Twitchen, and JM Baker. Hyperfine interaction in the ground state of the negatively charged nitrogen vacancy center in diamond. *Physical Review B*, 79(7):075203, 2009.

- [122] R Hanson, FM Mendoza, RJ Epstein, and DD Awschalom. Polarization and readout of coupled single spins in diamond. *Physical review letters*, 97(8):087601, 2006.
- [123] N Mizuochi, P Neumann, F Rempp, J Beck, V Jacques, P Siyushev, K Nakamura, DJ Twitchen, H Watanabe, S Yamasaki, F Jelezko, and J Wrachtrup. Coherence of single spins coupled to a nuclear spin bath of varying density. *Physical review B*, 80(4):041201, 2009.
- [124] D. Antonov, T. Häußermann, A. Aird, J. Roth, H.-R. Trebin, C. Müller, L. McGuinness, F. Jelezko, T. Yamamoto, J. Isoya, S. Pezzagna, J. Meijer, and J. Wrachtrup. Statistical investigations on nitrogen-vacancy center creation. *Applied Physics Letters*, 104(1):012105, 2014.
- [125] Helmut Mehrer. *Diffusion in solids: fundamentals, methods, materials, diffusion-controlled processes*. Springer Science & Business Media, 2007.
- [126] Bangshan Sun, Patrick S Salter, and Martin J Booth. High conductivity micro-wires in diamond following arbitrary paths. *Applied Physics Letters*, 105(23):231105, 2014.
- [127] B C Stuart, M D Feit, S Herman, AM Rubenchik, BW Shore, and MD Perry. Nanosecond-to-femtosecond laser-induced breakdown in dielectrics. *Physical review B*, 53(4):1749, 1996.
- [128] Sylke Uhlmann, Thomas Frauenheim, and Uwe Stephan. Molecular-dynamics subplantation studies of carbon beneath the diamond (111) surface. *Physical Review B*, 51(7):4541, 1995.

- [129] Margarita Lesik, Piernicola Spinicelli, Sébastien Pezzagna, Patrick Happel, Vincent Jacques, Olivier Salord, Bernard Rasser, Anne Delobbe, Pierre Sudraud, Alexandre Tallaire, Jan Meijer, and Jean-François Roch. Maskless and targeted creation of arrays of colour centres in diamond using focused ion beam technology. *physica status solidi (a)*, 210(10):2055–2059, 2013.
- [130] Barbara A Fairchild, Sergey Rubanov, Desmond WM Lau, Marc Robinson, Irene Suarez-Martinez, Nigel Marks, Andrew D Greentree, Dougal McCulloch, and Steven Prawer. Mechanism for the amorphisation of diamond. *Advanced Materials*, 24(15):2024–2029, 2012.
- [131] C Uzan-Saguy, C Cytermann, R Brener, V Richter, M Shaanan, and R Kalish. Damage threshold for ion-beam induced graphitization of diamond. *Applied Physics Letters*, 67(9):1194–1196, 1995.
- [132] Toyofumi Ishikawa, Kai-Mei C Fu, Charles Santori, Victor M Acosta, Raymond G Beausoleil, Hideyuki Watanabe, Shinichi Shikata, and Kohei M Itoh. Optical and spin coherence properties of nitrogen-vacancy centers placed in a 100 nm thick isotopically purified diamond layer. *Nano letters*, 12(4):2083–2087, 2012.
- [133] N Aslam, G Waldherr, P Neumann, F Jelezko, and J Wrachtrup. Photo-induced ionization dynamics of the nitrogen vacancy defect in diamond investigated by single-shot charge state detection. *New Journal of Physics*, 15(1):013064, 2013.

-
- [134] V.M. Acosta, C. Santori, A. Faraon, Z. Huang, K.-MC. Fu, A. Stacey, D.A. Simpson, K. Ganesan, S. Tomljenovic-Hanic, A.D. Greentree, S. Prawer, and R. G. Beusoleil. Dynamic stabilization of the optical resonances of single nitrogen-vacancy centers in diamond. *Physical review letters*, 108(20):206401, 2012.
- [135] Yumin Shen, Timothy M Sweeney, and Hailin Wang. Zero-phonon linewidth of single nitrogen vacancy centers in diamond nanocrystals. *Physical Review B*, 77(3):033201, 2008.
- [136] Yiwen Chu and Mikhail D Lukin. Quantum optics with nitrogen-vacancy centers in diamond. *arXiv:1504.05990*, 2015.
- [137] Felipe Fávoro de Oliveira, Denis Antonov, Ya Wang, Philipp Neumann, S Ali Momenzadeh, Timo Häußermann, Alberto Pasquarelli, Andrej Denisenko, and Jörg Wrachtrup. Tailoring spin defects in diamond. *arXiv:1701.07055*, 2017.
- [138] Linh My Pham, David Le Sage, Paul L Stanwix, Tsun Kwan Yeung, D Glenn, Alexei Trifonov, Paola Cappellaro, PR Hemmer, Mikhail D Lukin, Hongkun Park, Amir Yacoby, and Roland Walsworth. Magnetic field imaging with nitrogen-vacancy ensembles. *New Journal of Physics*, 13(4):045021, 2011.
- [139] Arnaud Courvoisier, Martin J Booth, and Patrick S Salter. Inscription of 3d waveguides in diamond using an ultrafast laser. *Applied Physics Letters*, 109(3):031109, 2016.

- [140] Belén Sotillo, Vibhav Bharadwaj, JP Hadden, Masaaki Sakakura, Andrea Chiappini, Toney Teddy Fernandez, Stefano Longhi, Ottavia Jedrkiewicz, Yasuhiko Shimotsuma, Luigino Criante, Roberto Osellame, Gianluca Galzerano, Maurizio Ferrari, Kiyotaka Miura, Roberta Ramponi, Paul E Barclay, and Shane Michael Eaton. Diamond photonics platform enabled by femtosecond laser writing. *Scientific reports*, 6(35566), 2016.
- [141] TV Kononenko, MS Komlenok, VP Pashinin, SM Pimenov, VI Konov, Martin Neff, Valerio Romano, and Willy Lüthy. Femtosecond laser microstructuring in the bulk of diamond. *Diamond and related materials*, 18(2):196–199, 2009.
- [142] Petr Siyushev, Mathias H Metsch, Aroosa Ijaz, Jan M Binder, Mihir K Bhaskar, Denis D Sukachev, Alp Sipahigil, Ruffin E Evans, Christian T Nguyen, Mikhail D Lukin, Philip R. Hemmer, Yuri N. Palyanov, Igor N. Kupriyanov, Yuri M. Borzdov, Lachlan J. Rogers, and Fedor Jelezko. Optical and microwave control of germanium-vacancy center spins in diamond. *arXiv:1612.02947*, 2016.
- [143] Mihir K Bhaskar, Denis D Sukachev, Alp Sipahigil, Ruffin E Evans, Michael J Burek, Christian T Nguyen, Lachlan J Rogers, Petr Siyushev, Mathias H Metsch, Hongkun Park, Fedor Jelezko, Marko Loncar, and Mikhail D Lukin. Quantum nonlinear optics with a germanium-vacancy color center in a nanoscale diamond waveguide. *arXiv:1612.03036*, 2016.
- [144] Lachlan J Rogers, Kay D Jahnke, T Teraji, Luca Marseglia, Christoph Müller, Boris Naydenov, Hardy Schauffert, C Kranz, Junichi Isoya, Liam P

McGuinness, and Fedor Jelezko. Multiple intrinsically identical single photon emitters in the solid-state. *Nature Communications*, 5(4739), 2014.